



**“STUDIES ON PREPARATION AND CHARACTERIZATION  
OF SPRAY DEPOSITED  $Zn_2SnO_4$  THIN FILMS”**

**A THESIS SUBMITTED TO  
BHARATI VIDYAPEETH UNIVERSITY, PUNE  
FOR AWARD OF DEGREE OF  
DOCTOR OF PHILOSOPHY  
IN  
PHYSICS  
UNDER THE FACULTY OF SCIENCE**

**SUBMITTED BY  
Mr. MAHENDRA ASARAM PATIL  
UNDER THE GUIDENCE OF  
Dr. H. P. DESHMUKH**

**BHARATI VIDYAPEETH UNIVERSITY  
PUNE- 411030 (INDIA)**

**JULY 2015**

**Dedicated  
To  
*My Beloved Father***

***Late Asaram Mahadu Patil***

***and***

***My Father in Law***

***Late Hindurao Pandurang  
Patil***



## **CERTIFICATE**

This is certified that work incorporated in the thesis entitled **“Studies on Preparation and Characterization of Spray Deposited  $Zn_2SnO_4$  Thin Films”** for the degree of **“Doctor of Philosophy”** in the subject of **Physics** under the faculty of science, has been carried out by **Mr. Mahendra Asaram Patil** in the Department of Physics, Yashwantrao Mohite College, Bharati Vidyapeeth University, Pune (India), during the period from July, 2009 to May 2015 under the guidance of **Dr. H. P. Deshmukh.**

Place: Pune

Date:

Principal  
Y. M. College, Pune

## **CERTIFICATE OF GUIDE**

This is to certify that the work incorporated in the thesis entitled, **“Studies on Preparation and Characterization of Spray Deposited Zn<sub>2</sub>SnO<sub>4</sub> Thin Films”** submitted by **Mr. Mahendra Asaram Patil** for the degree of **‘Doctor of Philosophy’** in the subject of **Physics** under the faculty of **science** has been carried out in the Department of Physics, Bharati Vidyapeeth’s Y. M. College, Pune during the period from July, 2009 to May 2015 under my direct supervision/guidance.

Place: Pune

Date:

**Dr. H. P. Deshmukh**

Research Guide

## DECLARATION BY THE CANDIDATE

I hereby declare that the thesis entitled, "**Studies on Preparation and Characterization of Spray Deposited Zn<sub>2</sub>SnO<sub>4</sub> Thin Films**" submitted by me to the Bharati Vidyapeeth University, Pune for the degree of Doctor of Philosophy (Ph.D) in Physics under the Science is original piece of work carried out by me under the supervision of Dr. H. P. Deshmukh. I further declare that it has not been submitted to this or any other university or Institution for the award of any degree or Diploma.

I also confirm that all the material which I have borrowed from other sources and incorporated in this thesis is duly acknowledged. If any material is not duly acknowledged and found incorporated in this thesis, it is entirely my responsibility. I am fully aware of the implications of any such act which might have been committed by advertently or inadvertently.

I further declare that the material obtained from other sources has been duly acknowledged in the thesis.

Place: Pune

Date:

**(Mr. Mahendra A. Patil)**

Research student

## ACKNOWLEDGEMENT

*It gives me great pleasure to express my sincere thanks to my research guide **Dr.H.P. Deshmukh** Ex- Head Department of Physics ,Ex-Vice-principal, Y.M.College, Bharati Vidhyapeeth , Pune , who had given me constant guidance , valuable suggestions , constant stimulation and encouragement during the entire tenure of research work.*

*I am greatly indebted to **Hon'ble Dr. Patangrao Kadam , Founder-chancellor** and **Hon'ble Prof. Dr. Shivajirao Kadam Vice-chancellor** , Bharati Vidyapeeth University, Pune as they have been a great source of inspiration.*

*I owe my sincere thanks to **principal Prof.K.D. Jadhav** ,Y.M.College, Pune for providing necessary laboratory facilities and valuable help when I needed it during my research work. I am also thankful to **Dr.B.N.Pawar** Head, Department of Physics and Vice-Principal, Y.M.College, Pune.*

*I am very pleased to acknowledge my sincere thanks to **Prof. Keshav Rajpure**, Shivaji University, Kolhapur, who introduced me to the world of research and development with great enthusiasm and encouragement during various stages of research work. I am also thankful to **Dr. Satish Ogale**, NCL Pune, **Prof. P. S. Patil** and **Prof. Dr.V.J. Phulari**, Dept. Physics, **Prof. Dr. D. V. Muley, Registrar**, Shivaji University, Kolhapur for providing time to time support to do some research work in their laboratories and other support.*

*I am grateful to **Dr. Arvind Bhurungale, Principal**, S.M.Joshi College Hadapsar, Pune for extending spirit and encourage during entire tenure of my research work. I am also grateful to **Dr. Arun Andhale, Principal** Mahatma Phule Mahavidyalaya Pimpri, Pune for teacher fellowship and his kind co-operation during my research work.*

*I am thankful to **Pri. Ashok Mahadar, Pri. Deepa Mahanawar, Pri. Dr. N.S. Gaikwad**, for their long time support and continuous inspiration.*

*Words are not sufficient to express my sincere thanks to **Dr. Sarfaraj Mujawar** and **Mr. Vinayak Ganbavle** for sharing their research experience, suggestions and help in my research work. I also extend my thanks to **Dr. Vivek Rane, Akbar Inamdar**, South Korea, **Dr. Datta Mhamane, Anil Suryawanshi, Mrs. Shruti Agarakar, Dr. Omkar Game, Vishal Thakre** NCL Pune and **Namdeo Harale, Archana kamble, Santosh, Amit, Ms. Sumayya, Ms. Shahin** Dept. of Physics Shivaji University, Kolhapur. Their help for sample characterization was immense.*

*I wish to express my thanks to **Dr. A. M. Dhumal** (vice principal), **Dr. R.S.Nimbalkar (HOD)**, my colleagues **Mrs. S. H. Pisal, Dr. M.L. Dongare, Prof. Jade, Dr. J. A. Magdum, Dr. S. P. Khunte, Mr. B. K. Waghmode, Dr. Date, Dr. Sanjay Mesri, Dr.Pandurang Lohote, Mr. Uddhav Ghodke, Ashwini, Nilrmala, Anjana, Vishal** and all teaching and non-teaching staff of Mahatma Phule college, Pimpri and S. M. Joshi college, Hadapsar for their kind co-operation during my research work.*

*I greatly appreciate the help from my co-workers **Mr. R.S. Gaikwad, Mrs. Guari Patil, Mrs. Shukla, Mr. Pradeep Atre, Mr. Sudhir Wavle , shri Tanaji kadam**, also all teaching and non-teaching staff of Y. M. College Pune.*

*I also my deep sense of gratitude to my beloved mother **Smt. Jayawantabai** and mother in law **Smt. Ushadevi**, without their constant support it could have been quite impossible for me to complete this task.*

*I must express my gratefulness to my relatives **Ad. B. K. Patil, Ad. Pravin Patil, Ad. Datta Patil, Avinash Patil, Ad. Ganesh Patil, Mr. B.S. Thorat, Tai, Usha, Bharati, Chhaya, Kanchan, Dr.Jeevan and Dr.Archana** for helping me every way.*

*I would like to take this opportunity to express my presumable gratitude to my wife **Dr. Indira** who always supported and kept me going towards completion of this work. I have no words to express my feelings for my daughters **Mrudula** and **Bhargavi** for their constant support, patience and understanding.*

*I dedicate all this work to my beloved father **Late Asaram Mahadu Patil** who encouraged during my childhood and education and my father in law **Late Hindurao Pandurang Patil** who gave me moral support so I could reach at this stage today.*

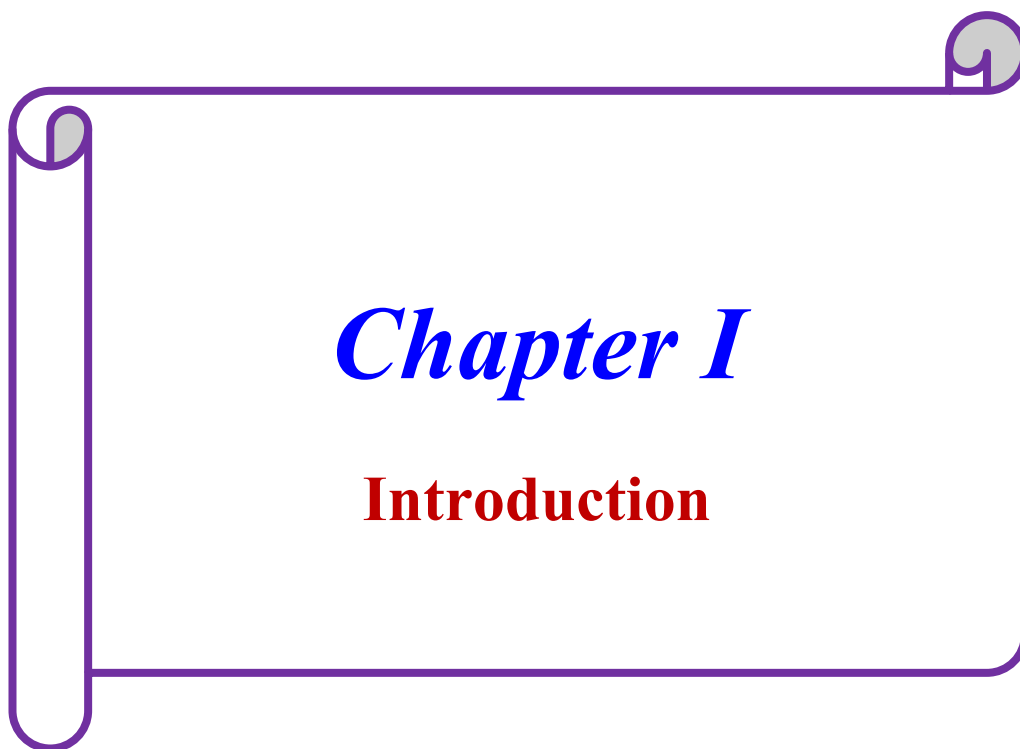
**Pune**

**July, 2015.**

**Mahendra Asaram Patil**

# INDEX

<b>CHAPTER NO.</b>	<b>CHAPTER TITLE</b>	<b>PAGE NO.</b>
<b>I</b>	Introduction	<b>9</b>
<b>II</b>	Thin Film Deposition and Characterization Techniques	<b>46</b>
<b>III-A</b>	Gas Sensing Properties of Zn <sub>2</sub> SnO <sub>4</sub> Thin Films Prepared by Spray Pyrolysis Technique using Alcohol as solvent	<b>67</b>
<b>III-B</b>	Gas Sensing Properties of Zn <sub>2</sub> SnO <sub>4</sub> Thin Films Prepared by Spray Pyrolysis Technique using water as solvent	<b>94</b>
<b>IV</b>	Spray Deposited Zn <sub>2</sub> SnO <sub>4</sub> thin films and their Dye Sensitized Solar Cell properties.	<b>117</b>
<b>V</b>	Photoelectrochemical Properties of Zn <sub>2</sub> SnO <sub>4</sub> /CdS Thin Films	<b>160</b>
<b>VI</b>	Summary and conclusion	<b>190</b>



**INDEX**  
**Chapter I**  
**Introduction**

- 1.1. Introduction
- 1.2 Crystal structure of Zinc Stannate
- 1.3 physical properties of Zinc Stannate
- 1.4 Applications of Zinc Stannate
  - 1.4.1 Gas Sensing
  - 1.4.2 Dye-Sensitized Solar Cell (DSSC)
  - 1.4.3 Lithium-ion Batteries
  - 1.4.4 Photo-catalysis
- 1.5 Introduction to Gas Sensing
  - 1.5.1 Applications of gas sensors
  - 1.5.2 Classification of gas sensor
  - 1.5.3 Metal Oxide semiconductor (MOS) gas sensors
  - 1.5.4 Gas sensing mechanism of MOS gas sensors
  - 1.5.5 Potential barrier model - gas sensing mechanism of MOS gas sensor
  - 1.5.6 Characteristics of gas sensor.
- 1.6 Introduction of Solar cell:
  - 1.6.1 Generations of Solar cells:
  - 1.6.2 Characteristics of Solar cells:
- 1.7 Survey of literature based on Synthesis methods
- 1.8 Applications based survey of literature
- 1.9 Orientation of the problem

# CHAPTER I

## Introduction

### 1.1 Introduction

The material science is the study of materials having long history right from Stone to Steel age and Semiconductor age. Presently, the semiconductor age together with nanotechnology age have had a profound impact on human kind as it was never before even though there were reports of using nanomaterials in the B.C. era. It is a fact that the research in nanotechnology has renewed the interest in material science with no exception to semiconducting materials. During 1960's, the importance of silicon (Si) and germanium (Ge) came to notice, since then binary semiconducting oxides have created huge interest.

The materials of interest for these applications were ZnO, TiO<sub>2</sub> and SnO<sub>2</sub>. With the advancement in material science and technology, there is an urgent need of engineered materials with precise material properties for specific applications. This gives rise to the development of ternary oxides from II-IV-VI groups of oxides as shown in Fig. 1.1

	III	IV	V	VI
	B 5	C 6	N 7	O 8
II	Al 13	Si 14	P 15	S 16
Zn 30	Ga 31	Ge 32	As 33	Se 34
Cd 48	In 49	Sn 50	Sb 51	Te 52
Hg 80	Tl 81	Pb 82	Bi 83	Po 84

**Figure 1.1 II-IV-VI group elements used for ternary oxides**

It is seen from the literature review that Zinc Stannate can be used as a base material for the above mentioned applications because of its extraordinary properties like more chemical stability [1] and high electron mobility [2] compared to binary semiconducting oxides. The properties like comparable

electrical conductivity [3-5] and attractive optical properties [5] of ternary semiconducting oxides make them suitable for applications in solar cells [6, 7], gas and humidity sensing [8-12], as a photocatalyst [13] and electrode materials for Lithium ion battery [14].

Out of the available ternary oxides from group II-IV-VI, only  $Zn_2SnO_4$  can be preferred because they are beneficial than ternary oxides containing cadmium (Cd) and lead (Pb) from environment point of view. Although there are very few reports and applications (such as flame retardant and smoke suppressant [15, 16]) of using  $Zn_2SnO_4$ , there is a need to work on  $Zn_2SnO_4$  by using novel material preparation and fabrication techniques to facilitate the wide range of applications.

## 1.2 Crystal structure of Zinc Stannate

Zinc stannate is available in two forms. One, a metastable form, which is known as zinc meta-stannate ( $ZnSnO_3$ ) is formed at temperature in the range of 300-500 °C [17]. The face-centered perovskite structure of Metastable  $ZnSnO_3$  is shown in Figure 2 (a).

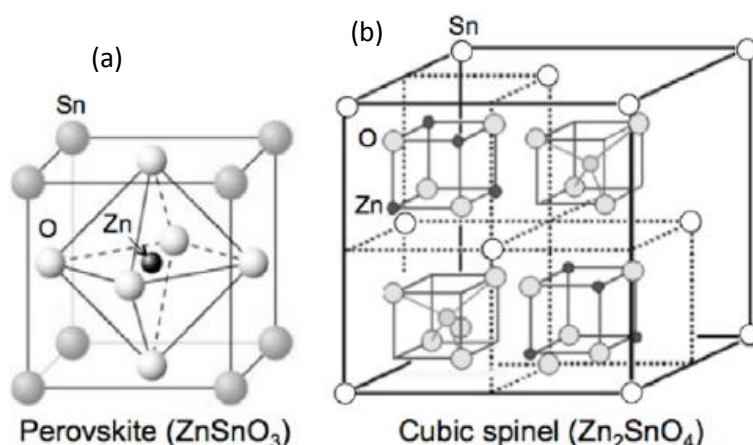


**Figure 1.2 (a) Perovskite  $ZnSO_3$  structure (b) cubic spinel structure of  $Zn_2SnO_4$**

A stable form of zinc stannate is formed above 600°C, which is known as zinc orthostannate ( $Zn_2SnO_4$ ) [17]. Fig. 2 (b) shows cubic spinel structure of the orthostannate  $Zn_2SnO_4$ . The phase pure synthesis of  $Zn_2SnO_4$  by using thermal

evaporation (high temperature) is difficult because the final product formed generally results in an impure phase [17].

### 1.3 physical properties of Zinc Stannate

Some important physical properties of Zinc Stannate are enlisted in Table 1.1.

**Table 1.1 physical properties of Zinc Stannate.**

Property	Particulars
Crystal system	Cubic
Space group	Fd3m
Space group number	227
a (Å): b (Å): c (Å)	8.6500
Alpha (°): Beta (°): Gamma (°):	90.0000
No. of formula units per unit cell (Z)	8.00
Optical Band gap at 300 K ( $E_g$ )	3.6 eV
Electron Effective mass ( $m_n^*/m_o$ )	0.16 – 0.26
Calculated Effective density of states ( $N_c$ )	$1.6-3.3 \times 10^{18} \text{ cm}^{-3}$
Resistivity	$10^{-2} \Omega\text{-cm}$

In last few decades the global research is catered around the environmental problems such as detection of toxic and hazardous gases, treatment of effluents (organic dyes and chemicals), energy generation and storage issues, medicine and agriculture. Gas sensing, dye-sensitized solar cell, rechargeable batteries with longer life and photo-catalysis are the areas of prime importance among the number of research areas in above mentioned fields. The backbone of the research in these areas is materials and their technologies in use. Some of the recent reports corresponding to the development in these fields are presented below.

### 1.4 Fields of application of Zinc Stannate

#### 1.4.1 Gas Sensing

Now a days environmental pollution is a global problem which urgently needs reliable and selective solid state sensors for monitoring automobile

exhaust and air quality. The development of sensors have been prompted because of the requirement to control the hazardous gases as volatile materials. MOS sensors have been used for detecting combustible and toxic gases. But their use have been limited because of more costly approach regarding sensitivity, selectivity and stability. The performance response of the materials have been significantly increased due to recent advances in the nanomaterials providing increase in the surface area. The performance of gas sensor might be uplifted due to the properties of nanoparticles such as increased surface to volume ratio and activity [18]. A lot of work is being carried out in gas sensors area. The nanostructured oxide semiconducting ceramics has been used as gas sensor which found to be more sensitive for LPG, Ethanol and Acetone [18], Chlorine [19], Liquid Petroleum Gas (LPG) only [20], H<sub>2</sub>S, NH<sub>3</sub> gas [21-24] etc.

#### **1.4.2 Dye-Sensitized Solar Cell (DSSC)**

The dye-sensitized solar cell (DSSC) is the focus of much research around the world till now since the pioneering work by Prof. Gratzel [25]. Since 1991, there has been noticeable progress in this field but not commercialized to large extent. A DSSC consist of two glass plates with a transparent conducting oxide (TCO) coating as the substrate. One glass plate coated with a nanocrystalline semiconductor layer and sensitized to visible light by an adsorbed dye behaves as a photo electrode. The other conducting glass works as the counter electrode, which is generally coated with metals like platinum, aluminium, copper etc.

The gap between the two electrodes is filled with an electrolyte. An electrolyte is used to fill the gap of the electrodes. The performance of the DSSC depends on dyes, electrolytes, nanocrystalline electrodes and counter electrodes [26]. Recently, ZTO has also been explored as semiconductor layer in DSSC owing to its band gap and stability.

#### **1.4.3 Lithium-ion Batteries**

Li-ion batteries is the key area of research owing to their high volumetric and gravimetric energy density. This technology has captured the market of electronic devices including cellular phones, lap-top computers and personal digital assistants (PDAs) [27]. But, the nanomaterial research is expected to solve two important issues of stability and durability regarding this. It is possible to

solve this problem by using composite electrodes made up of multifunctional materials. To gain high energy density, such materials should be electrochemically active; it should contain electronic and ionic conductor additives so that there will be proper transfer of electrons and ions at the electrode takes place.

One more requirement is that, these electrodes should exhibit a good mechanical characteristic for easy handling and guaranteed cell lifetime. ZTO can act as an electrode material and can fulfil some of the requirements mentioned above.

#### **1.4.4 Photo-catalysis**

It is necessary to remove or destroy the Organic chemicals (acting as pollutants) present in waste water of domestic and industrial effluents before discharging them into nature. Requirements of an ideal photocatalyst are that, they must be stable, cheap, harmless and extremely photoactive. One more important need to degrade organic compounds is that the redox potential of the  $H_2O/^*OH$  couple should lie within the band gap of the semiconductor [28].  $TiO_2$ ,  $WO_3$ ,  $SrTiO_3$ ,  $Fe_2O_3$ ,  $ZnO$ ,  $ZnS$ ,  $CdS$  and  $ZTO$  etc are examples semiconductors used for the photo-catalysis because of their proper band gap energies. Since  $ZTO$  possess suitable band gap and stability of performance, there is large research on  $ZTO$  as a competent photocatalytic material.

#### **1.5 Introduction to Gas Sensing**

The atmospheric pollution can be caused by stationary or mobile sources. Thermal power stations, hoses, oil refineries, metal refineries, chemical plants are stationary emitting sources while trains, automobiles and ships etc. are mobile sources. Hence to control deterioration of environment, detection and monitoring the pollution is quite necessary. There are different fields utilizing gas sensors.

##### **1.5.1 Applications of gas sensors**

Since there are extensive applications of gas sensing technology in various areas, it becomes very important technology in day to day life of human being. These applications are listed in Table 1.2.

**Table 1.2 Applications of gas sensor along with examples.**

<b>Field</b>	<b>Examples</b>	<b>References</b>
<b>Automobiles</b>	Filter control	29-41
	Polluting gases detection	
	Alcohol breath test	
	Car ventilation control	
<b>Environmental control</b>	Pollution monitoring	42-50
	Weather stations	
<b>Industrial production</b>	Process control	51-65
	Fermentation control	
	Gas detection in mines	
<b>Indoor air quality</b>	Air purifiers	66-74
	Cooking control	
	Ventilation control	
<b>Medicine</b>	Breath analysis	75-88
	Disease detection	

### **1.5.2 Classification of gas sensor**

Jacob Fraden [89] defined a general sensor as, “A sensor is a device that receives or stimulus and responds with an electrical signal.”

Another definition particularly, a gas sensor is, “A chemical sensor is a device that transforms chemical information, ranging from the concentration of a specific sample component to total composition analysis, into an analytically useful signal” [90]. The principle of gas sensor is based on detecting the change in any property of the sensor like resistance [91], capacitance [92], work function [93], mass [94] and impedance [95] at the time of interaction between the gas and sensor.

Generally sensor has two components a receptor and a transducer. The receptor translates chemical information into a suitable form of energy that transducer can measure. Later on transducer convert it as an electrical signal. There are number of ways to classify gas sensors. According to one type, classification based on the operating principle of the receptor, sensors can be categorised into chemical sensors and physical sensors. The chemical reaction between gas molecules and the receptor occurs in chemical sensors. However in physical sensor, there is physical change in parameters like, refractive index, temperature, conductivity, absorbance, mass takes place instead of chemical reaction. Magnetic sensor, acoustic sensor, pressure sensor, optical sensor are some examples of physical sensors. Other possible classifications are based on field of application, method of synthesis, sensor material [90].

The general and commonly used classification consist of two groups; one based on the change in electrical properties and other based on change in other properties like thermal, chemical, optical. This classification is represented in Figure 1.3.

First group, where change in electrical properties takes place consists of chemi-resistive, electrochemical, impedencemetric, capacitive, metal oxide field effect transistor gas sensors. Electrochemical sensors work on the principle that change in the voltage or current is produced due oxidation or reduction of the analyte gas at the electrode [96]. They are further divided into potentiometric and amperometric gas sensors. Electrochemical sensors can be used repeatedly [97]. Change in impedance of the sensor electrode can be noted by impedencemetric gas sensor using single electrode. In case of capacitive sensor, change in thickness of the dielectric layer is measured [97]. The working principle of MOSFET gas sensor is to measure the change in threshold voltage when interaction of the gas occurs with gate material [98].

Chemiresistive sensors are well accepted among the sensors based on electrical properties [99, 100]. They include Metal Oxide Semiconductors (MOS), polymers and carbon nanotubes. High sensitivity and fast response are main advantages of MOS sensors. MOS based sensors are durable, inexpensive easy to fabricate [101]. They are highly sensitive in nano-crystalline form. Polymers are used in case of detection of some volatile organic compounds (used

in household products and industrial processes) which cannot be detected by MOS sensors.

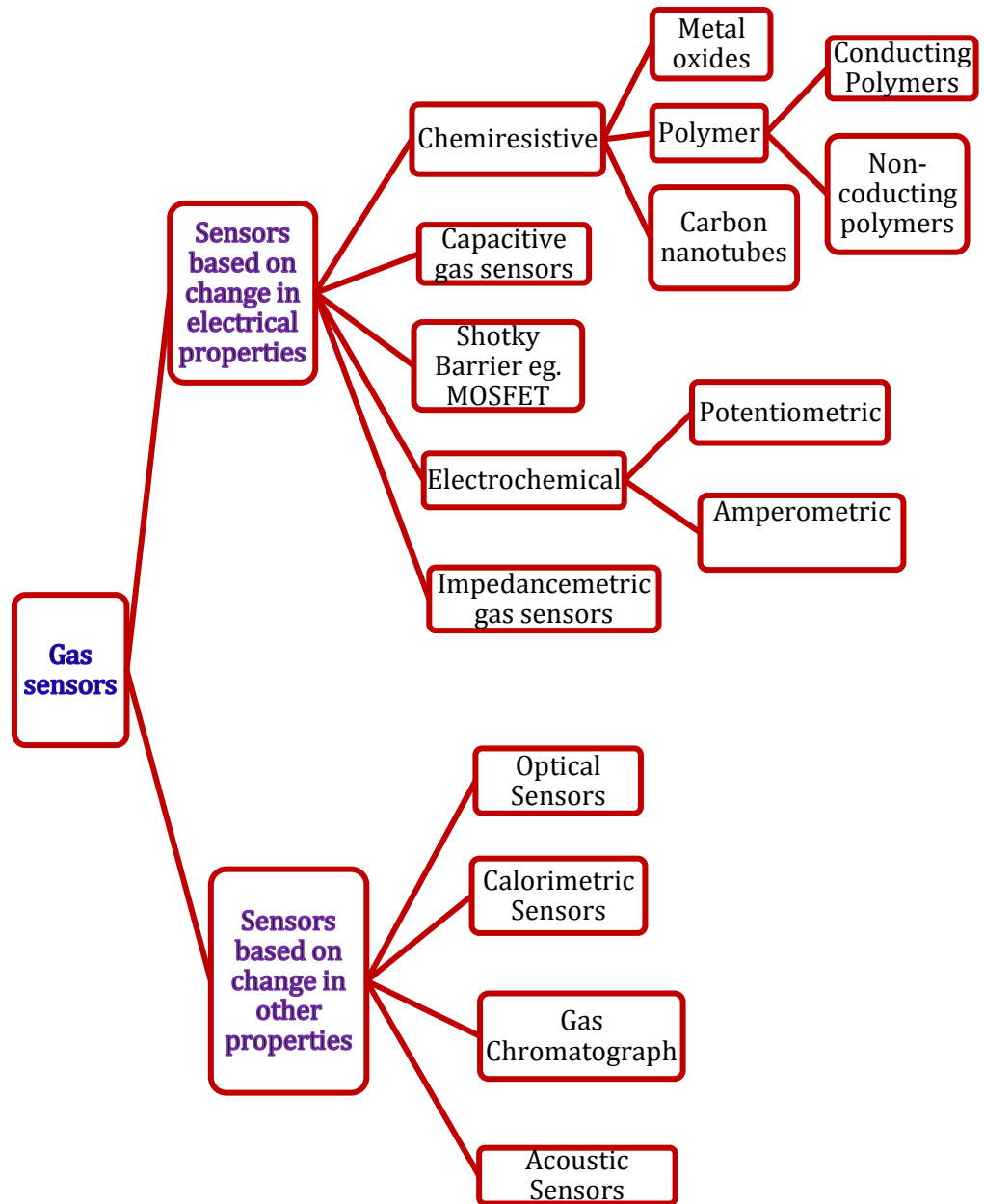


**Figure 1.3 Classification of gas sensors based on gas sensing**

Several studies are carried out for polymer-based gas sensing material used in detecting gases like CO<sub>2</sub> and H<sub>2</sub>O [74]. These sensors are extensively used to detect alcohols, halogenated compounds, aromatic compounds and a wide range

of volatile organic compounds. Polymer gas sensors are further classified into *conducting* polymers and *non-conducting* polymers as per the changes in physical properties. Polyaniline, Polythiophene, Polypyrrole are examples of some of the conducting polymers used as gas sensing materials [102]. The electrical conductivity of the conducting polymers changes with the exposure of organic and inorganic gases. On the basis of this fact, a no of groups [84, 85 and 103] investigated these materials. The changes in the monitored properties could be converted by the sensor devices into an electrical signal [65]. Polymer based gas sensors possess advantage of high sensitivities, short response times and low operating temperature. Because of their unique properties Carbon nanotubes (CNTs) are very important for gas sensing. CNTs are highly sensitive to very small quantity of gases like ammonia ( $\text{NH}_3$ ), alcohol, nitrogen oxide ( $\text{NO}_x$ ), carbon dioxide ( $\text{CO}_2$ ) at room temperature. CNTs possess large surface-to-volume ratio, great adsorptive capacity and quick response time producing large changes in electrical properties like capacitance and resistance [104].

Second group of sensors, where change in other properties (physical or chemical) take place, consists of optical sensors, calorimetric sensors, gas chromatograph and acoustic sensors.

### **1.5.3 Metal Oxide Semiconductor gas sensors**

In 1953, it was demonstrated for Germanium that the presence of impurities at the surface shows sensitiveness towards electrical resistance of a semiconductor [105]. Then after, sensitivity to the reactive gases in the air by the conductivity of ZnO thin films (300 °C) was reported [106].  $\text{SnO}_2$  also showed such properties with more stability [107].

Metal oxide-based sensor materials used in early stages suffered from many problems such as slow response, cross-sensitivity, long-term signal drift. To improve the performance towards gas sensing, number of metal-oxide semiconductors have been studied [108].  $\text{SnO}_2$ , ZnO, and  $\text{TiO}_2$  are the important materials which were extensively studied

The most commonly used MOS materials as chemi-resistive gas sensors are  $\text{SnO}_2$ , ZnO,  $\text{WO}_3$ ,  $\text{TiO}_2$ ,  $\text{In}_2\text{O}_3$  and  $\text{MnO}_2$  etc. It has been shown that the gas sensing properties like sensitivity, selectivity and stability of the MOS thin films

can be advanced by nanometer scale grain size [109]. Use of different crystal structures, improved morphology and small particle size may help to increase the performance of MOS gas sensors [110, 111]. Surface morphology plays important role in the performance of MOS gas sensor. The synthesis techniques are easy (along with controlled morphology) for MOS sensors therefore this field is continuously growing [112]. Different techniques have been used to synthesize MOS gas sensors, they may be listed as spray [113], sol-gel [114], chemical vapour deposition [115], electrodeposition [116], screen printing [117], hydrothermal [118], electrospinning [119], sputtering [120], SILAR [121], laser ablation [122], pulsed laser deposition [123], chemical bath deposition [124].

Along with commonly used materials like SnO<sub>2</sub>, ZnO, WO<sub>3</sub>, TiO<sub>2</sub>, In<sub>2</sub>O<sub>3</sub>, MnO<sub>2</sub> some new promising MOS like CuO, Al<sub>2</sub>O<sub>3</sub>, CoO, Bi<sub>2</sub>O<sub>3</sub>, NiO, Ga<sub>2</sub>O<sub>3</sub>, CdO, CeO<sub>2</sub>, Cr<sub>2</sub>O<sub>3</sub>, Fe<sub>2</sub>O<sub>3</sub>, In<sub>2</sub>O<sub>3</sub>, MoO<sub>3</sub>, Ta<sub>2</sub>O<sub>5</sub>, V<sub>2</sub>O<sub>5</sub>, Nb<sub>2</sub>O<sub>5</sub>, and ZrO<sub>2</sub> are also used as gas sensors. Now day's multicomponent complex systems of MOSs such as Zn<sub>2</sub>SnO<sub>4</sub>, CdIn<sub>2</sub>O<sub>4</sub>, Cd<sub>2</sub>SnO<sub>4</sub>, ZnWO<sub>4</sub>, BaSnO<sub>3</sub>, ZnTiO<sub>3</sub>, SrBiO<sub>3</sub>, ZnGa<sub>2</sub>O<sub>4</sub>, are also used as gas sensors.

Using low concentration of additives or dopant materials like Pd [125, 126], Au [127,128], Cu [129], Co [130], Pt [131] and Ag [132, 133], sensitivity of metal-oxide gas sensors can be increased considerably.

#### **1.5.4 Gas sensing mechanism of MOS gas sensors**

The MOS gas sensor (Chemiresistive) is tested by noting the change in the resistance. A variation in the number of electric charge carriers takes place when gas reacts with the sensing material. It is observed that, a number of electrons in the semiconductor increases when the analyte gas is reducing. This increase in conductivity decreases resistance of the film for *n*-type semiconductor. Reverse phenomenon occurs in *p*-type semiconductor. On the other hand, when analyte gas is oxidising, electrons are extracted from the film resulting in decreased conductivity (increased resistivity) for *n*-type semiconductor and vice versa for *p*-type semiconductor.

#### **1.5.5 Potential barrier model explaining gas sensing mechanism of MOS**

The mechanism that explains the gas response of MOS sensor is yet unknown and controversial, but essentially trapping of electrons at adsorbed

molecules and band bending induced by these charged molecules are responsible for a change in resistance of the sensor [134]. Potential barrier model is used to understand the gas sensing mechanism.

Closely placed grains on the surface of a semiconductor form active layer of the sensor. Surface of the sensor consists of dangling bonds, oxygen vacancies and defects such as interstitial atoms and anti-sites. The response of the sensor is decided by receptor and transducer function. Semiconductor crystals perform receptor function whereas transducer functions by the interfaces between grains. Chemical information is converted by receptor into a form of energy that transducer again transforms into detectable electrical signal. Formation of electron depletion region within grains and a double Schottky barrier across the grain contacts is proposed by potential barrier mechanism [135]. Figures 1.4 and 1.5 shows chemisorption of  $O_2$  and oxidizing gas ( $NO_2$ ), respectively and formation of double Schottky barriers at the inter-granular contacts

Generally, conductivity originates from oxygen vacancies in case of *n*-type semiconductors. During the warm up time of the sensor, Oxygen species get adsorbed on the surface and forms thin depletion region (figure 1.4). The adsorbed oxygen ions act as electron traps. Due to oxygen adsorption bending of band and change in the electronic affinity is observed relative to that before the gas adsorption. Total resistance of the sensor was found to be changed due to modification in the band bending induced by  $NO_2$  adsorption.

The reactions engaged in gas sensing could be represented as:

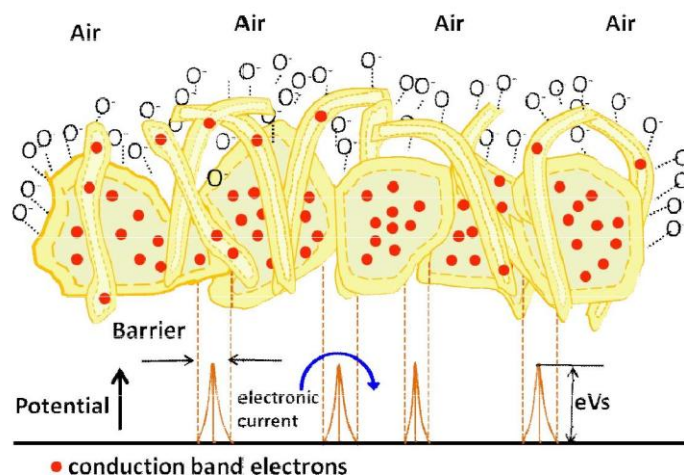
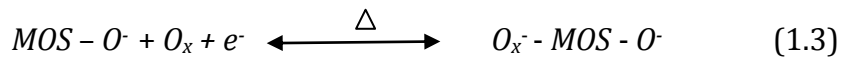


**Figure 1.4 Schematic of formation of depletion region at the intergranular contacts due to adsorption of oxygen.**

Width of the depletion layer increases due to oxidation of surface by the analyte gas, hence resistance of the films also increases by increasing potential required to cross the barrier (figures 1.4 and 1.5). The change in the width of the depletion region caused by the change in surface adsorption of oxidizing gas (e.g. NO<sub>2</sub>) is an overriding mechanism at lower NO<sub>2</sub> concentration. In figure,  $V_s$  represents the surface potential barrier and  $e$  is the charge on electron. The surface potential barrier height ' $eV_s$ ' depends on temperature and atmospheric oxygen pressure and/or oxidizing gas to which sensor is exposed. This results into linear gas response. However, if concentration of oxidizing gas is increased, due to the limited availability of adsorption sites, forms by-products restrict response.



This mechanism is useful for oxidising gas only. The reducing gas reacts with the adsorbed oxygen and releases trapped electrons in the sensor. The surface density of the negatively charged adsorbed oxygen is decreased in this way.

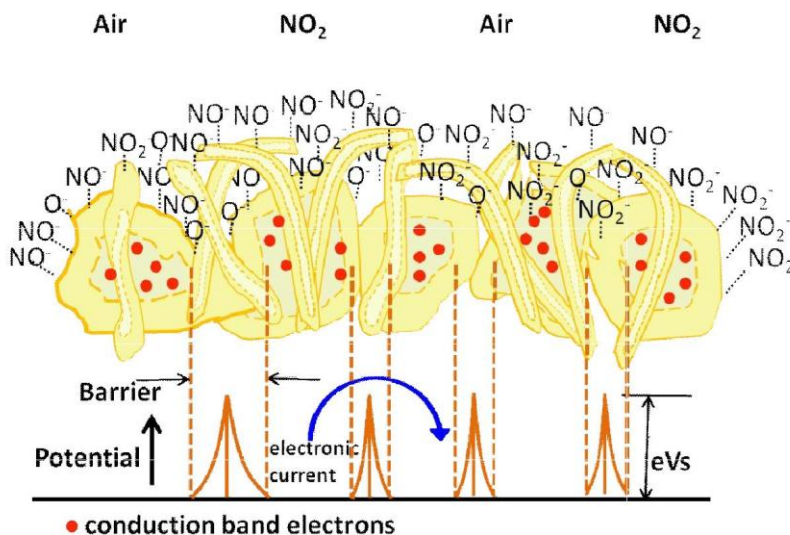


**Figure 1.5 Schematic of formation of depletion region at the intergranular contacts due to adsorption of NO<sub>2</sub>.**

This decreases the height of the barrier in the grain boundary and results into decrease in the sensor resistance for *n*-type semiconductor sensor. In the reducing environment of H<sub>2</sub>, CO, CH<sub>4</sub>, LPG or NH<sub>3</sub> preadsorbed oxygen reacts with the reducing gases producing by-products and freeing oxygen from the surface.



This lowers the oxygen density on the surface of the sensor and injects electrons into the MOS crystallites. Thus it lowers the of the potential barrier height which in turn results in decrease in sensor resistance of *n*-type semiconductor.

### 1.6 Introduction of Solar cell

A device which is capable to converts light energy into electric energy is known as solar cell and the effect is called as photovoltaic effect

Photovoltaic represents combination of Greek word phos means light and voltaic means electric potential. Volta is the name of the investigator Alessandro Volta (1745-1827), a leader in the study of electricity. In the year 1839 French physicists, A.E. Becquerel first observed Photovoltaic (PV) effect. Charles Fritts was the first man who developed the first solar cell in 1833. First p-n junction (Si based) PV device was reported in 1954. Thereafter tremendous development has taken place in the science and technology of PV devices (solar cells).

The working principle of solar cell is illustrate in the fig. 1.6

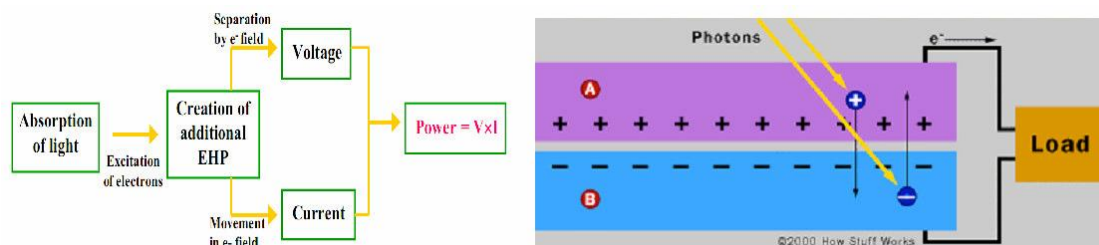


**Figure 1.6 Working principle of photovoltaic/solar cell**

Usually conventional solar cells available in the market are made up of silicon. The incident light energy on the cells gets absorbed in terms of photons. The electrons in the silicon are knocked out by absorbed energy, and flows through external circuit generating electricity.

### **1.6.1 Solar cell Generations**

One can divide solar cells into three generations.

More than 85% of solar cells in the market are of first generation. Extremely pure silicon was used for manufacturing of these solar cells. The theoretical efficiency of such efficient solar cells reached to 33%. Because of highly expensive manufacturing methods of first generation solar cells, they require years to pay for the cost. The first generation solar cells are of high-cost and high efficiency.

The second generation solar cells have been developed in the 90s and early 2000s. They are known as low-cost but also exhibit low-efficiency. Amorphous silicon, CIGS, CdTe, and Si are the materials mostly preferred for second generation solar cells. The theoretical efficiency of such efficient solar cells reached to 33%.

Second generation solar cells may be more cost effective than fossil fuel. Second generation materials have been developed by chemical route fabrication viz. Chemical Vapour deposition, electroplating, chemical bath deposition which are advantageous techniques to reduce manufacturing cost significantly

Third generation solar cells do not really commercially exist yet. They are just a research target. Reduction in cost and increase in efficiency of the cells are the goals of the third generation solar cell research. Main intention of the third generation technologies is to produce cells with high electrical performance and low cost in comparison with second generation. Current research is targeted towards achieving conversion efficiencies up to 30% along with reducing materials manufacturing cost. It is expected that the commercialization of third generation cells may start near about 2025. Nanostructured cells, multi junction photovoltaic cells and tandem cells are some of the technologies related with third generation cells. DSSCs-Graetzel cells, Hybrid, PEC; quantum dot sensitized solar cells are most commonly used devices amongst third generation. It is

supposed that the limit of proposed theoretical efficiency can be overcome by third generation solar cells.

### 1.7 Survey of literature based on Synthesis methods

As far as synthesis is concerned, tuning of physical properties and manipulation of defect states is very important. To synthesize Zinc Stannate number of techniques has been used which can be listed as hydrothermal synthesis, sputtering, sol-gel method, mechanical activation, thermal evaporation, co-precipitation, and spray pyrolysis.

A summary representing synthesis routes of  $Zn_2SnO_4$  is given below.

**Table 1.3 Synthesis method based Survey of Literature**

Method	Author	Description	Ref No
Hydrothermal	Xianliang Fu et al.	nanosized $Zn_2SnO_4$ (ZTO) particles	136
	A. Rong et al.	Uniform cube-shaped $Zn_2SnO_4$ and exhibits best performance as electrode material.	14
	Jia Zeng et al.	Urchin like ZTO nanoparticles	137
	X. J. Zhu et al.	inverse spinel structure $Zn_2SnO_4$	138
	Jun fang et al.	Synthesis of spinel $Zn_2SnO_4$ .	139
	Jae-Wook Lee et al	$Zn_2SnO_4$ anode powders	140
	Shen Lin et al.	Sharp decline in the band gap of $Zn_2SnO_4$ from 3.6 to 2.7 after the doping of $S_2^-$ ions.	141
	Guanxiang Ma et al.	Synthesis of octahedral $Zn_2SnO_4$ microcrystals.	142
	Ya-Qi Jiang et al.	cubic and quasi-cubic $Zn_2SnO_4$ particles with morphologies like irregular particles, cubes octahedra and truncated octahedra	143

	Ya-Qi Jiang et al.	zinc stannate ( $Zn_2SnO_4$ ) cube-like hierarchical structures assembled by nanoplate arrays .	144
	Zhengdao Li et al.	$Zn_2SnO_4$ nanoplate-octahedron	145
	Wentao Song et al	Preparation of $Zn_2SnO_4$ -nanocrystals/graphene-nanosheets ( $Zn_2SnO_4$ /G) nanohybrid	146
	Liang Shi et al.	$Zn_2SnO_4$ nanotubes	147
	Ya-Qi Jiang et al.	Zinc stannate ( $Zn_2SnO_4$ ) cube-like hierarchical structures assembled by nanoplate arrays.	148
	Zhe Chen et al.	$Zn_2SnO_4$ three dimensional superstructures	149
	Hui-Yuan Wang et al.	Co-doped $Zn_2SnO_4$ -graphene-carbon nanocomposites	150
	Kou et al.	$Zn_2SnO_4$ nanoparticles	151
	Bing Tan et al.	$Zn_2SnO_4$ nanoparticles	17
	Teresa Lana Villearel et al	$Zn_2SnO_4$ nanoparticles	7
	Mario et al.	$Zn_2SnO_4$ nanoparticles	152
	Aarthy Sivapunniam et al.	$Zn_2SnO_4$ nanoparticles	153
	Xiandong Lou et al.	$Zn_2SnO_4$ nanoparticles	154
	Nikolic M.V. et al.	single phase $Zn_2SnO_4$ thinfilms	155
	Yashushi Yamada et al.	Synthesized Sb-doped $Zn_2SnO_4$ thin film from pure Zn, Sn and Sb metal targets on alumina substrate in a r. f. magnetron sputtering system.	4

<b>Sputtering</b>	Cloutts et al.	Inter-grain scattering stronger in $Zn_2SnO_4$ than $Cd_2SnO_4$ . The carrier concentration was much lower for $Zn_2SnO_4$ films.	156
	David L. Young et al.	Reported basic structural, optical and electron-transport properties of zinc stannate thin films on glass substrate deposited by r.f. magnetron sputtering.	3
	D. L. Young et al	Deposition of polycrystalline $Zn_2SnO_4$ thin films for the study of crystal structure	8
	J.H. Ko et al.	ZTO films with wide compositional ranges of Sn 16-89 at% .	157
<b>Thermal Evaporation</b>	Wang et al.	single crystal ZTO nanowires and twinned nanowires.	158
	Jianseng Jie et al.	synthesis of $Zn_2SnO_4$ nanowires and $Zn_2SnO_4$ diameter modulated (DM) nanowires, morphology and structure of $Zn_2SnO_4$ nanowires.	159
	Jeedingunta et al.	high density single crystalline $Zn_2SnO_4$ nanowires by using simple , studied the PL spectrum	160
	Hanyan et al.	pseudoperiodic twinning structures of $Zn_2SnO_4$ nanowires	161
	Wang et al.	Preparation of single crystalline $Zn_2SnO_4$ nanobelts	162
<b>Mechanical Activation</b>	Yu and Choi	The current-voltage characteristics and CO gas sensing properties of porous $Zn_2SnO_4$ , interfacial effect between ZnO or $SnO_2$ and $Zn_2SnO_4$ .	163
	Nikolic et al.	reported synthesis of polycrystalline zinc stannate monophasic	164

		polycrystalline zinc stannate	
	Nikolic et al.	Polycrystalline Zn <sub>2</sub> SnO <sub>4</sub> powder	165
	Nikolic et al.	formation of spinel zinc stannate and the influence of grinding conditions on the mechanochemical reaction	166
	F. Belliard et al.	synthesis of single phase Zn <sub>2</sub> SnO <sub>4</sub>	167
	Wang et al.	prepared pure and Dy <sup>3+</sup> doped Zn <sub>2</sub> SnO <sub>4</sub> (ZTO) hollow spheres	168
	Wang Cun et al.	synthesis of nanosized Zn <sub>2</sub> SnO <sub>4</sub>	13
	M. Zhang et al.	synthesis of nanometer Zn <sub>2</sub> SnO <sub>4</sub>	169
	W. Wang et al.	Zn <sub>2</sub> SnO <sub>4</sub> nanowires synthesis	158
	Sunghoon Park et. al	synthesis of Zn <sub>2</sub> SnO <sub>4</sub> nanorods	170

## 1.8 Application based survey of literature

**Table 1.4 Application based survey of literature**

<b>Application</b>	<b>Author</b>	<b>Description</b>	<b>Ref. No</b>
<b>Li-ion Battery</b>	F. Belliard et al.	Observed a low insertion potential for ZTO with respect to Li metal and have a large reversible capacity.	167
	A. Rong et al.	Electrochemical capacity of 988 mA h/g, discharge capacity of 1384 mA h/g, relatively large discharge capacity of 580 mA h/g was observed after 50 cycles.	14
	X.J. Zhu et al.	1903.6 mAh/g of the initial discharge capacity and 1045.5 mAh/g of the first charge capacity, A specific discharge	138

		capacity of 644.7 mAh/g remained after 20 cycles.	
	Jae-Wook Lee et al	discharge capacity of the Zn <sub>2</sub> SnO <sub>4</sub> powders was 1526 mAh/g at a current density of 0.75 mA/cm <sup>2</sup> in 0.05–3.0 V, and their irreversible capacity loss was 433 mAh/g.	140
	Wentao Song et al.	Zn <sub>2</sub> SnO <sub>4</sub> /Graphene as a promising anode material for Li-ion batteries. Zn <sub>2</sub> SnO <sub>4</sub> /G nanohybrid shows better cycling stability and rate capability than bare Zn <sub>2</sub> SnO <sub>4</sub> .	146
	Hui-Yuan Wang et al.	Co-doped Zn <sub>2</sub> SnO <sub>4</sub> -graphene-carbon nanocomposites show Higher reversible capacity of 699 mA h/g after 50 cycles at 100 mA g <sup>-1</sup> and better cycling stability of 461 mA h/g after 200 cycles at 500 mA g <sup>-1</sup> . The reversible capacity of 418 mA h/g still remained even at a high current density of 1000 mA g <sup>-1</sup> .	150
	Haijian Huang	726.9 mA h g <sup>-1</sup> at a current density of 300 mA g <sup>-1</sup> after 50 cycles of the hollow Zn <sub>2</sub> SnO <sub>4</sub> boxes@C/graphene ternary composites.	171
	Christie T. Cherian	In the voltage range 0.005–3 V, nanowire electrode retains a capacity of 660 mA hg <sup>-1</sup> after 50 cycles and in the lower cut off voltage of 1.5 V, a capacity of 390 mAh g <sup>-1</sup> is delivered	172

		after 50 cycles.	
<b>Photo-catalytic Activity</b>	Xiangdong Lou et al.	the degradation rate for 20 mg L <sup>-1</sup> dyes can reach about 100% after under a 300-W high-pressure mercury lamp ( $\lambda_{\text{max}} = 365 \text{ nm}$ ) irradiating 2 h when the content of catalyst was 40 mg L <sup>-1</sup> . hydrothermal method.	154
	Lin et al.	The enhanced photocatalytic activity of S-doped Zn <sub>2</sub> SnO <sub>4</sub> for photo degradation of Rhodamine B (RHB) in aqueous solution under visible light.	141
	Jia zeng et al.	The lower particle size of photo catalysts with bigger surface-to-volume ratios and larger specific surface areas can enhance the photocatalytic activity	137
	Zhengdao Li et al.	Hybrid SnO <sub>2</sub> /Zn <sub>2</sub> SnO <sub>4</sub> microspheres can be used as photocatalyst with high-performance having better recyclability for the photodegradation of dyes. Hydrothermal method	173
	Wang Cun et al.	nano-sized Zn <sub>2</sub> SnO <sub>4</sub> materials as photocatalysts to decompose benzene in water solution.	13
	Supamas Danwittayakul et al.	The higher photocatalytic activity of ZnO/ZTO catalysts on ceramic substrates than polyester fiber membranes.	174
	Muhammad Najam Khan et al	the composite ZTO/ZnO showed better photodegradation under visible light irradiation compared to ZTO and ZnO	175

		nanoparticles with methylene blue (MB) as a test chemical contaminant.	
	Zhenfei Tian	Cube-like $Zn_2SnO_4$ and urchin-like $ZnSnO_3$ nanomaterials have shown high photocatalytic activity for methyl orange and 2, 5-DCP degradation	176
	Liang Shi et al.	The $Zn_2SnO_4$ nanotubes possess highly efficient photocatalytic activity.	147
	Cai hong Liu et al	very high photo catalytic efficiency under visible light with dye molecules almost fully degraded in 20 min by using $Zn_2SnO_4-SnO_2$ hetero-junction nanocrystal assemblies	177
	Zhengdao Li et al	Promotion of the photo catalytic reduction of greenhouse gas (carbon dioxide, $CO_2$ ) into renewable hydrocarbon fuel (methane, $CH_4$ ) in the presence of water vapour using $Zn_2SnO_4$ nanoplate/micro-octahedron has been obtained.	145
	Xianliang Fu et al.	ZTO showed the high activity and durability for photo degradation of MO. H-ZTO showed much higher activity than P25 for photocatalytic production of $H_2$ from ethanol solution.	136
<b>Dye Sensitized Solar Cell</b>	Bing Tan et al.	Fabrication of Dye Sensitized Solar Cell with the efficiency of 3.8% at 1	17
	Lana-villarreal et al.	Higher open circuit potential, but lower overall efficiency when compared with standard $TiO_2$ cells.	7

<b>(DSSC)</b>	Yu-fen Wang et al.	Hierarchical Zn <sub>2</sub> SnO <sub>4</sub> nanosheets photoelectrode showing a amazing improvement in power conversion efficiency (4.82%) compared to that of nanoparticles (4.01%)	178
	M. Mary Jacqueline et al.	conversion efficiency of 3.346 % under 1 sun illumination (AM 1.5 G, 100 mW cm <sup>-2</sup> ) The short-circuit current density of 7.859 mA cm <sup>-2</sup> was found to be increased with comparable open-circuit photo voltage (0.626 V) and fill factor (0.679).	179
	Kai Wang et.al	They improved the power conversion efficiency of Zn <sub>2</sub> SnO <sub>4</sub> -DSCs to 5.72%	180
	Jiajun Chen et al.	More than 0.1 V improvements in open circuit voltage when Zn <sub>2</sub> SnO <sub>4</sub> nanowires were used as the photoanode instead of Zn <sub>2</sub> SnO <sub>4</sub> nanoparticles.	181
	Zhengdao Li	Overall 4.72% photo conversion efficiency, when hybrid SnO <sub>2</sub> /Zn <sub>2</sub> SnO <sub>4</sub> microspheres were used as photoanode.	173
	Bihui et al.	Efficiency of 1.29% for ZTO-SnO <sub>2</sub> based DSSC. The efficiency increased by 43% from 0.90% to 1.29% compared with pure ZTO. The open circuit voltage of the cell based on ZTO-SnO <sub>2</sub> cell was 706 mV, the short-current density was 2.85 mA/cm <sup>2</sup> .	182
	Lihu Huang et al.	Indoline dye D131 sensitized solar cell showed an efficiency of 3.08%, which	183

		was higher than that with the D102 dye.	
	P. Jayabal et al.	Power conversion efficiency (PCE) of 0.64%, 0.05% and 0.02% for RB, EY and FY sensitized Zn <sub>2</sub> SnO <sub>4</sub> films, respectively.	184
	Zhengdao Li et al.	Photo conversion efficiency of 3.43% with nanosheet-assemblies of hierarchical Zn <sub>2</sub> SnO <sub>4</sub> microspheres, higher than that derived from dispersed nanosheets (DNSs) electrode (2.06%).	185
	Zhengdao Li et al.	Zn <sub>2</sub> SnO <sub>4</sub> nanoplate/micro-octahedron DSSC exhibited conversion efficiency ( $\eta$ ) of 3.1%, higher than the micro-octahedron DSSC (1.67%) and atactic particle DSSC (1.03%).	145
<b>Gas Sensing</b>	Y. Yamada et al.	Sb-doped Zn <sub>2</sub> SnO <sub>4</sub> thin film prepared by a multi-target sputtering system exhibited fairly good sensing properties to NO <sub>2</sub> over the range from 0 to 300 ppm at 600°C.	4
	Zhe Chen et al	Three dimensional superstructures of Zn <sub>2</sub> SnO <sub>4</sub> exhibiting good gas-sensing properties towards ethanol.	149
	Guanxiang Ma et al.	Improved sensing performances to H <sub>2</sub> S, C <sub>2</sub> H <sub>5</sub> OH and HCHO by hollow structures of zinc stannate.	142
	Xi-Guang Hana et al.	Polliwog-like Sn/ Zn <sub>2</sub> SnO <sub>4</sub> (P-Sn/ZTO) heterostructures exhibited excellent gas sensing properties toward ethanol.	186
	J.H. Yu and	porous Zn <sub>2</sub> SnO <sub>4</sub> showed the higher	163

	G.M. Choi	sensitivity values to CO gas than to H <sub>2</sub> gas at relatively low temperature	
	Sunghoon Park et.al	the response values of the Zn <sub>2</sub> SnO <sub>4</sub> nanorod sensor was increased 173 - 498 % to NO <sub>2</sub> concentrations of 1- 5 ppm at 300 °C the when multiple networked Zn <sub>2</sub> SnO <sub>4</sub> -core/ ZnO-shell nanorod sensors were used.	170
	Ya-Qi Jiang et al.	High gas sensing response of the cube-like Zn <sub>2</sub> SnO <sub>4</sub> . Better gas sensing response to n-C <sub>4</sub> H <sub>9</sub> NH <sub>2</sub> than other tested gases like HCHO, CH <sub>3</sub> CN and CHCl <sub>3</sub> .	148
	Ya-Qi Jiang et al.	quasi-cubic Zn <sub>2</sub> SnO <sub>4</sub> exhibit higher sensitivity toward alcohol than that using cubic Zn <sub>2</sub> SnO <sub>4</sub> .	143
	Aarthy Sivapunniam et al.	High response of 63% for 3000 ppm LPG at 250 °C was achieved when ZnO nanorods were surface modified using Zn <sub>2</sub> SnO <sub>4</sub> microcubes.	153
	Seung-Hoon Choi et al.	high selectivity for C <sub>2</sub> H <sub>5</sub> OH against CO and H <sub>2</sub> in both porous and dense Zn <sub>2</sub> SnO <sub>4</sub> nanostructures	187

### 1.9 Orientation of the problem

Zinc Stannate (Zn<sub>2</sub>SnO<sub>4</sub>) is chemically stable ternary oxide having extraordinary properties like high electron mobility, electrical conductivity and attractive optical properties as compared to binary oxides. Because of these properties Zinc Stannate have been used in several applications like solar cells, gas and humidity sensing, photocatalyst for organic pollutants and gas sensing. Out of the available ternary oxides from group II-IV-VI, only Zn<sub>2</sub>SnO<sub>4</sub> can be

preferred because they are beneficial than ternary oxides containing cadmium (Cd) and lead (Pb) from environment point of view.

Several physical and chemical method like hydrothermal, sputtering, mechanical activation, sol-gel and thermal evaporation have been reported for the synthesis of zinc stannate. Among different chemical method most reported is hydrothermal since it provides nanoparticulate structure with high crystallinity. Still there is scope to Spray Pyrolysis Technique as one step method to synthesize  $Zn_2SnO_4$  in thin film form, for their use as electrode for several applications like DSSC, PEC, Li-Ion Battery as well for gas sensing. Exceptional reports are available on preparation of  $Zn_2SnO_4$  thin films by Spray Pyrolysis Technique. Herewith we propose to prepare Zinc Stannate thin films by Spray Pyrolysis Technique on conducting and non-conducting substrates and test their applicability for gas sensing, dye sensitized solar cell and photoelectrochemical solar cell.

## References

- [1] Y. Zhang, M. Guo, M. Zhang, C. Yang, T. Ma, X. Wang, *J. Cryst. Growth*, 308 (2007) 99.
- [2] K. Nomura, H. Ohta, K. Ueda, T. Kamiya, M. Hirano, H. Hosono, *Microelectron. Eng.* 72(1) (2004) 294.
- [3] D. L. Young, H. Moutinho, Y. Yan, T. J. Coutts. *J. Appl. Phys.*, 92(1):310-319, 2002.
- [4] Y. Yamada, Y. Seno, Y. Masuoka, K. Yamashita, *Sensors and Actuators B*, 49 (1998) 248.
- [5] T. Minami, S. Takata, H. Sato, H. Sonohara, *J. Vac. Sci. Technol. A*, 13 (1995) 1095.
- [6] B. Tan, E. Toman, Y. Li, Y. Wu. *J. AM. CHEM. SOC.*, 129 (2007) 4162.
- [7] T. L. Villarreal, G. Boschloo, A. Hagfeldt. *J. Phys. Chem. C*, 111 (2007) 5549.
- [8] ] D. L. Young, D. L. Williamson, T. J. Coutts. *J. Appl. Phys.*, 91(3) (2002) 1464.
- [9] I. Stambolova, K. Konstantinov, D. Kovacheva, P. Peshev, T. Donchev, *J. Solid State Chem.*, 128 (1997) 305. [
- [10] C.G. Granqvist, A. Azens, A. Hjelm, L. Kullman, G.A. Niklasson, D. Ronnow, M.S. Mattsson, M. Veszelei, G. Vaivars, *Sol. Energy*, 63(4) (1998) 199.
- [11] J. H. Yu and G. M. Choi, *Sens. Actuators, B*, 72 (2001) 141.
- [12] J. H. Yu and G. M. Choi, *J. Electrochem. Soc.*, 148 (2001) 307.
- [13] W. Cun, W. Xinmingzhao, J. Bixian, S. Guoying, P. Ping'an, F. Jiamo, *Journal of material Science*, 37 (2002) 2989.
- [14] A. Rong, X. P. Gao, G. R. Li, T. Y. Yan, H. Y. Zhu, J. Q. Qu, D. Y. Song, *J. Phys. Chem. B*, 110 (2006) 14754.
- [15] A. Petsom, S. Roengsumran, A. Ariyaphattanakul, P. Sangvanich. *Polymer degradation and Stability*, 80(2003) 17.
- [16] P. A. Cusack, A. W. Monk, J. A. Pearce, S. J. Reynolds. *Fire Mater*, 14 (1989) 23.
- [17] S. Barua and J. Datta. *Sci. Technol. Adv. Mater.*, 12 (2011) 013004.
- [18] N. Iftimie, E. Rezlescu, P. D. Poppa, N. Rezlescu. *Journal Of Optoelectronics And Advanced Materials*, 8(3) (2006) 1001.
- [19] F. Tudorache, E. Rezlescu, P. D. Popa, N. Rezlescu. *Journal Of Optoelectronics And Advanced Materials*, 10(7) (2008) 1889.

- [20] A. B. Gadkari, T. J. Shinde, P. N. Vasambekar. *Sensors Journal*, IEEE 11 (4) 849.
- [21] S. O. Korposh, N. Takahara, J. J. Ramsden, S.W. Lee, T. Kunitake. *Journal of Biological Physics and Chemistry*, 6 (2006) 125.
- [22] V. Kumar, S. Sen, K.P. Muthe, N.K. Gaur, S.K. Gupta, J.V. Yakhmi. *Sensors And Actuators B*, 138 (2009) 587.
- [23] B. Timmer, W. Olthuis, A. V. D. Berg. *Sensors And Actuators B*, 107 (2005) 666.
- [24] D.N. Chavan, V. B. Gaikwad, G. E. Patil, D. D. Kajale, G. H. Jain. *Sensors and Transducers Journal*, 129( 6) (2011) 122.
- [25] B. O'Regan and M. Grätzel. *Nature*, 353 (1991) 737.
- [26] D. Li, C. Ding, H. Shen, Y. Liu, Y. Zhang, M. Li, J. Yan. *J. Phys. D: Appl. Phys.* 43 (2010) 015101.
- [27] G. Delaizir, V. Viallet, A. Aboulaich, R. Bouchet, L. Tortet, V. Seznec, M. Morcrette, J.M. Tarascon, P. Rozier, M. Dollé, *Adv. Funct. Mater.* 22: 2140–2147, 2012.
- [28] M.R. Hoffmann., S.T. Martin, W. Choi, D. Bahnemann, *Chemical Reviews*, 95 (1995) 69.
- [29] K. C. Ho, W. T. Hung, J. C. Yang, *Sensors* 3 (2003) 290.
- [30] I. Marr, S. Reiß, G. Hagen, R. Moos, *Sensors* 11 (2011) 7736.
- [31] T.J. Koplín, M. Siemons, C. Océń-Valéńtin, D. Sanders, U. Simon, *Sensors* 6 (2006) 298.
- [32] H. E. Endres, W. Göttler, R. Hartinger, S. Drost, W. Hellmich, G. Müller, C.B. Braunmühl, A. Krenkow, C. Perego, G. Sberveglieri, *Sens. Actuators B* 36 (1996) 353.
- [33] H. Zheng, In *Proceedings of 2008 International Workshop on Education Technology and Training and Geoscience and Remote Sensing (ETT and GRS)*, Shanghai, China, (2008) 175.
- [34] H. Miya, T. Shiina, T. Kato, K. Noguchi, T. Fukuchi, I. Asahi, S. Sugimoto, H. Ninomiya, Y. Shimamoto, In *Proceedings of 2009 Conference on Lasers and Electro-Optics/Pacific Rim (CLEOPR)*, Shanghai, China (2009) 1.
- [35] P. Tardy, J. R. Coulon, C. Lucat, F. Menil, *Sens. Actuators B*, 98 (2004) 63.
- [36] C. Caucheteur, M. Debliquy, D. Lahem, P. Megret, *IEEE Photonics Technol.*

*Lett.* 20 (2008) 96.

[37] M. Sonoyama, Y. Kato, H. Fujita, In *Proceedings of 2010 IEEE Sensors*, Kona, HI, USA, (2010) 2141.

[38] Frodl, R.; Tille, T. *IEEE Sens. J.* 6 (2006) 1697.

[39] E. Billi, J. P. Viricelle, L. Montanaro, C. Pijolat, *IEEE Sens. J.* 2 (2002) 342.

[40] S. Iannotta, T. Toccoli, M. Tonezzer A. Pallaoro, C. Corradi, M. Mazzola, N. Coppede, F. Siviero, A. Forleo, P. Siciliano, *et al.* In *Proceedings of 2008 IEEE Sensor*, Lecce, Italy, (2008) 1498.

[41] Belov, I.; Wingbrant, H.; Spetz, A.L.; Sundgren, H.; Thuner, B.; Svenningstorp, H.; Leisner, P. In *Proceedings of the 5<sup>th</sup> International Conference on Thermal and Mechanical Simulation and Experiments in Microelectronics and Microsystems*, Brussels, Belgium, (2004) 475.

[42] J. Zhang, J.Q. Hu, F. R. Zhu, H. Gong, S. J. O'Shea, *Sensors* 3 (2003) 404.

[43] I. C. Chen, S. S. Lin, T. J. Lin, C. L. Hsu, T. J. Hsueh, T. Y. Shieh, *Sensors* 10 (2010) 3057.

[44] H. Y. Dong, H. K. Chul, H. Hyung-Ki, K. Seung-Ryeol, L. Kyuchung, G. S. Ho, E. K. Ji, In *Proceedings of 1997 International Conference on Solid State Sensors and Actuators*, Chicago, IL, USA, 1(1997) 959.

[45] I. Jimenez, A. M. Vila, A. C. Calveras, J. R. Morante, *IEEE Sens. J.* 5 (2005), 385.

[46] M. K. Sofian, M. E. Oussama A. A. Imad C. K. Marsha , *Sensors*, 9 (2009) 8158.

[47] L. Yang, Z. Rongwei, D. Staiculescu, C. P. Wong, M. M. Tentzeris, *IEEE Antennas Wirel. Propag. Lett.* 8 (2009) 653.

[48] G. O. Keat, Z. Kefeng, C. A. Grimes, *IEEE Sens. J.* 2 (2002) 82.

[49] Y. Miao, Q. Yao N. Qiu, J. Zhang, In *Proceedings of 2010 China International Conference on Electricity Distribution (CICED)*, Nanjing, China, (2010) 1.

[50] K. Shi, J. F. KBurris, M. J. Newchurch, S. Johnson, S. Long. *IEEE Trans. Geosci. Remote*, 49 (2011) 557.

[51] D. Chen, S. Lei, Y. Chen, *Sensors* 11(2011) 6509.

[52] T. Anderson, F. Ren, S. Pearton, B. S. Kang, H. T. Wang, C. Y. Chang, J. Lin, *Sensors*, 9 (2009) 4669.

[53] J. Liu, W. Wang, S. Li, M. Liu, S. He, *Sensors* 11 (2011) 11871.

[54] C. Chinvongamorn, K. Pinwattana, N. Praphairaksit, T. Imato, O. Chailapakul, *Sensors*, 8 (2008) 1846.

- [55] Y. C. Chang, H. Bai, S. N. Li, C. N. Kuo, *Sensors* 11 (2011) 4060.
- [56] Y. Vashpanov, H. Choo, D. S. Kim, *Sensors* 11 (2011) 10930.
- [57] D. N. Huyen, N. T. Tung, N. D. Thien, L. H. Thanh, *Sensors* 11 (2011) 1924.
- [58] Y. Wang, M. M. Tong, D. Zhang, Z. Gao, *Sensors* 11 (2011) 19.
- [59] A. Manzoli, C. Steffens, R. T. Paschoalin, A. A. Correa, W. F. Alves, F. L. Leite, P. S. P. Herrmann, *Sensors* 11 (2011) 6425.
- [60] C. Wongchoosuk, A. Wisitsoraat, D. Phokharatkul, A. Tuantranont, T. Kerdcharoen, *Sensors* 10 (2010) 7705.
- [61] S. Chaisitsak, *Sensors* 11 (2011) 7127.
- [62] B. Alfeeli, G. Pickrell, A. Wang, *Sensors*, 6 (2006) 1308.
- [63] E. Cordos, L. Ferenczi, S. Cadar, S. Costiug, G. Pitl, A. Aciu, A. Ghita, M. Chintoanu, In *Proceedings of 2006 IEEE International Conference on Automation, Quality and Testing, Robotics*, Cluj-Napoca, Romania, (2006) 208.
- [64] F. Berger, J. Sanchez, O. Heintz, *Sens. Actuators B* 143 (2009) 152.
- [65] C. Hagleitner, D. Lange, A. Hierlemann, O. Brand, H. Baltes, CMOS single-. *IEEE J. Solid-St. Circ.* 37 (2002) 1867.
- [66] K. S. Kim, W. H. Baek, J. H. Kim, T. S. Yoon, H. H. Lee, C. J. Kang, Y. S. Kim, *Sensors*, 10 (2010) 765.
- [67] S. M. Chou, L. G. Teoh, W. H. Lai, Y. H. Su, M. H. Hon, *Sensors*, 6 (2006) 1420.
- [67] S. J. Kim, I. S. Hwang, Y. C. Kang, J. H. Lee, *Sensors*, 11 (2011) 10603.
- [69] A. M. Cubillas, J.M. Lazaro, O. M. Conde, M. N. Petrovich, J. M. Lopez-Higuera, *Sensors*, 9 (2009) 6261.
- [70] B. Ding, M. Wang, J. Yu, G. Sun, *Sensors*, 9 (2009) 1609.
- [71] S. D. Bakrania, M. S. Wooldridge, *Sensors*, 10 (2010) 7002.
- [72] L. Fraiwan, K. Lweesy, A. Bani-Salma, N. Mani, In *Proceedings of the 1<sup>st</sup> Middle East Conference on Biomedical Engineering (MECBME)*, Sharjah, United Arab Emirates, (2011) 11.
- [73] G. Xiao, Z. Zhang, J. Weber, H. Ding; H. McIntosh, D. Desrosiers, G. Nong, D. Won, J. Dunford, J. Tunney, *et al.* In *Proceedings of 2011 IEEE Instrumentation and Measurement Technology Conference (I2MTC)*, Hangzhou, China, (2011) 1.
- [74] T. A. Emadi, C. Shafai, M. S. Freund, D. J. Thomson, D. S. Jayasz, N. D. G. Whitex, In *Proceedings of the 2nd Microsystems and Nanoelectronics Research Conference (MNRC)*, Ottawa, ON, Canada, (2009) 112.

- [75] K. Song, Q. Wang, Q. Liu, H. Zhang, Y. Cheng, *Sensors*, 11 (2011) 485.
- [76] A. J. Lilienthal, A. Loutfi, T. Duckett, *Sensors* 6 (2006) 1616.
- [77] F. Tian, S. X. Yang, K. Dong, *Sensors* 5 (2005) 85.
- [78] A. Elia, C. di Franco, P. M. Lugarà, G. Scamarcio, *Sensors*, 6 (2006) 1411.
- [79] B. Bahraminejad, S. Basri, M. Isa, Z. Hambli, *Sensors*, 10 (2010) 5359.
- [80] V. V. Sysoev, I. Kiselev, M. Frietsch, J. Goschnick, *Sensors*, 4 (2004) 37.
- [81] J. Gonzalez-Jimenez, J. G. Monroy, J. L. Blanco, *Sensors*, 11 (2011) 6145.
- [82] Z. Xiaobo, Z. Jiewen, W. Shouyi, H. Xingyi, *Vinegar, Sensors*, 3 (2003) 101.
- [83] B.C. Munoz, G. Steinthal, S. Sunshine, *Sens. Rev.*, 19 (1999) 300.
- [84] A. G. Shrivastava, R. G. Bavane, A.M. Mahajan, In *Proceedings of International Workshop on Physics of Semiconductor Devices 2007( IWPSD 2007)*, Mumbai, India, (2007) 621.
- [85] J. V. Hatfid, P. Neaves, P. J. Hicks, K. Persaud, P. Travers, *Sens. Actuators B*, 18 (1994) 221.
- [86] Dowdeswell, R.M.; Payne, P.A. *Eng. Sci. Educ. J.*, 8 (1999) 129.
- [87] R. Rubio, J. Santander, N. Sabate, L. Fonseca, I. Gracia, C. Cane, M. Moreno, S. Marco, Thermopile. In *Proceedings of 2005 Spanish Conference on Electron Devices*, Barcelona, Spain, (2005) 503.
- [88] S. G. So, D. Chang, O. Al'Rifai, G. Wysocki, A. A. Kosterev, F. K. Tittel, In *Proceedings of CLEO/QELS 2008*, San Jose, CA, USA, (2008) 1.
- [89] J. Fraden, *Handbook of Mod. Sens.: Physics, Designs and Appl.*, AIP Press, 2nd edition, (1997).
- [90] A. Hulnnicki, S. Clab, and K. Ingm.in, *Pure & Appl. Chcm.* 63 (1991) 1247.
- [91] A. C. Nwanya, P. R. Deshmukh, R. U. Osuji, M. Maaza, C. D. Lokhande, F. I. Ezema, *Sensors and Actuators B: Chemical*, 206 (2015) 671.
- [92] D. Strle, B. Stefane, E. Zupanic, M. Trifkovic, M. Macek, G. Jaksa, I. Kvasic, I. Musevic, *Sensors*, 14 (2014) 11467.
- [93] N. Barsan, U. Weimar, *Journal of Physics: Condensed Matter*, 15 (2003) R813.
- [94] H. P. Lang, R. Berger, F. Battiston, J. P. Ramseyer, E. Meyer, C. Andreoli, J. Brugger, P. Vettiger, M. Despont, T. Mezzacasa, L. Scandella, H. J. Guntherodt, C. Gerber, J. K. Gimzewski, *Applied Physics A Materials Science & Processing*, 66, (1998) S61.

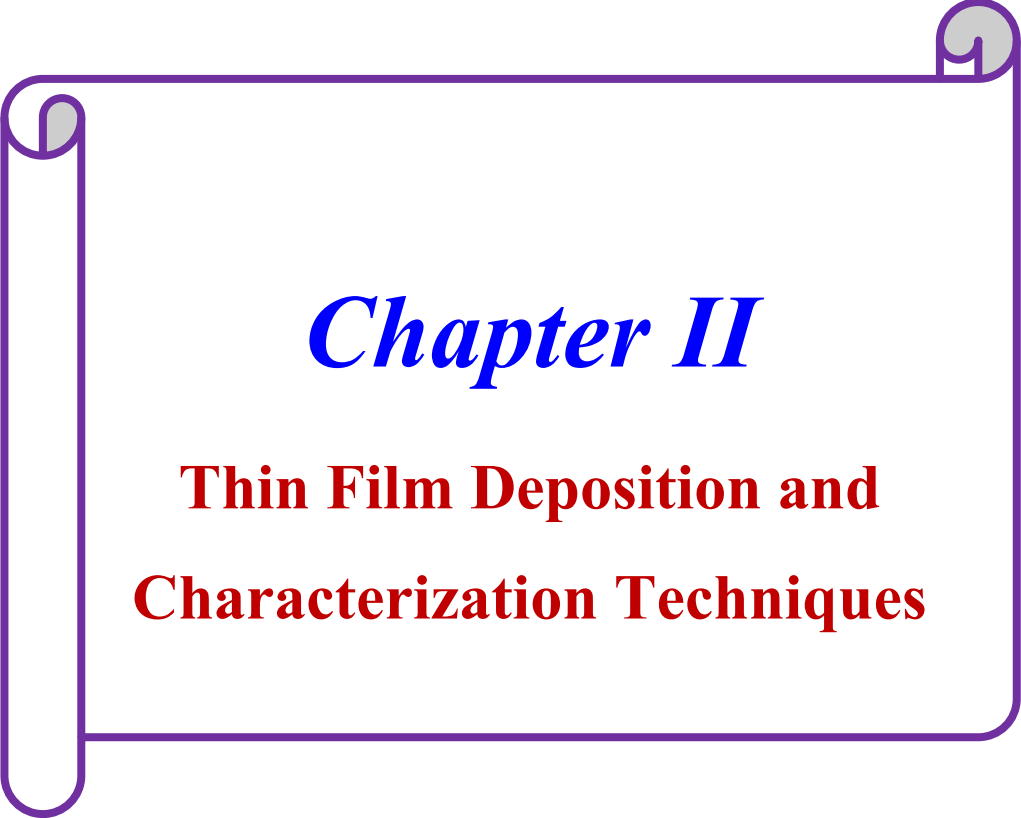
- [95] N. Yamazoe, *Sensors and Actuators B: Chemical*, 108 (2005) 2.
- [96] M. Deon, E. M. Caldas, D. S. Rosa, E. W. Menezes, S. L. Pereira Dias, M. B. Pereira, T. M. H. Costa, L. T. Arenas, E. V. Benvenuti, *Journal of Solid State Electrochemistry*, DOI:10.1007/s10008-014-2687-5.
- [97] T. Ishihara, S. Matsubara, *Journal of Electroceramics*, 2 (1998) 215.
- [98] E. Akbari, V. K. Arora, A. Enzevae, M. T. Ahmadi, M. Khaledian, R. Yusof, *Plasmonics*, 9 (2014) 987.
- [99] P. T. Moseley, *Measurement Science and Technology*, 8 (1997) 223.
- [100] E. Comini, *Analytica Chimica Acta*, 568 (2006) 28.
- [101] E. Comini, D. Zappa, C. Cerqui, A. Ponzoni, V. Sberveglieri, G. Sberveglieri, *Sensor Letters*, 12 (2014) 985.
- [102] H. Bai, G. Shi, *Sensors*, 7 (2007) 267.
- [103] Gardner, J.W.; Bartlett, P.N.. *Synth. Met.*, 55 (1993) 3665.
- [104] T. T. Thai, L. Yang, G.R. DeJean, M. M. Tentzeris, *IEEE Microw. Mag.*, 12 (2011) 84.
- [105] W. H. Brnttain and J. Bardeen, *Hell. Si/sf. Tech. j.*, 32 (1953) 1.
- [106] T. Seiyama, A. Kato, K. Fujiishi, and M. Nagatani, *Anal. Chem.*, 34 (1962) 1502.
- [107] N. Yamazoe and N. Miura, "Chemical Sensor Technology" (S. Yamauchi, Ed.), Vol. 4, p. 19. Kodansha, Tokyo, (1992).
- [108] H. Meixner and U. Lampe, *Sens. Actuators, B* 33 (1996) 198.
- [109] A. M. Gaskov, M. N. Rumyantseva, *Russian Journal of Applied Chemistry*, 74 (2001) 440.
- [110] N. V. Long, Y. Yang, M. Yuasa, C. M. Thi, Y. Cao, T. Nanng, M. Nogami, *RSC Advances*, 4 (2014) 6383.
- [111] J. Wang, F. Yang, X. Wei, Y. Zhang, L. Wei, J. Zhang, Q. Tang, B. Guo, L. Xu, *Physical Chemistry Chemical Physics*, 16 (2014) 16711.
- [112] L. Yin, D. Chen, M. Hu, H. Shi, D. Yang, B. Fan, G. Shao, R. Zhang, G. Shao, *Journal of Materials Chemistry A*, 2 (2014) 18867.
- [113] N. L. Tarwal, A. R. Patil, N. S. Harale, A. V. Rajgure, S. S. Suryavanshi, W. R. Bae, P. S. Patil, J. H. Kim, J. H. Jang, *Journal of Alloys and Compounds*, 598 (2014) 282.
- [114] B. W. Chen, Y. Bi, X. Luo, L. Zhang, *Materials Technology*, 30 (2015) 65.

- [115] D. Peeters, D. Barreca, G. Carraro, E. Comini, A. Gasparotto, C. Maccato, C. Sada, G. Sberveglieri, *Journal of Physical Chemistry C*, 118 (2014) 11813.
- [116] M. R. Kumar, S. Ryman, O. Tareq, D. A. Buchanan, M. S. Freund, *Sensors and Actuators B: Chemical*, 202 (2014) 600.
- [117] G. Sun, H. Wang, P. Li, Z. Liu, Z. Jiang, *Journal of Applied Physics*, 115 (2014) 124505.
- [118] L. Xu, M. L. Yin, S. Liu, *Journal of Alloys and Compounds*, 623 (2015) 127.
- [119] J. H. Byun, A. Katoch, S. W. Choi, J. H. Kim, S. S. Kim, *Journal of Nanoscience and Nanotechnology*, 14 (2014) 8253.
- [120] M. Kaur, N. S. Ramgir, U. K. Gautam, S. K. Ganapathi, S. Bhattacharya, N. Datta, V. Saxena, A. K. Debnath, D. K. Aswal, S. K. Gupta, *Materials Chemistry and Physics*, 147 (2014) 707.
- [121] R. B. Birajadar, A. Ghosh, A. Ghule, F. Singh, R. Sharma, *Sensors and Actuators B: Chemical*, 160 (2011) 1050.
- [122] M. H. S. Abadi, M. N. Hamidon, A. H. Shaari, N. Abdullah, R. Wagiran, *Sensors*, 11 (2011) 7724.
- [123] D. Padilla-Rueda, J. M. Vellido, J. J. Laserna, *Applied Surface Science*, 259 (2012) 806.
- [124] A. H. Mayabadi, V. S. Waman, M. M. Kamble, S. S. Ghosh, B. B. Gabhale, S. R. Rondiya, A. V. Rokade, S. S. Khadtare, V. G. Sathe, H. M. Pathan, S. W. Gosavi, S. R. Jadhkar, *Journal of Physics and Chemistry of Solids*, 75 (2014) 182.
- [125] T. B. Fryberger and S. Semancik, *Sens. Actuators*, B 2 (1990) 305.
- [126] S. Semancik and T. B. Fryberger, *Sens. Actuators*, B 1 (1990) 97.
- [127] U.-S. Choi, G. Sakai, K. Shimano, and N. Yamazoe, *Sens. Actuators*, B 107 (2006) 397.
- [128] O. Wurzinger and G. Reinhardt, *Sens. Actuators*, B 103, (2006) 104.
- [129] A. Galdikas, A. Mironas, and A. Setkus, *Sens. Actuators*, B 26 (1995) 29.
- [130] S. B. Patil, M. A. Patil, and P. P. More, *Sens. Actuators*, B 125 (2007) 126.
- [131] L. Madler, A. Roessler, S. F. Pratsinis, T. Sahm, A. Gurlo, N. Barsan, and U. Weimar, *Sens. Actuators*, B 114 (2006) 283.
- [132] M. K. Kennedy, E. E. Kruis, H. Eissan, B. R. Mentha, S. Stappert, and G. Dumpich, *J. Appl. Phys.*, 93 (2003) 551.
- [133] R. K. Joshi, F. E. Kruis, and O. Dmitrieva, *J. Nanopart. Res.*, 8 (2006) 797.

- [134] C. Wang, L. Yin, L. Zhang, D. Xiang, R. Gao, *Sensors*, 10 (2010) 2088.
- [135] S. Sharma, M. Madou, *Philosophical Transactions of the Royal Society A*, 370 (2012) 2448.
- [136] P. Grundler, "Chemical Sensors: An Introduction for Scientists and Engineers." Springer, Berlin, (2007).
- [137] X. Fu, X. Wang.; J. Long.; Z. Ding,T. Yan, G. Zhang, Z. Zhang, H. Lin, X. Fu, *Journal of Solid State Chemistry*, 182 (2009) 517.
- [138] J. Zeng, M. Xin, K. Li, H. Wang, H. Yan, W. Zhang, *J. Phys. Chem. C*, 112 (2008) 4159.
- [139] X.J. Zhua, L.M. Genga, F.Q. Zhangb, Y.X. Liua, L.B. Chenga, *Journal of Power Sources*, 189 (2009) 828.
- [140] J. Fanga, A. Huanga, P. Zhua, N. Xua, J. Xiea, J. Chia, S. Fengb, R. Xub, M.i Wua. *Materials Research Bulletin*, 36 (2009) 1391.
- [141] J.W. Lee, C. H Lee, *J. of Supercritical Fluids*, 55 (2010) 252.
- [142] Y. Lin, S. Lin, M Luo, J Liu , *Materials Letters*, 63 (2009) 1169.
- [143] G. Ma, R. Zou, L. Jiang, Z. Zhang, Y. Xue, L. Yu, G. Song, W. Li, J. Hu. *Cryst Eng Comm*, 14 (2012) 2172.
- [144] Y.Q. Jiang, X.X. Chen, R. Sun, Z. Xiong, L.S. Zheng, *Materials Chemistry and Physics*, 129 (2011) 53.
- [145] Y. Q. Jiang, C. X. He, R. Sun, Z. X. Xie, L.S. Zheng, *Materials Chemistry and Physics*, 136 (2012) 698.
- [146] Z. Li, Y. Zhou, J. Zhang, W. Tu, Q. Liu, T. Yu, Z. Zou. *Cryst Growth*, 12 (2012) 1476.
- [147] W. Song, J. Xie, W. Hu, S. Liu, G. Cao, T. Zhu, X. Zhao, *Journal of Power Sources*, 229: (2013)6.
- [148] L. Shi, Y. Dai, *J. Mater. Chem. A*, 1 (2013) 2981.
- [149] Y.Q. Jiang, C. X. He, R. Sun, Z. X. Xie, L.S. Zheng, *Materials Chemistry and Physics*, 136 (2012) 698.
- [150] Z. Chen, M. Cao,C. Hu, *J. Phys. Chem. C*, 115 (2011) 5522.
- [151] H.Y. Wang, B.Y. Wang, J.K. Meng, J.G. Wang, Q.C. Jiang, *J. Mater. Chem. A*, 3 (2015) 1023.
- [152] H. Kou, S. Yang, *J. Phys. Chem. C*, 116 (2012) 6376.

- [153] A. M. A. Alpuche, Y. J. Wu, *J. Am. Chem. Soc.*, 131 (2009) 3216. [30]
- [154] A. Sivapunniam, N. Wiromrat, M. T. Z. Myint, J. Dutta. *Sensors and Actuators B*, 157 (2011) 232.
- [155] X. Lou, X. Jia, J. Xub, S. Liu, Q. Gaob, *Materials Science and Engineering A*, 432 (2006)221.
- [156] M.V. Nikolić, T. Ivetić, D.L. Young, K.M. Paraskevopoulos, T.T. Zorba, V. Blagojević, P.M. Nikolić, D. Vasiljević-Radović, M.M. Ristić, *Materials Science and Engineering B*, 138(2007) 7.
- [157] T. J. Coutts, D. L. Young, X. Li, W. P. Mulligan, X. Wu, *J. Vac. Sci. Technol. A*, 18 (6) (2000) 2646.
- [158] J. H. Ko, I. H. Kim, D. Kim, K. S. Lee, T. S. Lee, B. Cheong, W. M. Kim, *Applied Surface Science* 253 (2007) 7398.
- [159] J. Wang, X. W. Sun, S. Xie, W. Zhou, Y. Yang, *Crystal Growth and Design*, 8(2) (2008) 707
- [160] J. Jie, G. Wang, X. Han, J. Fang, Q. Yu, Y. Liao, B. Xu, Q. Wang, J. G. Hou, *Phys. Chem. B*, 108 (2004) 8249.
- [161] S. Jeedigunta, M.K. Singh, A. Kumar, M. Shamsuzzoha, *J. Nanosci. Nanotechnol.*, 7(2) (2007) 486.
- [162] H. Chen, J. Wang, H. Yu, H. Yang, S. Xie, J. Lee, *J. Phys. Chem. B*, 109 (7) (2007) 2573.
- [163] J. X. Wang, S. S. Xie, H. J. Yuan, X. Q. Yan, D.F. Liu, Y. Gao, Z. P. Zhou, L. Song, L. F. Liu, X. W. Zhao, X. Y. Dou, W. Y. Zhou, G. Wang, *Solid State Communications*, 131 (2004) 435.
- [164] J.H. Yu and G.M. Choi. *Sensors and Actuators B*, 72 (2001) 141.
- [165] N. Nikolic', T. Srec'kovic', M.M. Ristic', *Journal of the European Ceramic Society*, 21 (2001) 2071.
- [166] M.V. Nikolić, T. Ivetić, K.M. Paraskevopoulos, K.T. Zorbas, V. Blagojević, D. Vasiljević-Radović, *Journal of the European Ceramic Society*, 27 (2007) 3727.
- [167] N. Nikoloc, Z. Marinkovic, T. Sreckovic, *journal of material science*, 39(2004) 5239
- [168] F. Belliard, P.A. Connor, J.T.S. Irvine, *Solid State Ionics*. 135 (2000) 163.
- [169] S. Wang, Z. Yang, M. Lu, Y. Zhou, G. Zhou, Z. Qiu, S. Wang, H. Zhang, A. Zhang, *Materials Letters*, 61 (2007) 3005.

- [170] M. Zhang, T. An, X. Hu, C. Wang, G. Sheng, J. Fu. *Applied Catalysis A: General*, 260 (2004) 215.
- [171] S. Park, S. An, H. Ko, C. Jin, C. Lee, *Ceramics International*, 39 (2013) 3539.
- [172] H. Huang, Y. Huang, M. Wang, X. Chen, Y. Zhao, K. Wang, H. Wu, *Electrochimica Acta*, 147 (2014) 201.
- [173] C. T. Cherian, M. Zheng, M. V. Reddy, B. V. R. Chowdari, C. H. Sow, *ACS Appl. Mater. Interfaces*, 5 (2013) 6054.
- [174] Z. Li, Y. Zhou, W. Mao, Z. Zou, *Journal of Power Sources*, 274 (2015) 575.
- [175] S. Danwittayakul, M. Jaisai T. Koottatep, J. Dutta. *Ind. Eng. Chem. Res.*, 52 (2013) 13629.
- [176] M. N. Khan, M. A. Hinai, A. A. Hinai, J. Dutta, *Ceramics International*, 4 (2014) 8743.
- [177] Z. Tian, C. Liang, J. Liu, H. Zhang, L. Zhang, *J. Mater. Chem.*, 22 (2012) 17210.
- [178] C. Liu, R. Röder, L. Zhang, Z. Ren, H. Chen, Z. Zhang, C. Ronning, P.X. Gao, *J. Mater. Chem. A*, 2(2014) 4157.
- [179] Y. Wang, K. Li, Y. Xu, C. Su, D. Kuangn, *Nano Energy*, 2(2013) 1287.
- [180] M. Maryjaculine, C. J. Raj, H. J. Kim, A. J. Rajendran, S. J. Das. *Materials Science in Semiconductor Processing*, 25 (214) 52.
- [181] K. Wang, Y. Shi, W. Guo, X. Yu, T. Mac, *Electrochimica Acta*, 135 (2014) 242.
- [182] J. Chen, L. Lu, and W. Wang, *J. Phys. Chem. C*, 116 (2012) 10841.
- [183] B. Li, L. Luo, T. Xiao, X. Hu, L. Lu, J. Wang, Y. Tang, *Journal of Alloys and Compounds*, 509 (2011) 2186.
- [184] L. Huang, L. Jiang, M. Wei, *Electrochemistry Communications*, 12 (2010) 319.
- [185] P. Jayabal, V. Sasirekha, J. Mayandi, V. Ramakrishnan, *Superlattices and Microstructures*, 75 (2014) 775.
- [186] Z. Li, Y. Zhou, H.;Yang, R. Huang, Z. Zou, *Electrochimica Acta*, 152 (2015 ) 25.
- [187] X.G. Han, X. W. Cao, L. Li , C. Wang, *Sensors and Actuators B*, 185 (2013) 383.
- [188] S.H. Choi, I. S. Hwang, J.H. Lee, S.G. Oha, Il-D. Kim. *Chem. Commun.*, 47 (2011) 9315.



# *Chapter II*

## **Thin Film Deposition and Characterization Techniques**

## **INDEX**

### **Chapter II**

#### **Thin Film Deposition and Characterization Techniques**

##### 2.1 Thin Film Deposition Techniques

###### 2.1.1 Introduction

###### 2.1.2 Spray Pyrolysis Technique (SPT)

##### 2.2. Characterization Techniques

###### 2.2.1 Differential Thermal Analysis and Thermo Gravimetric Analysis (DTA -TGA)

###### 2.2.1.1 Thermo Gravimetric Analysis (TGA)

###### 2.2.2 Thickness measurement

###### 2.2.3 Structural and morphological characterizations

###### 2.2.3.1 X-ray Diffraction technique (XRD)

###### 2.2.3.2 Scanning Electron Microscopy (SEM)

###### 2.2.3.3 Atomic Force Microscopy (AFM)

###### 2.2.3.4 Optical Absorption Studies

##### 2.3 Gas sensing measurement

## CHAPTER-II

### Thin Film Deposition and Characterization Techniques

#### 2.1 Thin Film Deposition Techniques

##### 2.1.1 Introduction

Technological progress in the society depends on the development in material science and engineering community's ability to recognize the new materials with astonishing combination of physical and mechanical properties [1]. Different methods used for preparation of thin films are classified as shown in Table 2.1.

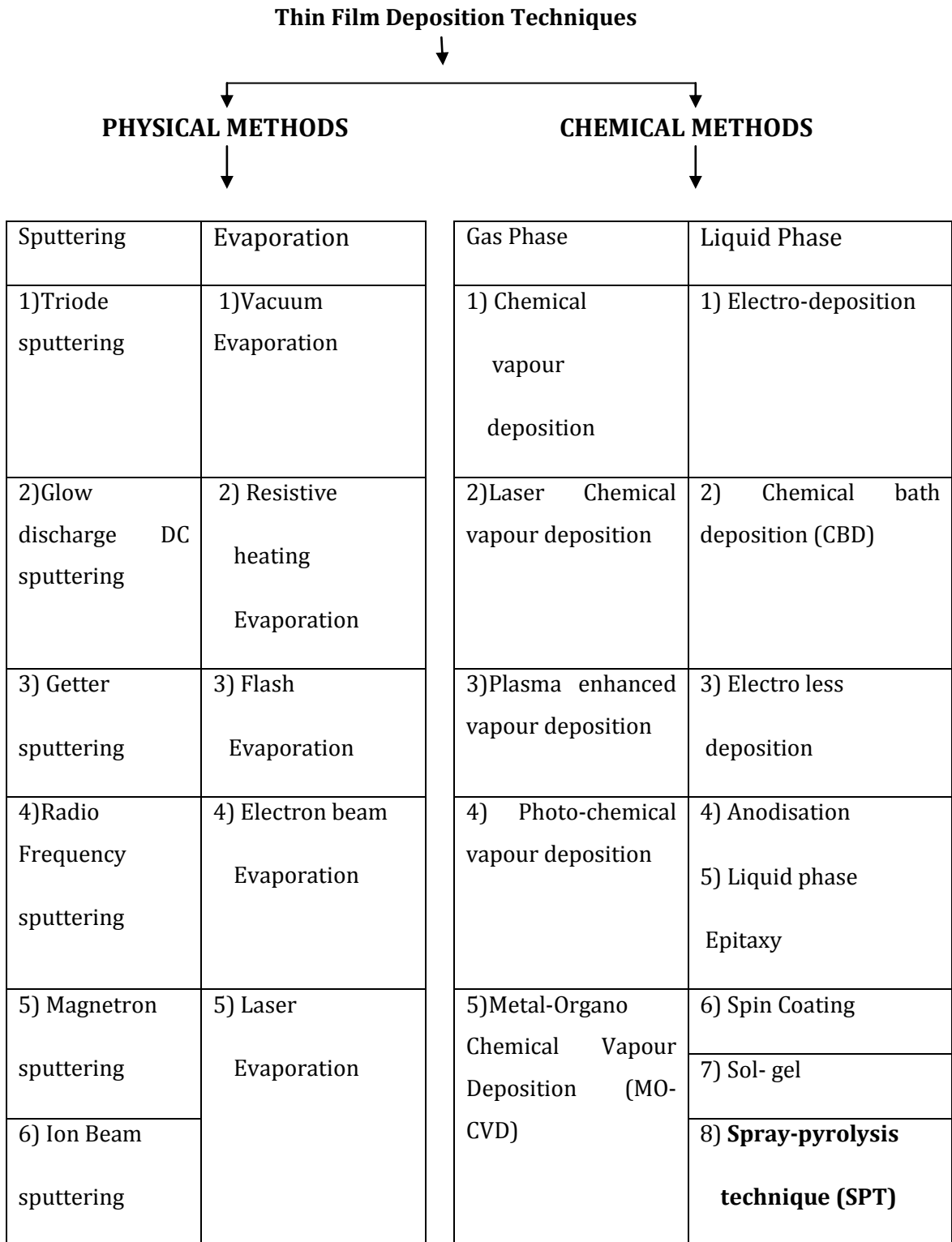
Amongst these the chemical methods are less expensive and easier than the physical methods. Among the chemical methods, the spray pyrolysis technique (SPT) is popular now a day due to its versatility in preparation of conducting and semiconducting thin films. It is also extensively used because of its simplicity and low cost. Using SPT thin films can be prepared on variety of substrates like ceramic, glass, metallic etc. The innovative work has been done by Chamberline and Skarmann [2] in 1966, on cadmium sulphide (CdS) films for solar cells. Due to high yield of this technique and simplicity of the apparatus, it offered productive way for the preparation of thin films of metal oxides [3-12], metallic spinel type oxides [13-16], binary chalcogenides [17-22], ternary chalcogenides [23,24], superconducting oxides [25-28] etc.

In addition to simplicity, spray pyrolysis technique has several other advantages;

- (1) In contrast with closed chemical vapour deposition method, spray pyrolysis do not require high quality targets and/or substrates or vacuum at any stage.
- (2) Spray pyrolysis technique operates at sensible temperature (100-550°C) therefore it can produce films on less tough material
- (3) It can be used to prepare layered films and the films having composition gradients throughout the thickness by changing composition of the spray solution during the spray process.
- (4) It presents very simple way to dope films by any element in required proportion by simply adding it in solution form to the spray precursor solution. But the knowledge of solution miscibility and solubility is essential.

(5) Local over-heating can be avoided by using SPT which is harmful for materials to be deposited as compared to other high power methods like radio frequency sputtering (RFS).

**Table 2.1 Classification of thin film deposition techniques**



8) A.C.	6) R. F. Heating		9) Ultrasonic (SPT)
Sputtering	7) Arc		10) Polymer assisted deposition (PAD)

### 2.1.2 Spray Pyrolysis Technique (SPT)

Figure 2.1 shows the schematic of the spray pyrolysis technique. Main parts of this technique are (a) air tight metallic chamber (b) hot plate with temperature controlling arrangement (c) spray nozzle and (d) gas regulator valve.

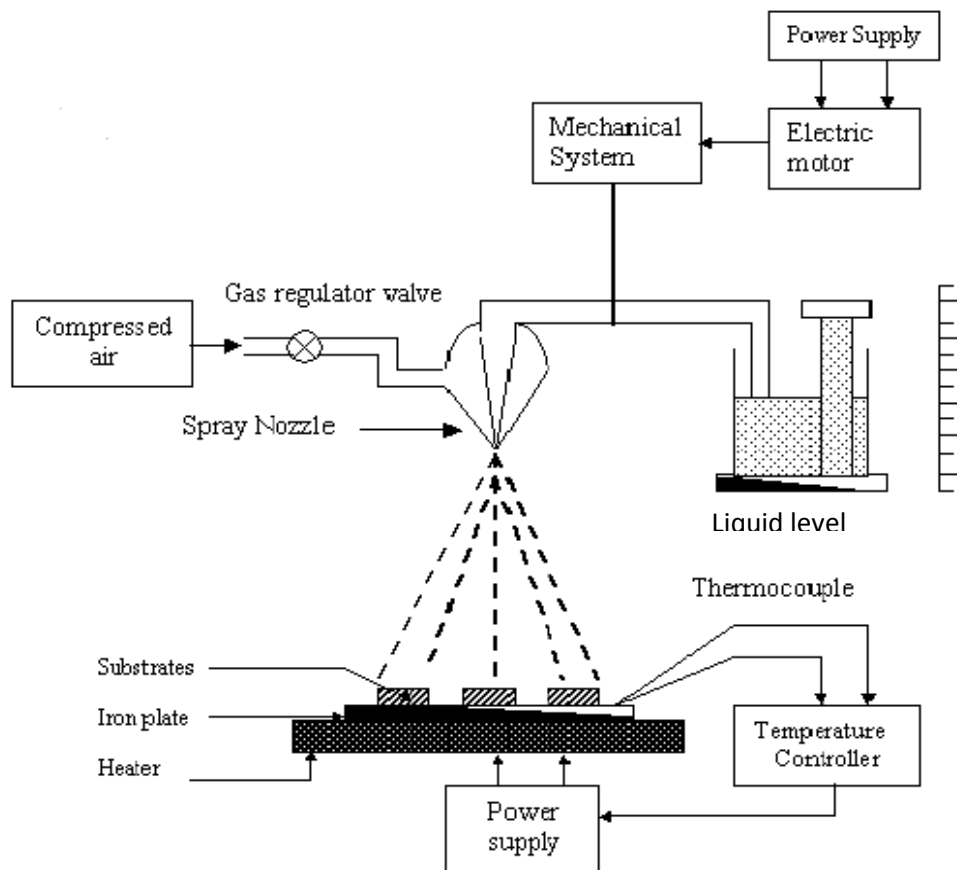


Figure 2.1 Schematic diagram of the spray pyrolysis technique

(a) Air tight metallic chamber

Since several gases are evolved during the spray, it is required to house the spray unit in an airtight metallic chamber. An outlet of the chamber was connected to exhaust in order to remove the gasses generated during spray deposition.

#### **(b) Hot plate with temperature controlling arrangement**

The iron plate having diameter 15 cm and 2.5 cm thick was placed on the electric heater (1500 W). This heater can provide maximum temperature up to 500 °C. Chromel-alumel thermocouple is used to monitor the temperature of the substrates. It is mounted on the surface of the iron disc. The temperature controller (model Aplab make) is used to measure the temperature of hot plate, with accuracy  $\pm 5^\circ\text{C}$ . Digital display directly indicates the temperature of hot plate.

#### **(c) Spray nozzle**

The glass spray nozzle consists of the inner solution capillary covered by the gas tube through which carrier gas flows. As soon as pressure is applied to the carrier gas, vacuum is generated near the tip of the nozzle and the solution gets sucked automatically which causes the spray. The size of the droplets is determined by the diameter of the solution capillary and gas flow rate.

#### **(d) Gas regulator valve**

To monitor the gas flow, gas regulator valve was used. It can control the flow of the gas from 0 to 10 litre/min.

## **2.2. Characterization Techniques**

### **Introduction**

The films developed at very low solution concentrations, and airflow rate with most favorable SND can outcome in columnar grains oriented roughly perpendicular to the substrate surface. Since the film is to be developed over a longer time period, the crystallites must grow without each drop nucleating new grain.

The development in science has taken place in the past years mostly with the invention of new novel materials. Characterization of materials is an essential step in the development of new materials. The total characterization of any material includes phase analysis, structural elucidation, compositional characterization, surface characterization and morphological analysis which have solid impact on the material properties. This made needful to the develop variety of advanced techniques in the field of materials

science. Different techniques used to characterize thin films prepared in our studies are described in this section.

## **2.2.1 Differential Thermal Analysis and Thermo Gravimetric Analysis (TGA)**

### **2.2.1.1 Thermo Gravimetric Analysis (TGA)**

It traces directly the loss or gain in weight with time or temperature as a result of oxide phase formation, dehydration or decomposition. Thermogravimetric curves represents characteristic of compound or systems under investigation with respect to change in its temperature. These curves present data relating to the kinetics of chemical reactions, reaction mechanism, and the intermediate and final reaction products.

#### **Specifications**

The instrument is SDT-2960 from TA Instruments, USA. Both differential Scanning Calorimeter (DSC) and Thermo Gravimetric Analysis (TGA) can be accomplished by it at the same time. Differential Thermal Analysis (DTA) can also be carried out using SDT 2960. It measures the heat flow and weight changes coupled with transitions and reactions in material over the temperature range from room temperature to 1500°C. Such experiments are generally performed in environments like N<sub>2</sub>, O<sub>2</sub>, Ar or air at pre-decided flow-rate (ml/min) and heating rate (°C/min). The gas-switching accessory is used to turn on and off or to switch between two different purge gases during SDT experiment. Heat-flow accuracy is equal to 1% where as DTA sensitivity is 0.001°C and that of weight is 0.1 µgm. This SDT- 2960 controller is connected to PC and the special software makes the thermal analysis. It runs the analysis programs as well as stores the data [29].

#### **Applications**

Melting point, glass transition temperature, crystallization behavior thermal stability, oxidation, dehydration, phase-transition, reaction kinetics, specific heat etc can be determined.

## **2.2.2 Thickness measurement**

Film thickness is an important parameter in the study of the film properties. Surface profiler is used for the measurement of film thickness.

### 2.2.3 Structural and morphological characterizations

Broadly, the characterization of materials can be classified into several main titles like phase (compositional and structural), physical and chemical properties. The characterization of physical properties of a material is typically regarding with electrical, magnetic, optical and dielectric properties. Main priority is given to the phase and structural characterizations along with morphological and topographical characterizations before any study of a solid-state material. The characterizations used are as below

1. Phase formation : X-ray Diffraction Technique (XRD)
2. Surface Morphology: Scanning Electron Microscopy (SEM)
3. Roughness of films: Atomic Force Microscopy (AFM)

These techniques are discussed in detail as follows.

#### 2.2.3.1 X-ray Diffraction technique (XRD)

Since the present work is concerning the thin films, the study of phase analysis, crystal orientation etc, is important. The principle of XRD can be found in large number of textbooks [30-35].

Figure 2.3 represents the schematics diagram of X-ray machine.

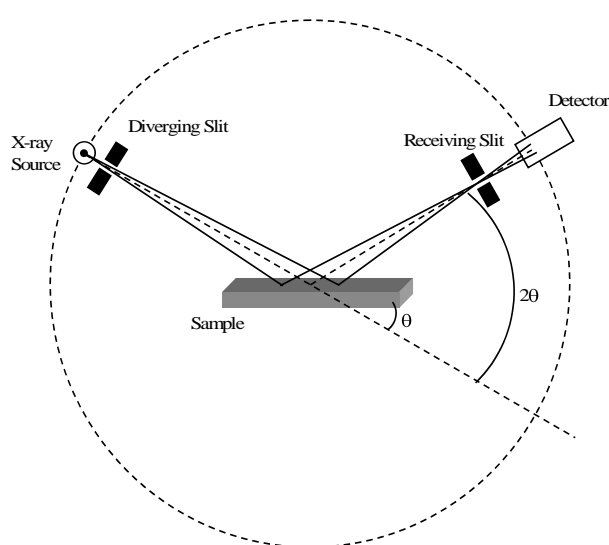


Figure 2.3 Schematics of X-ray diffractometer

Bragg's law of diffraction is given as,

$$2d \sin\theta = n\lambda \quad \dots (2.1)$$

Where,

d = interplaner spacing

$\theta$  = angle of diffraction

$\lambda$  = x-ray wavelength used for diffraction

n = diffraction order

In crystalline solids, the interatomic spacing is comparable to the wavelength of x-rays, which is usually in the range of 0.5 to 2.5 Å. Hence, such crystalline solids can be used as gratings for the diffraction of x-rays. The diffracted x-rays give information about the atomic arrangements and hence the crystal structure, phase formation and their orientation can be confirmed by studying XRD pattern.

The way of satisfying Bragg's condition can be done by continuously varying either  $\theta$  or  $\lambda$  during the XRD scan. The three main diffraction methods are differentiated according to, which of these quantities mentioned earlier are varied. The distinction is tabulated in Table 2.2.

**Table 2.2 X-ray diffraction methods**

Method	$\lambda$	$\theta$
Laue Method	Variable	Fixed
Rotating crystal Method	Fixed	Variable (in part)
Powder Method	Fixed	Variable

### Crystallite Size

The particle calculating size is calculated by using Scherrer formula [33] is given as,

$$t = \frac{0.9 \lambda}{\beta \cos \theta_B} \quad \dots (2.2)$$

Where the notations represents,  $t$  = size of particle,  $\theta_B$ = angle of diffraction,  $\lambda$  =X-ray wavelength and  $\beta$  is line broadening at Full Width Half Maxima (FWHM).

### **Instrument specifications**

Model: PW 3710/ PW1710 PHILIPS, Holland

Angle ( $2\theta$ ):  $10^\circ$  to  $100^\circ$

Target: Cu.

Normal mode: PW3710/PW 1710 APD Controller.

Specimen: Fine Powder (quantity approximately  $1 \text{ cm}^3$ )

Applications: Crystallographic studies, Quantitative analysis of organic, inorganic minerals, metals and alloys.

### 2.2.3.2 Scanning Electron Microscopy (SEM)

Information obtained from Interaction of electrons with atoms of elements can be used for characterizing the materials. When electron strikes the atom, variety of interaction with an atom evolved viz. emission of secondary, back scattered and Auger electrons etc.

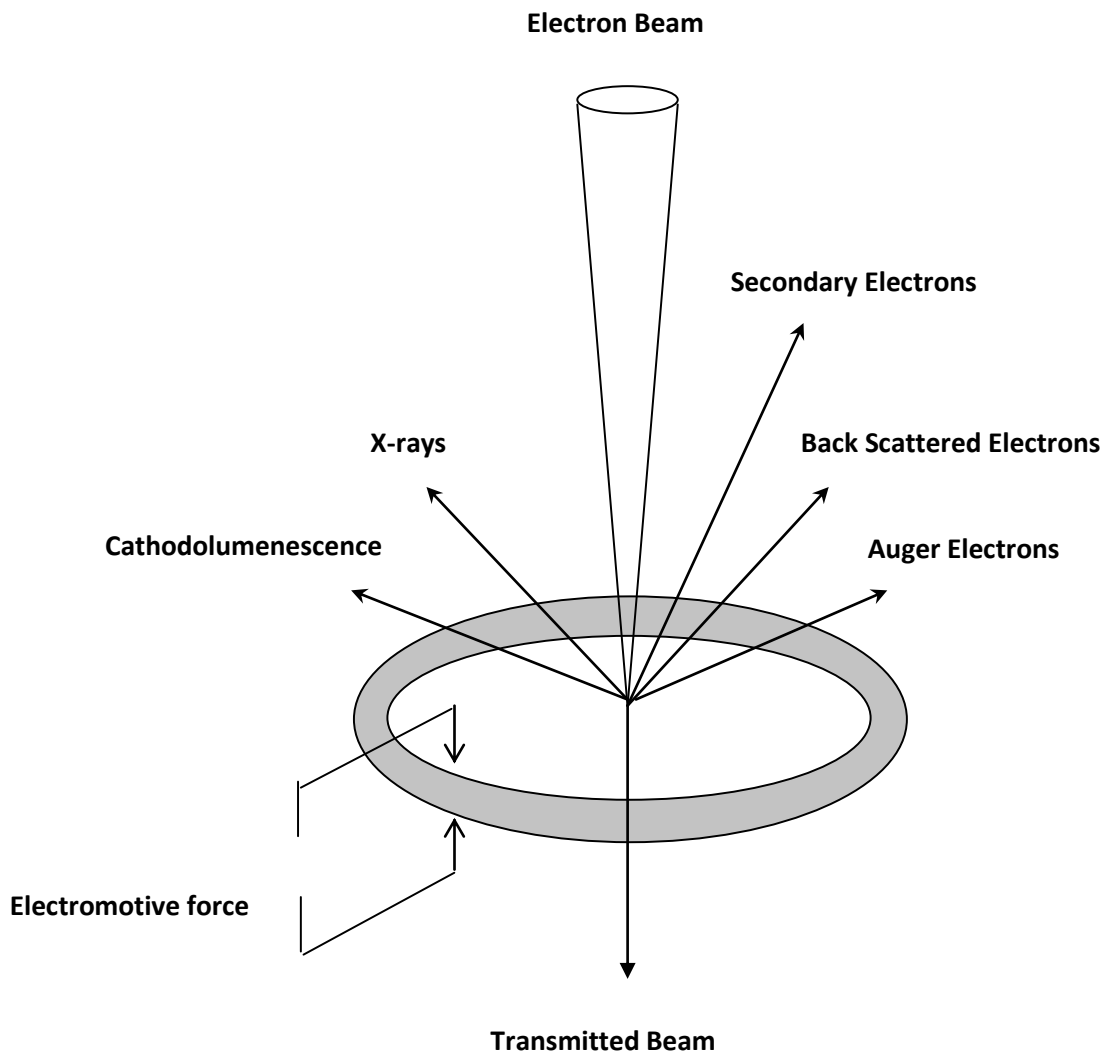


**Figure 2.4 Variety of interaction products evolved due to interaction of electron beam and sample**

Figure 2.4 illustrates the various interactions of an electron after striking the specimen atom. Backscattered electrons and secondary electrons are generated due to scattering of incident electron from the electrons of the atom.

## Principle of Scanning Electron Microscope

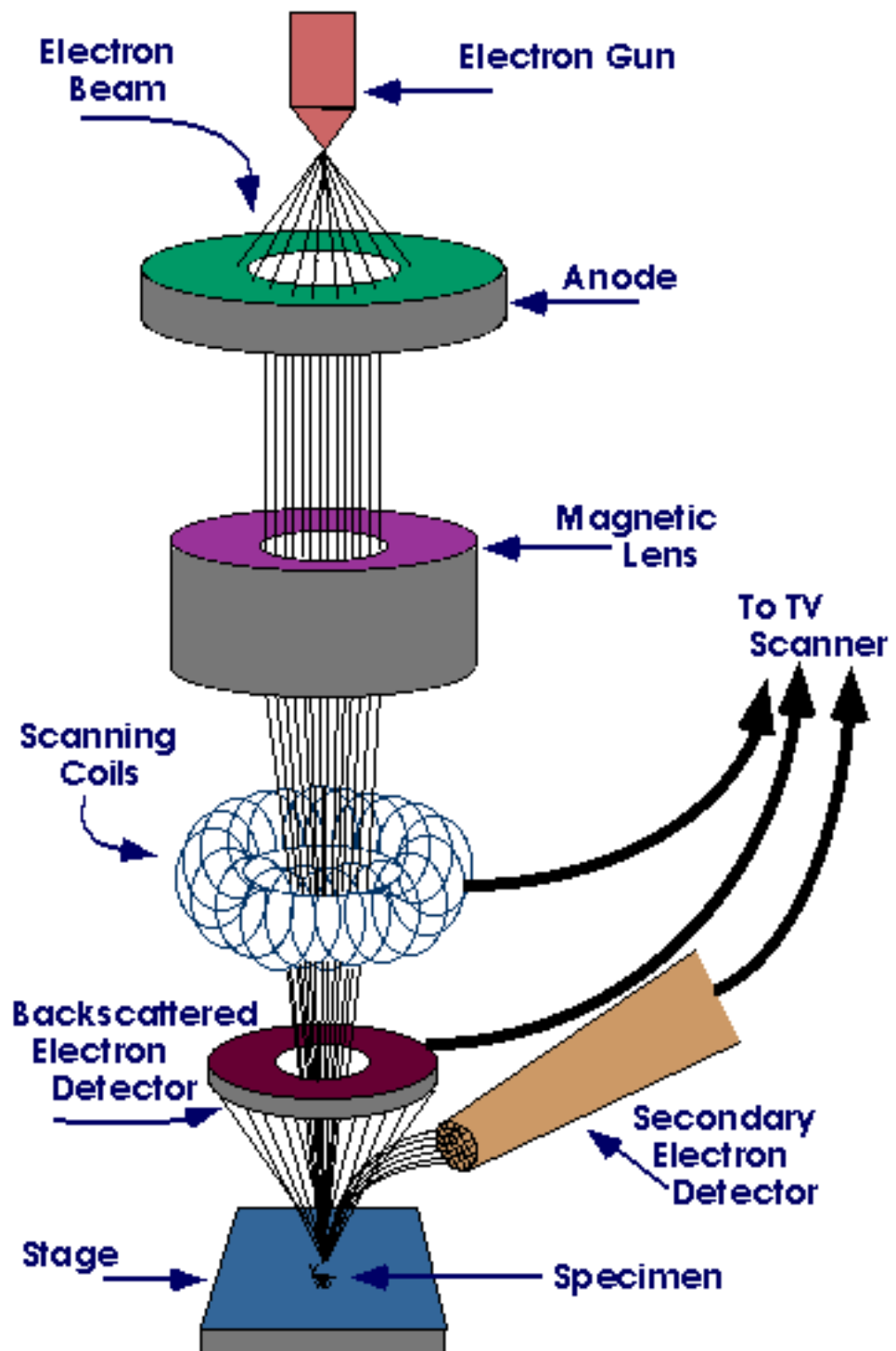


Figure 2.5

The ray diagram of scanning electron microscope

A mono-energetic (~25KeV) beam of electron is allowed to incident on a specimen sample which generates different informative signals as stated above. secondary electrons are used for image producing in SEM application. They are collected, and amplified for the brightness control on a CRT.

### 2.2.3.3 Atomic Force Microscopy (AFM)

Figure 2.6 shows the dependence of the Van der Waals force on the distance between the AFM tip and the specimen under study. AFM can be operated in two modes depending on sample conditions (a) the contact mode: cantilever is close to a distance less than few angstroms from the sample surface, and the repulsive inter-atomic force acts between the cantilever and the sample (b) non-contact mode: In non-contact mode, cantilever is operated from a distance of hundreds of angstroms from specimen surface. The attractive inter-atomic forces act between the cantilever and sample. Figure 2.7 shows diagram of Atomic Force Microscope (AFM).

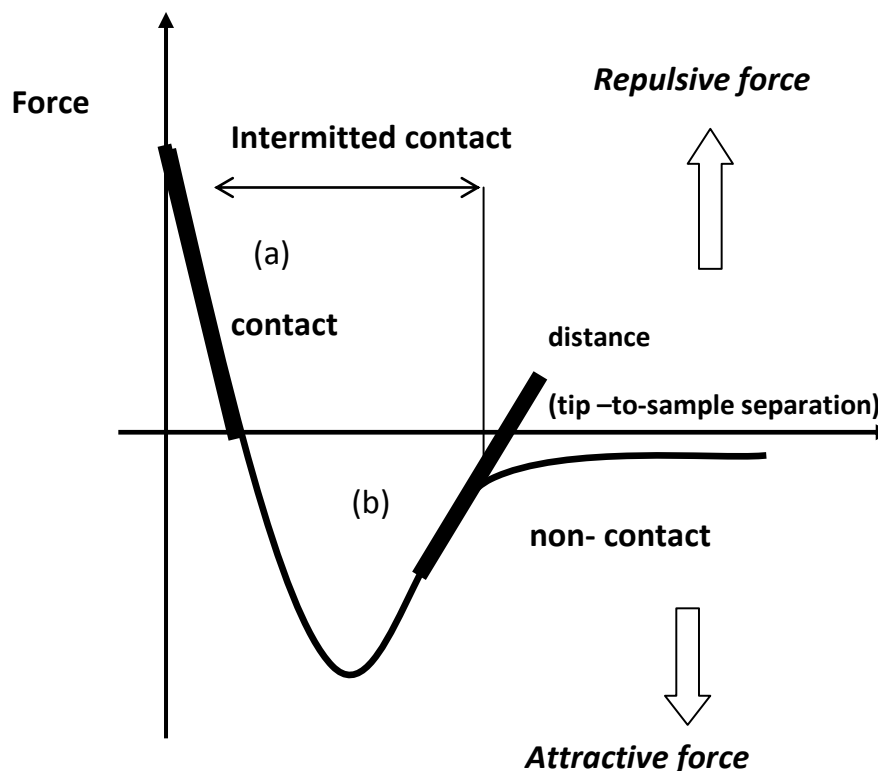
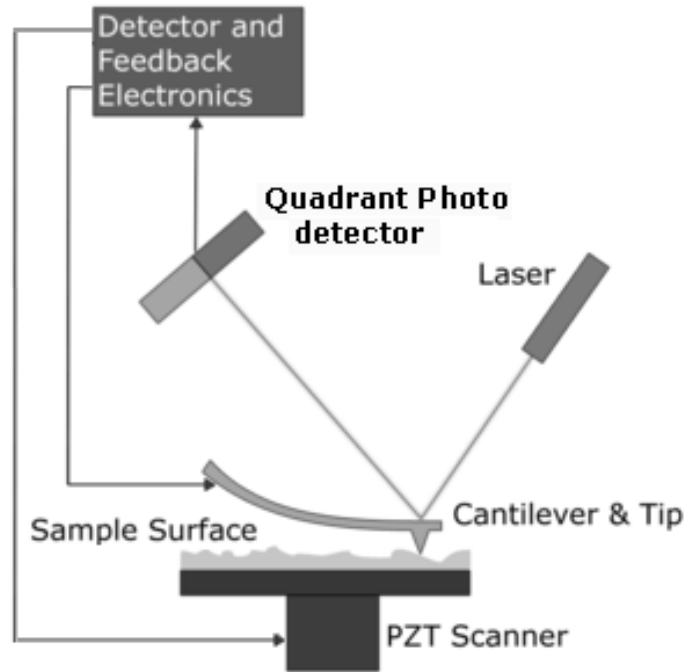


Figure 2.6 Inter-atomic forces versus distance curve for the operation of AFM



**Figure 2.7 Schematic diagram of Atomic Force Microscope (AFM)**

#### 2.2.3.4 Optical Absorption Studies

The optical Properties are studied using UV-VIS spectrophotometer. As Shown in figure below, the optical transition is represented by a vertical upward narrow. Absorption coefficient  $\alpha$  for simple parabolic bands and for direct transition is expressed by the relation (2.4) [36].

$$\alpha = \alpha_0 (h\nu - E_g)^n / h\nu \quad \dots\dots\dots(2.4)$$

where  $E_g$  - distance between bottom of the conduction and top of the valence band.  $h\nu$  - the photon energy.  $n$  - is constant and its values are 1/2 or 3/2 depending on whether transition is allowed or forbidden and  $\alpha_0$  - a constant depending upon the transition probability for direct transition.  $n = 1/2$  for allowed direct transitions.  $n = 2$  for allowed indirect transition. Hence for direct allowed transition the plot of  $(\alpha h\nu)^2$  against  $h\nu$  is

linear. By extrapolating the linear portion of the curve to the energy axis at  $=0$ , one can find out the band gap energy  $E_g$ .

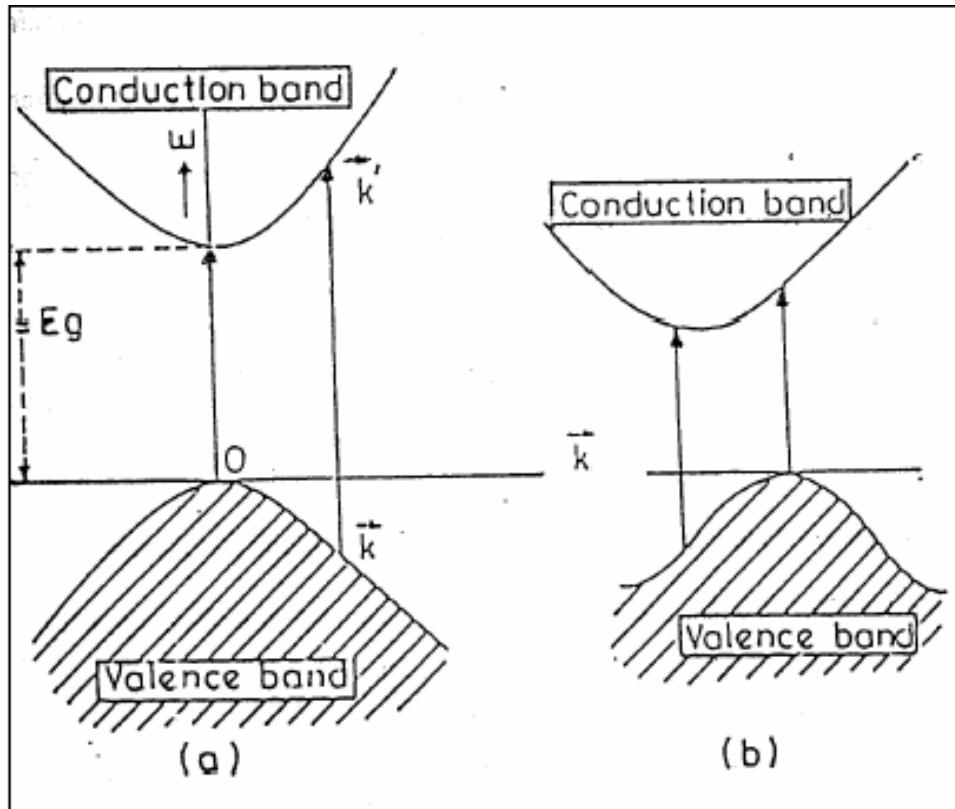


**Figure 2.8 E-k diagrams showing (a) direct and (b) indirect inter- band transition.**

### 2.3 Gas sensing measurement

To identify different characteristics of performance of the sensor, Characterization of gas sensor is essential. Mechanism involved in gas sensing is rather difficult since operating conditions and performance characteristics are mutually dependent. In order to produce sensors on commercial scale testing of sensors is important. Response of a MOS gas sensor is determined by noting change in the resistance of the thin film in air as well as in the presence of a known amount of the analyte gas. The gas sensing was carried out in following stages.

- 1) The thin film sensor is placed in an enclosed chamber of known volume.
- 2) A known amount of gas with known concentration is injected into the test chamber using a syringe.

- 3) The resistance of the sensor as a function of time is measured till the steady state is achieved.
- 4) The recovery of the sensor is studied by removing gas out of the chamber by exposing it to air.

**Construction:** The gas sensor measurement set up consists of following components.

[64] Temperature controller: It is observed that the MOS thin film sensors show considerable response at elevated temperatures. Thus, a digital temperature controller (DTC) is used to set desired temperature at which the response of sensor towards the analyte gas is to be measured.

[65] Septum for gas insertion: Analyte gas of known concentration is inserted in the test chamber through a small opening with rubber gasket which ensures no leak back of the gas.

[66] Hot plate: A hot plate heated to the operating temperature set by the DTC acts as a thin film sensor stage. A thin film of 1 cm × 1 cm dimension is mounted on the hot plate and heated before the measurements for warming up the sensor.

[67] Electrical contacts and probes: Silver paste is used to draw electrical contacts on the thin film which is connected to electrometer by means of two probes.

[68] Probes to electrometer: The probes are extended out to connect with an electrometer (Regol electrometer) to measure the change in resistance before and on inserting of analyte gas in the test chamber.

f) Stainless steel housing: The test chamber consists of a stainless steel box having volume 250 ml. Stainless still housing is used in order to protect the test chamber from corrosion.

Output of this gas sensing setup is given to Regol electrometer which is then interfaced with the computer for recording the data at various time intervals (figure 2.9).

**Working:** A locally assembled unit was used to carry out the sensor measurements. This unit was preferentially fabricated for static environment gas response measurements. The sensor film was raised to desired temperature by the DTC and hot plate, before injection of gas into the test chamber. Sensor is kept at given operating temperature till

its resistance stabilizes and variations in the resistance are minimum.

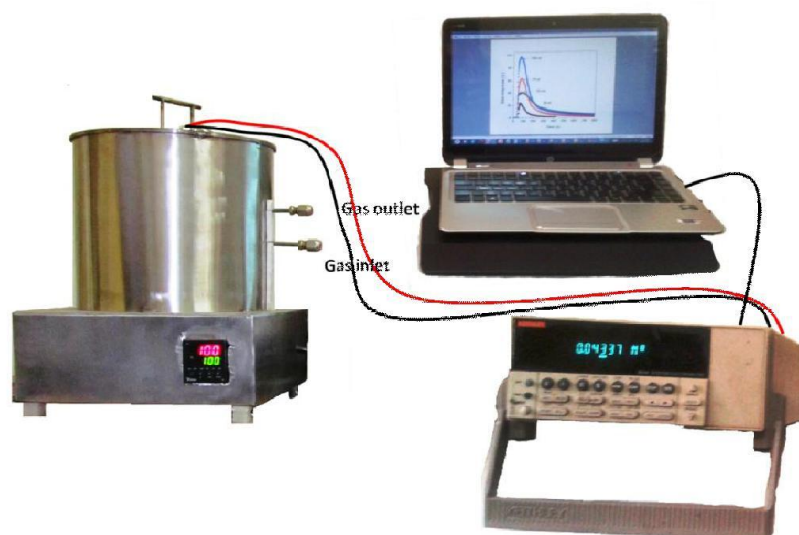


**Figure 2.9 Gas sensing measurement unit along with Rigol electrometer interfaced with laptop.**

With the help of microsyringe, known quantity of analyte gas was then taken from calibrated gas canister. This gas was carefully injected in the test chamber via the leak proof septum.

Rigol electrometer monitored the change in the resistance of the sensor due to the adsorption and reaction of the gas with the sensor surface. This is response plot of sensor with respect to the time where change in resistance with respect to time after purging gas is plotted. To obtain recovery of resistance, gas is removed out from chamber by opening the outlet valve and the gas response in presence of air is measured. The sensing properties of the sensor were recorded at different temperatures to optimize the operating temperature. The electrical character of the MOS was obtained directly by measuring the resistance of the thin film in presence of analyte gas and air

using electrometer interfaced with the monitor.

Sensitivity of the sensor can be calculated by measuring gas response at different gas concentrations. Selectivity of the sensor is calculated by measuring gas response towards various gases.

## References

- [1] K. L. Chopra and I. J. Kaur, "Thin Film Device Applications", Plenum Press, New York, 1983.
- [2] R. R. Chamberline and J. S. Skarmann., J. Electrochem. Soc., 113 (1966) 86.
- [3] P. S. Patil, Mater. Chem. Phys., 59 (1999) 185.
- [4] M. Fujimoto, T. Urano, S. Murai and Y. Nishi, Jpn. J. Appl. Phys., 28 (1989) 2587.
- [5] I. Yagi, K. Kakizawa, K. Murakami and S. Kaneko, J. Ceram. Soc. Jap., 102 (1994) 296.
- [6] A. I. Y. Tok , F.Y. C. Boey, X. L Zhao, Journal of Materials Processing Technology 178 (2006) 270.
- [7] A. Aoki and G. Nogami, J. Electrochem. Soc., 143 (1996) 191.
- [8] P. S. Patil and P. R. Patil, Tr. J. Phys., 18 (1994) 1330.
- [9] L. D. Kadam, C. H. Bhosale and P. S. Patil, Tr. J. Phys., 21 (1997) 1037.
- [10] Hyun-Suk Kim, Chang Sool Kim, Sun-Geon Kim, journal of Non-Crystalline Solids 352 (2006) 2204.
- [11] P. S. Patil and R. S. Patil, Bull. Mater. Sci., 18 (1995) 911.
- [12] P. S. Patil, E. A. Ennaoui, C. D. Lokhande, M. Muller, M. Giersig, K. Diesner and H. Tributsch, Thin Solid Films, 310 (1997) 57.
- [13] C. H. Chem., A. A. J. Buysman, E. M. Kelder and J. Schoonman, Solid State Ionics, 80 (1995) 1.
- [14] R. N. Singh, J. F. Koenig, G. Poillerat and P. Chartier, J. Electroanal. Chem., 314 (1991) 214.
- [15] B. William, Jr. Ingler, U. M. Shahed Khan, International Journal of Hydrogen Energy 30 (2005) 821.
- [16] C. S. Huang, C. S. Tao and C. H. Lee, J. Electrochem. Soc., 144 (1997) 3556.
- [17] A. G. Valyomana, S. Mathew, K. P. Vijaykumar and C. Purushottam, Bull. Mater. Sci.,

16 (1993) 55.

- [19] J. De Merchant and M. Cocivera, *J. Electrochem. Soc.*, 143 (1996) 4054.
- [20] K. Y. Rajpure , A. M. Patil, C. D. Lokhande and C. H. Bhosale, *Thin Solid Films* , 331 (1997) 114.
- [21] V. V. Killedar, C. D. Lokhande and C. H. Bhosale, *Thin Solid Films*, 289 (1996) 14.
- [22] S. Lopez, S. Granados and A. Ortiz, *Semi. Sci. Technol.*, 11 (1996) 433.
- [23] W. A. S. A. Ghafor, A. A. Awad and N. S. Othman, *Ind. J. Pure Appl. Phys.*, 31 (1993) 123.
- [25] Y. D. Tembhurkar and J. P. Hirde, *Bull. Mater. Sci.*, 17 (1994) 465.
- [25] Ko Jae-Woong, Yoo Jaimoo, Young-Kuk Kim, Kook Chae Chung, Sang-Im Yoo, Xiao Lin Wang and Shi Xue Dou, *Physica C* 445–448 (2006) 797.
- [26] A. Kumar, P. Singh, D. Kaur, *Cryogenics* 46 (2006) 749.
- [27] S. H. Pawar and P. N. Pawaskar, *Mater. Res. Bull.*, 30 (1995) 277.
- [28] Y. Moriwaki, T. Sugano, C. Gasser, A. Fukuoka, K. Nakanishi, S. Adachi and K. Tanabe, *Appl. Phys. Lett.*, 69 (1996) 3423.
- [29] Willard, Merritt, Dean, Settle, *Instrumental methods of analysis*, Sixth edition, CBS publishers and distributors, 606.
- [30] M. J. Buerger, “X-ray Crystallography”, Wiley, New York, (1942).
- [31] H. P. Klug and L. E. Alexander, “X-ray Diffraction Procedures”, Wiley, New York, (1954).
- [32] B. D. Cullity, “Elements of X-ray Diffraction”, Addison Wesley, Massachusetts (1956).
- [33] A. Taylor, “X-ray Metallography”, Wiley, New York, (1942).
- [34] A. Guinier, “X-ray Diffraction “, Freeman, San Francisco, (1963).
- [35] C. S. Barrett and T.B. Massalski, “Structure of metals”, McGraw-Hill, New York, (1966).

[36] F. Micheltti and P. Mark, J. Appl. Phys. Lett., 10 (1967) 136.

# *Chapter III-A*

**Gas Sensing Properties of  
 $\text{Zn}_2\text{SnO}_4$  Thin Films Prepared by  
Spray Pyrolysis Technique Using  
Alcohol as Solvent**

## INDEX

### Chapter III-A

## Gas Sensing Properties of $Zn_2SnO_4$ Thin Films Prepared by Spray Pyrolysis Technique using alcohol as solvent

3.1 Introduction

3.2 Experimental Procedure

3.3 Results and discussion

3.3.1 Reaction mechanism

3.3.2 Structural characterization of  $Zn_2SnO_4$  thin films

3.3.2.1 X-ray diffraction study

3.3.2.2 Scanning electron microscopy study

3.3.2.3 Atomic force microscopy study

3.3.3 Optical characterization of  $Zn_2SnO_4$  thin films

3.3.3.1 UV-Visible analysis of  $Zn_2SnO_4$  thin films

3.3.4 Gas sensing study of  $Zn_2SnO_4$  thin films

3.3.4.1 Optimization of operating temperature and sensitivity for  
 $NO_2$

gas sensing

3.3.4.1.1 Variation of gas response with operating  
temperature

3.3.4.1.2 Variation of gas response with  $NO_2$   
concentration

3.3.4.2 Response and Recovery time

3.3.4.3 Selectivity of  $Zn_2SnO_4$  thin film sensor

3.3.4.4 Stability of  $Zn_2SnO_4$  thin film sensor

3.3.4.5 Gas sensing of Pd sensitized  $Zn_2SnO_4$  thin films

3.4 Conclusions

## CHAPTER III-A

### Gas Sensing Properties of $Zn_2SnO_4$ Thin Films Prepared by Spray Pyrolysis Technique Using Alcohol as Solvent

#### 3.1 Introduction

The human activities and industries are basis to raise the level of the polluting gases. The micro, nano-structure based sensors are highly sensitive, having high spatial resolution and fast response because of the high surface-to-volume ratio [1]. Metal oxide gas sensors ( $WO_3$ ,  $ZnO$ ,  $SnO_2$  etc.) are principal solid state gas sensors used in many places which includes domestic use as well as in industrial use [2]. Many advantages of MOS include low cost, easy synthesis, smaller size and durability [2]. Nevertheless, researchers are trying to enhance gas sensing performance and detection limit by means of advanced techniques and simultaneously attempts have been made to carefully synthesis novel nanostructures showing high gas sensing performance with a low sensing limit using simple chemical methods such as CBD, SILAR, spray pyrolysis [1-2]. However, during the past few years, an enormous attention has been made to develop new types of gas sensors and to test possible alternatives to binary metal oxides such as using ternary complex oxides [3], hybridizing MOS with polymers [4] and hetero-junction [5]. Among these alternatives use of ternary complex MOS systems of the form  $A^{II}_2 B^{IV} O_4$ , [6] such as cadmium stannate ( $Cd_2SnO_4$ )[7], zinc stannate ( $Zn_2SnO_4$ ) [8], zinc titanate ( $Zn_2TiO_4$ ) [3] has received enormous interest these days.  $Zn_2SnO_4$  is a multifunctional material [6] with higher electron mobility and conductivity, wide band gap and fascinating optical properties that makes it possible to use  $Zn_2SnO_4$  for variety of applications, such as dye sensitized solar cells [9], gas sensors [10], negative electrode material for Li-ion battery [11] and photoelectrode for water purification [12] or as a photodetector [13]. Due to higher selectivity and sensitivity of  $Zn_2SnO_4$  films towards oxidizing as well as reducing gases[14-17] spinel  $Zn_2SnO_4$  has often been used to detect various gases such as  $i-C_4H_{10}$ ,  $NO_x$  and ethanol [18]. Sensing performance of  $Zn_2SnO_4$  sensor towards LPG, was improved by synthesizing microcubes of  $Zn_2SnO_4$  on the surface of  $ZnO$  nanorods

by Sivapunniam et al [19]. Hung et al. developed a template-free aqueous solution route combined with subsequent thermal treatment to synthesize porous ZnSnO<sub>3</sub> cubes for gas sensing toxic volatile organic compounds (VOCs) [20]. The phase controlled synthesis of well-defined faceted cubic ZnSnO<sub>3</sub> and octahedral Zn<sub>2</sub>SnO<sub>4</sub> microcrystals scale by a one-step facile solution chemical route for sensor with high sensitivity, fast response, and short recovery time to H<sub>2</sub>S and C<sub>2</sub>H<sub>5</sub>OH was reported [21]. The photoanodic performance of the Zn<sub>2</sub>SnO<sub>4</sub> film synthesized by a simple sol-gel route was reported by Uchiyama et al. [22]. Gautam et al. [23] reported on the electronic structure of Zn<sub>x</sub>Sn<sub>1-x</sub>O<sub>2</sub> nanorods synthesized via a versatile solvothermal method. Microstructural evolution of spinel Zn<sub>2</sub>SnO<sub>4</sub> nanofibers was manipulated by Choi et al. [24] via an in situ phase separation process of inorganic precursors and a matrix polymer during electrospinning and calcination. They reported chemiresistive gas sensors using porous Zn<sub>2</sub>SnO<sub>4</sub> fibres exhibiting superior C<sub>2</sub>H<sub>5</sub>OH sensing response.

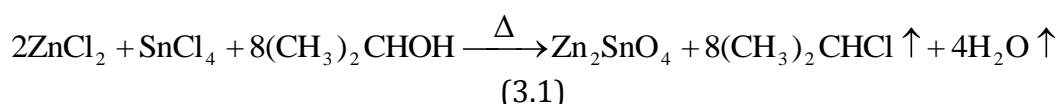
### **3.2. Experimental Procedure**

The chemicals used for the synthesis of the zinc stannate (Zn<sub>2</sub>SnO<sub>4</sub>) thin films were zinc chloride (ZnCl<sub>2</sub>) and stannic chloride (SnCl<sub>4</sub>.5H<sub>2</sub>O) as sources of zinc and tin, respectively and 2-propanol was used as a homogenizing agent for the both precursors. The chemicals were procured from S.D.Fine Chem. Ltd., Mumbai, and used as received without any further treatment. To obtain the Zn<sub>2</sub>SnO<sub>4</sub> thin films, ZnCl<sub>2</sub>, SnCl<sub>4</sub> of required quantity were dissolved in 50 ml of 2-propanol to form 0.1 M solution keeping Zn/Sn ratio 2:1. The solution was then stirred for half an hour till it becomes clear. The precursor solution formed is then sprayed onto the preheated glass substrates at different temperatures ranging from 325 to 400 °C. The spray solution quantity (50 ml), spray rate (5 ml/cc) and the nozzle to substrate distance (28 cm) were optimized by observing uniformity and adherence of the films.

### **3.3 Results and discussion**

#### **3.3.1 Reaction mechanism**

Synthesis of multicomponent metal oxide thin films composed of ternary compounds using the spray pyrolysis method is a challenging job, since the probability of growth of individual oxides or formation of composite materials or formation of both phases unanimously is more [28]. Making both components to deposit simultaneously on the substrate, rigorous attempts are necessary to optimize the preparative parameters. The deposited films are highly uniform, desired thickness (~250 nm) and well adherent. The reaction involved in the synthesis of the oxide system of Zn<sub>2</sub>SnO<sub>4</sub> is as follows:



When the atomized precursor solution travels through the temperature gradient, precursor solution decomposes within the aggregates, due to the evaporation of the solvent. Nucleation and growth of the film start as this partially decomposed part reaches the hot substrate and the crystallization reaction of the precursors result in the Zn<sub>2</sub>SnO<sub>4</sub> films after complete decomposition of the precursor.

### 3.3.2 Structural characterization of Zn<sub>2</sub>SnO<sub>4</sub> thin films

The study of structural characteristics of Zn<sub>2</sub>SnO<sub>4</sub> thin films include (i) Structural characterization using XRD (ii) Surface morphology using SEM and (iii) AFM

#### 3.3.2.1 X-Ray diffraction study

X-ray diffraction (XRD) studies of the Zn<sub>2</sub>SnO<sub>4</sub> were carried out using Bruker D2 phaser. The patterns were recorded in the 2θ range of 20–80° with step width 0.02° using CuKα radiation of wavelength 1.54056 Å. The patterns were analyzed by matching with the JCPDS cards and indexed accordingly.

The identification of crystal structure of the as-prepared films was done by X-ray diffraction (XRD) studies. XRD patterns of Zn<sub>2</sub>SnO<sub>4</sub> thin films deposited at different substrate temperatures along with the stick pattern of JCPDS card No. 24-1470 are presented in the Fig. 3.1. As observed from Fig 3.1 the XRD patterns matches well with the JCPDS card No. 24-1470 and possesses perfect cubic inverse spinel crystal structure [29-30]. The nanocrystalline nature of the films is evidenced from the observed broad peaks. The calculated lattice

parameter of the sample deposited at 375 °C about 8.6826 Å which is in good agreement with the reported value in the above mentioned JCPDS. Diffraction peaks from other phases of zinc stannate ( $\text{ZnSnO}_3$ ) and other impurities were not observed [16, 31]. The diffraction peaks observed at  $2\theta$  value of 34.18, 36.53 and 51.55°, can be assigned respectively to (311), (222) and (422) planes of the cubic crystal structure of  $\text{Zn}_2\text{SnO}_4$ . . Intensity of the diffraction peaks slowly increases with an increase in the substrate temperature, representing that the crystallinity of the material enhanced with increasing substrate temperature. At higher temperature (400 °C) peak intensity of (311) plane decreases. It may be due to the decrease in the film thickness. At higher temperatures, precursor solution decomposes before reaching substrate, decreasing the film thickness. Shift in the position of (311) peak is observed with increase in substrate temperature indicating change in lattice constant and structure becoming perfect cubic. Crystallite size (D) was estimated (table 3.1) from the XRD peaks using the Scherrer formula for the prominent peaks corresponding to the plane (311).

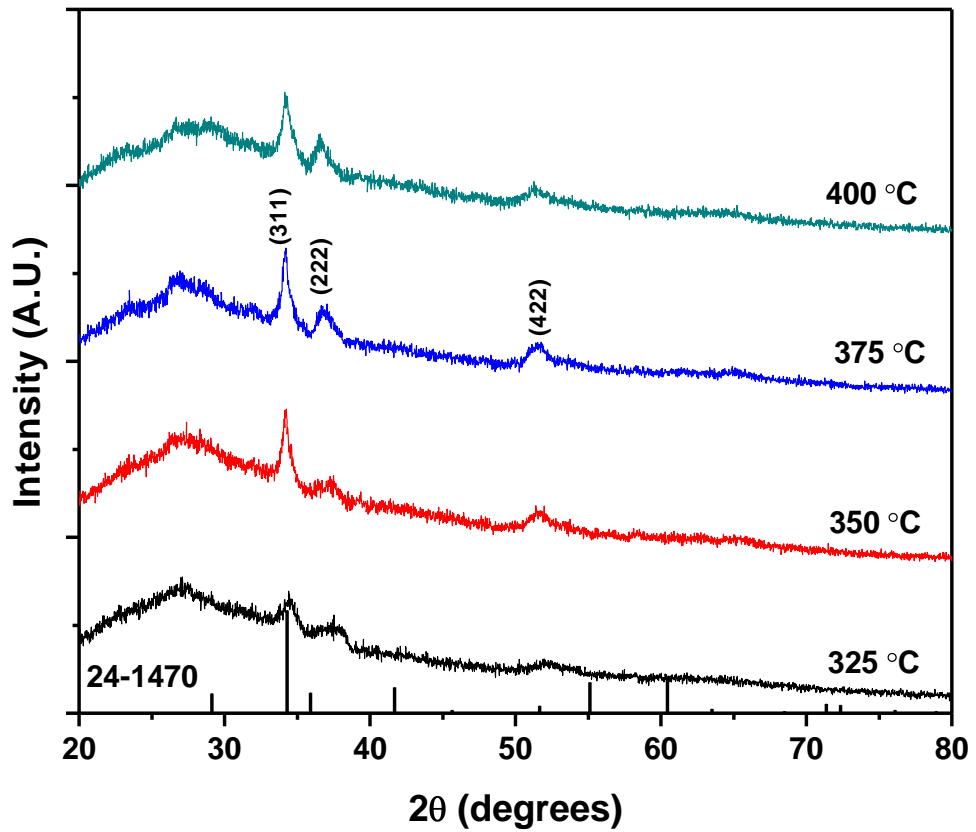
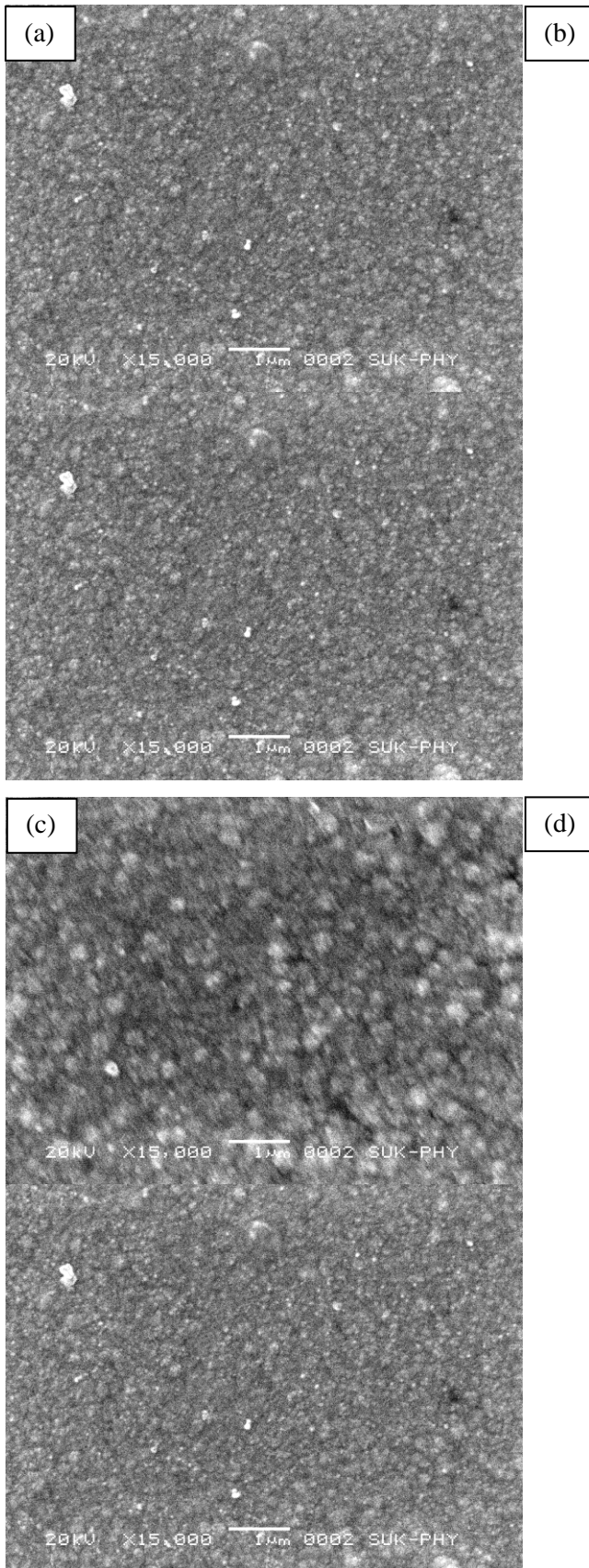


Figure 3.1 XRD patterns of the  $Zn_2SnO_4$  thin films deposited at various substrate temperatures

Table 3.1 Crystallite size and thickness of  $Zn_2SnO_4$  thin films deposited at various substrate temperatures.

Substrate temperature (°C)	Crystallite Size (nm)	Thickness (nm)
325	10.3	375
350	12.5	315
375	14.4	267
400	16.7	148

### 3.2.2 Scanning electron microscopy (SEM) study



**Figure 3.2 SEM micrographs of Zn<sub>2</sub>SnO<sub>4</sub> thin films prepared at (a) 325°C (b) 350°C (c) 375°C (d) 400°C substrate temperature.**

Surface morphology of the Zn<sub>2</sub>SnO<sub>4</sub> thin films was studied using scanning electron microscopy technique. A scanning electron microscopy SEM (SEM Model: JEOL JSM 6360) operating at 20 kV was employed to characterize the samples.

Figure 3.2(a, b, c and d) shows the SEM micrographs of the Zn<sub>2</sub>SnO<sub>4</sub> thin films prepared at substrate temperatures 325°C, 350°C, 375°C and 400°C respectively. All the SEM images are recorded at 15000 X magnification for comparison.

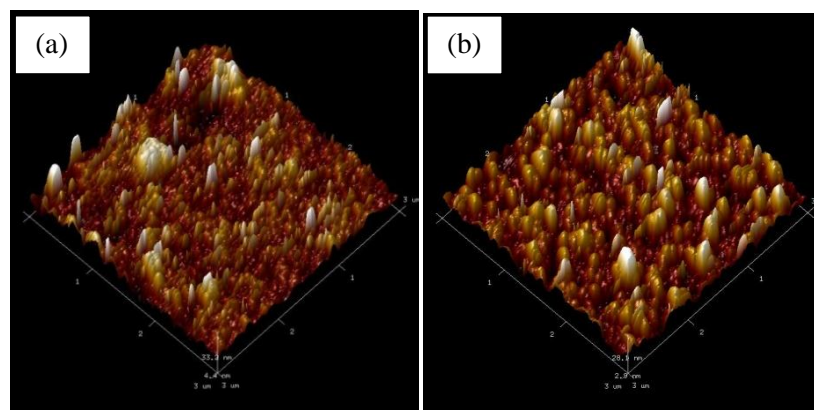
Microstructures of Zn<sub>2</sub>SnO<sub>4</sub> thin films were uniform having moderately packed grains with different grain sizes as shown in Fig 3.2. With increase in the substrate temperature, no considerable change in surface structure is observed but the particle size increased. For the films deposited at substrate temperature up to 375°C randomly distributed moderately packed spherical grains of various sizes are observed (Fig 3.2 a, b, c). Whereas, for the films deposited at higher substrate temperature (Fig 3.2 d) non uniform growth with larger grains is observed. When the substrate temperature increased, the small spherical grains are transformed into irregular cuboids along with spherical grains (Fig. 3.2 c). As reported by Jiang et al [32], it is known that Zn<sub>2</sub>SnO<sub>4</sub> particles in quasi-cubic structure have lower surface-to-volume ratio than the ideal cubic phase Zn<sub>2</sub>SnO<sub>4</sub>, hence when changing grain shape from spherical to cubic gas response increases, it is also evidenced from our results. At much higher temperature (>400 °C) films is non uniform and solution boils in the nozzle itself making it difficult to deposit thin films.

### **3.3.2.3 Atomic force microscopy study**

Atomic force microscope (Bruker, USA -INNOVA 1B3BE) was used to study the topography and to measure surface roughness of the films.

Figure 3.3 shows AFM images of the Zn<sub>2</sub>SnO<sub>4</sub> thin films deposited at four different substrate temperatures *viz.* 325°C, 350°C, 375°C and 400°C. It can be seen that, with increasing the substrate temperature, morphology of the samples becomes rougher. At lower substrate temperatures Zn<sub>2</sub>SnO<sub>4</sub> thin films show the

particulate structure. In the film deposited at substrate temperature 400 °C the overgrown particles can be seen and the same is also confirmed from the SEM images. The increase in the particle size with substrate temperature is due to the rapid formation of the grains due to the faster reaction rate at high temperature. At lower substrate temperature growth rate of the film is slow due to the less reaction rate and droplets reach substrates causing smaller grains whereas when substrate temperature growth rate of films is higher causing coalescence of residue resulting in larger grains. The surface area exposed to the analyte gas and thus the surface roughness of the films is a key factor deciding the performance of a gas sensor [33]. Due to the spherical grains on the surface, actual surface area is larger than the projected surface area of the films. The RMS (root mean square) surface roughness and actual surface area the films deposited at various temperatures were evaluated over a  $3 \times 3 \mu\text{m}^2$  area from the AFM micrographs and listed are the table 2. The surface roughness of the films increased from 9.5 to 24.4 nm with increase in the substrate temperature from 300 to 375 °C and then it reduced to 12.4 nm at 400°C. Highest roughness and thus the surface area are observed for a film deposited at 375°C. This supports an increase in the gas response with increase in substrate temperature, further at higher temperature (400°C) particles are larger and sensing sites available for gas adsorption are less, thereby decreasing gas response. Also actual surface area is decreased at highest substrate temperature resulting in decrease in gas response.



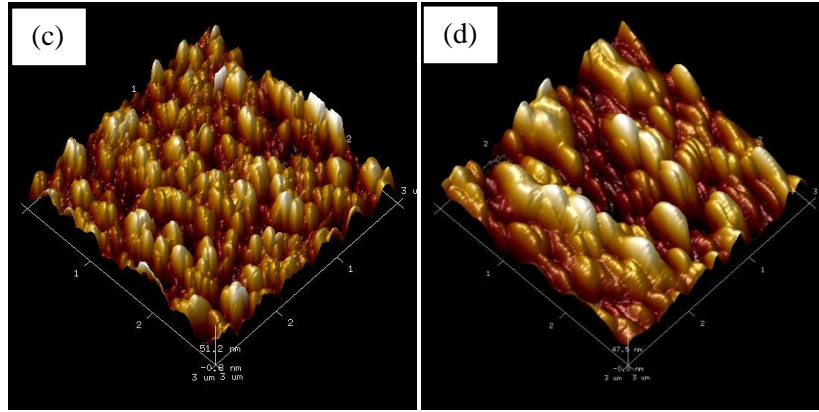


**Figure 3.3 AFM images of Zn<sub>2</sub>SnO<sub>4</sub> thin films prepared at (a) 325°C (b) 350°C (c) 375°C (d) 400°C substrate temperature.**

**Table 3.2 RMS roughness and actual surface area of projected 9 μm<sup>2</sup> image area of Zn<sub>2</sub>SnO<sub>4</sub> thin films deposited at various substrate temperatures.**

<b>Substrate temperature (°C)</b>	<b>RMS Roughness (nm)</b>	<b>Actual surface area of 3×3 μm<sup>2</sup> scan</b>
<b>325</b>	9.5	9.34
<b>350</b>	18.2	9.49
<b>375</b>	24.4	9.68
<b>400</b>	12.4	9.39

### **3.3.3 Optical characterization**

#### **3.3.3.1 Thickness measurement of the Zn<sub>2</sub>SnO<sub>4</sub> thin films**

Thickness of the film was calculated by using interferometric method comparing observed spectra with the standard spectra of known thickness of the same material on the similar substrates. Reflectance was recorded over the region of wavelength 400 to 1100 nm, wherein well developed interference patterns were observed. Thickness is calculated by fitting observed and standard reflectance pattern [34], and observed thickness is shown in table 3.1. Film thickness decreases with an increase in the substrate temperature due to the decomposition of the precursor solution prior to the film surface.

### 3.3.3.2 UV-Visible analysis of Zn<sub>2</sub>SnO<sub>4</sub> thin films

In order to estimate the band gap energy of the films, optical transmission of Zn<sub>2</sub>SnO<sub>4</sub> films is studied at room temperature in the wavelength range of 300–1100 nm. Fig. 3.4 shows the variation of transmittance with wavelength for Zn<sub>2</sub>SnO<sub>4</sub> thin films deposited at various substrate temperatures. Films are highly transparent in the visible region and the average transmission in the visible region varies from 70% to 90% depending upon the substrate temperature. It is due to the fact that the reflectivity is low and there is no (or less) absorption due to transfer of electrons from valence band to conduction band owing to optical interference effects, it is possible to maximize the transmission of thin film at particular region of wavelengths. Relatively higher transmittance of about 90% at 850 nm for films deposited at 375°C has been observed. In metal oxides, stoichiometry and crystalline structure is responsible for resulting transparency. In the present case films exhibit relatively higher transparency due to resulted better crystallinity and homogeneity. Films having better crystallinity would show better gas response due to decreased scattering of the charge carriers. In the interband transition region (365–390 nm) [35], the transmittance decreased because of the onset of fundamental absorption.

Optical absorption coefficient ( $\alpha$ ) is calculated using transmittance; it varies with photon energy and has a sharp absorption edge. ' $\alpha$ ' is of the order of  $10^4 \text{ cm}^{-1}$  following the direct and allowed band transition. The variation of  $(\alpha h\nu)^2$  with  $h\nu$  (Fig. 3.5) has a straight line portion demonstrating that transition observed is direct allowed type [36]. Extrapolating the linear portion to the energy axis to  $(\alpha h\nu)^2=0$  band gap is determined; it is observed to be 3.71 eV higher than the value of  $E_g = 3.6 \text{ eV}$  reported for single crystal Zn<sub>2</sub>SnO<sub>4</sub> [36]. At higher substrate temperature (400°C) it is narrowed to 3.45 eV due to the stoichiometric differences [32]. As reported by Aviles et al the fundamental band-gap of Zn<sub>2</sub>SnO<sub>4</sub> is 3.60-3.70 eV, due to the inclusion of excess Zn into the Zn<sub>2</sub>SnO<sub>4</sub> network and after heat treatment, band gap is narrowed up to 3.25 eV [37]. On the other hand, based on the discussion of the Jiang et al [32] the red-shift in the fundamental band-gap for quasi-cubic Zn<sub>2</sub>SnO<sub>4</sub> is attributed to differences in the crystal structure.

Thin films often show a small band gap widening and the absorption edge moves to a shorter wavelength than that of the bulk material.

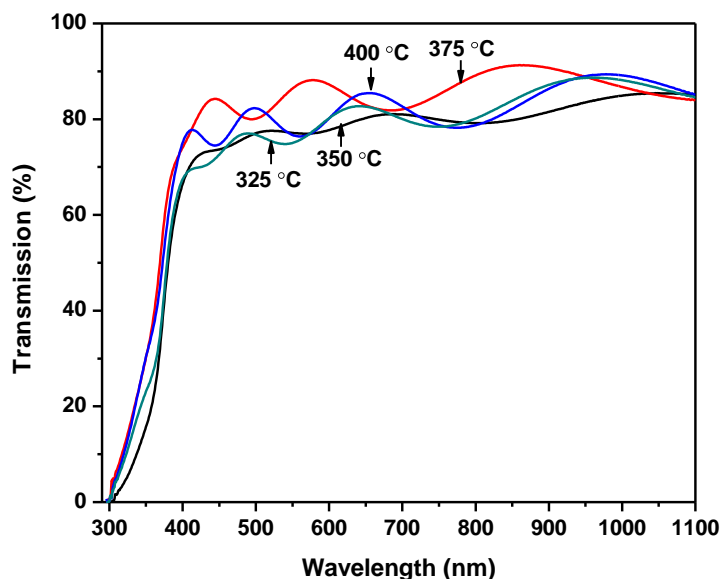


**Figure 3.4 Transmittance spectra of the  $Zn_2SnO_4$  thin films deposited at various substrate temperatures.**

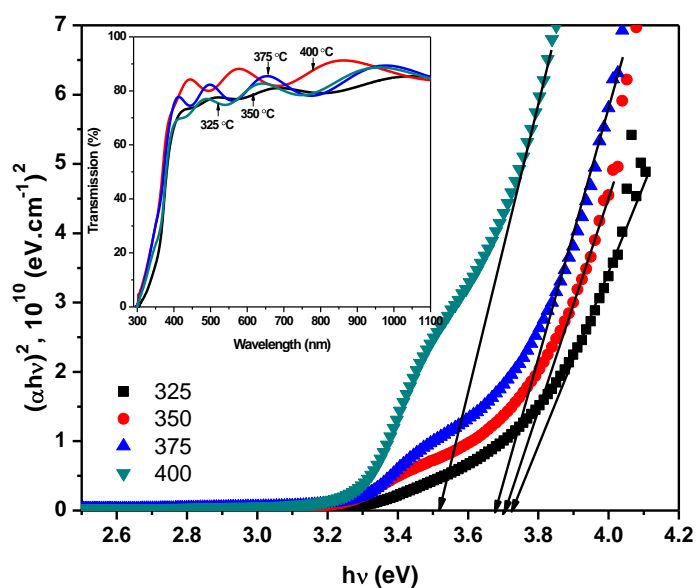


**Figure 3.5 Tauc plots to measure band gap energy and inset shows transmittance spectra of the  $Zn_2SnO_4$  thin films deposited at various substrate temperatures.**

### 3.3.4 Gas sensing study of $Zn_2SnO_4$ thin films

The gas sensing performance of the  $Zn_2SnO_4$  thin films towards  $NO_2$  is studied at different operating temperatures and gas concentrations.. The

selectivity of the films was tested using the different analyte gases at the optimized operating temperature and gas concentrations. Gas response was calculated by measuring the change in the resistance of the film as  $(R_a - R_g) / R_a$  where  $R_a$  is the resistance of the film in the air and  $R_g$  is the resistance of the film in the vicinity of gas. Response time is determined by the time taken by the sensor to reach 90% of its final value when subjected to analyte gas concentration and recovery time is the time taken by the sensor to reach 10% of the value it had before exposure to the gas. To obtain the gas atmospheres for measurements of sensor resistance fresh air was passed into a glass test box at room temperature, and then a pure test gas was injected into the box to obtain a desired concentration. Gas response and selectivity for various gases viz.  $\text{NH}_3$ , CO, LPG (Propane: Butane, 6:4),  $\text{SO}_2$ ,  $\text{H}_2\text{S}$  and  $\text{NO}_2$  were tested.

#### **3.3.4.1 Optimization of operating temperature and sensitivity for $\text{NO}_2$ gas sensing**

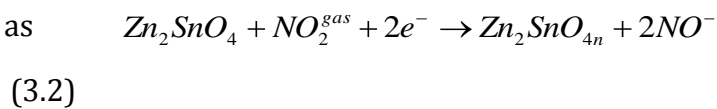
The operating temperature was optimized by comparing gas response for  $\text{Zn}_2\text{SnO}_4$  thin films deposited at various substrate temperatures at different operating temperatures for 200 ppm of  $\text{NO}_2$ . The sensitivity was optimized by studying gas response for  $\text{Zn}_2\text{SnO}_4$  thin films deposited at various substrate temperatures optimized operating temperatures for different  $\text{NO}_2$  concentrations.

##### **3.3.4.1.1 Variation of gas response with operating temperature**

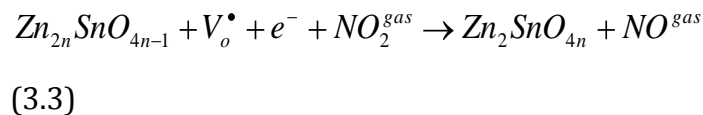
It is well studied that the operating temperature plays an important role not only in determining the gas response, but also response and recovery times of the sensors [1, 33]. To determine the operating temperature of the sensors, we measured gas response, response and recovery times of the sensors at various operating temperatures ranging from 100 to 250°C. Variation in the gas response at various operating temperatures is shown in Figure 3.6. The sensor response towards  $\text{NO}_2$  has been studied for all the films and a maximum  $\text{NO}_2$  sensitivity has been recognized at 200°C. It can be observed that gas response increases upto 200°C and decreases at higher operating temperature. Thermal energy assists the reactions involved in sensing mechanism and overcome the corresponding activation energy barriers. [38]. At higher operating temperature

(>200 °C), the pre-adsorbed oxygen species and NO<sub>2</sub> molecules on the surface of the film are decreased and therefore limiting gas response at higher operating temperatures. Moreover, at lower operating temperatures (<200°C) NO<sub>2</sub> gas molecules do not have sufficient thermal energy to dissociate and adsorb on the surface and thus the low response is observed at lower operating temperatures. Maximum gas response 2.66 is observed for the film deposited at 375°C substrate temperature. On either side of this substrate temperature gas response is less for all the films. Taking into account the response to gas, the effect of ambient temperature, stability and repeatability, operating temperature 200 °C is believed to be the optimum and use for all further investigations. The operating temperature is moderately low as compared with the few earlier reports [16-17, 27]. NO<sub>2</sub> is known to be highly oxidizing gas, having a higher electron affinity (2.27 eV) in comparison with preadsorbed oxygen (0.44 eV) [39]. Interaction of NO<sub>2</sub> with the surface of the sensor is of two types. The monomolecular adsorption of NO<sub>2</sub> is observed for well oxidized samples, whereas; dissociation of NO<sub>2</sub> takes place at the oxygen deficient centers [40]. Thus, partially reduced cations i.e. Sn<sup>+4</sup> and Zn<sup>+2</sup> play the role of NO<sub>2</sub> chemisorption centres at comparatively low temperature 200°C. Availability of the cations in turn depends on the degree of stoichiometry of the metal oxide surface.

Monomolecular adsorption of NO<sub>2</sub> occurs on cations of the outermost surface layers as



A dissociative adsorption of NO<sub>2</sub> on the sensor surface takes place on the oxygen vacancies and forms adsorbed oxygen species:



where V<sub>o</sub><sup>•</sup> is the oxygen vacancy.

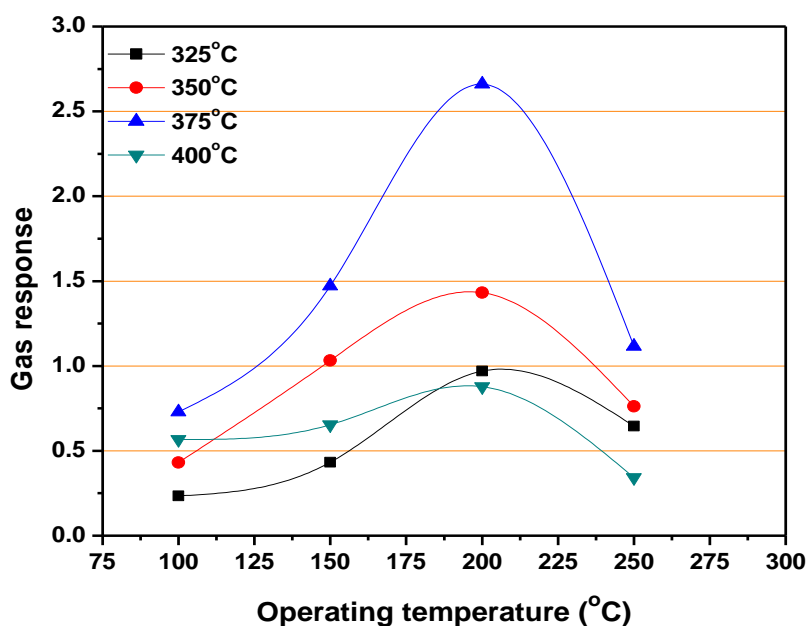


**Figure 3.6 Variation in gas response for Zn<sub>2</sub>SnO<sub>4</sub> thin films deposited at various substrate temperatures at different operating temperatures for 200 ppm of NO<sub>2</sub>.**

#### **3.3.4.1.2 Variation of gas response with NO<sub>2</sub> concentration**

The variation of gas response of films for various NO<sub>2</sub> concentrations at 200°C operating temperatures deposited at various substrate temperatures is shown in the Fig 3.7. It can be seen that the concentration of the analyte gas was varied and the gas response was significant even for the concentration as low as 50 ppm. As expected, the gas response increases noticeably with increase in gas concentration, at higher concentrations >200 ppm it saturates and remains nearly constant. At low NO<sub>2</sub> gas concentrations due to the enough availability of the adsorption sites gas response is directly proportional to the NO<sub>2</sub> concentration. However, at a higher NO<sub>2</sub> concentration due to the limited availability of the adsorption sites only fixed NO<sub>2</sub> molecules adsorbs and a saturation of gas response is observed. As a result, the gas response is determined by the surface reaction rate, till certain value of gas concentration after which it saturates [41]. The highest response was noted for the films deposited at substrate temperature 375°C for all the three concentrations.

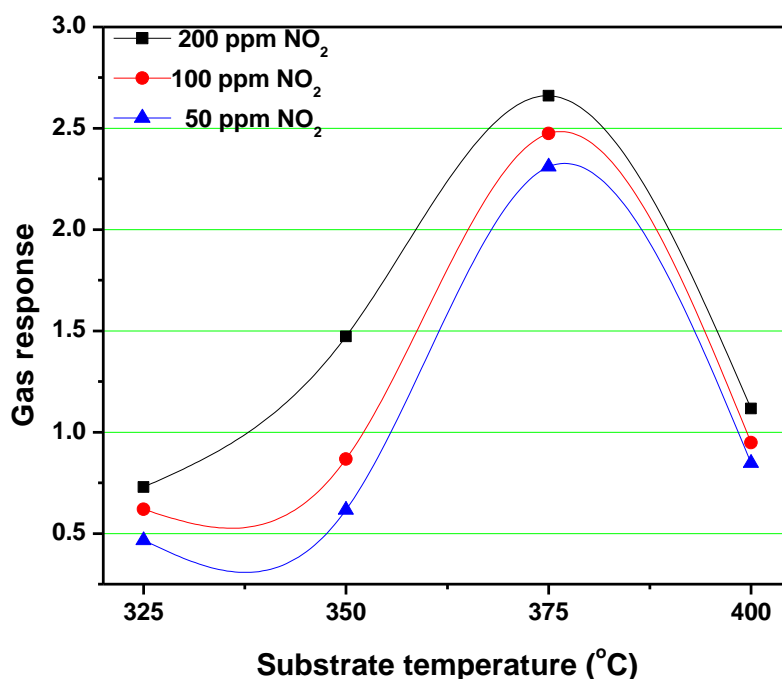
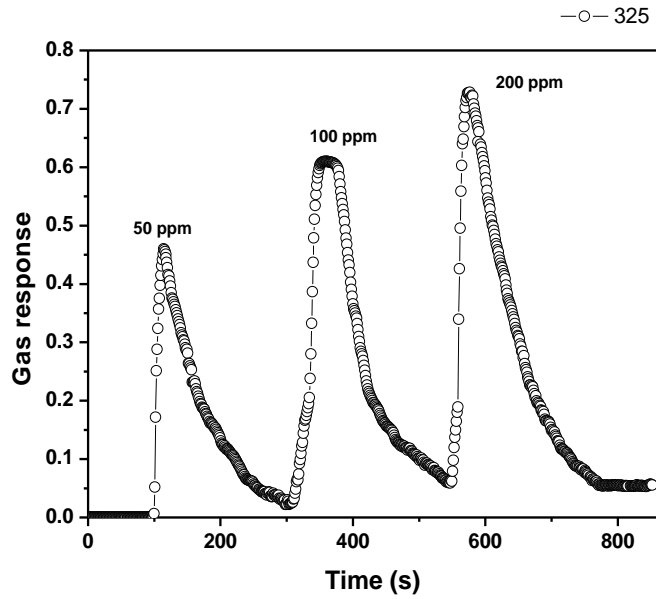


**Figure 3.7 Variation in gas response for Zn<sub>2</sub>SnO<sub>4</sub> thin films deposited at various substrate temperatures at 200 °C operating temperatures for different NO<sub>2</sub> concentrations.**

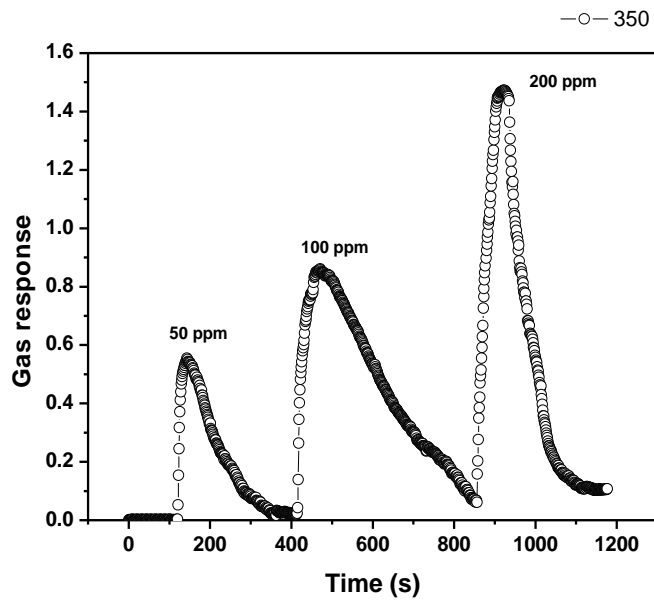
#### **3.3.4.2 Response and Recovery time**

Figure 3.8 (a, b, c and d) shows transient response of Zn<sub>2</sub>SnO<sub>4</sub> film deposited at four different substrate temperatures *viz.* 325 °C, 350 °C, 375 °C and 400°C for 50-200 ppm NO<sub>2</sub> gas concentration at 200 °C operating temperature. From Figure 3.8 (a, b, c and d) it is observed that gas response increases with NO<sub>2</sub> concentration and response and recovery times also increases simultaneously. For the film deposited at 375 °C [Fig 3.8(d)], as the film is switched between the gas on and gas off states, gas response of the film changes almost by 20 times in tens of seconds and recovers within a few minutes for the NO<sub>2</sub> gas.

From Figure 3.9, the trend in the response and recovery times of the films deposited at various substrate temperatures for different gas concentration can be seen. The response time and recovery time values of the films deposited at 375°C for 200 ppm NO<sub>2</sub> gas read as 25 and 282 s respectively.



**Figure 3.8(a) Gas responses vs. time for Zn<sub>2</sub>SnO<sub>4</sub> thin film deposited at 325°C for 50, 100, 200 ppm NO<sub>2</sub> at 200°C operating temperature.**



**Figure 3.8(b) Gas responses vs. time for Zn<sub>2</sub>SnO<sub>4</sub> thin film deposited at 350°C for 50, 100, 200 ppm NO<sub>2</sub> at 200°C operating temperature.**

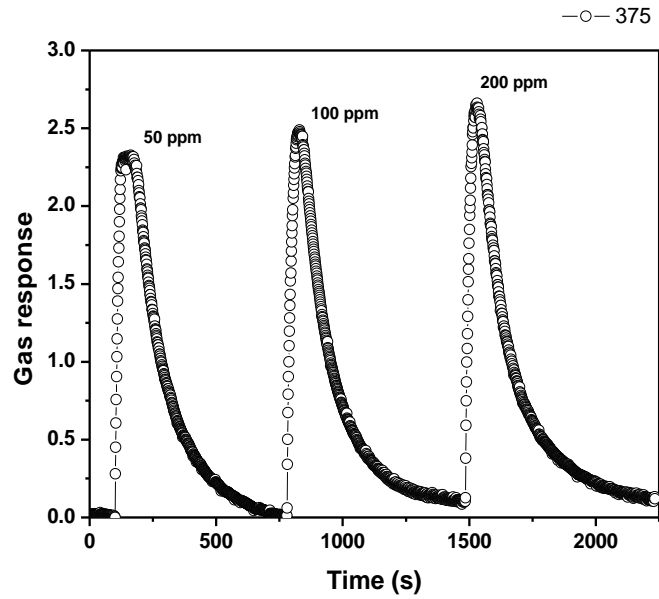


Figure 3.8(c) Gas responses vs. time for  $Zn_2SnO_4$  thin film deposited at  $375^\circ C$  for 50, 100, 200 ppm  $NO_2$  at  $200^\circ C$  operating temperature.

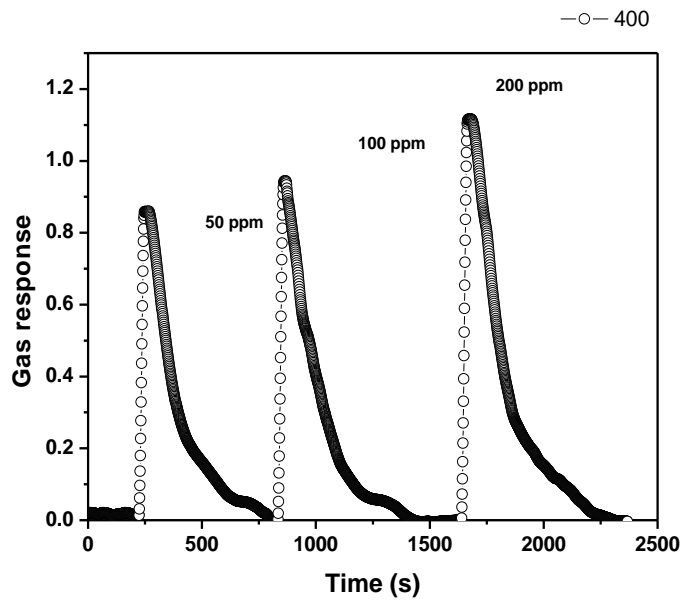
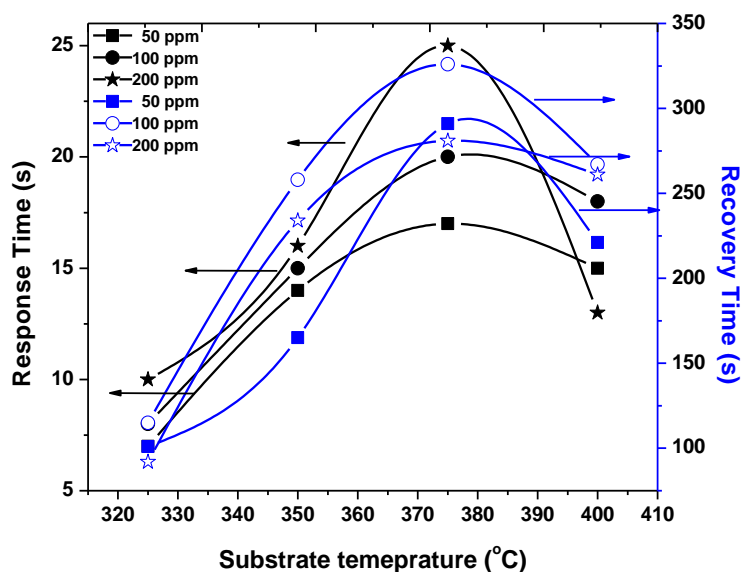


Figure 3.8 (d) Gas responses vs. time for  $Zn_2SnO_4$  thin film deposited at  $400^\circ C$  for 50, 100, 200 ppm  $NO_2$  at  $200^\circ C$  operating temperature.



**Figure 3.9 Response and recovery times of the  $Zn_2SnO_4$  thin films for various  $NO_2$  concentrations at  $200^\circ C$  operating temperature**

### 3.3.4.3 Selectivity of $Zn_2SnO_4$ thin film sensor

Response times vary for test gases viz.  $NH_3$ , CO, LPG,  $SO_2$ ,  $H_2S$  and  $NO_2$  which were used in the determination of selectivity of the films. The films deposited at  $375^\circ C$  were exposed to 200 ppm concentration of above listed gases at  $200^\circ C$  operating temperature. Gas response and selectivity for various gases viz.  $NH_3$ , CO, LPG (Propane: Butane, 6:4),  $SO_2$ ,  $H_2S$  and  $NO_2$  were tested. Fig 3.10 shows gas response for various gases viz.  $NH_3$ , CO, LPG (Propane: Butane, 6:4),  $SO_2$ ,  $H_2S$  and  $NO_2$  gases at  $200^\circ C$  for 200 ppm gas concentration.

The maximum response of around 25 times the response of other gases was noticed for the  $NO_2$  gas as seen in the bar graph in Fig 3.10. The selectivity of  $Zn_2SnO_4$  thin films towards the gases varied as  $NH_3 < CO < LPG < SO_2 < H_2S < NO_2$ . Therefore, the sensor based on  $Zn_2SnO_4$  thin film can be used for the selective detection of  $NO_2$  when there is a mixture of  $NO_2$  and other gases. Further, it is observed that for repeated (10 times) on and off responses there is no major change in the signal.

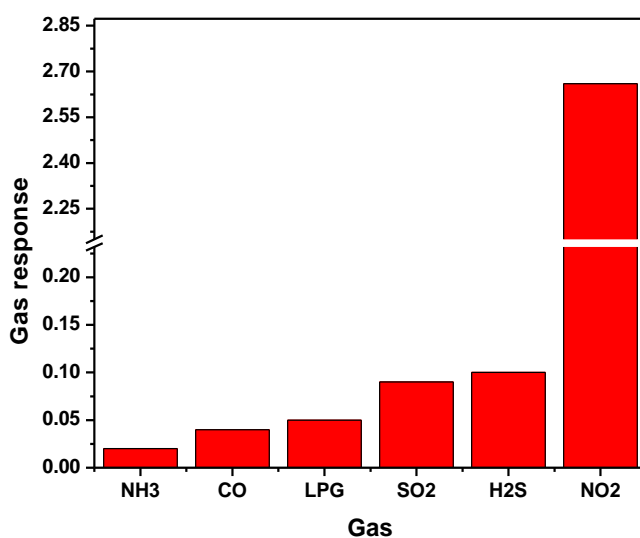


**Figure 3.10 Selectivity studies of typical  $Zn_2SnO_4$  thin film sensor for various gases at 200°C for 200 ppm gas concentration.**

#### **3.3.4.4 Stability of $Zn_2SnO_4$ thin film sensor**

In order to check durability and ruggedness of the sensor,  $NO_2$  response of the films deposited at 375 °C was tested after every month and it is found that gas response decreases fast initially and remains nearly constant after 240 days (Figure 3.11). This decrease in the gas response with the number of days can be attributed to the formation of layer oxides/moisture. To check the deterioration in the films causing the decrease in gas response film deposited at 375°C were annealed at 400 °C for 6 hours. After annealing film, gas response increased and restored to a value observed after one month. The gas response of annealed film is presented in the Figure 3.12.

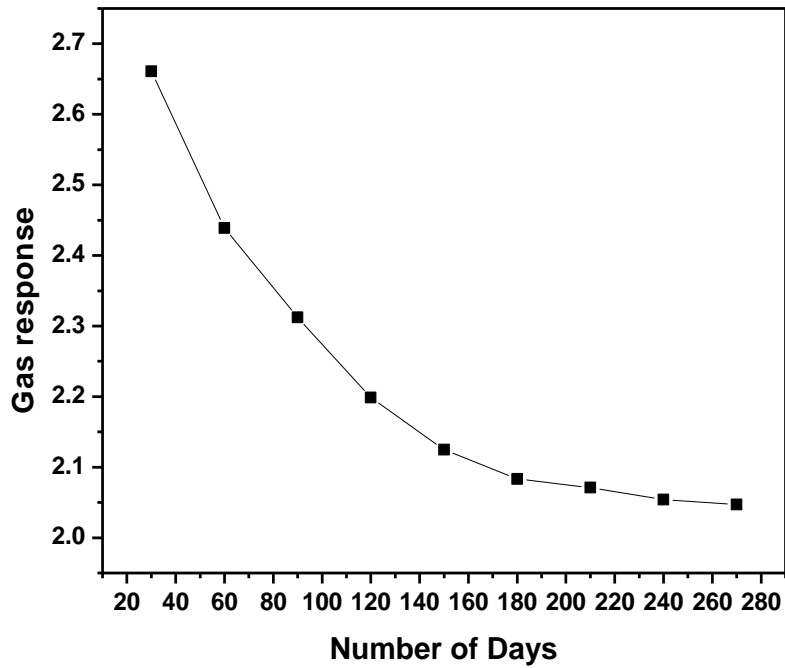


**Figure 3.11** NO<sub>2</sub> response as a function of time for the Zn<sub>2</sub>SnO<sub>4</sub> thin film deposited at 375 °C (Operating temperature =200 °C, NO<sub>2</sub> concentration = 200 ppm).

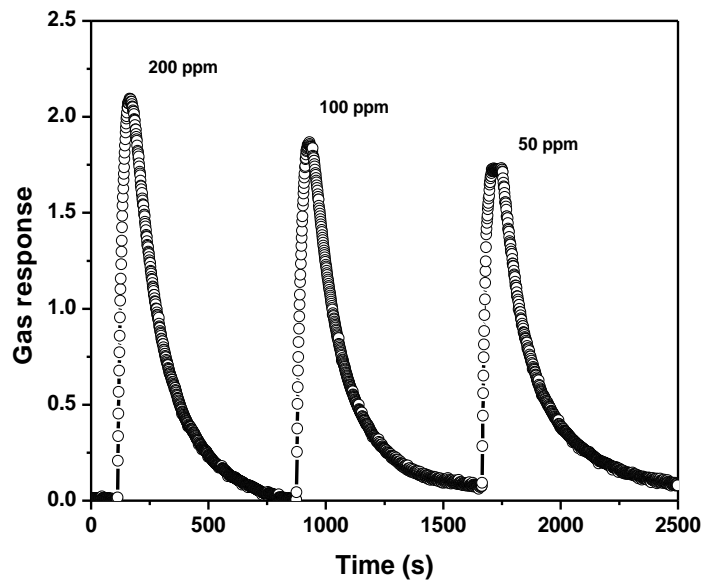


**Figure 3.12 Gas response vs. time of typical Zn<sub>2</sub>SnO<sub>4</sub> thin film annealed after 270 days towards 200 ppm NO<sub>2</sub> at 200°C operating temperature.**

### **3.3.4.5 Gas sensing of Pd sensitized Zn<sub>2</sub>SnO<sub>4</sub> thin films**

The gas sensor with high response, high selectivity, low response and recovery times are considered to be a good sensor. In order to improve the response and recovery times, the Zn<sub>2</sub>SnO<sub>4</sub> films were sensitized with Pd and the gas response measurements were carried out keeping the sensing parameters same as in previous measurements. Gas response with respect to time for the Pd sensitized Zn<sub>2</sub>SnO<sub>4</sub> thin film deposited at 375 °C is shown in Fig (3.13). Pd sensitization causes fast spillover of the gas resulting in enhancement in the response and recovery times. There is an overall reduction in both response and recovery times and particularly for 200 ppm NO<sub>2</sub> concentration, the response time was dropped from 25 s to 6 s while the recovery time reduced from 282 s to 221 s. The gas response was enhanced from 2.66 to 3.31. The table 3.3 presents comparison of the gas response, response and recovery times of the Zn<sub>2</sub>SnO<sub>4</sub> films deposited at 375 °C and the Pd sensitized Zn<sub>2</sub>SnO<sub>4</sub> films. The gas sensing results achieved are comparable to the previous reports [42-44]. Further attempts will be made to reduce the lower detection limit and improve the recovery time of the sensor as the recovery time is much higher (37 times) than the response time even after Pd sensitization.

**Table 3.3 Comparison of gas response, response and recovery times of Pd sensitized and Zn<sub>2</sub>SnO<sub>4</sub> thin film deposited at 375 °C for 200 ppm gas concentration at 200 °C operating temperature.**

Gas concentration (ppm)	Zn <sub>2</sub> SnO <sub>4</sub>			Pd Sensitized Zn <sub>2</sub> SnO <sub>4</sub>		
	Response time (s)	Recovery time (s)	Gas response	Response time (s)	Recovery time (s)	Gas response
50	17	290	2.31	5	179	2.78
100	20	325	2.44	5	201	3.01

200	25	282	2.66	6	221	3.31
-----	----	-----	------	---	-----	------

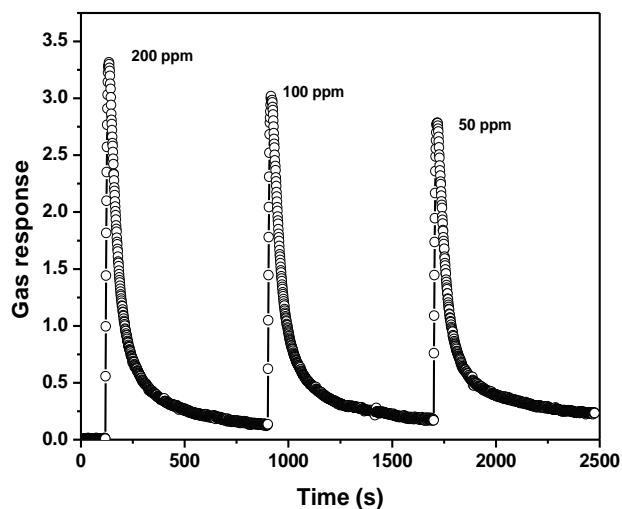


**Figure 3.13 Gas response vs. time of Pd sensitized  $Zn_2SnO_4$  thin film deposited at  $375^\circ C$  towards 200 ppm  $NO_2$  at  $200^\circ C$  operating temperature.**

### 3.4 Conclusions

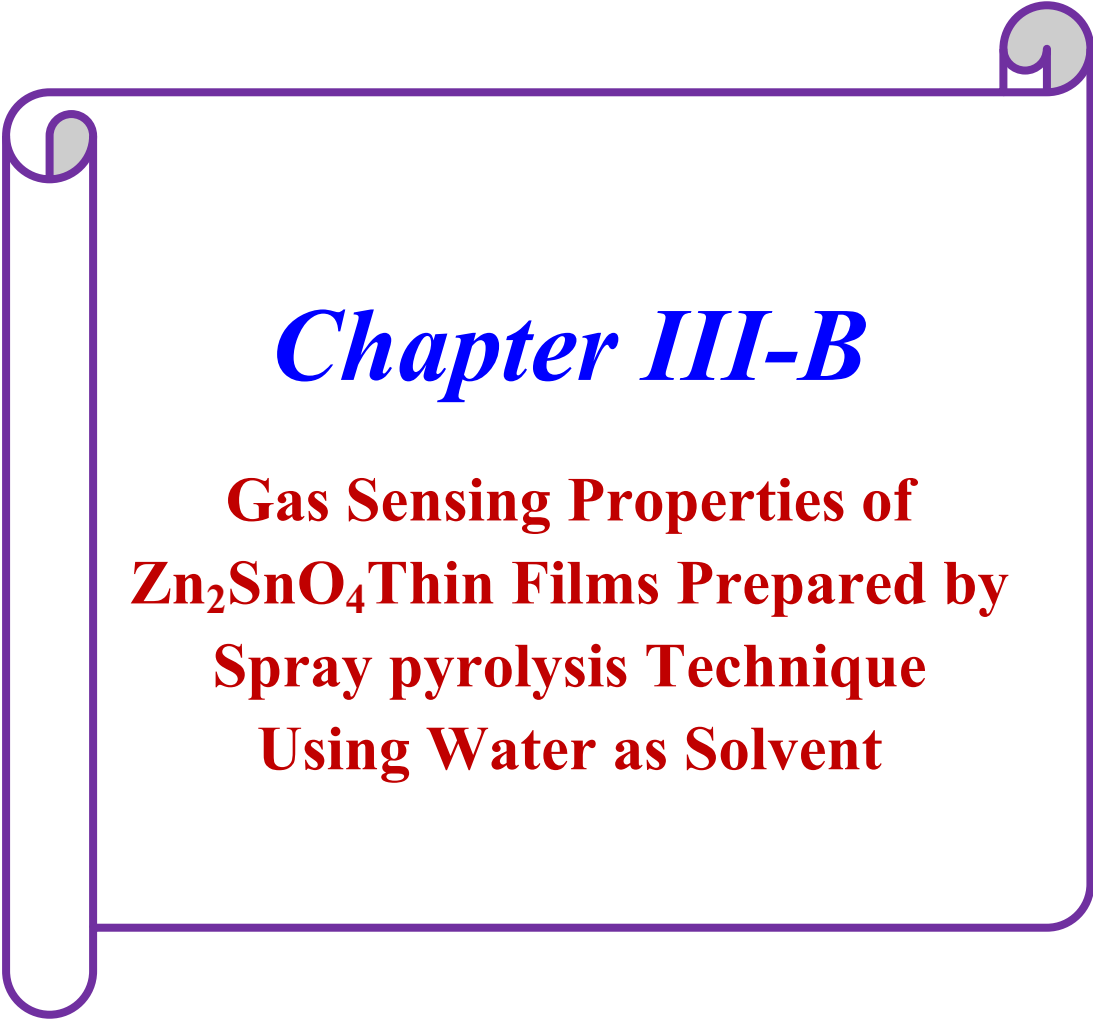
The ternary oxide  $Zn_2SnO_4$  films based  $NO_2$  sensors were successfully deposited by spray pyrolysis method. The formation of the  $Zn_2SnO_4$  was confirmed by the XRD measurements. The films were very highly sensitive and selective towards  $NO_2$  gas. The operating temperature of the sensor was moderately low ( $200^\circ C$ ) showing highest gas response of 2.66 for 200 ppm of  $NO_2$ . The films deposited at  $375^\circ C$  substrate temperature consisting of microstructured granules are highly active towards the sensing of the  $NO_2$  gas among the mixture of gases viz.  $NH_3$ ,  $CO$ ,  $LPG$ ,  $SO_2$ ,  $H_2S$  and  $NO_2$ . The response time for the films varies from 4 to 25 s while recovery time is relatively higher than the response time. The films showed acceptably good gas response up to 240 days. This is indicative of appropriate sensitivity, fast response, stability and durability of the spray deposited  $Zn_2SnO_4$  films. Pd sensitization further improved the gas response, response and recovery times of the sensor.

## References

- [1] C. Wang, L. Yin, L. Zhang, D. Xiang, R. Gao, *Sensors* 10 (2010) 2088.
- [2] Y. F. Sun, S. B. Liu, F. L. Meng, J. Y. Liu, Z. Jin, L. T. Kong, J. H. Liu, *Sensors* 12 (2012) 2610.
- [3] B. C. Yadav, A. Yadav, S. Singh, K. Singh, *Sensors and Actuators B: Chemical*, 177 (2013) 605.
- [4] S.T. Navale, G.D. Khuspe, M.A. Chougule, V.B. Patil, 75 (2014) 236.
- [5] Y. Q. Liang, Z. D. Cui, S. L. Zhu, Z. Y. Li, X. J. Yang, Y. J. Chen, J. M. Ma, *Nanoscale*, 5 (2013) 10916.
- [6] S. Baruah, J. Dutta, *Sci. Technol. Adv. Mater.* 12 (2011) 013004.
- [7] Y. L. Liu, Y. Xing, H. F. Yang, Z. M. Liu, Y. Yang, G. L. Shen, R. Q. Yu, *Analytica Chimica Acta*, 527 (2004) 21.
- [8] E. Comini, G. Faglia, G. Sberveglieri, L. Zanott, *Materials and Manufacturing Processes*, 21 (2006) 229.
- [10] Z. Wang, J. Liu, F. Wang, S. Chen, H. Luo, X. Yu, *J. Phys. Chem. C* 2010, 114, 13577.
- [11] A. Rong, X. P. Gao, G. R. Li, T. Y. Yan, H. Y. Zhu, J. Q. Qu, D. Y. Song, *J. Phys. Chem. B* 110 (2006) 14754.
- [12] X. Lou, X. Jia, J. Xu, S. Liu, Q. Gao, *Mater. Sci. Eng. A* 432 (2006) 221.
- [13] Y. Zhang, J. Wang, H. Zhu, H. Li, L. Jiang, C. Shu, W. Hu, C. Wang, *J. Mater. Chem.*, 20 (2010) 9858.
- [14] P. Wadkar, D. Bauskar, P. Patil, *Talanta* 105 (2013) 327–332.
- [15] P. Song, Q. Wang, Z. Yang, *Materials Letters* 65 (2011) 430.
- [16] S. Park, S. An, H. Ko, C. Jin, C. Lee, *Ceramics International* 39 (2013) 3539.
- [17] Y. Yamada, Y. Seno, Y. Masuoka, K. Yamashita, *Sensors and Actuators B* 49 (1998) 248.
- [18] W. J. Moon, J. H. Hu, G. M. Choi, *Sensors and Actuators B* 80 (2001) 21.
- [19] A. Sivapunniam, N. Wiromrat, M. T. ZarMyint, J. Dutta, *Sensors and Actuators B*, 157 (2011) 232.
- [20] J. Huang, X. Xu, C. Gu, W. Wang, B. Geng, Y. Sun, J. Liu, *Sensors and Actuators B* 171–172 (2012) 572 5.

- [21] G. Ma, R. Zou, L. Jiang, Z. Zhang, Y. Xue, L. Yu, G. Song, W. L. J. Hu, *Cryst. Eng. Comm*, 14 (2012) 2172.
- [22] H. Uchiyama, R. Nagao, H. Kozuka, *Journal of Alloys and Compounds* 554 (2013) 122.
- [23] S. Gautam, A. Thakur, A. Vij, J. Suk, I. J. Lee, Y. J. Park, T. J. Shin, M. G. Kim, H. J. Shin, J. M. Lee, J. M. Chen, J. Song, K. H. Chae, *Thin Solid Films* 556 (2013) 250.
- [24] S. H. Choi, I. S. Hwang, J. H. Lee, S. G. Oha, I. D. Kim, *Chem. Commun.*, 47 (2011) 9315.
- [25] I. Stambolova, K. Konstantinov, D. Kovacheva, P. Peshev, and T. Donchev, *Journal of Solid State Chemistry* 128 (1997) 305.
- [26] S. Matsushima, S. Kunitsugu, K. Kobayashi, G. Okada, *Journal of the Ceramic Society of Japan*, 103 (1995) 302.
- [27] G. Eranna, B. C. Joshi, D. P. Runthala, R. P. Gupta, *Critical Reviews in Solid State and Materials Sciences*, 29 (2004) 111.
- [28] P. X. Gao, P. Shimpi, H. Gao, C. Liu, Y. Guo, W. Cai, K. T. Liao, G. Wrobel, Z. Zhang, Z. Ren, H. J. Lin, *Int. J. Mol. Sci.* 13 (2012) 7393.
- [29] M. A. Alpuche-Aviles, Y. Wu, *J. Am. Chem. Soc.*, 131 (2009) 3216.
- [30] D. L. Young, D. L. Williamson, T. J. Coutts, *J. Appl. Phys.*, 91 (2002) 1464.
- [31] Z. Lu, Y. Tang, *Materials Chemistry and Physics*, 92 (2005) 5.
- [32] Y. Jiang, X. Chen, R. Sun, Z. Xiong, L. Zheng, *Materials Chemistry and Physics* 129 (2011) 53.
- [33] M. Fleischer, *Meas. Sci. Technol.* 19 (2008) 042001.
- [34] S.S. Shinde, P.S. Shinde, R.T. Sapkal, Y.W. Oh, D. Haranath, C.H. Bhosale, K.Y. Rajpure, *Journal of Alloys and Compounds* 538 (2012) 237.
- [35] Y. Li, J. Gong, M. McCune, G. He, Y. Deng, *Synthetic Metals*, 160 (2010) 499.
- [36] B. Tan, E. Toman, Y. Li, Y. Wu, *J. AM. CHEM. SOC.*, 129 (2007) 4162.
- [37] M.A. Alpuche-Aviles, Y. Y. Wu, *J. Am. Chem. Soc.* 131 (2009) 3216.
- [38] C. Wongchoosuk, A. Wisitsoraat, D. Phokharatkul, A. Tuantranont, T. Kerdcharoen, *Sensors*, 10 (2010) 7705.
- [39] N. D. Hoa, N. V. Quy, D. Kim, Nanowire structured SnO<sub>x</sub>-SWNT composites: high performance sensor for NO<sub>x</sub> detection, *Sensors and Actuators B: Chemical* 142 (2009) 253.

- [40] A. Stanoiu, C. E. Simion, S. Somacescu, *Sensors and Actuators B* 186 (2013) 687.
- [41] L. Shi, A. J. T. Naik, J. B. M. Goodall, C. Tighe, R. Gruar, R. Binions, I. Parkin, J. Darr, *Langmuir* 29 (2013) 10603.
- [42] S. Maeng, S. W. Kim, D. H. Lee, S. E. Moon, K. C. Kim, A. Maiti, *Appl. Mater. Interfaces* 6 (2014) 357.
- [43] P. Rai, R. Khan, S. Raj, S. M. Majhi, K. K. Park, Y. T. Yu, I. H. Lee, P. K. Sekhar, *Nanoscale*, 6 (2014) 581.
- [44] F. Sun, X. Li, L. Liu, 184 (2013) 220.



## *Chapter III-B*

**Gas Sensing Properties of  
 $Zn_2SnO_4$  Thin Films Prepared by  
Spray pyrolysis Technique  
Using Water as Solvent**

## INDEX

### Chapter III-B

#### **Gas Sensing Properties of Zn<sub>2</sub>SnO<sub>4</sub> Thin Films Prepared by Spray Pyrolysis Technique using alcohol as solvent**

3.1 Introduction

3.2 Experimental Procedure

3.3 Results and discussion

3.3.1 Reaction mechanism

3.3.2 Structural characterization of Zn<sub>2</sub>SnO<sub>4</sub> thin films

3.3.2.1 X-ray diffraction study

3.3.2.2 Scanning electron microscopy study

3.3.2.3 Atomic force microscopy study

3.3.3 Optical characterization of Zn<sub>2</sub>SnO<sub>4</sub> thin films

3.3.3.1 UV-Visible analysis of Zn<sub>2</sub>SnO<sub>4</sub> thin films

3.3.4 Gas sensing study of Zn<sub>2</sub>SnO<sub>4</sub> thin films

3.3.4.1 Optimization of operating temperature and sensitivity for  
NO<sub>2</sub>

gas sensing

3.3.4.1.1 Variation of gas response with operating  
temperature

3.3.4.1.2 Variation of gas response with NO<sub>2</sub> concentration

3.3.4.2 Response and Recovery time

3.3.4.3 Selectivity of Zn<sub>2</sub>SnO<sub>4</sub> thin film sensor

3.3.4.4 Stability of Zn<sub>2</sub>SnO<sub>4</sub> thin film sensor

3.3.4.5 Gas sensing of Pd sensitized Zn<sub>2</sub>SnO<sub>4</sub> thin films

3.4 Conclusions

## CHAPTER III-B

### **Gas Sensing Properties of $Zn_2SnO_4$ Thin Films Prepared by Spray Pyrolysis Technique using alcohol as solvent**

#### **3B.1 Introduction**

Improvement in the selectivity of the MOS can be achieved by different techniques and ideas which include synthesis of nano structured films, use of Metal oxides semiconductors (MOS) have been proved as the most suitable materials for solid state gas sensors for the past few decades [1]. This is due to their inherent properties such as ease of fabrication, fast and high response, and excellent recovery [2]. MOS can be used for detection of different oxidizing and reducing gases and with the advancement of technology it is possible now to detect ppm to ppb level gas concentration when operating at room temperature even while operating under harsh environments [3, 4]. The major drawback in MOS gas sensor is the selectivity of the sensor MOS based sensors are less selective and show significant response towards variety of gases [5]. Various dopants, using different substrates and even interdigitated electrodes of gold and platinum [6, 7]. One of the best alternatives to improve performance of the sensor is to use composite materials or to use ternary or even quaternary MOS consisting of two or more metal elements [8]. It is also reported that, desired sensing properties can be achieved by altering the polymorphic phase of a single oxide material by using another suitable transition metal [9]. It has been reported that SnO is the most suitable and widely studied material used for gas sensing and it is followed by ZnO,  $In_2O_3$  and mixed metal oxides [1]. Large number of reports is available [1] on these materials used as film gas sensors in various fields for the detection of toxic and polluting gases. Thus it is worth to use Zn and Sn in a ternary system forming  $Zn_2SnO_4$  for the possible selective gas detection.

Ma et al. [10] synthesized cubic  $ZnSnO_3$  and octahedral  $Zn_2SnO_4$  microcrystals by using one-step chemical solution route and studied their utility towards  $H_2S$ ,  $C_2H_5OH$  and  $HCHO$ . Different faceted structures of zinc stannate ( $ZnSnO_3$  and  $Zn_2SnO_4$ ) have been synthesized by changing the stannic precursors. Polycrystalline  $Zn_2SnO_4$  thin films were synthesized by Young et al.

[11] using rf magnetron sputtering and their structural properties were investigated. The multiple networked Zn<sub>2</sub>SnO<sub>4</sub>-core/ZnO-shell nanorod sensors were synthesized by Park et al. [12] and results showed a response of 173–498% towards 1-5 ppm NO<sub>2</sub> concentrations operating at 300 °C. Thermal evaporation followed by atomic layer deposition at 1000 °C was employed for the synthesis of Zn<sub>2</sub>SnO<sub>4</sub>-core/ZnO-shell nanorod structure. Using hydrothermal method Ai et al. [13] synthesized Zn<sub>2</sub>SnO<sub>4</sub> microcubes for the removal of NO and HCHO from the indoor air to maintain air quality. They have shown that air having concentration less than 400 ppb of NO and 2 ppm HCHO can be maintained using Zn<sub>2</sub>SnO<sub>4</sub> microcubes. NO<sub>2</sub> response of 5 (R<sub>g</sub>/R<sub>a</sub>) is reported by Stambolova et al. for spray deposited Zn<sub>2</sub>SnO<sub>4</sub> films at 420 °C operating temperature [14].

Even though various methods have been reported for the synthesis of Zn<sub>2</sub>SnO<sub>4</sub> films [15], hydrothermal method is widely used. Herewith we report use of spray pyrolysis method for the synthesis of the Zn<sub>2</sub>SnO<sub>4</sub> films. To best of our knowledge and available reports synthesis of Zn<sub>2</sub>SnO<sub>4</sub> films by spray pyrolysis are not available [14, 16, 17]. Here we report synthesis of Zn<sub>2</sub>SnO<sub>4</sub> films using spray pyrolysis system and effect of substrate temperatures on the physical and NO<sub>2</sub> sensing properties of Zn<sub>2</sub>SnO<sub>4</sub> films. Enhanced NO<sub>2</sub> response along with selectivity is observed even at moderate operating temperature of 200 °C.

### **3B.2 Experimental Procedure**

Zn<sub>2</sub>SnO<sub>4</sub> thin films have been synthesized using, zinc chloride (ZnCl<sub>2</sub>) and stannic chloride (SnCl<sub>4</sub>.5H<sub>2</sub>O) are as cationic precursors of zinc and tin, respectively and double distilled water is used as solvent. The chemicals were procured from S. D. Fine Chemicals Limited, Mumbai, and used as received without any further treatment. To obtain the Zn<sub>2</sub>SnO<sub>4</sub> thin films, ZnCl<sub>2</sub>, SnCl<sub>4</sub> were taken in the ratio of 2:1 and dissolved in required amount of distilled water. Thus respective concentrations of ZnCl<sub>2</sub>, SnCl<sub>4</sub> in the precursor solutions were 0.2 M and 0.1 M respectively. The precursor solution formed was then sprayed onto the preheated glass substrates at different temperatures. The deposition temperature was varied as 300, 350 and 400 °C respectively. To achieve optimum thickness of the films solution quantity was fixed to 200 ml.

Other spray parameters such as spray rate (10 ml/min) and the nozzle to substrate distance (28 cm) were optimized by observing uniformity and adherence of the films.

Gas sensing performance was studied using locally fabricated testing chamber equipped with Rigol digital multimeter (DM3000). Sensor of size 1 cm × 1 cm was fabricated and silver contacts were drawn for good electrical contacts. Thin film sensor was mounted in 250 ml airtight container where it is preheated at required temperature using temperature controller. Sensor was heated until its resistance stabilized and the time required for this was around two hours. Thin film sensors were then exposed to the analyte gas of desired concentration in the gas sensor unit and change in the resistance was monitored using digital multimeter. After each successive measurement, fresh air was passed in to the test box and then required amount of analyte gas was injected into the box to obtain a desired concentration. Selectivity studies were carried out by monitoring change in resistance of the film by purging various gases of desired concentration. Various canisters of H<sub>2</sub>S, CO, CO<sub>2</sub>, NH<sub>3</sub>, SO<sub>2</sub>, NO<sub>2</sub> and LPG, and gases having 1,000 ppm gas concentration were used as analyte gases procured from Shreya Enterprises Pvt. Ltd. Mumbai, Maharashtra, India.

Figure 3B.1 shows XRD patterns of Zn<sub>2</sub>SnO<sub>4</sub> films deposited at different substrate temperatures. Phase change of the synthesized films can be clearly observed in the Figure 1. The film prepared at 300 and 350 °C exhibits mixed phases of ZnO, SnO<sub>2</sub> and Zn<sub>2</sub>SnO<sub>4</sub> with major contribution of Zn<sub>2</sub>SnO<sub>4</sub>. Contribution to the XRD phase from SnO<sub>2</sub> phase at 300 °C is higher than ZnO. It can also be notified that with increase in substrate temperature (350 °C) contribution of SnO<sub>2</sub> peak decreases and that of ZnO phase is almost disappeared. XRD pattern of the film deposited at 400 °C matches well with the JCPDS card No. 73-1725 confirming cubic face centered crystal structure. It is observed that with change in substrate temperature of the film crystal orientation changes due to the different growth rate of the films at different substrate temperatures.

### 3B.3 Results and discussion

#### 3B.3.1 Structural characterization of $Zn_2SnO_4$ thin films

The structural characteristics of  $Zn_2SnO_4$  thin films was carried out by XRD, SEM and AFM.

##### 3B.3.1.1 X-ray diffraction study

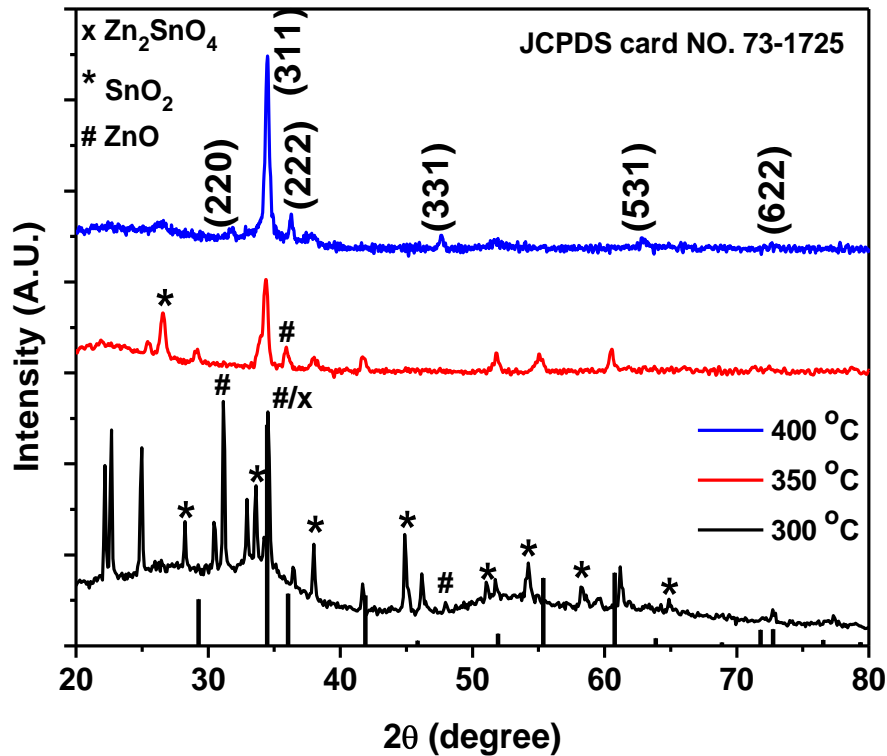


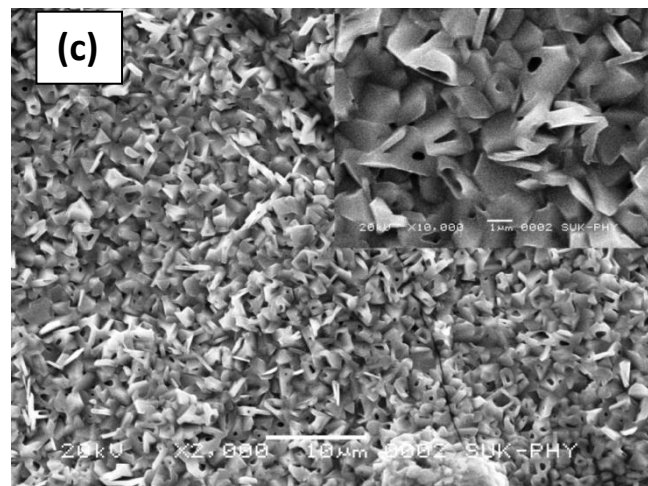
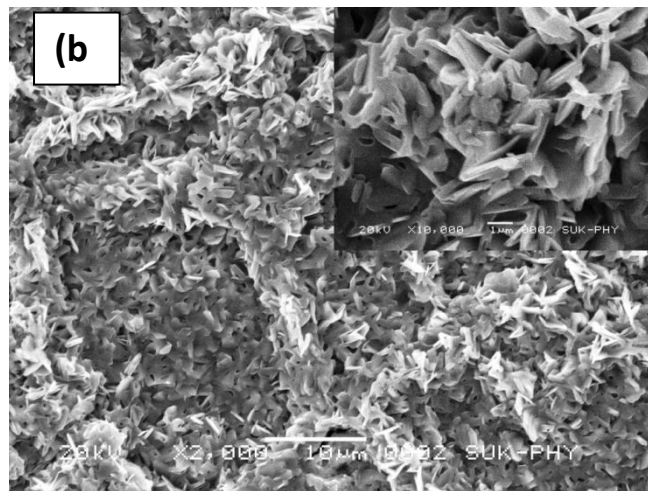
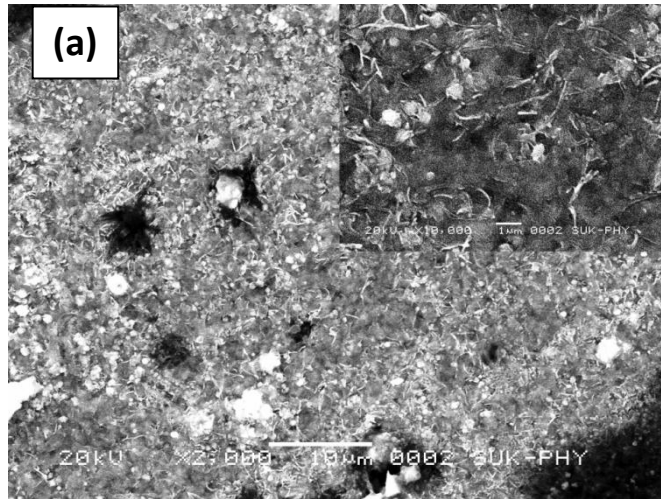
**Figure 3B.1 XRD patterns of  $Zn_2SnO_4$  films deposited at different substrate temperatures.**

Initially at 300 °C films are polycrystalline while with increase in temperature, its preferentially orientated along (3 1 1) plane. The existence of well defined reflection along (3 1 1) plane at angle  $34.3^\circ$  and well matching of  $2\theta$  and 'd' values with JCPDS card No. 73-1725 depicts the formation of phase pure  $Zn_2SnO_4$  thin film with cubic face centered crystal structure at 400 °C. As compared with our earlier results [16] increased thickness and change in solvent enhanced crystallinity of the films and increased preferential orientation along (3 1 1) plane [18]. Peaks belonging to different mixed oxide phases  $ZnO$  and  $SnO_2$

are identified in Figure 3B.1 separately using corresponding JCPDS cards. Crystallite size is calculated using Scherer's formula [19] for the (3 1 1) plane. Crystallite size increases with increase in substrate temperature as 20, 41 and 84 nm for 300, 350 and 400 °C substrate temperatures, respectively. Crystallite size increases with increase in the substrate temperature due to annealing effect and agglomeration of smaller crystallites in to larger crystallites.

### **3B.3.1.2 Scanning electron microscopy study**

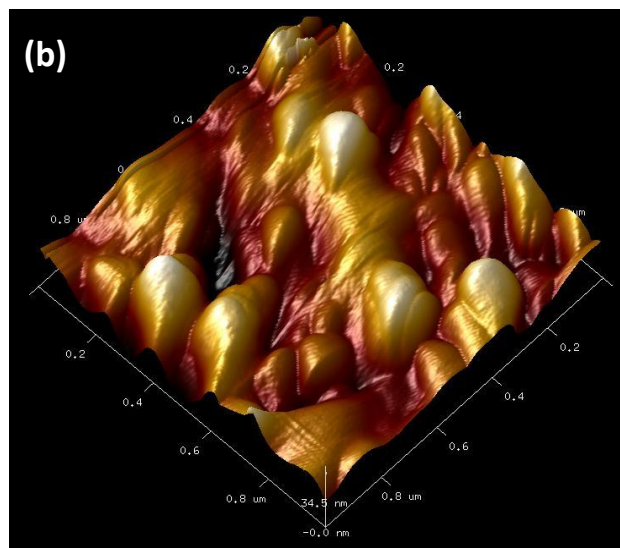
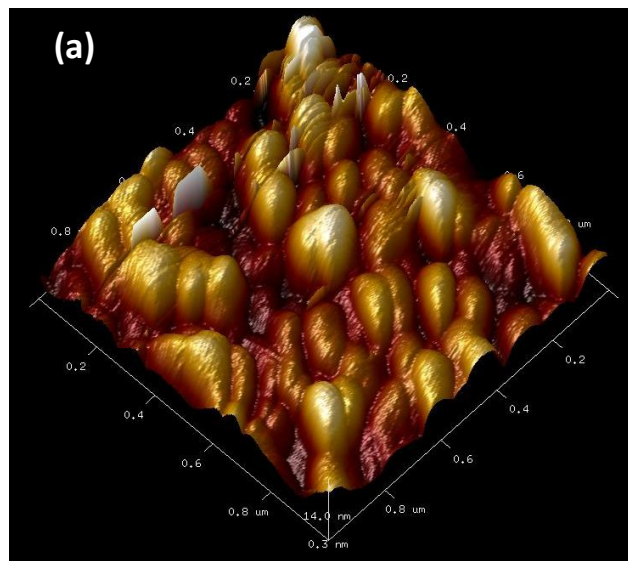
Figure 3B.2 shows SEM images of Zn<sub>2</sub>SnO<sub>4</sub> films deposited at different substrate temperatures and inset of Figure 3B.2 shows enlarged images. SEM images depicts that the surface morphology is characterized by the presence of cubical micro-flakes. It can easily be observed that films start to grow with increase in substrate temperatures and randomly orientated flakes, which are strongly faceted, can be observed in the inset of the film deposited at 400 °C. Agglomeration of the randomly oriented flakelike grains makes surface considerably rough and also numerous hollow voids are formed due to overlapping of the flakes increasing the effective surface area. Film deposited at 300 °C shows that growth of the film just started and that at 350 °C shows randomly oriented flakes branched in some direction. Increase in substrate temperature increases flakes size and flakes are well distributed at 400 °C than that at 350 °C due to agglomeration of the smaller crystallites. The characteristic feature of cubical flakelike is clearly evident in the Figure 3B.2 (c). The average size of these cubical flakelike is 1 μm. These flakes provide porous structure which increases effective surface area and thus is very helpful for adsorption of the NO<sub>2</sub>. It is important to note that effective surface area increases linearly for the samples deposited at 300, 350, and 400 °C. The cubical flakelike geometry observed from the SEM images supports the findings from XRD analysis



**Figure 3B.2 SEM images of  $Zn_2SnO_4$  thin films deposited at different substrate temperatures (a) 300 (b) 350 and (c) 400 °C, respectively.**

### **3B.3.1.3 Atomic force microscopy study**

An atomic force microscopy (AFM) was used to study topography and measure the surface roughness of the films in tapping mode. For each sample, images were scanned for different areas to check for uniformity of the thin films. Figure 3B.3 shows AFM images of  $Zn_2SnO_4$  films deposited at various substrate temperatures. Increase in the surface roughness is observed with increase in substrate temperature. Roughness of the films is 8, 28 and 35 nm for films deposited at 300, 350 and 400 °C, respectively. It is maximum for the film deposited at 400 °C supporting the observations in the SEM studies.



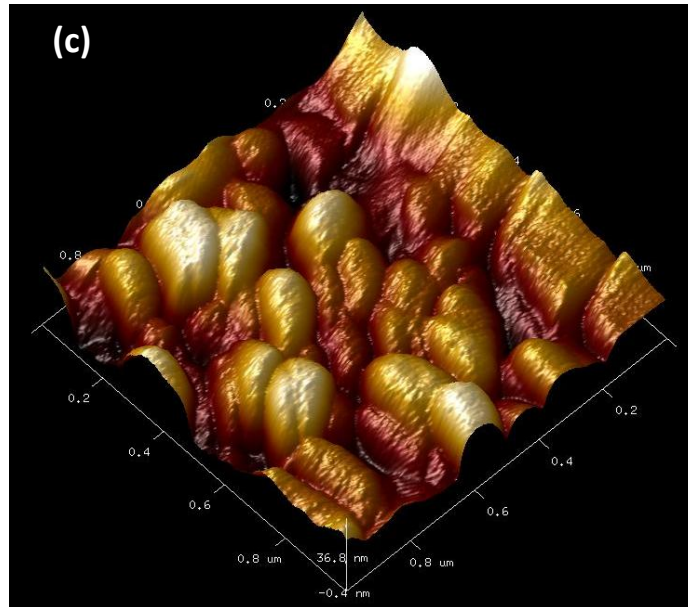


**Figure 3B.3 AFM images of  $Zn_2SnO_4$  thin films deposited at different substrate temperatures (a) 300 (b) 350 and (c) 400 °C, respectively.**

### **3B.3.2 Optical characterization of $Zn_2SnO_4$ thin films**

#### **3B.3.2.1 UV-Visible analysis of $Zn_2SnO_4$ thin films**

Figure 3B.4 shows graph of  $(ah\nu)^2$  versus  $h\nu$  calculated using optical absorption confirming direct band gap of the  $Zn_2SnO_4$  to be 3.49 eV which is less than reported band gap of  $Zn_2SnO_4$  (3.7 eV). Band gap was calculated by measuring absorbance of the films in transmission mode and using Tauc equation [21] for direct allowed transitions. As reported by Aviles et al the fundamental band-gap of  $Zn_2SnO_4$  is 3.60-3.70 eV, due to the incorporation of excess Zn into  $Zn_2SnO_4$  matrix and after heat treatment, band gap is narrowed up to 3.25 eV [18]. On the other hand, based on the discussion of the Jiang et al [22] the red-shift in the fundamental band-gap for quasi-cubic  $Zn_2SnO_4$  is attributed to differences in the crystal structure. Absorbance of the film decreases with increase in the substrate temperature of the films due to the decrease in the film thickness. At higher substrate temperature film thickness decreases due to the increase in the thermophoretic force which causes evaporation of droplets prior to the surface of substrates [23]. Band gap increases linearly with increase in substrate temperature due to the formation of  $Zn_2SnO_4$ . For higher film thickness

plane orientation changes and hence there is increase in the band gap of film. It is also reported that oxygen content influences the absorption across the band gap and shift in absorption edge is due to the change in the lattice oxygen [24]. Decrease in the lattice oxygen is due to the high growth rate at higher substrate temperatures. . Blue shift in the band gap confirms the increase in the optical band gap, which is useful for gas sensors [25].

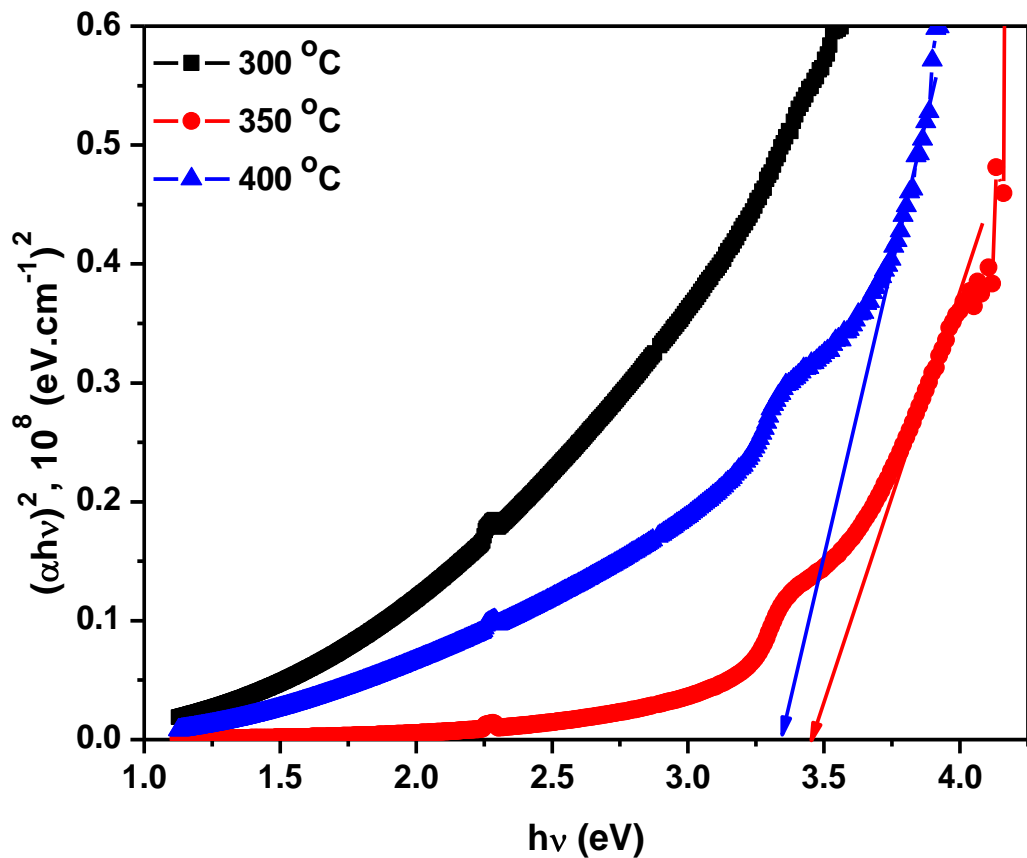


Figure 3B.4  $(\alpha h\nu)^2$  versus  $h\nu$  curves of spray deposited  $Zn_2SnO_4$  films deposited at different substrate temperatures.

### 3B.3.3 Gas sensing study of Zn<sub>2</sub>SnO<sub>4</sub> thin films

Gas sensing measurements of the Zn<sub>2</sub>SnO<sub>4</sub> thin films deposited at different substrate temperatures were done towards various gases, gas concentrations and different operating temperatures. Gas response is calculated using formula (3B.1)

$$S = \frac{R_g}{R_a} \quad (3B.1)$$

where R<sub>a</sub> is the resistance of the sensor in air and R<sub>g</sub> is the resistance of the sensor in presence of gas. Response time is measured as time taken by the sensor to reach 90% of its maximum gas response upon purging analyte gas in the test chamber and recovery time is the time taken by the sensor to reach 10% of the maximum gas response value upon removal of gas.

#### 3B.3.3.1 Selectivity of Zn<sub>2</sub>SnO<sub>4</sub> thin film sensor

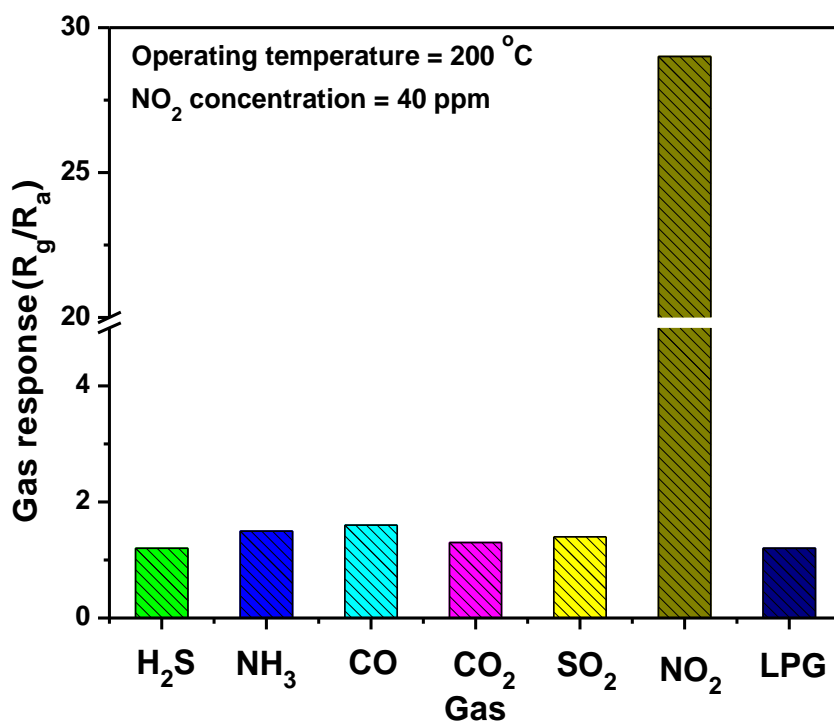


Figure 3B.5 Selectivity study of Zn<sub>2</sub>SnO<sub>4</sub> film towards NO<sub>2</sub> operating at 200 °C temperature.

Initially selectivity of the fabricated sensor is measured towards various oxidizing and reducing gases and corresponding bar graph is plotted in Figure 3B.5. It is observed that gas response is higher towards NO<sub>2</sub> and it is less for all other gases confirming Zn<sub>2</sub>SnO<sub>4</sub> films are exclusively selective towards NO<sub>2</sub>. Underlying origin of this exclusive selectivity towards NO<sub>2</sub> is the highly oxidizing nature and higher electron affinity (2.27 eV) of NO<sub>2</sub> in comparison with electron affinity of the preadsorbed oxygen species (0.44 eV) and other gases [26]. This results in higher gas response of Zn<sub>2</sub>SnO<sub>4</sub> films towards NO<sub>2</sub> as compared with other gases. The highest gas response towards NO<sub>2</sub> is estimated to be 29 which is much higher than that towards other studied gases (less than 2). Noting these facts further measurements were carried out towards NO<sub>2</sub> at different operating temperatures and at different NO<sub>2</sub> concentrations.

In order to quantify the selectivity, the selectivity coefficient of the sensor is calculated using equation 2 and the values are tabularized in Table 3B.1.

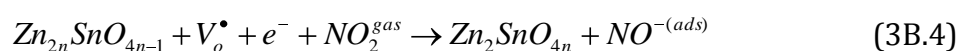
$$K = \left| \frac{S_t}{S_i} \right| \quad (3B.2)$$

where S<sub>t</sub> is the gas response of the target gas and S<sub>i</sub> is the gas response of interfering gas. Selectivity coefficient varies from 19.3 to 24.2 for optimal sensor operating at 200 °C towards 40 ppm gas concentrations. Pronounced selectivity towards NO<sub>2</sub> in presence of SO<sub>2</sub> is observed, which is another major representative coexisting air pollutant.

**Table 3B.1 Selectivity coefficient of Zn<sub>2</sub>SnO<sub>4</sub> films deposited at 400 °C towards various gases.**

Gas	Selectivity Coefficient
H <sub>2</sub> S	24.2
NH <sub>3</sub>	19.3
CO	18.1
CO <sub>2</sub>	22.3
SO <sub>2</sub>	20.7
NO <sub>2</sub>	1.00
LPG	24.2

Many reports have been published describing NO<sub>2</sub> sensing mechanism by a MOS sensor of transition metal [27-28]. The NO<sub>2</sub> adsorption takes place in two different ways depending on the type of site it is being adsorbed. Monomolecular adsorption (NO<sub>2</sub><sup>-</sup>) and adsorption by dissociation in to NO<sup>-</sup> as discussed elsewhere [29]. Reactions involved in the adsorption and reaction are as follows.



where V<sub>o</sub><sup>•</sup> is the oxygen vacancy. This reactions shows that variation in the gas response is depend on the adsorption and charge transfer reaction which involves oxygen vacancies free charge carriers in the film.

### 3B.3.3.2 Variation of gas response with operating temperature

Figure 3B.6 shows variation in gas response of different Zn<sub>2</sub>SnO<sub>4</sub> films operating at different operating temperatures towards 40 ppm NO<sub>2</sub> concentration. It is worth to note that gas response increases with increase in substrate temperature which in result causes change in phase of films. It is

maximum for the film deposited at 400 °C having pure Zn<sub>2</sub>SnO<sub>4</sub> phase and it decreases for other films containing ZnO and SnO<sub>2</sub> mixed oxide phase. Increase in the gas response with change in phase is attributed to the increase in the adsorption sites. At higher substrate temperatures gas response increases due to the change in orientation of the film. It is observed from the XRD patterns that film deposited at 400 °C shows maximum gas response having preferred orientation along (311) plane. Change in preferred orientation changes adsorption energy of the analyte gas molecules and activation energy of the point defects in the crystallites [30].

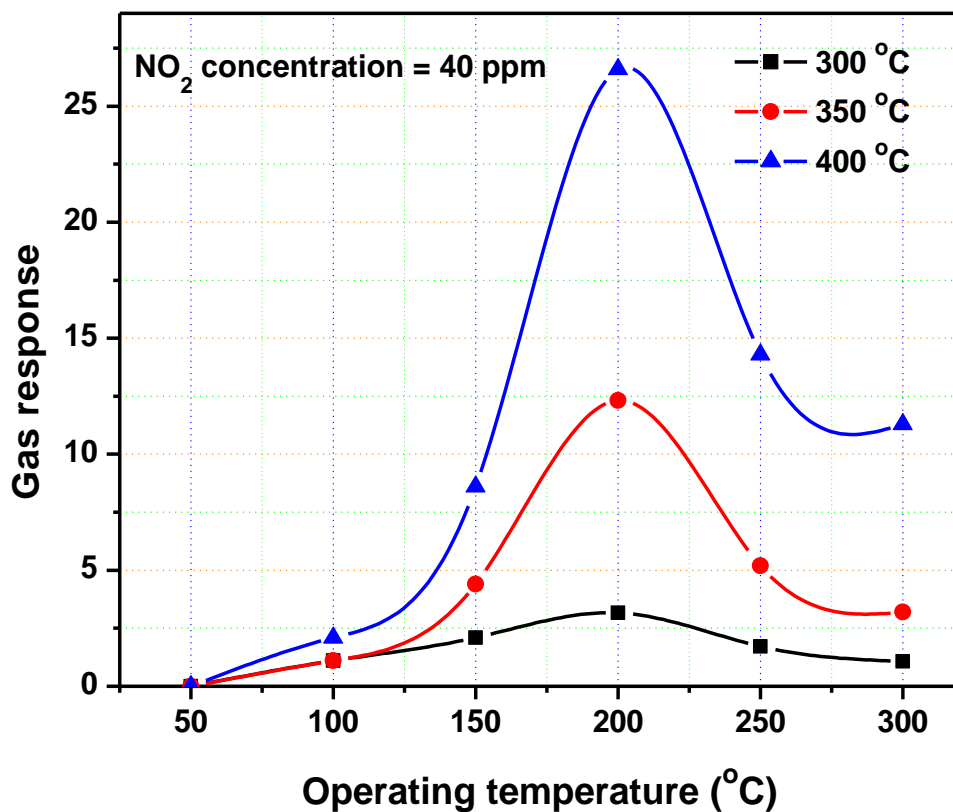


**Figure 3B.6 Effect of operating temperature on Zn<sub>2</sub>SnO<sub>4</sub> films deposited at different substrate temperatures towards 40 ppm NO<sub>2</sub>.**

This changes the chemisorption characteristics of the crystallites from one crystal orientation to another [30, 31, 32]. It can also be noted that gas response is higher for pure phase film orientated along (3 1 1) plane and it decreases for the mixed oxide phase having no preferred orientation. Similar results were reported by Kim et al. [33], they report SnO<sub>2</sub> film oriented along

different planes showed the different gas response and different temperature dependence of gas response. Moon et al. reported that response time is closely related to the surface roughness but there was little association with the orientation of planes [34].

Thermal energy assists the adsorption of  $\text{NO}_2$  as  $\text{NO}_2^-$  or  $2\text{NO}^-$  by charge transfer from electrons or through the pre-adsorbed oxygen species, respectively. A dynamic equilibrium state between the adsorption and the subsequent desorption of oxygen and  $\text{NO}_2$  occurs and it changes as the operating temperature is changed changing response values. Knowing this, in order to optimize operating temperature gas sensing is carried out at varied temperature range of 50-300 °C towards 40 ppm  $\text{NO}_2$  (Figure 3B.6). It is observed that, gas response increases with increase in the operating temperature and maximum is observed at 200 °C and gas response decreases with further increase in temperature. Initially at 50 °C gas response is zero since gas could not adsorb and react with the film surface [35] due to low temperature. Gradual increase in gas response at 100 °C is observed and with further increase in operating temperature significant rise in the response value is seen. It is observed that, gas response increases with increase in the operating temperature and maximum is observed at 200 °C and gas response decreases with further increase in temperature. Initially at 50 °C gas response is zero since gas could not adsorb and react with the film surface [35] due to low temperature. Gradual increase in gas response at 100 °C is observed and with further increase in operating temperature significant rise in the response value is seen.

This increases the respective activation energy barriers by increasing length of depletion layers and highest response value is noted at 200 °C. With further increase in the operating temperature above 200 °C response is reduced. At higher operating temperature (>200 °C), the adsorbed analyte gas species decrease on the film surface due to the higher desorption rate than adsorption rate of the analyte gas. Decrease in the depletion length is observed thereby owing to decrease in the gas response at higher operating temperatures [36]. Film deposited AT 400 °C has higher gas response for all operating temperatures as compared with other films. Enhanced gas response can be attributed to the higher crystallinity, porosity, and surface roughness of the film compared with

other films. This shows that substrate temperature has noteworthy effect on the gas sensing properties of  $Zn_2SnO_4$  films. Since all the films shows highest gas response at 200 °C operating temperature further measurements were carried out at 200 °C.

### 3B.3.3.3 Variation of gas response with $NO_2$ concentration

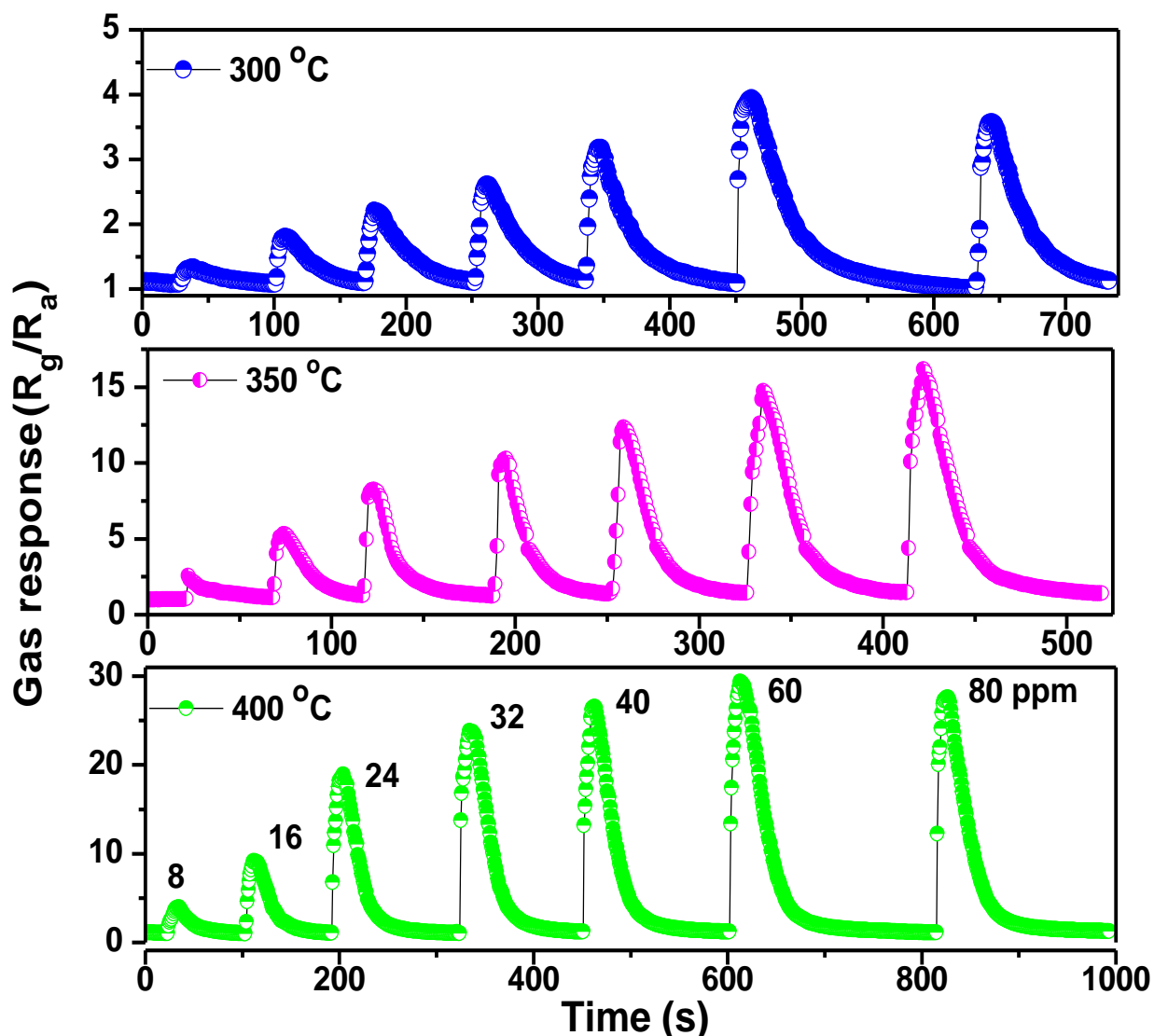


**Figure 3B.7** Transient response curves of  $Zn_2SnO_4$  films towards various concentrations of  $NO_2$  operating at 200 °C temperature.

Apart from this, we have also examined gas response of  $Zn_2SnO_4$  films as a function of  $NO_2$  concentration. Figure 3B.7 shows transient response curves of

Zn<sub>2</sub>SnO<sub>4</sub> films towards various concentrations of NO<sub>2</sub> operating at 200 °C temperature. As expected, response of the sensor increases quickly as soon as gas is in and returns to its initial value when gas is evacuated out of the test chamber. It shows purely reversible gas response for all the sensors operated at different operating temperatures. Gas response increases with increase in NO<sub>2</sub> concentration from 1.32 to 29.27 for 8 to 80 ppm NO<sub>2</sub> concentration.

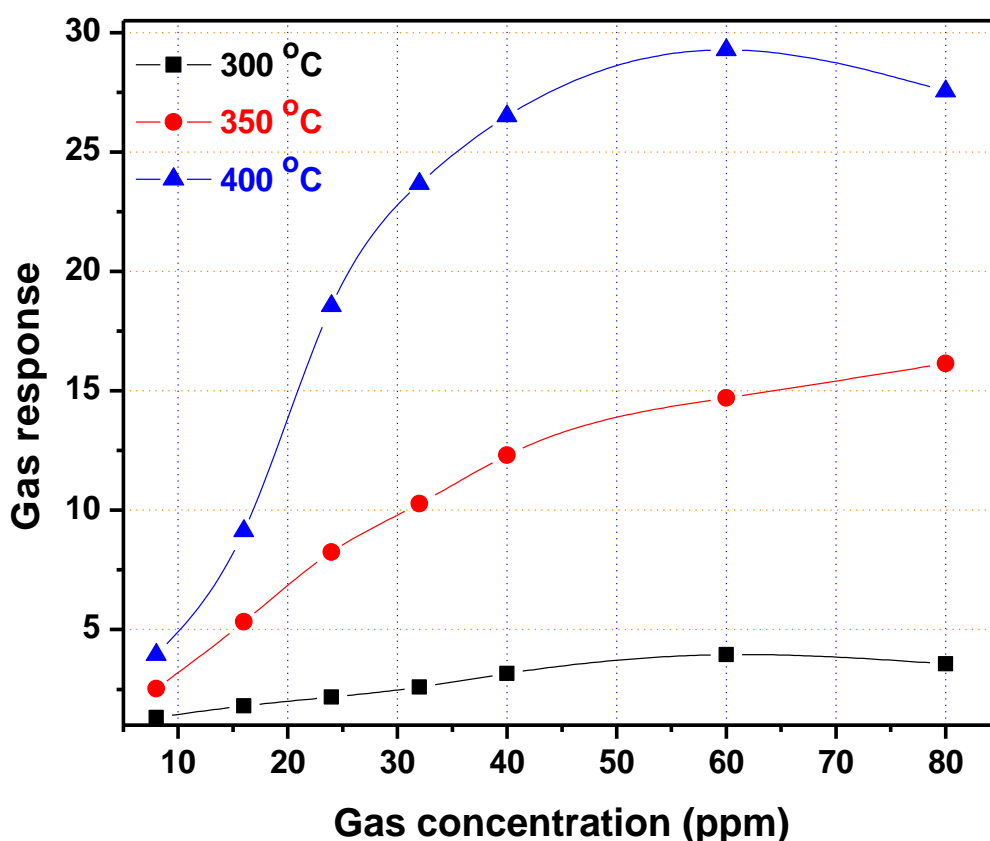


**Figure 3B.8** Effect of NO<sub>2</sub> concentration on gas response of Zn<sub>2</sub>SnO<sub>4</sub> films deposited at different substrate temperatures at 200 °C operating temperature.

Clearly, the response increases sharply as the NO<sub>2</sub> concentration increases from 8 to 40 ppm but saturates when the concentration increases further to 80 ppm. It is worth noting that a response corresponding to concentration of 24 ppm is as high as 18.56 above the value 15, a criterion required for practical application of the sensor [37]. The major difference

between three curves is that the response for the film deposited at 400 °C is substantially larger than that for the films deposited at 300 and 350 °C.

### 3B.3.3.4 Response and Recovery time

**Table 3B.2 Response and recovery times of Zn<sub>2</sub>SnO<sub>4</sub> films deposited at different substrate temperatures.**

Gas concentration (ppm)	300 °C		350 °C		400 °C	
	Response time	Recovery time	Response time	Recovery time	Response time	Recovery time
8	4	35	1	23	8	35
16	5	35	3	27	8	40
24	6	45	4	34	9	45
32	6	50	4	34	9	55
40	8	55	5	36	8	58
60	8	71	8	42	9	61
80	8	34	8	46	7	55

The response and recovery times are two key parameter of a sensor as far as gas sensor are concerned. Table 3B.2 shows response and recovery kinetics of Zn<sub>2</sub>SnO<sub>4</sub> sensors. It is important to note that response of the sensor is faster than recovery for all the NO<sub>2</sub> concentrations. Response and recovery times are measured in light of the definitions and optimal values are 8 and 58 s, respectively, for highest response value. The response and recovery times also meet the basic demands for an industrial application of the sensor [37]. It is worth noting that the response observed for the Zn<sub>2</sub>SnO<sub>4</sub> sensor is higher than sever earlier reports based on NO<sub>2</sub> sensors [12, 16, 27, 38, 39]. Along with this response and recovery times of Zn<sub>2</sub>SnO<sub>4</sub> sensor are fast, films are highly selective towards NO<sub>2</sub> and operating at moderately lower operating temperature. Pristine films show excellent gas sensing characteristics without use of any Nobel metal

or surfactant. These high responses, short times, together with the higher selectivity, suggest that the  $Zn_2SnO_4$  sensors may hold the potential for developing a  $NO_2$  gas sensor.

### 3B.3.3.5 sensitivity of $Zn_2SnO_4$ thin film sensor

Sensitivity of the sensor is calculated using slope of the graph of gas response versus gas concentration as shown in Figure 3B.8. Sensitivities of the  $Zn_2SnO_4$  sensors synthesised at different temperatures are mentioned Table 3B.3.

**Table 3B.3 Sensitivity of  $Zn_2SnO_4$  films deposited at different substrate temperature towards 40 ppm  $NO_2$  operating at 200 °C.**

<b>Substrate temperature (°C)</b>	<b>Sensitivity (ppm<sup>-1</sup>)</b>
<b>300</b>	0.056
<b>350</b>	0.306
<b>400</b>	0.746

Sensitivity increases with increase in substrate temperature and film deposited at 400 °C shows higher sensitivity.

### 3B.4 Conclusions

The ternary oxide  $Zn_2SnO_4$  films were successfully deposited by spray pyrolysis method using DI water as solvent. XRD analysis was used to confirm formation of  $Zn_2SnO_4$ . The sensitivity and selectivity of  $Zn_2SnO_4$  thin films towards  $NO_2$  gas was tested. Both parameters were found to be high at moderately low (200°C) operating temperature of the sensor for the films deposited at substrate temperature 400°C. Gas response varies from 1.32 to 29.27 for 8 to 80 ppm  $NO_2$  concentration. The response time for the films varies from 3 to 8 s while recovery time is relatively higher than the response time.

## References

- [1] G. Eranna, B. C. Joshi, D. P. Runthala, R. P. Gupta, *Critical Reviews in Solid State Materials Science*, 29 (2004) 111.
- [2] Y. Laor, D. Parker, T. Page, *Reviews in Chemical Engineering*, 30 (2014) 139.
- [3] G. F. Fine, L. M. Cavanagh, A. Afonja and R. Binions, *Sensors*, 10 (2010) 5469.
- [4] L. Wang, A. Teleki, S. E. Pratsinis, P. I. Gouma, *Chemistry of Materials*, 20 (2008) 4794.
- [5] G. Korotcenkov, *Materials Science and Engineering B*, 139 (2007) 1.
- [6] M. Zhang, W. Luo, Z. Li, T. Yu, Z. Zou, *Applied Physics Letters*, 97 (2010) 042105.
- [7] W. H. Zhang, W. D. Zhang, *Sensors and Actuators B: Chemical*, 134 (2008) 403.
- [8] C. Chen, J. Li, R. Mia, Y. Liu, *Analytical Methods*, 7 (2015) 1085.
- [9] C. Wang, L. Yin, L. Zhang, D. Xiang, R. Gao, *Sensors*, 10 (2010) 2088.
- [10] G. Ma, R. Zou, L. Jiang, Z. Zhang, Y. Xue, L. Yu, G. Song, W. Li, J. Hu, *Crystal Engineering Communicaiton*, 14 (2012) 2172.
- [11] D. L. Young, D. L. Williamson, T. J. Coutts, *Journal of Applied Physics*, 91 (2002) 1464.
- [12] S. Park, S. An, H. Ko, C. Jin, C. Lee, *ACS Applied Materials and Interfaces*, 4 (2012) 3650.
- [13] Z. Ai, S. Lee, Y. Huang, W. Ho, L. Zhang, *Journal of Hazardous Materials*, 179 (2010) 141.
- [14] I. Stambolova, K. Konstantinov, D. Kovacheva, P. Peshev *physica status solidi (a)*, 167 (1998) R11.
- [15] Y. Zhao, L. Hu<sup>1</sup>, H. Liu, M. Liao, X. Fang, L. Wu, *Scientific Reports*, 4 (2014) 6847.
- [16] V. V. Ganbavle, M. A. Patil, H. P. Deshmukh, K. Y. Rajpure, *Journal of Analytical and Applied Pyrolysis*, 107 (2014) 233.
- [17] I. Stambolova, K. Konstantinov, D. Kovacheva, P. Peshev, and T. Donchev, *Journal of Solid State Chemistry*, 128 (1997) 305.
- [18] M. A. Alpuche-Aviles, Y. Wu, *Journal of American Chemical Society*, 131 (2009) 3216.

- [19] S. V. Mohite, K. Y. Rajpure, *Optical Materials*, 36 (2014) 833.
- [20] V. V. Ganbavle, S. K. Patil, S.I. Inamdar, S. S. Shinde, K.Y. Rajpure, *Sensors and Actuators A: Physical*, 216 (2014) 328.
- [21] M. Z. Ahmad, A. Z. Sadek, M. H. Yaacob, D. P. Anderson, G. Matthews, V. B. Golovkod, W. Wlodarski, *Sensors and Actuators B*, 179 (2013) 125.
- [22] Y. Jiang, X. Chen, R. Sun, Z. Xiong, L. Zheng, *Materials Chemistry and Physics*, 129 (2011) 53.
- [23] L. Filipovic, S. Selberherr, G. C. Mutinati, E. Brunet, S. Steinhauer, A. Kock, J. Teva, J. Kraft, J. Siegert, F. Schrank, *Microelectronic Engineering*, 117 (2014) 57.
- [24] R. S. Vemuri, M. H. Engelhard, C. V. Ramana, *ACS Applied Materials and Interfaces*, 4 (2012) 1371.
- [25] B. C. Yadav, A. Yadav, S. Singh, K. Singh, *Sensors and Actuators B*, 177 (2013) 605.
- [26] N. D. Hoa, N. V. Quy, D. Kim, *Sensors and Actuators B: Chemical*, 142 (2009) 253.
- [27] Y. Gonullu, A. A. Haidry, B. Saruhan, *Sensors and Actuators B*, 217 (2015) 78.
- [28] A. Stanoiu, C. E. Simiona, S. Somacescu, *Sensors and Actuators B*, 186 (2013) 687.
- [29] V.V. Ganbavle, S. V. Mohite, G. L. Agawane, J. H. Kim, K. Y. Rajpure, *Journal of Colloid and Interface Science*, 451 (2015) 245.
- [30] G. Korotcenkov, *Materials Science and Engineering R*, 61 (2008) 1.
- [31] S. Ashraf, C. S. Blackman, R. G. Palgrave, S. C. Naisbitt, I. P. Parkin, *Journal Materials Chemistry*, (2007) 3708.
- [32] Y. Qin, M. Liu, Z. Ye, *Journal of Molecular Structure*, 1076 (2014) 546.
- [33] D. H. Kim, W. S. Kim, S. B. Lee, S. H. Hong, *Sensors and Actuators B*, 147 (2010) 653.
- [34] W. T. Moon, K. S. Lee, Y. K. Jun, H. S. Kim, S. H. Hong, *Sensors and Actuators B*, 115 (2006) 123.
- [35] C. Wongchoosuk, A. Wisitsoraat, D. Phokharatkul, A. Tuantranont, T. Kerdcharoen, *Sensors*, 10 (2010) 7705.
- [36] V. V. Ganbavle, S. V. Mohite, J. H. Kim, K. Y. Rajpure, *Current Applied Physics*, 15 (2015) 84.

- [37] W. Zeng, T. Liu, Z. Wang, S. Tsukimoto, M. Saito, Y. Ikuhara, *Sensors* ,9 (2009) 9029.
- [38] L. T. Hoa, H. N. Tien, V. H. Luan, J. S. Chung, S. H. Hur, *Sensors and Actuators B*, 185 (2013) 701.
- [39] L. Zhou, Q. Yuan, X. Li, J. Xu, F. Xia, J. Xiao, *Sensors and Actuators B*, 206 (2015) 311.

## *Chapter IV*

**Spray Deposited Zn<sub>2</sub>SnO<sub>4</sub> thin  
Films and Their Dye Sensitized  
Solar Cell properties.**

**INDEX**  
**Chapter IV**

**Spray Deposited Zn<sub>2</sub>SnO<sub>4</sub> thin films and their Dye Sensitized Solar Cell properties.**

- 4.1 History of Dye-Sensitized Solar Cells .
- 4.2 Details of DSSC components
  - 4.2.1 The working electrode (The nanocrystalline semiconductor electrode)
  - 4.2.2. The counter electrode
  - 4.2.3. The dye
  - 4.2.4. Electrolyte ( redox couple)
- 4.3 Working of Dye Sensitized Solar Cell.
  - 4.3.1 Basic Operating Principle of Dye-Sensitized Solar Cells.
  - 4.3.2 DSSC Cell Performance
  - 4.3.3 Time scales of different processes involved in the working of DSSC
- 4.4 Zinc Stannate as a working electrode for dye sensitized solar cell (DSSC).
  - 4.4.1 Preparation and characterization of SnO<sub>2</sub> thin films by spray pyrolysis method
    - 4.4.1.1 Thermogravimetric analysis of Stannic Chloride (SnCl<sub>4</sub>.5H<sub>2</sub>O) powder.
    - 4.4.1.2 Substrate Cleaning.
    - 4.4.1.3 Preparation of precursor solution and Spray Pyrolytic synthesis of tin oxide (SnO<sub>2</sub>) thin films.
    - 4.4.1.4 X-ray diffraction Studies of the SnO<sub>2</sub> thin film prepared by spray pyrolysis method.
    - 4.4.1.5 Scanning electron Microscopy (SEM) Studies of the SnO<sub>2</sub> thin films prepared by spray pyrolysis method
    - 4.4.1.6 UV-VIS absorption Spectroscopy studies of SnO<sub>2</sub> thin films prepared by spray pyrolysis method.
  - 4.4.2 Synthesis and Characterization of Zinc Oxide (ZnO) thin films by Spray Pyrolysis Method.

- 4.4.2.1 Thermogravimetric analysis of zinc chloride ( $\text{ZnCl}_2 \cdot 5\text{H}_2\text{O}$ ) powder.
- 4.4.2.2 Preparation of precursor solution and spray pyrolytic synthesis of ZnO thin films.
- 4.4.2.3 X-ray diffraction studies of the ZnO thin films prepared by spray pyrolysis.
- 4.4.2.4 Scanning electron Microscopy (SEM) image of the ZnO thin film prepared by spray pyrolysis
- 4.4.2.5 UV-VIS absorption Spectroscopy of ZnO thin film prepared by spray pyrolysis
- 4.4.3 Synthesis and characterization of  $\text{Zn}_2\text{SnO}_4$  thin films by spray pyrolysis method and their Dye Sensitized Solar cell (DSSC) properties.
  - 4.4.3.1 Preparation of precursor solution and Spray Pyrolytic synthesis of Zinc Stannate ( $\text{Zn}_2\text{SnO}_4$ ) thin films
  - 4.4.3.2 X-ray Diffraction Studies of Zinc Stannate ( $\text{Zn}_2\text{SnO}_4$ ) thin films by spray pyrolysis method.
  - 4.4.3.3 Scanning electron microscopy (SEM) Studies of Zinc Stannate ( $\text{Zn}_2\text{SnO}_4$ ) thin films by spray pyrolysis method.
  - 4.4.3.4 UV-VIS optical absorption spectroscopy studies of  $\text{Zn}_2\text{SnO}_4$  thin film prepared by spray pyrolysis.
  - 4.4.3.5 Atomic force microscopy (AFM) Studies of Zinc Stannate ( $\text{Zn}_2\text{SnO}_4$ ) thin films by spray pyrolysis method.
  - 4.4.3.6 Cyclic Voltammetric (CV) Studies of Tin Oxide ( $\text{SnO}_2$ ), Zinc Oxide (ZnO) and Zinc Stannate ( $\text{Zn}_2\text{SnO}_4$ ) thin films by spray pyrolysis method.
  - 4.4.3.7 Fabrication of  $\text{Zn}_2\text{SnO}_4$  photoanodes and Dye sensitized Solar cell Properties measurements.
- 4.5 Conclusions.
- References

## CHAPTER IV

# Spray Deposited $\text{Zn}_2\text{SnO}_4$ Thin Films and Their Dye Sensitized Solar Cell Properties.

### 4.1. History of Dye-Sensitized Solar Cells

Within last two decades dye-sensitized solar cells (DSSCs) are extensively studied as a new way to construct low-cost photovoltaics. These cells are invented by M. Gratzel and B. O'Regan 1991 [1]. There are different types of solar cells such as solid state DSSC [2], quantum dot solar cells [3, 4], and perovskite solar cells [5-8]. Now a day Perovskite solar cells are interesting topic since 2012. The dye sensitized solar cell basically a sandwich structure of following components

1. The working electrode
2. The counter electrode
3. Dye
4. Electrolyte ( redox couple).

### 4.2 Details of DSSC components

#### 4.2.1 The working electrode (The nanocrystalline semiconductor electrode)

Use of a mesoporous nanocrystalline material the surface area of electrode can be tailored up to 1000-fold. Different semiconductors which can be used for the working electrode are shown in Figure 4.1. [9].

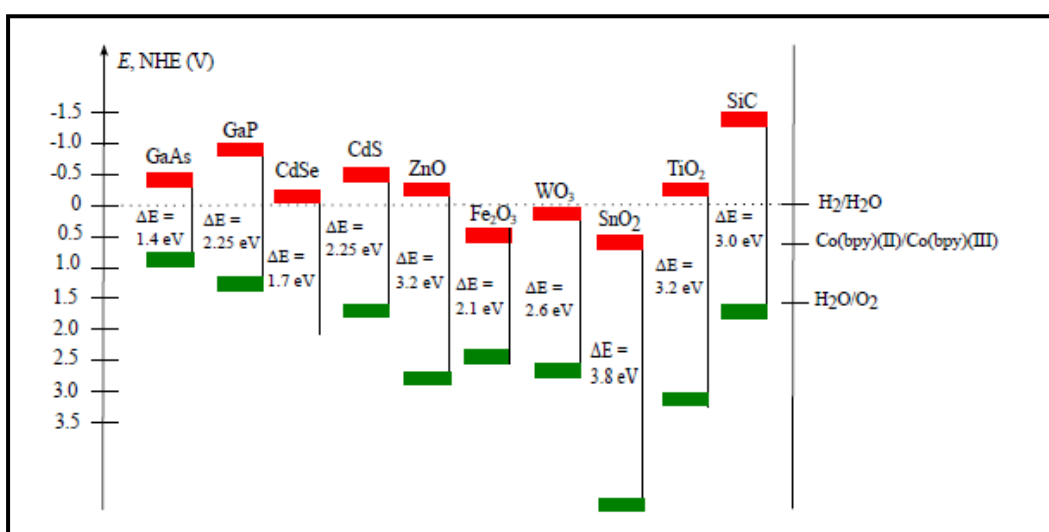


Figure 4.1 Band positions of different semiconducting materials used as working electrode for as DSSCs

#### **4.2.2 The counter electrode**

The task of the counter electrode is to recharge redox couple by the reducing the oxidized species. Low resistance materials are useful to improve the efficiency of DSSC. Commonly used material for counter electrode with iodide/triiodide redox system has been sputter coated platinum nanoparticles. Now a day low cost electrodes based on carbon nanotube (CNTs) and graphenes with conducting polymers like PEDOT, Polyaniline are also introduced.

#### **4.2.3 The dye**

Dye is used to harvest the photons as many as possible. The harvested photons excite the electrons and inject excited electrons into the conduction band of semiconductor. Since the band gap of the semiconducting oxide materials are so wide that they can only absorb light in the UV region, therefore dyes are used as visible light absorber in DSSCs. Ruthenium based dyes are common for DSSC application among metal based dyes because of their encouraging properties like broad absorption, long lived excited state, suitable energy levels and good stability [10]. Most commonly used ruthenium based dyes for DSSC are; N719 and the "Black dye".

#### **4.2.4 Electrolyte ( redox couple)**

Grätzel in 1991 introduced Iodide/tri-iodide as a redox couple for DSSC [1]. The highest reported efficiency is 13% for DSSCs which is obtained by using cobalt complex as redox couple [11].

### **4.3 Working of Dye Sensitized Solar Cell**

#### **4.3.1. Basic Operating Principle of Dye-Sensitized Solar Cells:**

Different processes involved in DSSC solar cell are illustrated in figure.

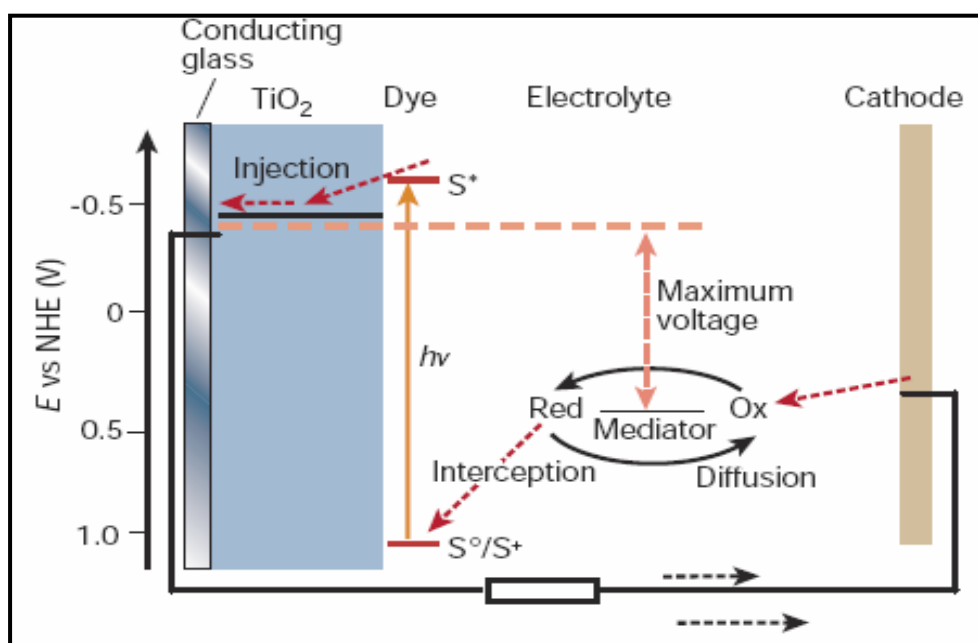


**Figure 4.2 illustrates the different processes involved in a DSSC.**

1. Absorption of photon and generation of electron-hole pairs  
(dye is excited )
2. The excited electron is further injected into the conduction band of semiconductor.
3. The electron is extracted by the backside conducting electrode and transferred through the circuit to perform electrical work.
4. At counter electrode oxidized species of the redox couple in the electrolyte is reduced by the electron.
5. The reduced species of the electrolyte is regenerated by diffusing it to the oxidized dye .

#### 4.3.2 DSSC Cell Performance

Figure 4.4 shows equation of solar cell performance. The conversion efficiency ( $Eff$ ) is given by Eq. 4.1 and 4.2.

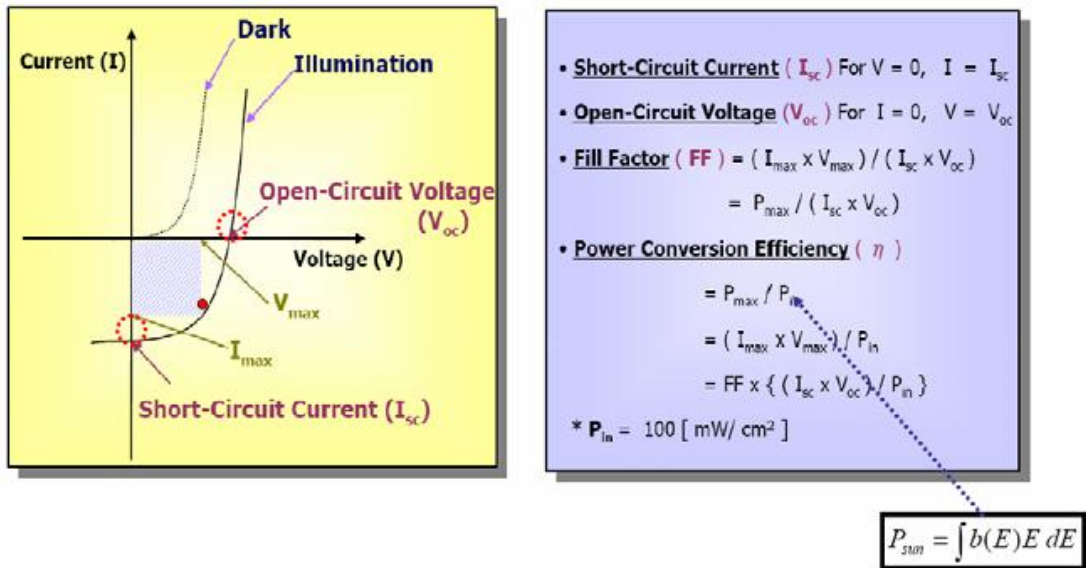


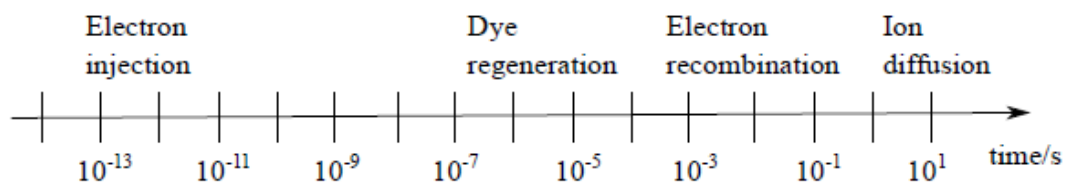
**Figure 4.4 Equation of solar cell performance**

$$Eff = (V_{oc} \times J_{sc} \times ff) / P_{in} \quad \text{----- (4.1)}$$

$$ff = (J_{mpp} \times V_{mpp}) / (V_{oc} \times J_{sc}) \quad \text{----- (4.2)}$$

where  $V_{oc}$  - open circuit voltage,  $J_{sc}$  - short circuit current,  $ff$  - fill factor, described in Eq. 4.17 and  $P_{in}$  - incident light power, which is normalized at 1000  $W/m^2$  for solar cell testing. The current and voltage at the maximum power point in the fourth quadrant of the current-voltage characteristics are referred as  $J_{mpp}$  and  $V_{mpp}$ .

### 4.3.3 Time scales of different processes involved in the working of DSSC



**(a)**

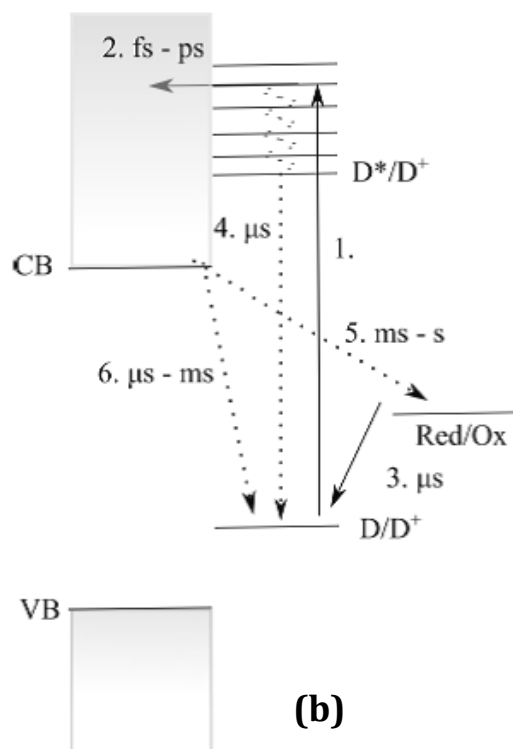


**Figure 4.5 (a) and (b). Schematic picture showing time scales of different processes in the DSSC.**

1. When the photon hits the dye, the electron is excited from the HOMO level to the LUMO-level instantaneously.
2. In DSC, the process of injection of electrons into the semiconductor requires 100 fs-100 ps. This time is dependent on experimental conditions. The injection kinetics has been discussed by S. Ardo and co-workers [12]
3. Marcus theory for the kinetic of the regeneration process has been studied by Feldt and co-workers [13].
4. Process where the electron goes back to ground state may be, both by radiative and non-radiative processes.
5. Recombination of photo-injected electrons in the conduction band with the oxidized species in the electrolyte.
6. Recombination of photo-injected electrons in the conduction band to the oxidation level of the oxidized dye.

#### **4.4. Zinc Stannate as a working electrode for dye sensitized solar cell (DSSC)**

Within last two decades DSSC's are studied extensively as an alternative to high cost traditional silicon solar cells. A typical DSS cell consists of a dye loaded photoanode of nanocrystalline metal oxide, a liquid electrolyte having  $I^-/I_3^-$  redox couple, and a platinum counter electrode [1]. Among these the photoanode has to play dual role by providing high surface area for dye loading and rapid transport of photo-generated electrons towards conducting electrode avoiding its recombination and hence governing the device performance. Several binary metal oxides have been extensively studied for their plausible use as photoanode in DSSC. Among these binary oxides nanocrystalline  $TiO_2$  proved its potential candidature with consistently improved photoconversion efficiency (PCE) from 7.1% in 1991 to 12.3% in 2012 [1, 14,15]. Apart from these binary oxides nowadays ternary oxides are being recognized as suitable candidates for photovoltaics [16-18]. Since the chemical and physical properties of ternary metal oxides can be easily changed by varying the composition of different components, Synthesis of these materials is more flexible than those of binary oxides [19]. Zinc stannate (ZTO) is a ternary metal oxide of class  $A^{II}{}_2B^{IV}O_4$  ZTO with band gap of 3.6 eV and high electron mobility ( $10-15 \text{ cm}^2\text{v}^{-1}\text{s}^{-1}$ ) [20]. Owing to its complex crystal structure it provides improved stability in adverse conditions [21] as compared to binary oxides [19]. From last 10 years consistent efforts are being taken by scientific community for the synthesis of ZTO nanostructures to improve PCE of  $Zn_2SnO_4$ -based DSCs. Wu et al. prepared  $Zn_2SnO_4$  based DSSCs and recorded efficiency of 3.8% [22, 19]. Hong and his co-workers could improve PCE from 4.7% for ZTO DSSC to 6.0% for the DSSC device architecture containing ZTO compact layer and ZTO/ZnO core shell nanoparticles, using uniform  $Zn_2SnO_4$  nanoparticles (8 nm) [23,24]. Kim and co-workers noted that  $Zn_2SnO_4$ -DSCsbased on organic donor-conjugate-acceptor (D- $\pi$ -A) structured orange organic dye displayed significantly improved performance compared to the ruthenium complex sensitized DSCs [25]. Wang et.al. reported that Multi-functional, hierarchical  $Zn_2SnO_4$  spheres containing nanoparticles are effective photoanodes for DSCs, with PCE of 5.36% [26]. Mac and his co-workers improved the power conversion efficiency of  $Zn_2SnO_4$ -DSSCs from 3.47% for bare ZTO to 5.72% surface modified ZTO through surface modification with  $TiO_2$  [27]. Recently Zou and his co-workers reported overall

photo conversion efficiency up to 3.43% for nano sheet-assembling hierarchical  $\text{Zn}_2\text{SnO}_4$  microspheres (NHMSs) based anode of 19 micrometer thickness [28].

In the present work we investigate the applicability of simple and inexpensive spray pyrolysis technique for the synthesis of uniform and well adherent Zinc Stannate ( $\text{Zn}_2\text{SnO}_4$ ) thin films. These films were further examined for structural optical and morphological studies.

To synthesize the Zinc Stannate thin films by spray pyrolysis technique it was necessary to optimize the preparative parameters like Concentration of precursors, substrate temperature, etc. Since no more reports were available on the thin film preparation of Zinc Stannate by SPT we have initiated our studies with considering individual precursors viz. Zinc Chloride and Stannic Chloride and further these were mixed in proper proportion to obtain phase pure zinc stannate. From earlier studies of Zinc Stannate nanoparticles reported by different authors, it was confirmed that Zn:Sn optimum ratio was 2:1.

**The chapter is divided into three subparts**

- A. Preparation and characterization of  $\text{SnO}_2$  thin films by spray pyrolysis method.
- B. Preparation and characterization of  $\text{ZnO}$  thin films by spray pyrolysis method.
- C. Preparation and characterization of  $\text{Zn}_2\text{SnO}_4$  thin films by spray pyrolysis method and their plausible application as an anode material for Dye Sensitized Solar cell (DSSC).

#### 4.4.1 Preparation and characterization of tin oxide (SnO<sub>2</sub>) thin films by spray pyrolysis method

##### 4.4.1.1 Thermogravimetric analysis of Stannic Chloride (SnCl<sub>4</sub>.5H<sub>2</sub>O) powder:

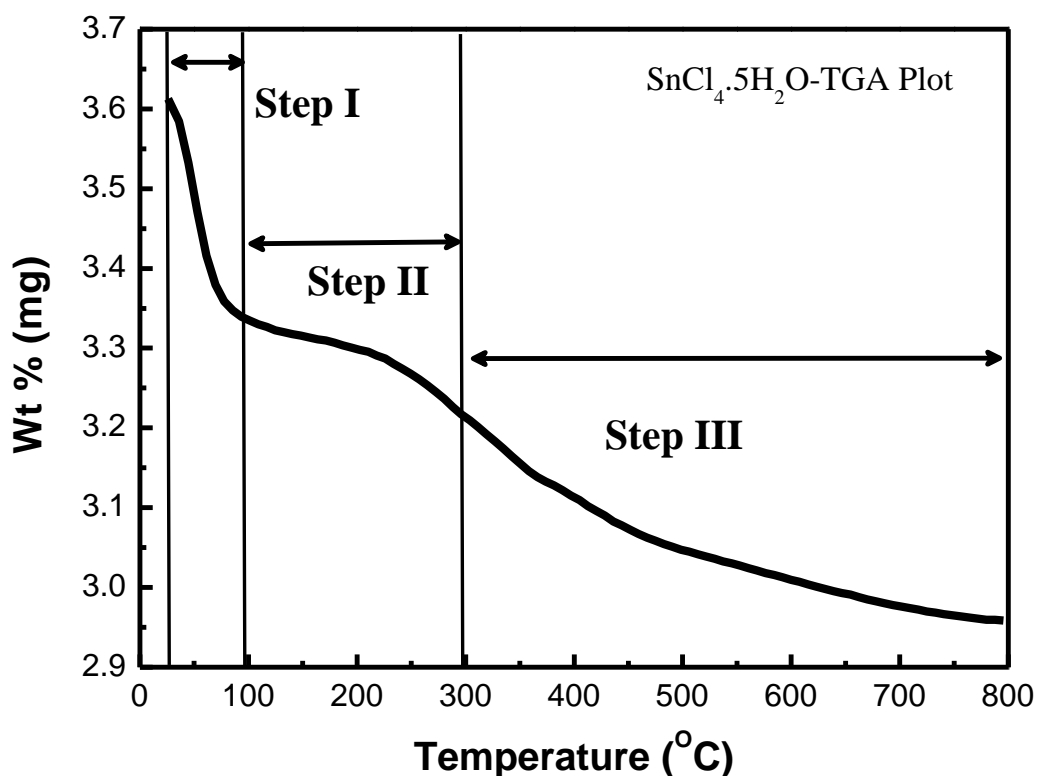


**Figure 4.6 TGA thermogram for the stannic chloride (SnCl<sub>4</sub>.5H<sub>2</sub>O) powder**

Figure 4.6 shows TGA thermogram for the stannic chloride (SnCl<sub>4</sub>.5H<sub>2</sub>O) powder. The sample was heated at constant pressure in the temperature range from room temperature to 800°C at the heating rate of 20°C per minute. The left Y-axis shows the weight loss pertains to thermo gravimetric analysis (TGA). The thermal decomposition of SnCl<sub>4</sub>.5H<sub>2</sub>O in oxygen atmosphere takes place in three consecutive steps. The weight loss begins at 40°C. The weight loss of 35% is observed (Fig.4.6) in the temperatures range from 40 to 80°C and this weight loss is due to loss of water content in the sample. Further weight loss of 15% in the temperature range of 80-275°C is due removal of chlorine from the SnCl<sub>4</sub>. The

third step of 50% weight loss is observed in the temperature range (275-600°C) which belongs to decomposition and crystallization of SnO<sub>2</sub>.

#### **4.4.1.2 Substrate Cleaning**

Substrate cleaning is degree of cleanness required and nature of contaminants to be removed. Grease important factor for thin film depositions. It influences the adherence, smoothness and uniformity of the film. The techniques to be used for cleaning depend on nature of substrate, adsorbed water, air borne dust and oil particles are the common contaminants.

The following cleaning procedure was used for glass substrates.

- 1) The substrates were cleaned with the labogent detergent solution and then soaked in double distilled water for complete removal of detergent.
- 2) Substrates were further sonicated in Acetone bath for 20 min.
- 3) The substrates were again sonicated in alcohol bath for 20 min.
- 4) Finally, the substrates were dried at room temperature and cleaned.

#### **4.4.1.3 Preparation of precursor solution and spray pyrolytic synthesis of tin oxide (SnO<sub>2</sub>) thin films.**

For the synthesis of tin oxide (SnO<sub>2</sub>) thin films, stannic chloride (SnCl<sub>4</sub>.5H<sub>2</sub>O) was used as cationic precursor of tin and de-ionized (DI) water was used as solvent. The chemicals were obtained from S. D. Fine Chem. Ltd., Mumbai, and used as received without any further treatment. To prepare precursor solution of 0.1 M SnO<sub>2</sub>, required quantity of SnCl<sub>4</sub>.5H<sub>2</sub>O is dissolved in 100 ml of DI water. The precursor solution formed is then sprayed onto the preheated glass substrates at 400°C temperature. The spray solution quantity (200 ml), spray rate (9-10 ml/min) and the nozzle to substrate distance (28 cm) were optimized by observing uniformity and adherence of the films.

#### 4.4.1.4 X-ray diffraction Studies of SnO<sub>2</sub> thin films prepared by spray pyrolysis method.

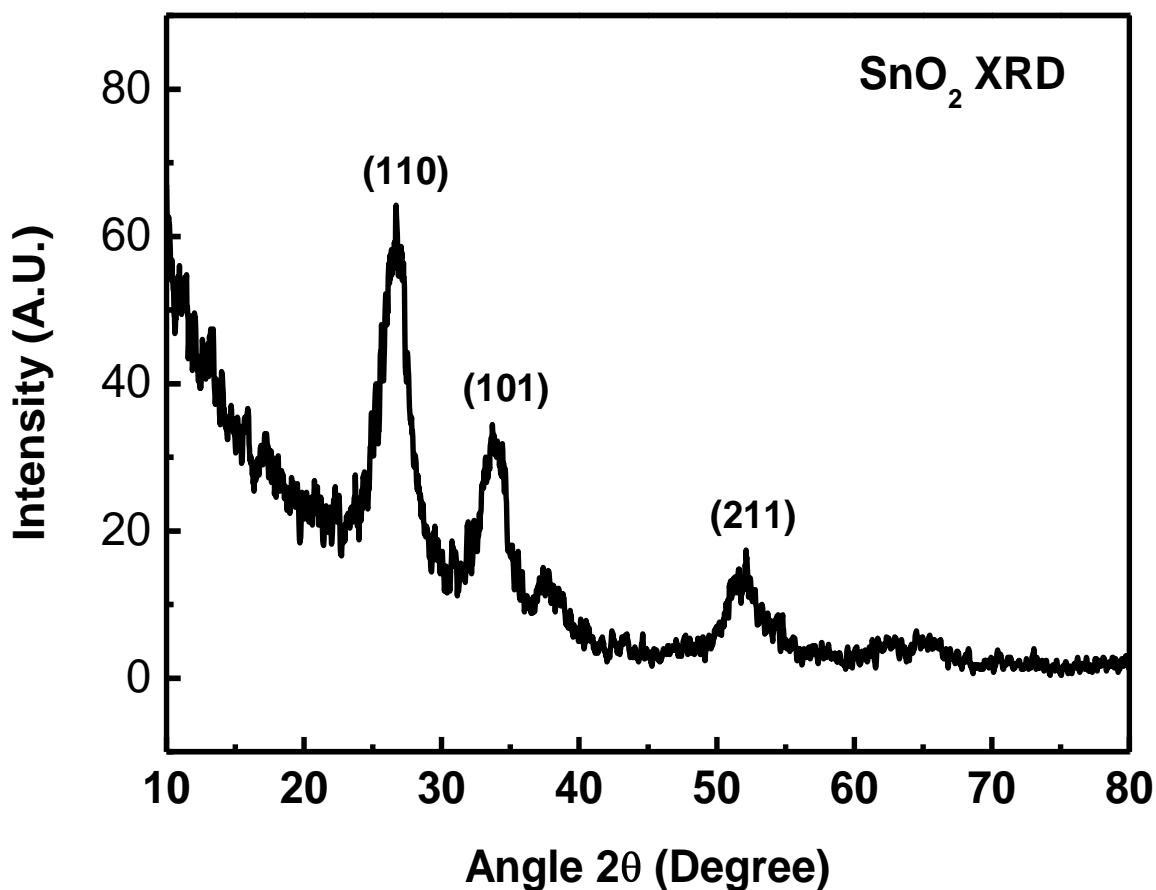


**Figure 4.7 X-ray diffraction spectra for SnO<sub>2</sub> thin film prepared by spray pyrolysis method**

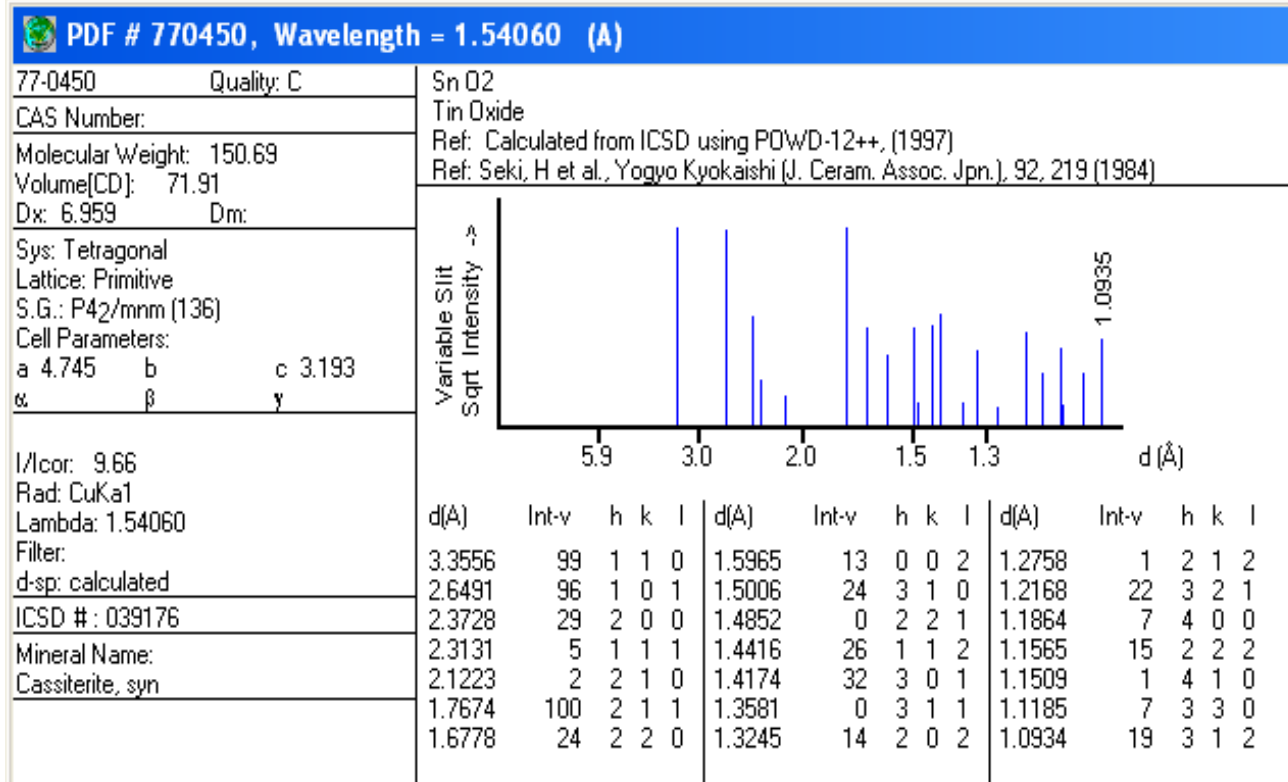
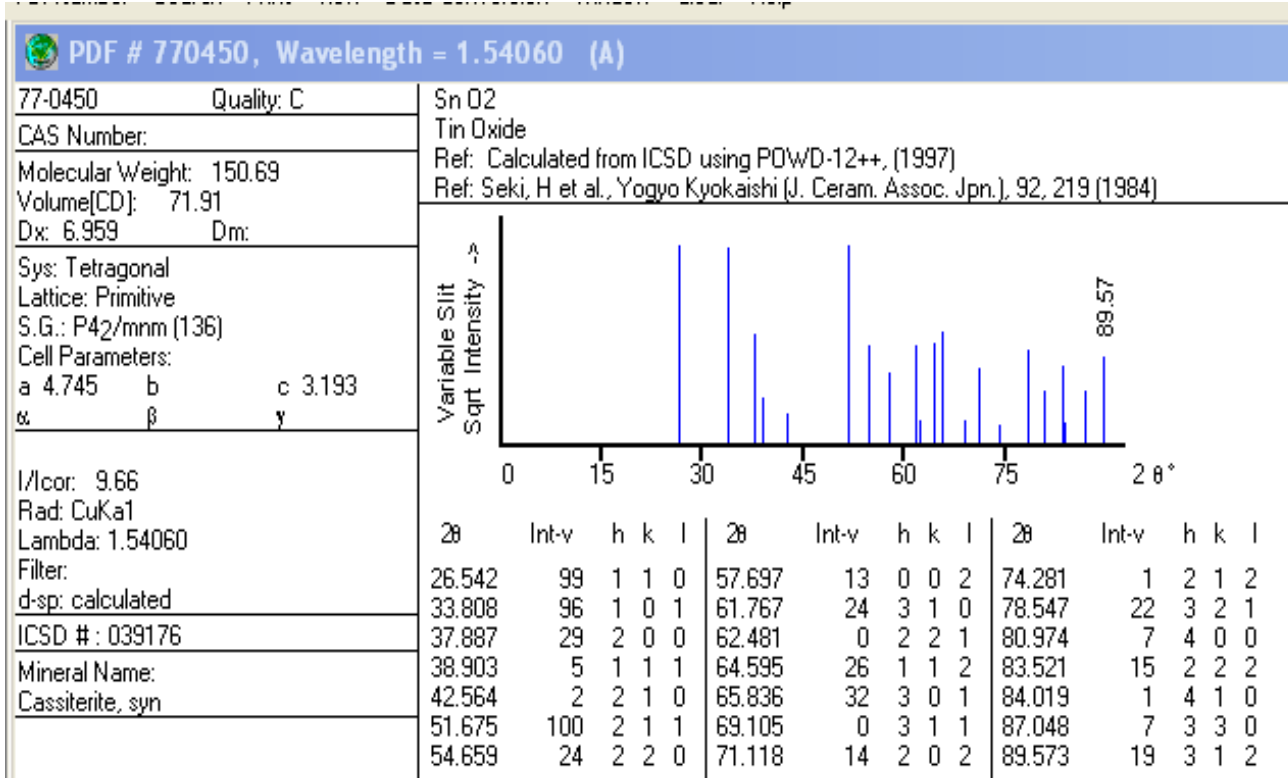
Figure 4.7 shows X-ray diffraction pattern of the SnO<sub>2</sub> sample synthesized by spray pyrolysis method. Figure shows well defined reflections occurred at  $2\theta$  values  $26.7^\circ$ ,  $33.9^\circ$ ,  $51.75^\circ$  for planes (110), (101) and (211) correspondingly. The well matching between observed 'd' and  $2\theta$  values with standard values from JCPDS data file no. 770450 gives confirmation of SnO<sub>2</sub> phase formation with tetragonal structure. The observed  $2\theta$ , standard  $2\theta$  and 'd' values for XRD pattern of SnO<sub>2</sub> are presented in table 4.1. The nanocrystalline nature of SnO<sub>2</sub> was confirmed from the appearance of broad peaks in the XRD pattern. The size of the crystallites oriented along (110) plane can be deduced using Scherer's formula mentioned earlier by equation 2.3.

The calculated value of crystallite size of SnO<sub>2</sub> nanoparticle was found to be 3.5 nm.

**Table 4.1 The observed 2θ, standard 2θ and d values for SnO<sub>2</sub> thin films.**

SnO <sub>2</sub>	Observed	Standard	'd' value	Plane	JCPDS file No 770450
	'2θ'	'2θ'	(Å <sup>0</sup> )	(hkl)	
	(Degree)	(Degree)			
	26.7	26.5	3.3556	110	
33.9	33.80	2.6491	101		
51.75	51.67	1.7674	211		

JCPDS data for Tin Oxide (SnO<sub>2</sub>) File No: 770450



4.4.1.5 Scanning electron Microscopy (SEM) studies of SnO<sub>2</sub> thin films prepared by spray pyrolysis method.

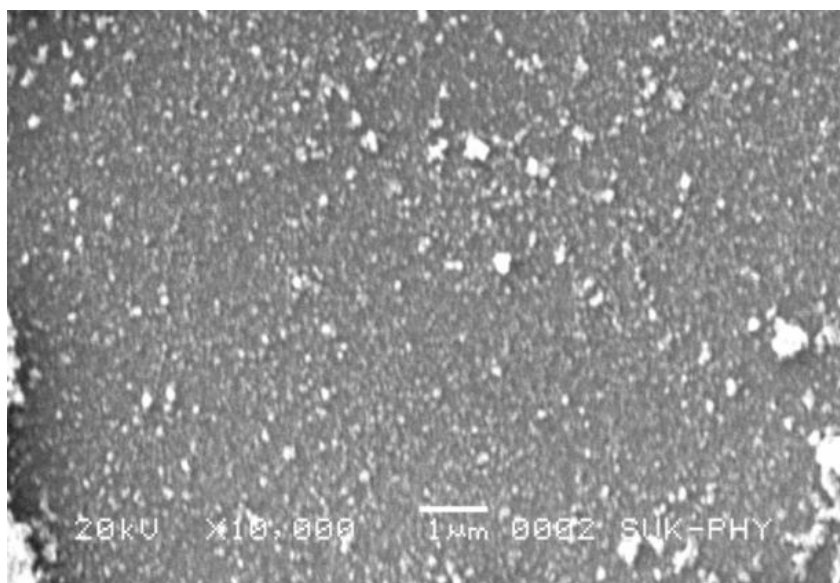


**Figure 4.8 Scanning electron micrographs of Tin Oxide (SnO<sub>2</sub>) thin films**

Figure 4.8 shows scanning electron micrograph of SnO<sub>2</sub> thin film prepared by spray pyrolysis method. Figure clearly showed that no well defined grains were observed in the film. The film surface was smooth and crack free. The nanocrystalline nature of SnO<sub>2</sub> was also verified from SEM, which was in good agreement with the broad peaks seen from X-ray diffraction pattern.

#### **4.4.1.6 UV-VIS absorption Spectroscopy studies of SnO<sub>2</sub> thin films prepared by spray pyrolysis method**

Figure 4.9(a) shows the UV-VIS absorption spectra recorded in 300 to 1000 nm and Figure 4.9(b) Tauc plot for the SnO<sub>2</sub> thin film prepared by spray pyrolysis method from figure 4.9(a) it is observed that the optical absorption increases at around 335 nm. From Tauc plot the observed band gap energy value of SnO<sub>2</sub> thin film is 3.7 eV, which is in good agreement with the reported values [29].

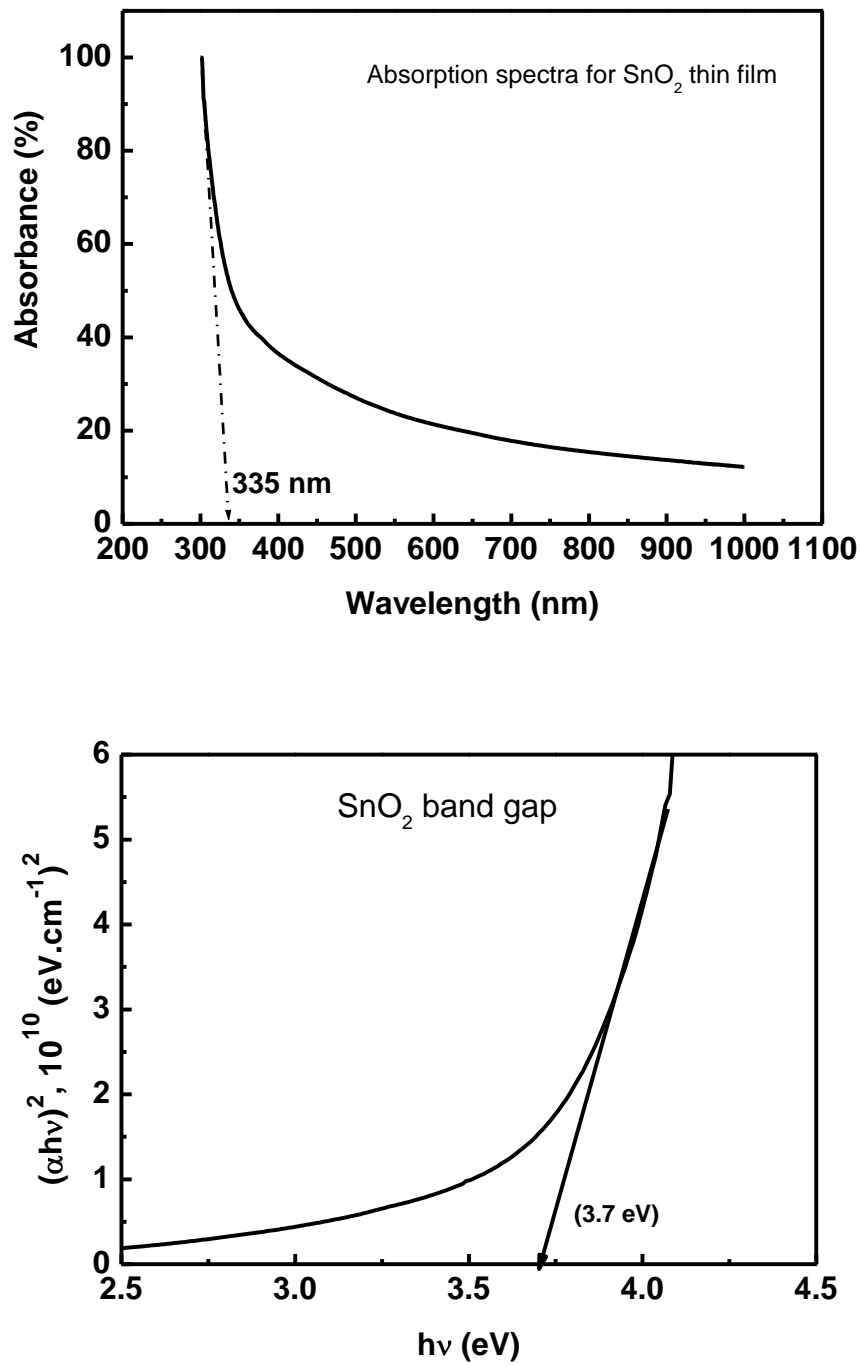


**Figure 4.9 (a) UV-VIS absorption spectra and (b) tauc Plot for the SnO<sub>2</sub> thin film prepared by spray pyrolysis method**

#### **4.4.2 Synthesis and Characterization of ZnO thin films by Spray Pyrolysis Method**

##### **4.4.2.1 Thermogravimetric analysis of Zinc Chloride (ZnCl<sub>2</sub>.5H<sub>2</sub>O) powder**

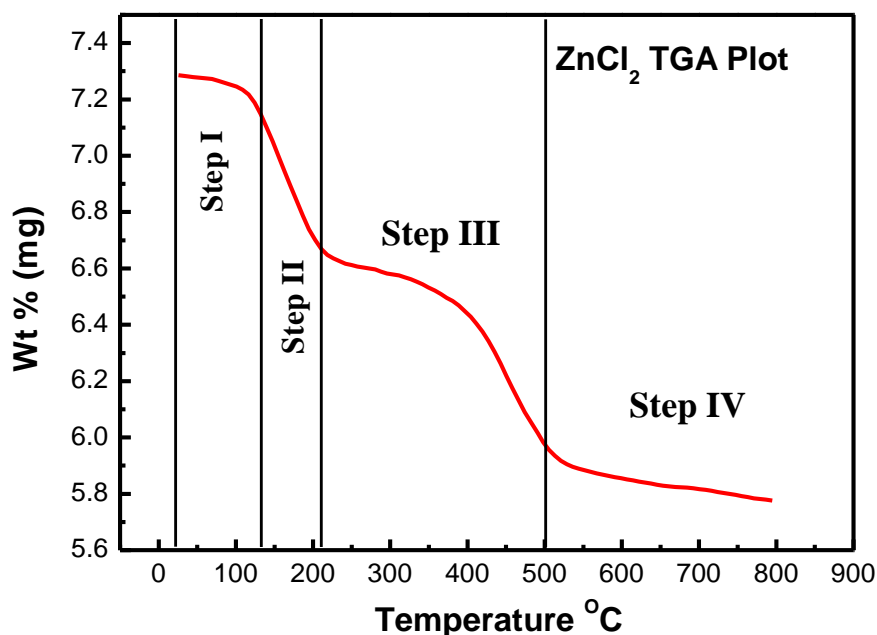


**Figure 4.11 TGA thermogram for the Zinc chloride (ZnCl<sub>2</sub>) powder**

Figure 4.11 shows TGA thermo-gram for the zinc chloride (ZnCl<sub>2</sub>) powder. The sample was heated at constant pressure in the temperature range from room temperature to 800°C at the heating rate of 20°C per minute. The left Y-axis shows the weight loss pertains to thermo gravimetric analysis (TGA). The thermal decomposition of ZnCl<sub>2</sub> in oxygen atmosphere takes place in three/ four consecutive steps. The weight loss begins at 21°C. The weight loss of 7% is observed (Fig. 4.11) in the temperatures range from 21 to 132°C and this weight loss is due to loss of water content in the sample. Further weight loss of 40% in the temperature range of 132-210°C is due removal of chlorine from the ZnCl<sub>2</sub>. In the third step 53% weight loss is observed in the temperature range 210-500°C which belongs to decomposition and crystallization of ZnO. No major weight loss is seen in the sample after 500°C, during the fourth step.

#### **4.4.2.2 Preparation of precursor solution and spray pyrolytic synthesis of ZnO thin films.**

For the synthesis of zinc oxide (ZnO) thin films, zinc chloride (ZnCl<sub>2</sub>) is used as cationic precursors of zinc and de-ionized (DI) water is used as solvent. The chemicals were procured from S. D. Fine Chem. Ltd., Mumbai, and used as

received without any further treatment. To obtain the ZnO thin films, required quantity of ZnCl<sub>2</sub> was dissolved in 200ml of DI water to form 0.1 M solution keeping. The precursor solution prepared is then sprayed onto the preheated glass substrates at 400°C. The spray solution quantity (200 ml), spray rate (9-10 ml/min) and the nozzle to substrate distance (28 cm) were optimized to prepare uniform and well adherent thin films.

#### 4.4.2.3 X-ray diffraction studies of the ZnO thin film prepared by spray pyrolysis:

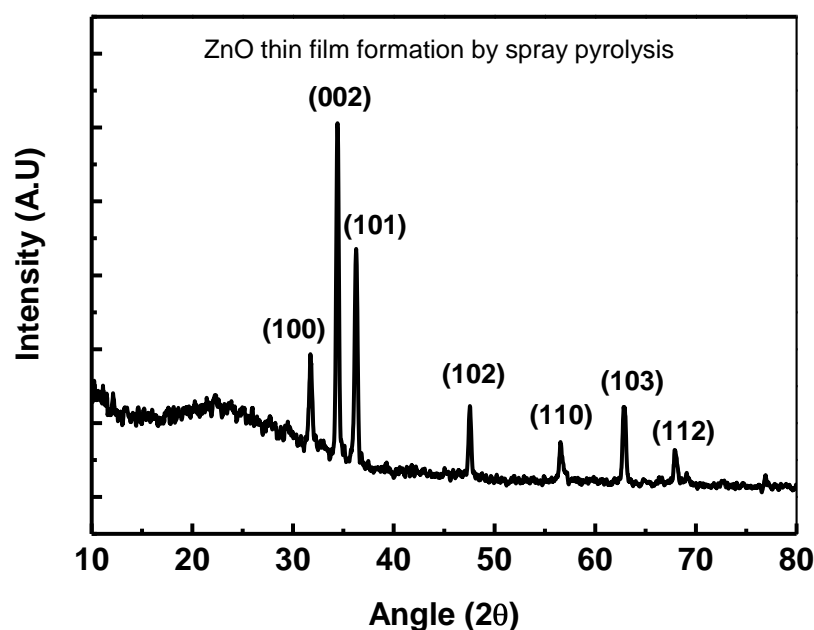


**Figure 4.12 X-ray diffraction spectra for the Zinc Oxide (ZnO) thin films**

#### **prepared by spray pyrolysis method**

Figure 4.12 shows X-ray diffraction pattern of the ZnO thin film prepared by spray pyrolysis method. Figure showed well defined reflections at angles ( $2\theta'$  values) 31.67°, 34.47°, 36.30°, 47.66°, 56.58°, 62.78°, 67.99° corresponding to the planes (100), (002), (101), (102), (110), (103), (112). The well matching of these observed  $2\theta'$  values with standard  $2\theta'$  values from JCPDS data file no. 790208 confirms the formation of ZnO. The maximum intensity of (002) peak indicates the c-axis orientation of the film. The size of the crystallites oriented along (002) plane can be deduced using Scherer's formula (Equation 2.2). The calculated value of crystallite size is 374 nm.

**Table 4.2 The observed 2 $\theta$ , standard 2 $\theta$  and d values for ZnO thin films.**

	<b>Observed '2<math>\theta</math>' (Degree)</b>	<b>Standard '2<math>\theta</math>' (Degree)</b>	<b>'d' value A<sup>o</sup></b>	<b>Planes (hkl)</b>	<b>Phase</b>
<b>ZnO</b>	31.67	31.619	2.8274	(100)	<b>JCPDS File No 790208</b>
	34.47	34.335	2.6096	(002)	
	36.30	36.100	2.4862	(101)	
	47.66	47.367	1.9176	(102)	
	56.58	56.313	1.6324	(110)	
	62.78	62.646	1.4817	(103)	
	67.99	67.641	1.3839	(112)	

PCPDFWIN

PDFNumber Search Print View Data Conversion Window Clear Help

PDF # 790208, Wavelength = 1.54060 (Å)

79-0208	Quality: C	Zn O
CAS Number:		Zinc Oxide
Molecular Weight: 81.38		Ref: Calculated from ICSD using POWD-12++, (1997)
Volume[CD]: 48.18		Ref: Albertsson, J., Abrahams, S.C., Kvik, A., Acta Crystallogr., Sec. B: Structural Science, 45, 34 (1989)
Dx: 5.610	Dm:	
Sys: Hexagonal		
Lattice: Primitive		
S.G.: P63mc (186)		
Cell Parameters:		
a 3.264	b	c 5.219
$\alpha$	$\beta$	$\gamma$
I/cor: 5.06		
Rad: CuK $\alpha$ 1		
Lambda: 1.54060		
Filter:		
d-sp: calculated		
ICSD #: 065122		
Non-Ambient Temperature		

$2\theta$	Int-v	h	k	l	$2\theta$	Int-v	h	k	l	$2\theta$	Int-v	h	k	l
31.619	51	1	0	0	62.646	38	1	0	3	76.588	6	2	0	2
34.335	40	0	0	2	66.033	6	2	0	0	81.109	3	1	0	4
36.100	100	1	0	1	67.641	34	1	1	2	89.189	11	2	0	3
47.367	26	1	0	2	68.738	17	2	0	1					
56.313	43	1	1	0	72.362	3	0	0	4					

PDF # 790208, Wavelength = 1.54060 (Å)

79-0208	Quality: C	Zn O
CAS Number:		Zinc Oxide
Molecular Weight: 81.38		Ref: Calculated from ICSD using POWD-12++, (1997)
Volume[CD]: 48.18		Ref: Albertsson, J., Abrahams, S.C., Kvik, A., Acta Crystallogr., Sec. B: Structural Science, 45, 34 (1989)
Dx: 5.610	Dm:	
Sys: Hexagonal		
Lattice: Primitive		
S.G.: P63mc (186)		
Cell Parameters:		
a 3.264	b	c 5.219
$\alpha$	$\beta$	$\gamma$
I/cor: 5.06		
Rad: CuK $\alpha$ 1		
Lambda: 1.54060		
Filter:		
d-sp: calculated		
ICSD #: 065122		
Non-Ambient Temperature		

d(Å)	Int-v	h	k	l	d(Å)	Int-v	h	k	l	d(Å)	Int-v	h	k	l
2.8274	51	1	0	0	1.4817	38	1	0	3	1.2430	6	2	0	2
2.6096	40	0	0	2	1.4137	6	2	0	0	1.1847	3	1	0	4
2.4860	100	1	0	1	1.3839	34	1	1	2	1.0971	11	2	0	3
1.9176	26	1	0	2	1.3645	17	2	0	1					
1.6324	43	1	1	0	1.3048	3	0	0	4					

JCPDS data for Zinc Oxide (ZnO) File No: 790208

#### 4.4.2.4 Scanning electron Microscopy (SEM) image of the ZnO thin film prepared by spray pyrolysis

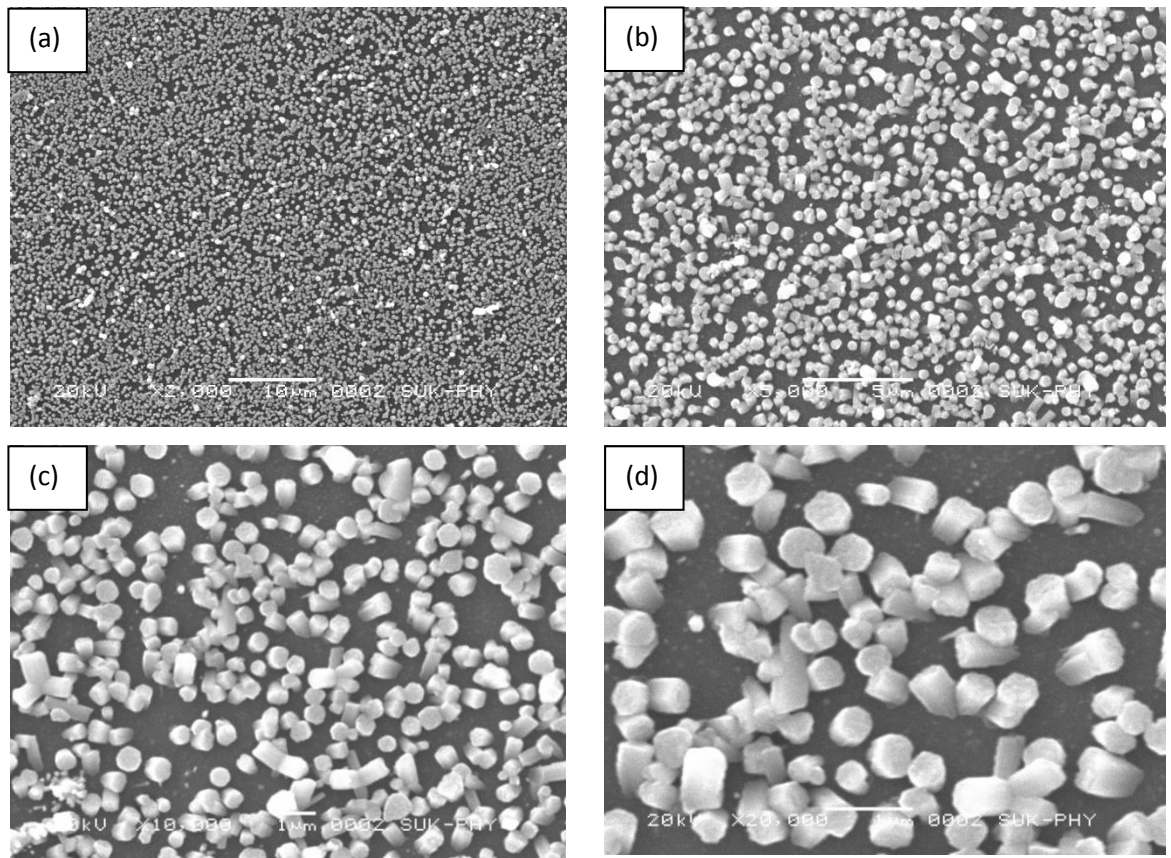


**Figure 4.13(a), (b), (c) and (d) Scanning electron micrographs of Zinc Oxide (ZnO) thin films at magnifications 2000, 5000, 10000 and 20000 X.**

Figure 4.13 (a), (b),(c) and (d) above shows Scanning electron Microscopy (SEM) image of 2000, 5000, 10000 and 20000 X magnifications respectively for the Zinc Oxide (ZnO) thin film prepared by spray pyrolysis. From figure it is observed that the film exhibits nano-crystalline nature with hexagonal rod like morphology. The average diameter and length of the rod are of the order 300-400nm and 700-800 nm respectively.

#### 4.4.2.5 UV-VIS absorption Spectroscopy of ZnO thin film prepared by spray pyrolysis

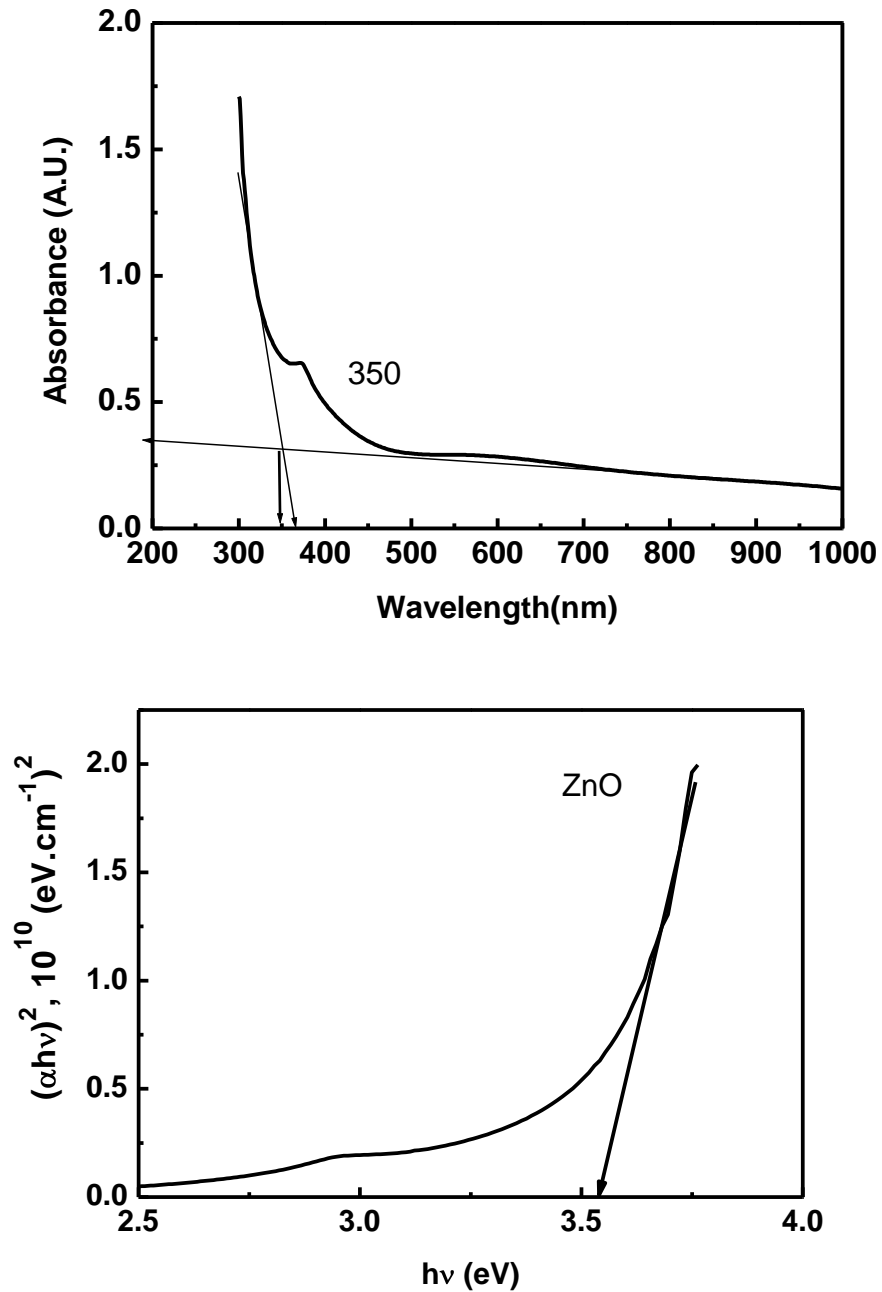


Figure 4.14 (a) UV-VIS absorption spectra and (b) Tauc plot for the ZnO thin film prepared by spray pyrolysis method.

Figure 4.14 (a) and (b) shows the UV-VIS absorption spectra recorded in 300 nm to 1000nm and Tauc plot respectively for the ZnO thin film prepared by

spray pyrolysis method. From figure 4.14 (a) it is observed that the optical absorption increases at around 350 nm. Tauc plot (Figure 4.14(b)) shows that the band gap energy value of ZnO is 3.5 eV. The observed band gap of nanocrystalline ZnO is well matching with reported values [30].

#### **4.4.3 Synthesis and characterization of Zn<sub>2</sub>SnO<sub>4</sub> thin films by spray pyrolysis method and their Dye Sensitized Solar cell (DSSC) properties.**

##### **4.4.3.1 Preparation of precursor solution and Spray Pyrolytic synthesis of Zinc Stannate (Zn<sub>2</sub>SnO<sub>4</sub>) thin films:**

For the synthesis of zinc stannate (Zn<sub>2</sub>SnO<sub>4</sub>) thin films, zinc chloride (ZnCl<sub>2</sub>) and stannic chloride (SnCl<sub>4</sub>·5H<sub>2</sub>O) are used as cationic precursors of zinc and tin, respectively and de-ionized (DI) water is used as solvent. The chemicals were procured from S. D. Fine Chem. Ltd., Mumbai, and used as received without any further treatment. To obtain the Zn<sub>2</sub>SnO<sub>4</sub> thin films, required quantity of ZnCl<sub>2</sub> and SnCl<sub>4</sub> was dissolved in 100ml of DI water to form 0.1 M solution keeping Zn/Sn ratio 2:1. The precursor solution formed is then sprayed onto the preheated glass substrates at different temperatures ranging from 300 to 400°C in the interval of 50°C. The spray solution quantity (100 ml), spray rate (9-10 ml/min) and the nozzle to substrate distance (28 cm) were optimized by observing uniformity and adherence of the films. The as prepared films were further annealed at 500°C in air atmosphere for 12 Hrs.

Figure 4.15 shows XRD spectra recorded for the thin film prepared by using Zn:Sn ratio other than 2:1. From figure it is clearly indicated that the sample is representing mixed phase. So in further studies Zn:Sn ratio is kept constant as 2:1.

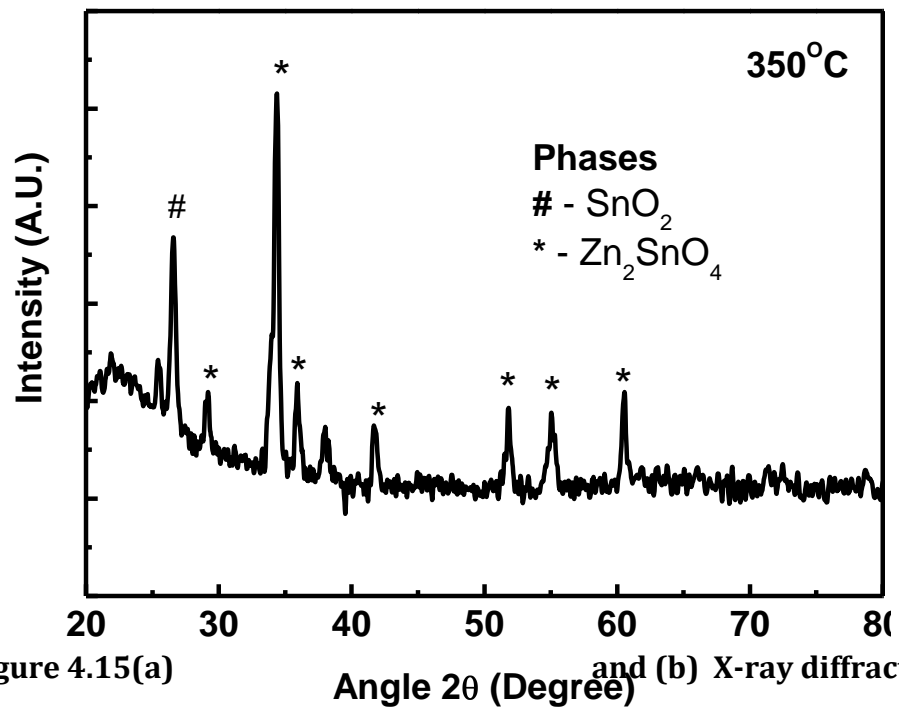
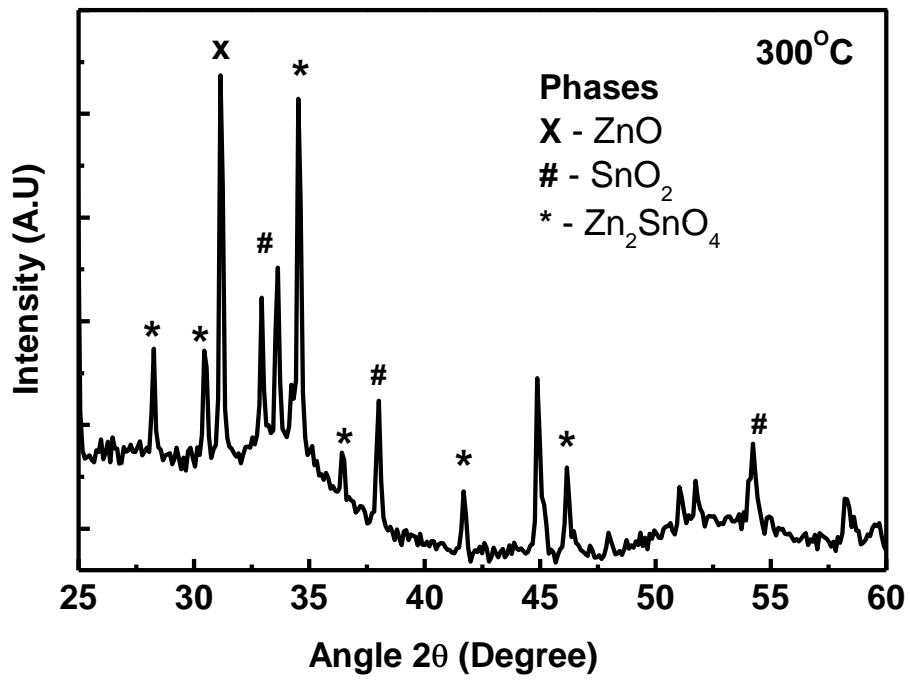


Figure 4.15(a) and (b) X-ray diffraction spectra for thin films prepared at 300 and 350°C respectively by spray pyrolysis method

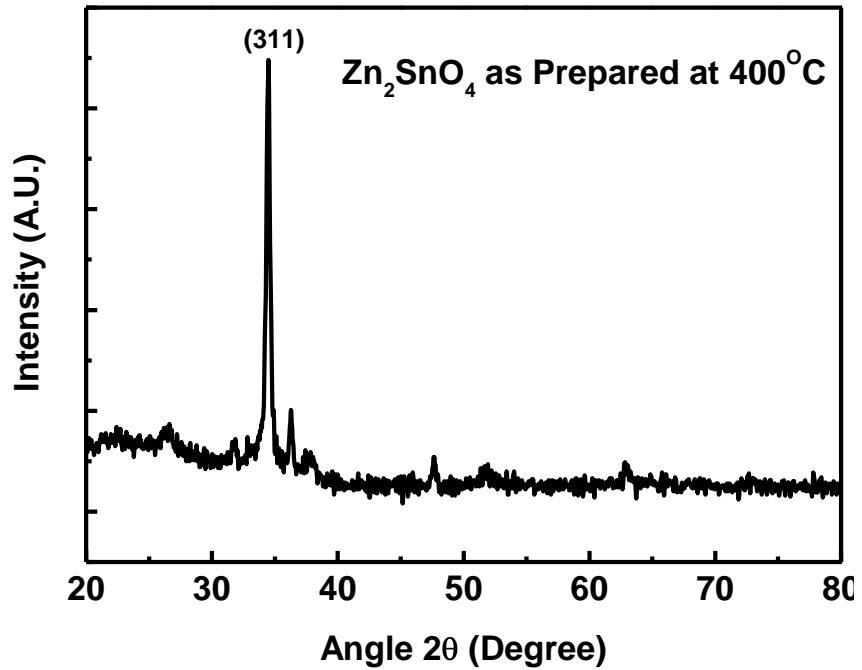


Figure 4.15 (c) X-ray diffraction spectra for thin films prepared at 400°C

by  
method

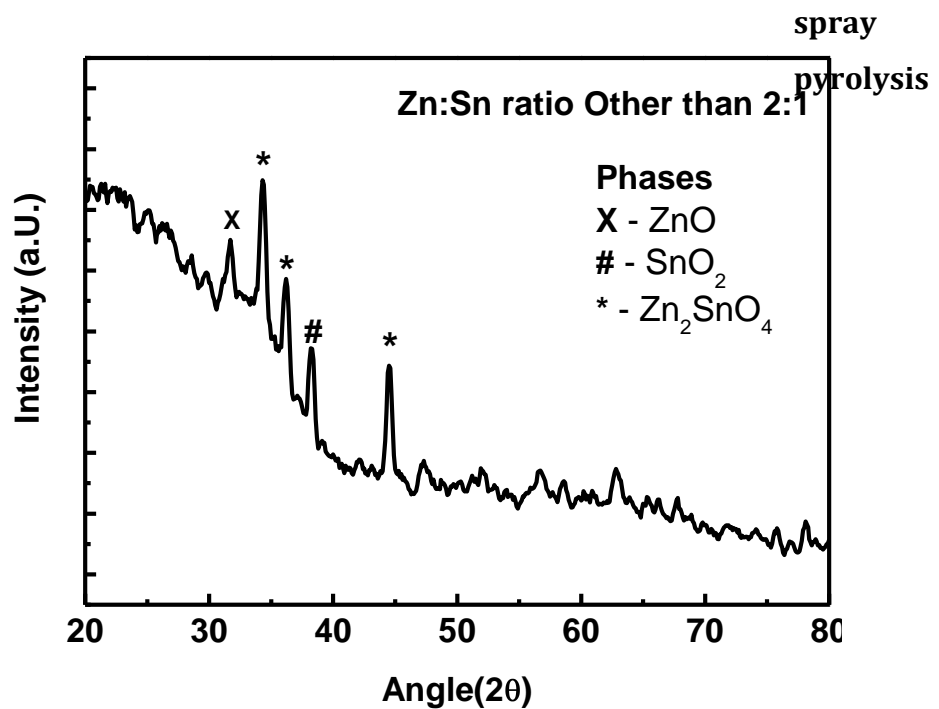


Figure 4.15 (d) X-ray diffraction spectra for thin films prepared by using Zn:Sn ratio other than 2:1. using spray pyrolysis method

**Table 4.3 The observed 2 $\theta$ , standard 2 $\theta$  and d values for thin films deposited at 300, 350 and 400 $^{\circ}$ c temperatures.**

Sample Prepared at	Observed '2 $\theta$ ' (Degree)	Standard '2 $\theta$ ' (Degree)	'd' value A $^{\circ}$	Planes (hkl)	Phase
<b>300<math>^{\circ}</math>C</b>	28.7	29.3	3.0441	(220)	<b>Zn<sub>2</sub>SnO<sub>4</sub></b>
	34.49	34.522	2.596	(311)	
	36.35	36.109	2.4854	(222)	<b>JCPDS</b>
	46.13	45.90	1.9752	(331)	<b>73-1725</b>
	54.44	54.65	1.6778	(220)	<b>SnO<sub>2</sub></b> <b>JCPDS</b> <b>77-0450</b>
	31.43	31.61	2.8274	(100)	<b>ZnO</b> <b>JCPDS</b>
<b>350<math>^{\circ}</math>C</b>	26.51	26.54	3.3556	(110)	<b>SnO<sub>2</sub></b> <b>JCPDS</b> <b>77-0450</b>
	29.12	29.31	3.0441	(220)	<b>Zn<sub>2</sub>SnO<sub>4</sub></b>
	34.49	34.52	2.596	(311)	
	35.95	36.109	2.4854	(222)	<b>JCPDS</b>
	41.96	41.93	2.1525	(400)	<b>73-1725</b>
<b>400<math>^{\circ}</math>C</b>	34.49	34.52	2.596	(311)	<b>Zn<sub>2</sub>SnO<sub>4</sub></b>

					JCPDS 73-1725
--	--	--	--	--	------------------

#### 4.4.3.2 X-ray Diffraction Studies of Zinc Stannate ( $Zn_2SnO_4$ ) thin films by spray pyrolysis method

X-ray diffraction (XRD) studies were carried out for the identification of crystal structure of the as-prepared and annealed films. Figure 4.15 (a), (b) and (c) shows XRD pattern of as prepared film at 300, 350 and 400°C respectively. The film prepared at 300°C exhibits mixed phases of ZnO, SnO<sub>2</sub> and Zn<sub>2</sub>SnO<sub>4</sub> with major contribution of Zn<sub>2</sub>SnO<sub>4</sub>. Sample prepared at 350°C shows relatively less number of peaks belonging to SnO<sub>2</sub> phase and contribution of ZnO phase is almost disappeared. This sample confirms major contribution of Zn<sub>2</sub>SnO<sub>4</sub> phase with increasing number of peaks belonging to Zn<sub>2</sub>SnO<sub>4</sub> phase. For the sample prepared at 400°C the existence of well defined reflection along (311) plane at 2 theta = 34.3° and well matching of 2 theta and 'd' values with JCPDS card No. 73-1725 depicts the formation of phase pure Zn<sub>2</sub>SnO<sub>4</sub> thin film with cubic face centered crystal structure [27, 31] in which all Sn<sup>4+</sup> atoms are octahedrally coordinated, while half of the Zn<sup>2+</sup> atoms are distributed in tetrahedral coordination and the other half in octahedral coordination [32].

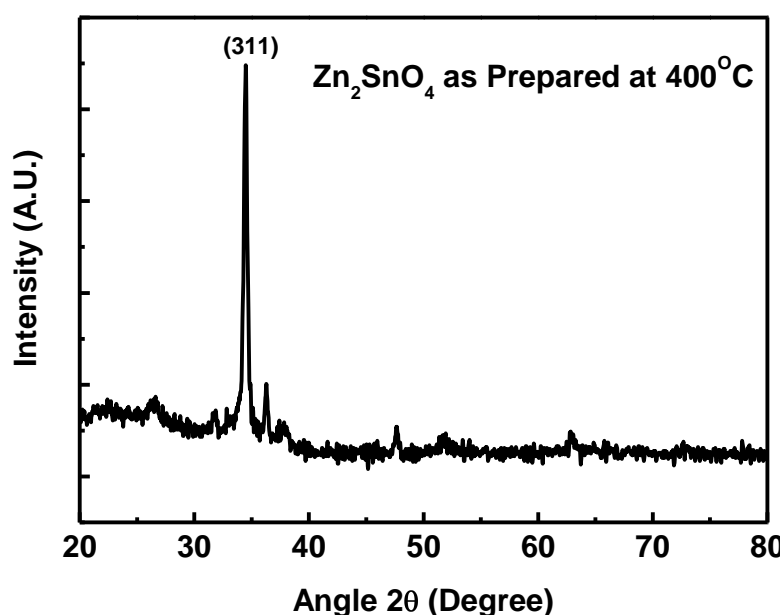


**Figure 4.16 (a) X-ray diffraction spectra for the  $Zn_2SnO_4$  thin film prepared by spray pyrolysis at  $400^\circ C$**

For further study, the prepared sample of  $Zn_2SnO_4$  (at  $400^\circ C$ ) was then annealed for 12 hrs. at  $500^\circ C$ .

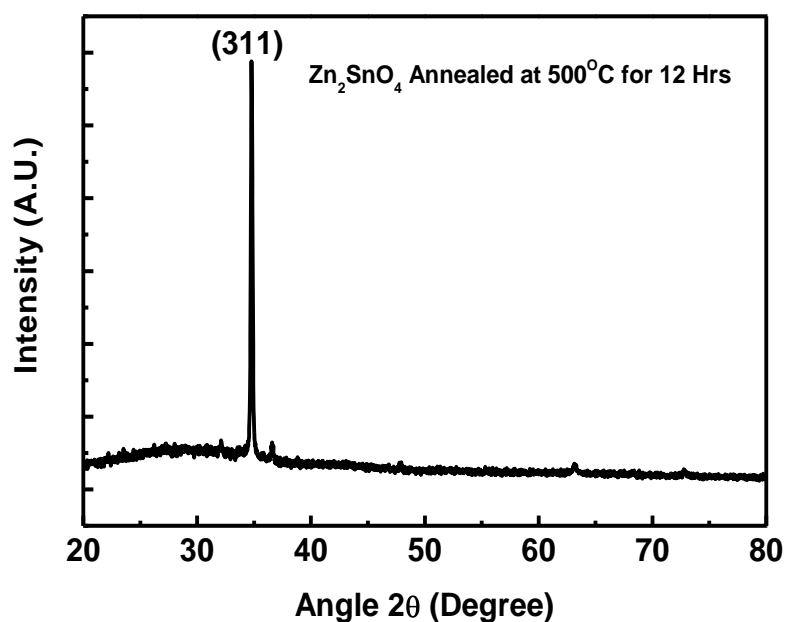


**Figure 4.17 X-ray diffraction spectra for the  $Zn_2SnO_4$  thin film annealed at  $500^\circ C$  for 12 Hrs**

Figure 4.17 shows XRD spectra for the annealed sample. Slight shift in (311) peak towards higher  $2\theta=34.5^\circ$  is observed upon annealing, [figure 4.18 (a) and (b)] which may be due to the removal of residual stresses in the films causing decrease in interplaner spacing. After annealing the marginal enhancement observed in the peaks intensity depicts improvement in the crystallinity of  $Zn_2SnO_4$  thin film. The estimated lattice parameter is  $8.6098 \text{ \AA}$ , which is in good agreement with the reported value of  $8.610 \text{ \AA}$  for  $Zn_2SnO_4$ . In order to determine the crystallite size, a slow scan of XRD pattern in between  $34^\circ$  to  $37^\circ$  was carried out within the step of  $0.02^\circ \text{ min}^{-1}$  for both the samples. The size of the crystallites oriented along (311) plane can be deduced using Scherer's formula (Equation 2.2)

The calculated values of crystallite size are 13nm and 41nm for as prepared and annealed sample respectively.

**Table 4.4 The observed  $2\theta$ , standard  $2\theta$  and d values for  $Zn_2SnO_4$  thin films.**

	<b>Observed '<math>2\theta</math>' (Degree)</b>	<b>Standard '<math>2\theta</math>' (Degree)</b>	<b>'d' value A<sup>o</sup></b>	<b>Planes (hkl)</b>	<b>JCPDS File No. 731725</b>
<b><math>Zn_2SnO_4</math></b>	34.484	34.522	2.5960	311	
	36.28	36.109	2.4854	222	

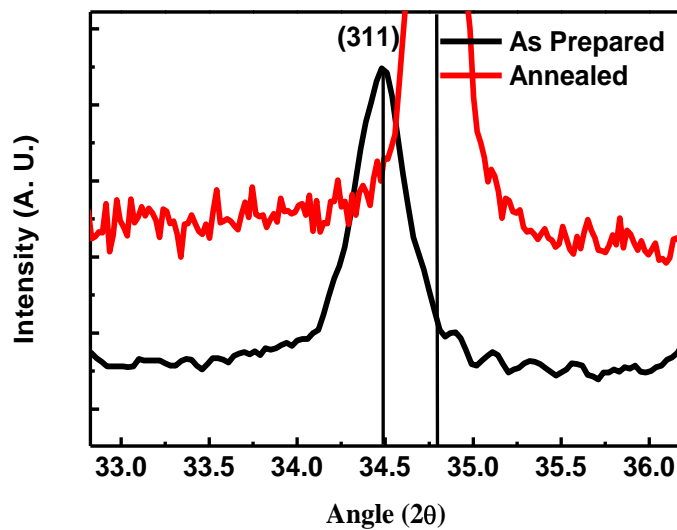
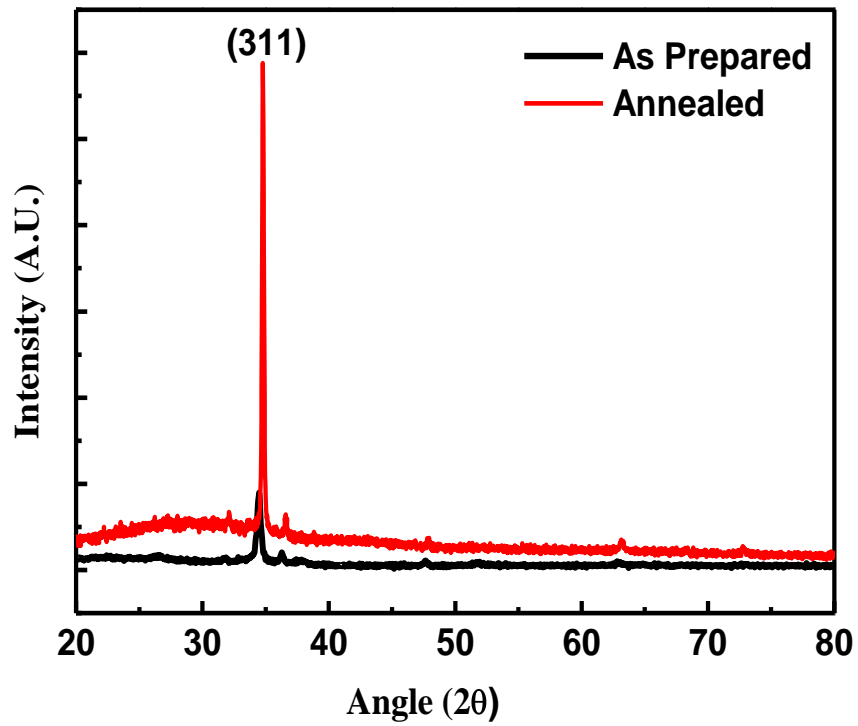
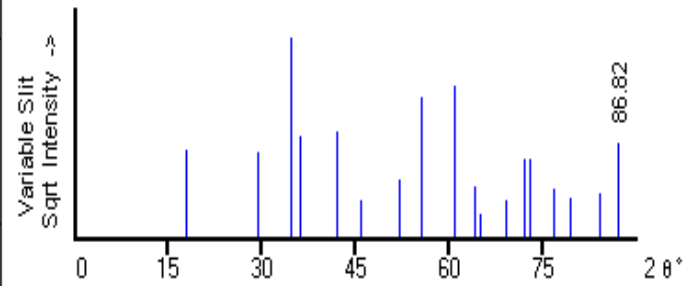


Figure 4.18 (a) X-ray diffraction spectra showing peak shift in  $Zn_2SnO_4$  thin film (b) enlarged view between 33-36° after annealed at 500°C for 12 Hrs  
JCPDS Zinc Stannate ( $Zn_2SnO_4$ ) File No: 731725data for

PDF # 731725, Wavelength = 1.54060 (Å)

73-1725 Quality: C  
 CAS Number:  
 Molecular Weight: 313.45  
 Volume[CD]: 638.28  
 Dx: 6.524 Dm:  
 Sys: Cubic  
 Lattice: Face-centered  
 S.G.: Fd3m (227)  
 Cell Parameters:  
 a 8.610 b c  
 α β γ  
 I/lor: 7.48  
 Rad: CuKα1  
 Lambda: 1.54060  
 Filter:  
 d-sp: calculated  
 ICSD #: 024234

Zn<sub>2</sub>SnO<sub>4</sub>  
 Zinc Tin Oxide  
 Ref: Calculated from ICSD using POWD-12++, (1997)  
 Ref: Barth, T.F.W., Posnjak, E., Z. Kristallogr., Kristallgeom., Kristallphys., Kristallchem., 82, 325 (1932)

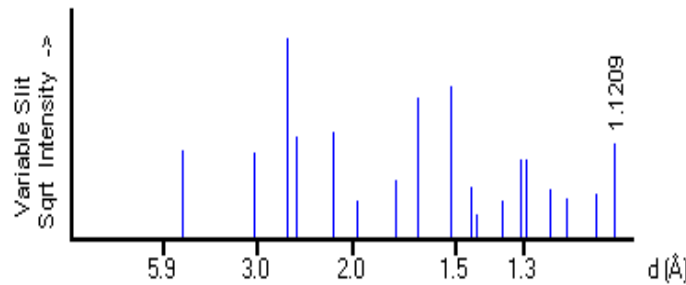


2θ	Int-v	h	k	l	2θ	Int-v	h	k	l	2θ	Int-v	h	k	l
17.829	19	1	1	1	51.990	8	4	2	2	71.842	14	5	3	3
29.316	18	2	2	0	55.404	48	5	1	1	72.804	15	6	2	2
34.522	100	3	1	1	60.808	56	4	4	0	76.608	5	4	4	4
36.109	25	2	2	2	63.914	6	5	3	1	79.422	3	5	5	1
41.938	28	4	0	0	64.931	0	4	4	2	84.057	4	6	4	2
45.906	3	3	3	1	68.920	3	6	2	0	86.817	22	7	3	1

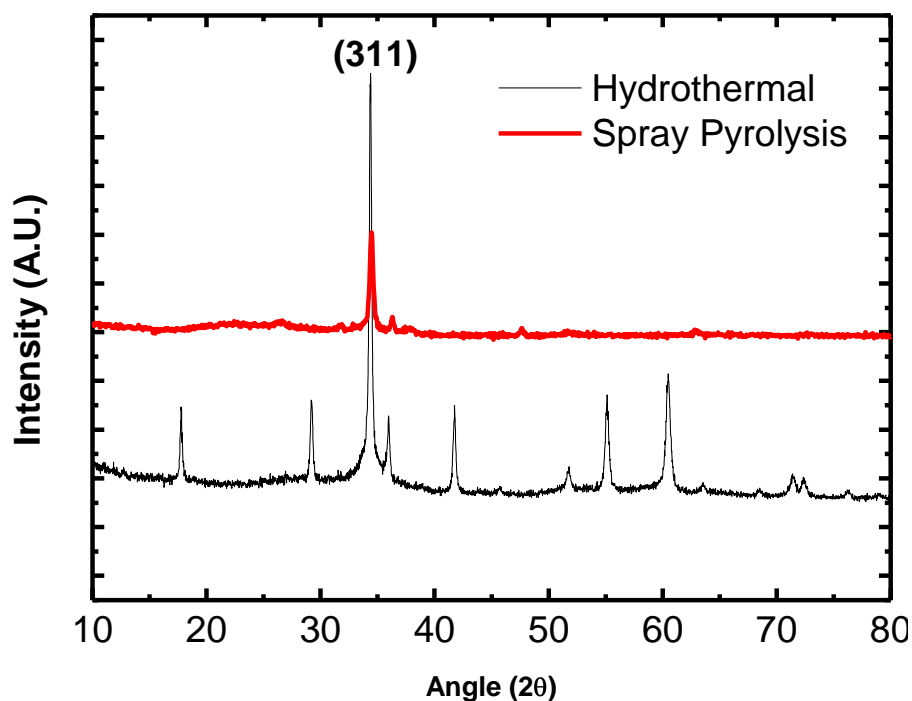
PDF # 731725, Wavelength = 1.54060 (Å)

73-1725 Quality: C  
 CAS Number:  
 Molecular Weight: 313.45  
 Volume[CD]: 638.28  
 Dx: 6.524 Dm:  
 Sys: Cubic  
 Lattice: Face-centered  
 S.G.: Fd3m (227)  
 Cell Parameters:  
 a 8.610 b c  
 α β γ  
 I/lor: 7.48  
 Rad: CuKα1  
 Lambda: 1.54060  
 Filter:  
 d-sp: calculated  
 ICSD #: 024234

Zn<sub>2</sub>SnO<sub>4</sub>  
 Zinc Tin Oxide  
 Ref: Calculated from ICSD using POWD-12++, (1997)  
 Ref: Barth, T.F.W., Posnjak, E., Z. Kristallogr., Kristallgeom., Kristallphys., Kristallchem., 82, 325 (1932)



d(Å)	Int-v	h	k	l	d(Å)	Int-v	h	k	l	d(Å)	Int-v	h	k	l
4.9709	19	1	1	1	1.7575	8	4	2	2	1.3130	14	5	3	3
3.0441	18	2	2	0	1.6570	48	5	1	1	1.2980	15	6	2	2
2.5960	100	3	1	1	1.5220	56	4	4	0	1.2427	5	4	4	4
2.4854	25	2	2	2	1.4553	6	5	3	1	1.2056	3	5	5	1
2.1525	28	4	0	0	1.4350	0	4	4	2	1.1505	4	6	4	2
1.9752	3	3	3	1	1.3613	3	6	2	0	1.1209	22	7	3	1



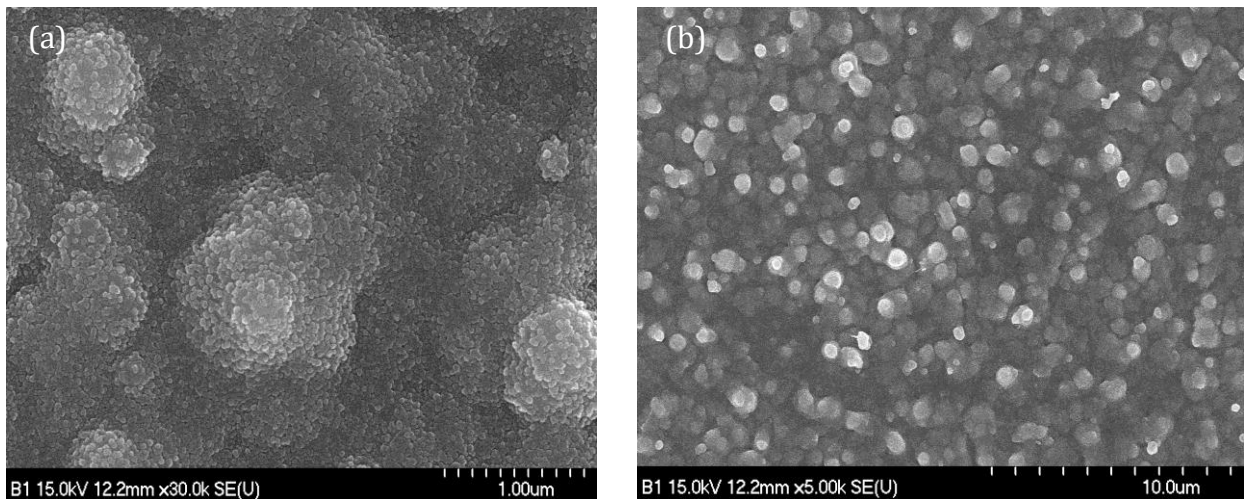
**Figure 4.19 Comparative X-ray diffraction spectra for the  $Zn_2SnO_4$  thin film prepared by spray pyrolysis and  $Zn_2SnO_4$  powder prepared by Hydrothermal Method.**

Figure 4.19 shows comparative XRD spectra for hydrothermally synthesized  $Zn_2SnO_4$  nanoparticles and spray pyrolytically deposited  $Zn_2SnO_4$  thin film. For the hydrothermal synthesis of  $Zn_2SnO_4$  nanocrystals, decomposition of a mixture of zinc and tin tert-butylamine complex is carried out by hydrothermal method. In a typical synthesis, 0.525 g of zinc chloride (98%, S. D. Fine Chem. Ltd., Mumbai) and 0.675 g of tin (IV) chloride pentahydrate (98%, S. D. Fine Chem. Ltd., Mumbai) and reported method is followed for the synthesis of nanoparticles [33]. The precipitates from the autoclave were washed several times with water to remove the left amine, finally by alcohol and then dried at room temperature and further characterized for XRD. The existence of single peak in the XRD of spray pyrolytically prepared thin film reveals preferential growth of nanocrystalline film along (311) plane. Morinaga and Sumetha Suwanboon [31, 34] proposed a qualitative idea for the formation mechanism of the preferential orientated thin films may be the

minimization of the surface free energy of each crystal plane and usually films grow so as to minimize the surface energy. Due to the minimization of the surface energy heterogeneous nucleation readily happens at the interface of thin film and substrate.

#### 4.4.3.3 Scanning electron microscopy (SEM) Studies of Zinc Stannate ( $\text{Zn}_2\text{SnO}_4$ ) thin films by spray pyrolysis method

Figure 4.20 shows the scanning electron micrograph (SEM) of as deposited (a) and annealed (b)  $\text{Zn}_2\text{SnO}_4$  thin film. From the figure, it is clear that no well defined grains were observed in case of as deposited sample whereas the annealed sample shows crystallites of an average diameter developed in the film



**Figure 4.20 (a), (b) Scanning electron Microscopy micrograph of the Zinc Stannate ( $\text{Zn}_2\text{SnO}_4$ ) thin film before and after annealing respectively.**

#### 4.4.3.4 UV-VIS optical absorption spectroscopy studies of $\text{Zn}_2\text{SnO}_4$ thin film prepared by spray pyrolysis.

Fig. 4.21 shows variation of  $(\alpha h\nu)^2$  as a function of photon energy ( $h\nu$ ). The optical absorption data was analyzed by the classical equation (2.4)

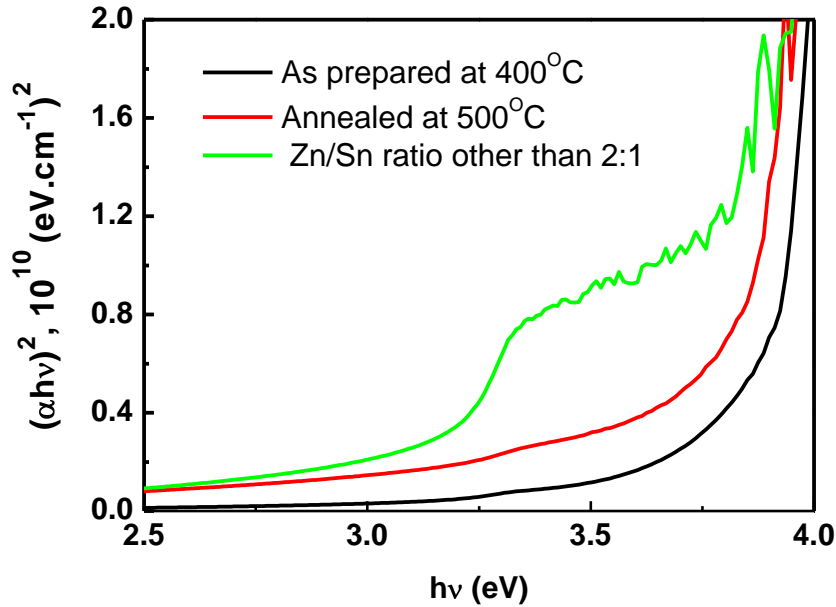


**Figure 4.21 Tauc Plot of  $\text{Zn}_2\text{SnO}_4$  thin film before and after annealing**

Where  $n$  - constant and  $E_g$  - separation between bottom of the conduction band and top of the valence band,  $h\nu$  - photon energy. Figure 4.21 shows that the optical band gap energy of  $\text{Zn}_2\text{SnO}_4$  after annealing decreases from 3.9 to 3.7 eV. The band gap values of zinc stannate based semiconductors were found to be ranging from 3.2 eV to 4.1 eV in different reports [35, 36].

These two band gap energy values of ZTO nanocrystals are apparently greater than the value for bulk ZTO (3.6 eV), the observed increase in the band gap of the ZTO nanostructures is indicative of quantum confinement effects arising from the small size regime [37] because the size of nanostructures is smaller in comparison with the bulk materials, as indicated by FESEM observations. The plot with two absorption edge is observed for the sample prepared with Zn:Sn other than 2:1

#### **4.4.3.5 Atomic force microscopy (AFM) Studies of Zinc Stannate ( $\text{Zn}_2\text{SnO}_4$ ) thin films by spray pyrolysis method**

Fig. 4.22(a)–(c) shows 3D and 2D images recorded for samples as prepared and annealed sample respectively. Table 4.5 shows that after annealing crystallinity of the  $\text{Zn}_2\text{SnO}_4$  film increases from 51.8 to 278 nm and leads to decrease in the surface roughness from 166 (as prepared ) to 71 (annealed) nm.

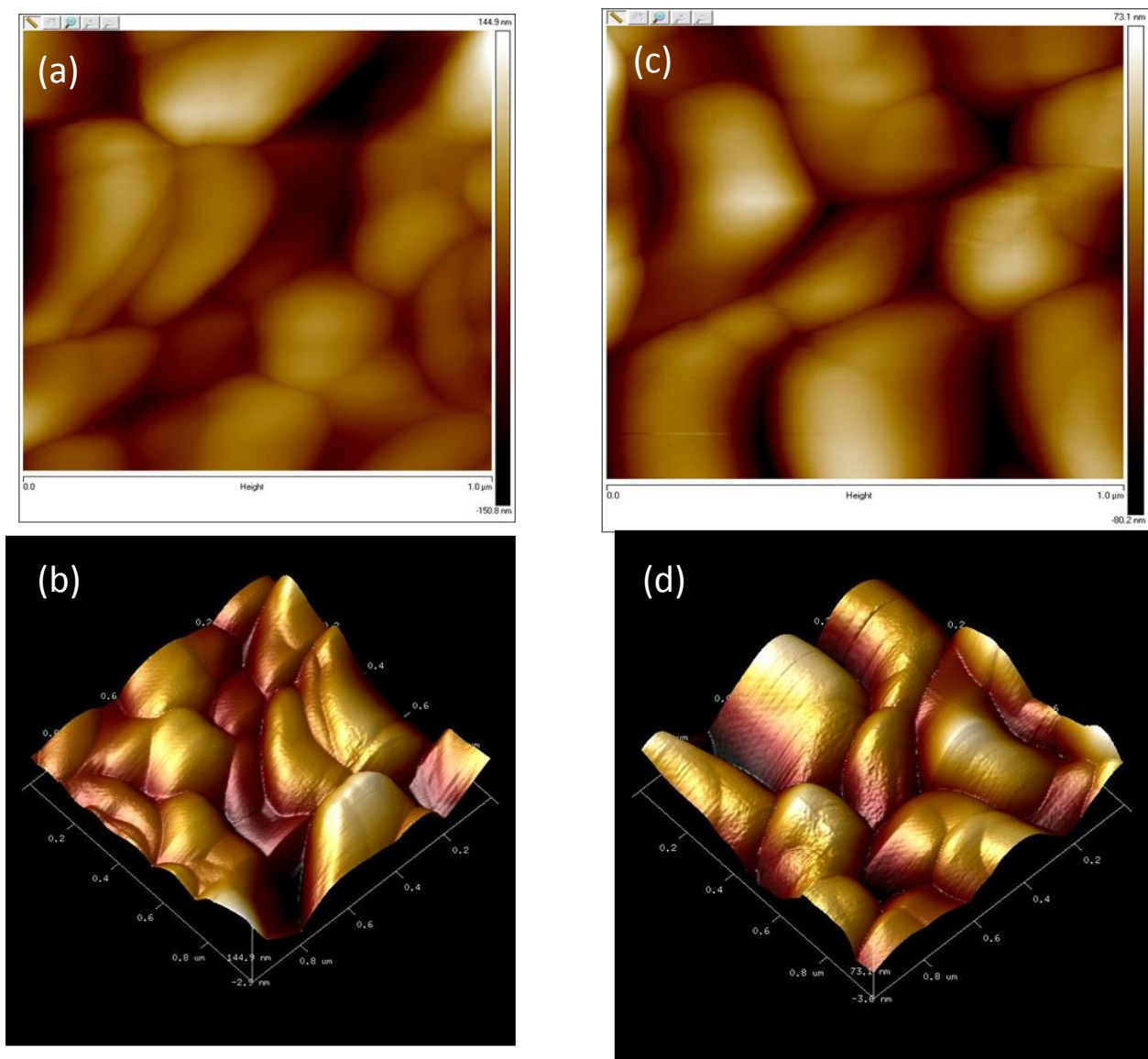


**Figure 4.22** 2D and 3D AFM images of as prepared (a), (b) and annealed (c), (d)  $\text{Zn}_2\text{SnO}_4$  thin films.

**Table 4.5 Roughness and particle size measurement of as deposited and annealed Zn<sub>2</sub>SnO<sub>4</sub> thin films.**

Sample ID	Roughness (nm)	Particle size (nm)
As prepared	166	51.8
Annealed	71	278

#### 4.4.3.6 Cyclic Voltammetric (CV) Studies of Tin Oxide (SnO<sub>2</sub>), Zinc Oxide (ZnO) and Zinc Stannate (Zn<sub>2</sub>SnO<sub>4</sub>) thin films by spray pyrolysis method

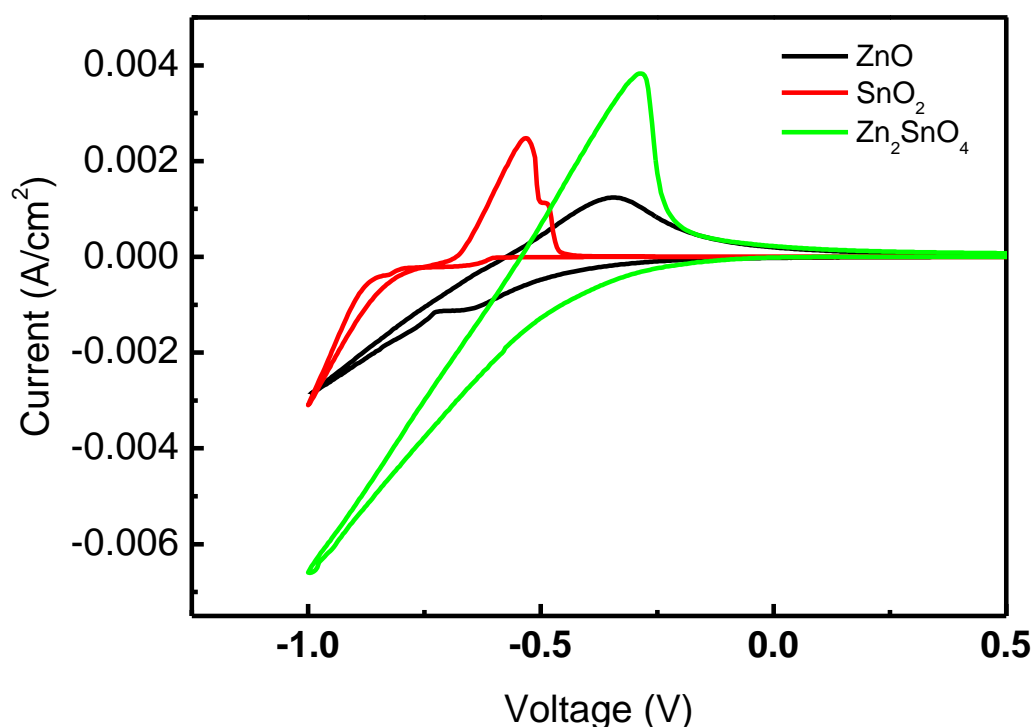


**Figure 4.23 Cyclic Voltammogram recorded in -1 to 0.5 Volt for SnO<sub>2</sub>, ZnO and Zn<sub>2</sub>SnO<sub>4</sub> Sample in 0.1 M H<sub>2</sub>SO<sub>4</sub> Electrolyte**

Figure 4.23 shows cyclic voltammogram recorded in -1 to 0.5 Volt for SnO<sub>2</sub>, ZnO and Zn<sub>2</sub>SnO<sub>4</sub> Samples in 0.1 M H<sub>2</sub>SO<sub>4</sub> Electrolyte with Graphite as counter and SCE as reference electrode. From figure it is observed that, for all the three samples redox curves are having different area, which clearly entails that the maximum area of Zn<sub>2</sub>SnO<sub>4</sub> is analogous to its maximum conductivity and charge storage capacity as compared to SnO<sub>2</sub> and ZnO. The observed oxidation

peak potentials are -0.052, -0.35, -0.28 V for SnO<sub>2</sub>, ZnO and Zn<sub>2</sub>SnO<sub>4</sub> samples respectively.

The different Oxidation peak potential and charge storage capacity also proves that the samples are of different chemical composition.

#### **4.4.3.7 Fabrication of Zn<sub>2</sub>SnO<sub>4</sub> photoanodes and Dye sensitized Solar cell Properties measurements.**

Spray pyrolysis technique is used to fabricate Zn<sub>2</sub>SnO<sub>4</sub> films on fluorine-doped tin oxide conductive glass (Asahi Glass Co.Ltd.; 10 ohm/square). Film thickness was 7-8 μm. For the preparation of CNT-Zn<sub>2</sub>SnO<sub>4</sub> thin films appropriate amount of functionalized carbon nano tubes (CNTs) were added in the spray solution and sonicated for 10 Hrs for their uniform dispersion. Subsequently films were dipped in a dye solution of 5×10<sup>-4</sup> M N719 dissolved in acetoni-trile and 4-tert-butyl alcohol (volume ratio=1:1), and kept at room temperature for 12 h. The solar cells were assembled using a dye-sensitized Zn<sub>2</sub>SnO<sub>4</sub> photoanode, a sputtered Pt counter electrode and a redox (I<sup>-</sup>/I<sub>3</sub><sup>-</sup>) electrolyte solution. The current density–voltage (J-V) curves of DSCs were recorded under simulated AM 1.5 illumination. The performance of Zn<sub>2</sub>SnO<sub>4</sub> DSSCs for as prepared and annealed film was measured. The plot of current density–voltage (J-V) characteristics of as prepared and annealed ZTO based solar cells are shown in Figure 4.24. J-V measurements of both the devices were carried out by simulated sun light of power 100 mW/cm<sup>2</sup> irradiation.

The illuminated area of ZTO working electrode was 0.25 cm<sup>2</sup> (0.5 cm x 0.5 cm). The obtained photo-electrochemical parameters of DSSCs such as short circuit current density (J<sub>sc</sub>), open circuit voltage (V<sub>oc</sub>), fill factor (FF) and power conversion efficiency (PCE) are summarized in Table 4.6.

**Table 4.6 Photo-electrochemical parameters of DSSCs of as deposited and annealed Zn<sub>2</sub>SnO<sub>4</sub> thin films.**

Sample ID	Jsc (mA/cm <sup>2</sup> )	Voc (V)	Fill factor	Efficiency (%)
As prepared	6.4	0.73	57.72	2.7
Annealed	8.4	0.68	48.86	2.85
CNT doped	7.5	0.73	57.3	3.1

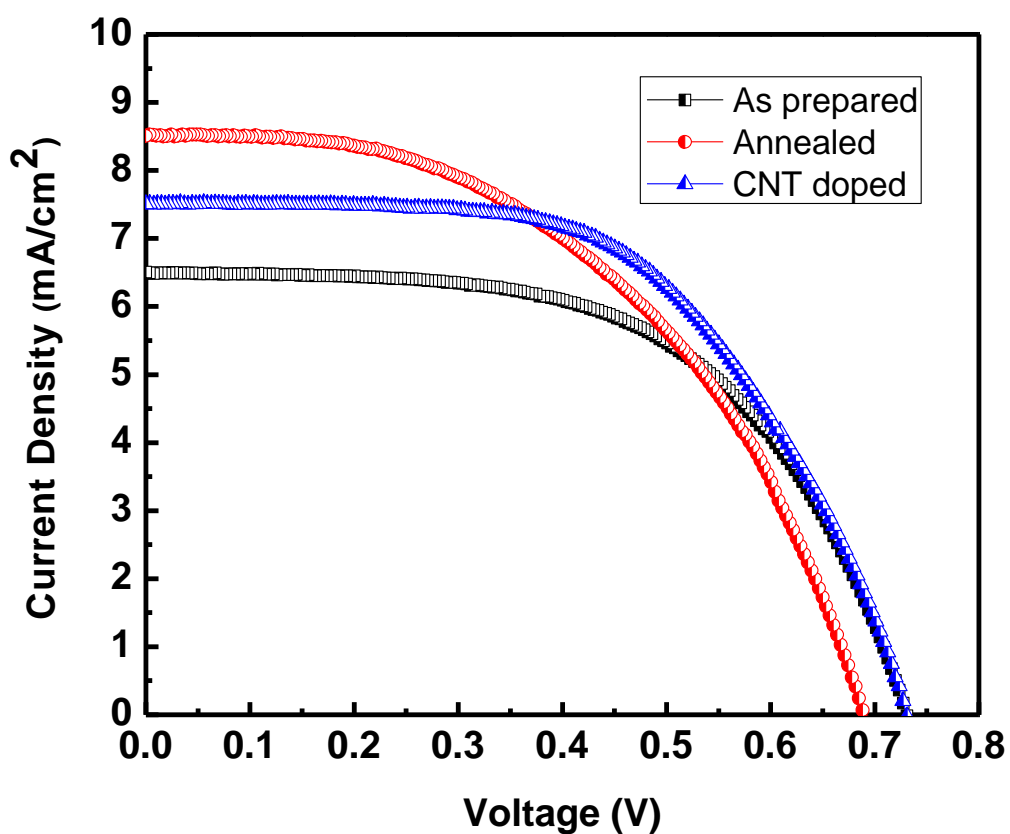


**Figure 4.24 I-V Characteristics of Zn<sub>2</sub>SnO<sub>4</sub> DSSC Solar Cell.**

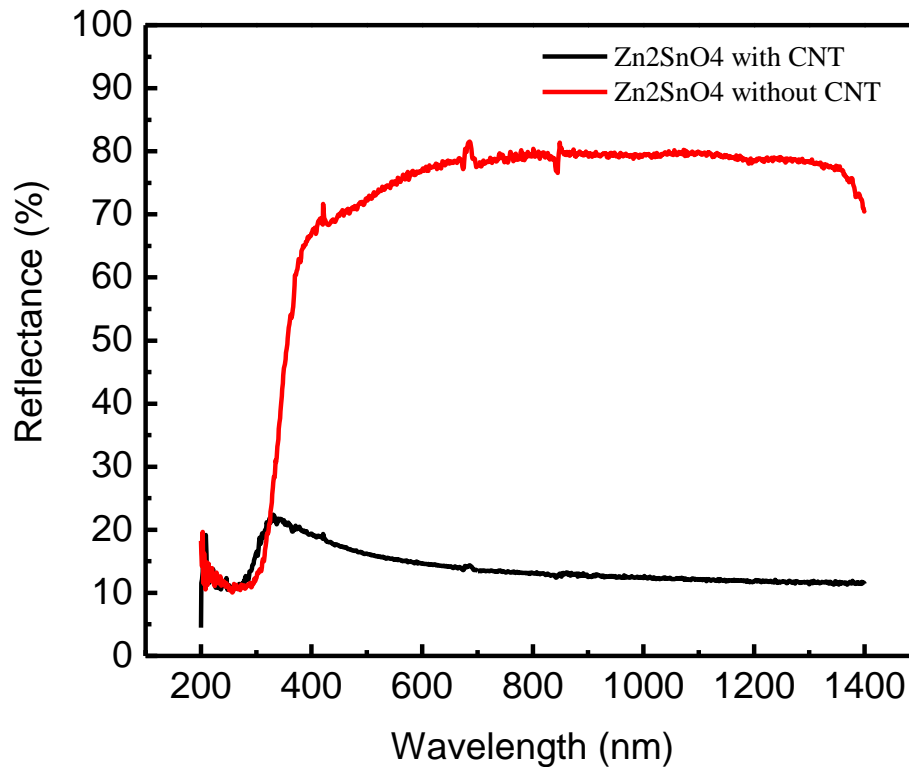


**Figure 4.25 DRS Spectra of Undoped and CNT doped Zn<sub>2</sub>SnO<sub>4</sub> thin film.**

The as prepared ZTO device produced short circuit photocurrent density 6.4 mA/cm<sup>-2</sup> whereas for the post-annealed ZTO device it is 8.4 mA/cm<sup>-2</sup>. The observed improvement in the J<sub>sc</sub> may be due to the improved crystallinity of the sample which can promote easy charge transport within the film due to less grain boundary scattering. Open circuit voltage in DSSC is governed by the difference in conduction band (CB) edge of photo-anode and LUMO level of organic dye. After annealing, shrinkage in band gap causing the lowering of conduction band edge is observed and hence Voc decreased from 0.73 to 0.68V. It is observed that the photo-conversion efficiency of CNT doped sample increased by 0.25% than that of annealed sample. The observed increase in the efficiency may be the collective effect of provision of conducive channels by CNTs for the transport of photo-generated electrons and from figure 4.25 it is also observed that the reflectance of CNT doped films decreased drastically as compared to undoped films, which may trap more photons and enhance photogenerated charge carriers [38]. For CNT doped films J<sub>sc</sub> found to be

increased upto 7.5 mA/cm<sup>2</sup>. The overall photoconversion efficiencies for the as-prepared, post-annealed and CNT doped samples were 2.7, 2.85 and 3.1% respectively. The fill factor and the efficiency of the cells were calculated by the following equations

$$ff = \frac{V_m J_m}{V_{OC} J_{SC}} \text{--- --- --- (4.3)}$$

$$\eta = \frac{V_{OC} J_{SC} ff}{P_{in}} \text{--- --- --- --- --- (4.4)}$$

Where  $V_m$  is the voltage and  $I_m$  is the current at point of maximum power correspondingly,  $V_{oc}$  is the open circuit photo voltage,  $J_{sc}$  is the short circuit photocurrent density and  $P_{in}$  represents power of incident radiation.

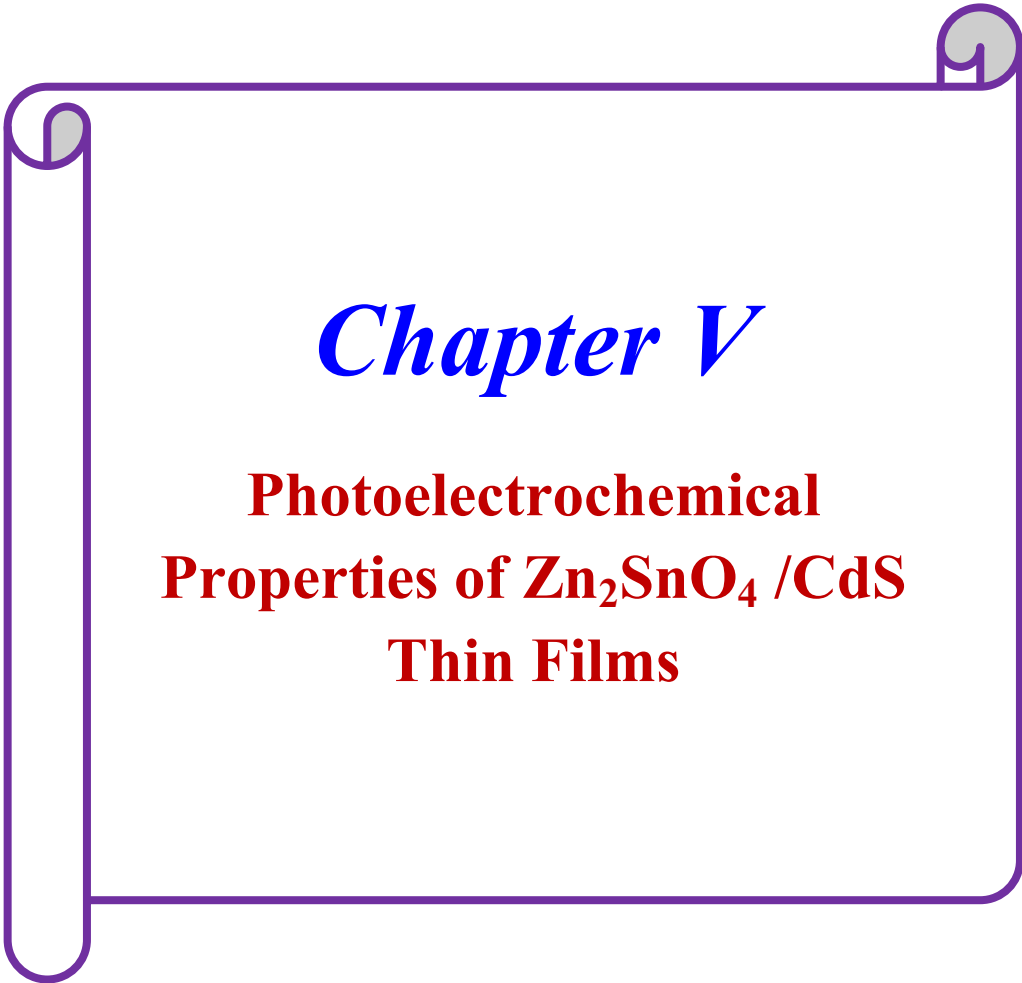
#### 4.5 Conclusions

The zinc stannate (ZTO) thin films were prepared on FTO glass substrate by spray pyrolysis technique (SPT) at different substrate temperatures. The XRD patterns of these revealed that phase pure ZTO is formed at 400 °C with Zn:Sn molar ratio 2:1. Improvement in the crystallinity of Zn<sub>2</sub>SnO<sub>4</sub> thin film was observed after annealing. The ZTO thin film prepared by SPT was compared with hydrothermally synthesized ZTO nanoparticles. Single peak in XRD pattern of ZTO thin film prepared by SPT indicated preferential orientation along specific direction. The as prepared ZTO thin film on FTO glass substrate was used as photoanode in dye sensitized solar cell. The photo voltaic measurements of DSCs were carried using as prepared, annealed and CNT doped ZTO electrodes. It is observed that the photocoverion efficiency of DSC increases on annealing and CNT doping.

#### References

- [1] B. O'Regan, M. Grätzel, *Nature* 353 (1991) 737.
- [2] U. Bach, D. Lupo, P. Comte, J. E. Moser, F. Weissortel, J. Salbeck, H. Spreitzer, M. Grätzel, *Nature*, 395 (1998) 583.
- [3] Prashant V. Kamat, *Accounts of Chemical Research*, 45(11) (2012) 1906.
- [4] I. J. Kramer, E. H. Sargent, *Chemical Reviews*, 114 (2014) 863.
- [5] A. Kojima, K. Teshima, Y. Shirai, T. Miyasaka, *Journal of American Chemical Society*, 131 (2009) 6050.
- [6] M. M. Lee, J. Teuscher, T. Miyasaka, T. N. Murakami, H. J. Snaith, *Science*, 338 (2012) 643.
- [7] H.-S. Kim, C.-R. Lee, J.-H. Im, K.-B. Lee, T. Moehl, A. Marchioro, S.-J. Moon, R. Humphry-Baker, J.-H. Yum, J. E. Moser, M. Grätzel, N.-G. Park, *Scientific reports*, 2 (2012) 591.
- [8] J. Burschka, N. Pellet, S. J. Moon, R. Humphry-Baker, P. Gao, M. K. Nazeeruddin, M. Grätzel. *Nature*, 499 (2013) 316.
- [9] M. Grätzel, *Nature*, 414 (2001) 338.
- [10] A. Hagfeldt, G. Boschloo, L. Sun, L. Kloo, H. Pettersson, *Chemical Reviews*, 110(11) (2010) 6595.
- [11] S. Mathew, A. Yella, P. Gao, R. Humphry-Baker, B. F. E. Curchod, N. Ashari-Astani, I. Tavernelli, U. Rothlisberger, M. K. Nazeeruddin, M. Grätzel, *Nat. Chem.*, 6 (2014) 242.
- [12] S. Ardo, G. J. Meyer, *Chemical Society Reviews*, 38 (2009) 115.
- [13] S. M. Feldt, P. W. Lohse, F. Kessler, M. K. Nazeeruddin, M. Grätzel, G. Boschloo, A. Hagfeldt, *Physical Chemistry Chemical Physics*, 15 (2013) 7087.
- [14] Q. Wang, S. Ito, M. Grätzel, F. Fabregat-Santiago, I. Mora-Sero, J. Bisquert, T. Bessho, H. Imai, *J. Phys. Chem. B* 110 (2006) 25210-25221.
- [15] A. Yella, H. Lee, H. Tsao, C. Yi, A. Chandiran, M. Nazeeruddin, E. Diau, C. Yeh, S. M. Zakeeruddin, M. Grätzel, *Science*, 334 (2012) 629.
- [16] W.X. CunWang, *J. Mater. Sci.*, 37 (2002) 2989.
- [17] X. Lou, X. Jia, J. Xu, S. Liu, Q. Gao, *Mater. Sci. Eng. : A*, 432 (2006) 221.
- [18] X. Fu, X. Wang, Z. Ding, D. Y. C. Leung, Z. Zhang, J. Long, W. Zhang, Z. Li, X. Fu, *Appl. Catal. B: Environ.*, 91(1-2) (2009) 67.
- [19] B. Tan, E. Toman, Y. Li, Y. Wu, *J. Am. Chem. Soc.*, 129 (14) (2007) 4162.

- [20] J. Zeng, M. Xin, K. Li, H. Wang, H. Yan, W. Zhang, *J. Phys. Chem. C*, 112 (11) (2008) 4159.
- [21] Y. Zhang, M. Guo, M. Zhang, C. Yang, T. Ma, X. Wang, *J. Cryst. Growth*, 308 (1) (2007) 99.
- [22] M. Alpuche-Aviles, Y. Wu, *J. Am. Chem. Soc.*, 131 (2009) 3216.
- [23] D. Kim, S. Shin, I. Cho, S. Lee, D. Kim, C. Lee, H. Jun, K. Hong, *Nanoscale*, 4 (2012) 557.
- [24] S. S. Shin, D. W. Kim, D. Hwang, J. H. Suk, L. S. Oh, B. S. Han, D. H. Kim, J. S. Kim, Kim, J. Y. Kim, K. S. Hong, *Chem Sus Chem*, 7 (2014) 501.
- [25] S. Choi, D. Hwang, D. Kim, Y. Kervella, P. Maldivi, S. Jang, R. Demadrille, I. Kim, *Adv. Funct. Mater.*, 23 (2013) 3146.
- [26] Y. Wang, K. Li, Y. Xu, H. Rao, C. Su, D. Kuang, *Nanoscale* 5 (2013) 5940.
- [27] K. Wang, Yantao Shia, Wei Guob, Xiaoqiang Yua, Tingli Mac, *Electrochimica Acta* 135 (2014) 242.
- [28] Z. Li, Y. Zhou, H. Yang, R. Huang, Z. Zou, *Electrochimica Acta*, 152 (2015) 25.
- [29] J.C. Manificier, M. De Murcia, J.P. Fillard, E. Vicario. (1977). *TSF*. 41: 127.
- [30] Z. Khan, M. Arif, A. Singh, *International Nano Letters* (2012), 2:22.
- [31] Morinaga Y, Sakuragi R, Fujishima N., *Journal of Crystal Growth* (1997) 174.
- [32] F. Mechelti, P. Mark, *J. Appl. Phys. Lett.* 10 (1967) 136.
- [33] D. L. Young, D. L. Williamson, T. J. Coutts, *J. Appl. Phys.* 91 (2002) 1464.
- [34] S. Suwanboon, *Naresuan University journal*, Vol, 16, No. 2, (2008) 173.
- [35] D. L. Young, H. Moutinho, Y. Yan, T. J. Coutts, *J. Appl. Phys.* 92 (2002) 310.
- [36] K. Satoh, Y. Kakehi, A. Okamoto, S. Murakami, F. Uratani, Yotsuya, T. *Jpn. J. Appl. Phys.*, Part 2 (2005) 44, L34.
- [37] J. Zeng, M. Xin, Li K, H. Wang, H. Yan, W. Zhang, *J. Phys. Chem. C* 112 (2008) 4159.
- [38] S. Muduli, W. Lee, V. Dhas, S. Mujawar, M. Dubey, K. Vijaymohan, S.H Han, S. B. Ogale, *ACS Applied Materials and Interfaces*, 1(9) (2009) 2030.



# *Chapter V*

## **Photoelectrochemical Properties of $\text{Zn}_2\text{SnO}_4$ /CdS Thin Films**

## Chapter V

### Photoelectrochemical Properties of $Zn_2SnO_4$ /CdS Thin Films

#### 5.1 Introduction.

5.1.1. Construction of PEC solar cell.

5.1.2. Requirements of PEC cells.

5.1.3 Survey of literature on Cadmium sulphide (CdS).

#### 5.2. Synthesis and characterization of Cadmium Sulphide thin films by chemical

##### bath deposition (CBD).

5.2.1. Preparation of CdS thin films by chemical bath deposition.

5.2.2. X-ray Diffraction studies of CdS thin films Prepared by chemical bath deposition.

5.2.3 Scanning electron microscopy (SEM) studies of CdS thin films prepared by chemical bath deposition.

5.2.4. UV-VIS absorption spectroscopy studies of CdS thin films Prepared by chemical bath deposition.

#### 5.3. Preparation of $Zn_2SnO_4$ /CdS thin films electrodes and their photoelectrochemical solar cell testing.

5.3.1. Introduction

5.3.2. Preparation of  $Zn_2SnO_4$  thin films by spray pyrolysis technique.

5.3.3. X-ray Diffraction Studies of Zinc Stannate ( $Zn_2SnO_4$ ) thin films.

5.3.4. Scanning electron microscopy (SEM) studies of  $Zn_2SnO_4$  /CdS thin film electrodes.

5.3.5. UV-VIS absorption studies of  $Zn_2SnO_4$  thin film electrodes.

5.3.6. Preparation of  $Zn_2SnO_4$ /CdS thin films electrodes.

5.3.7. X-ray diffraction studies of  $Zn_2SnO_4$ /CdS thin films electrodes.

5.3.8. Scanning electron microscopy (SEM) studies of  $Zn_2SnO_4$ /CdS thin film electrodes.

5.3.9. UV-VIS absorption studies of  $Zn_2SnO_4$ /CdS thin film electrodes.

#### 5.4. Photoelectrochemical characterization.

5.4.1. Result of photo-electrochemical measurements.

## CHAPTER V

### Photoelectrochemical Properties of $Zn_2SnO_4$ /CdS Thin Films

#### 5.1 Introduction

##### 5.1.1 Construction of PEC solar cell

A PEC solar cell is an electrochemical cell in which one or both electrodes are semiconductors such that irradiation of the semiconductor results in the non-spontaneous flow of current in the external circuit. This type of cell is different from a photogalvanic cell in the manner that light absorption occurs in the solution instead of electrode. Figure 5.1(a) represents PEC cell that has elements like semiconductor photoanode, an electrolyte and a counter electrode. The photoelectrode and counter electrode are 1 cm. apart.

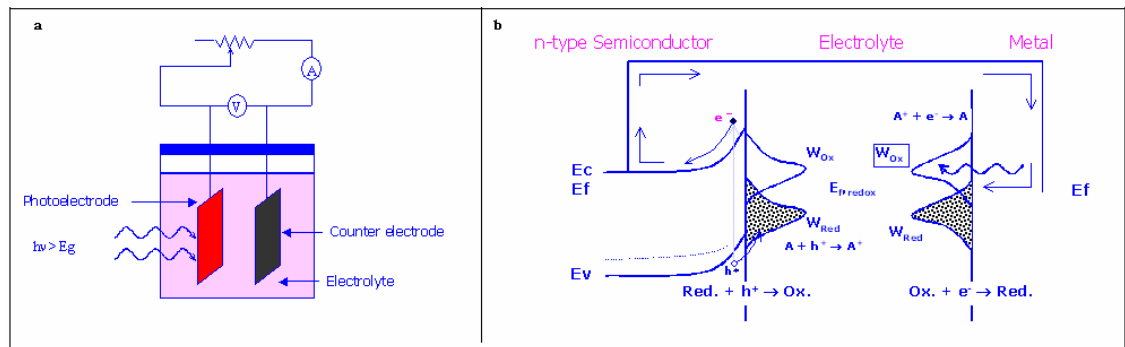


**Figure 5.1 (a) - A typical electrochemical photovoltaic cell and (b) - Current flow and energy level diagram for n- semiconductor PEC cell.**

##### 5.1.2 Requirements of PEC cells

Good performance of the PEC cell is achieved by following requirements.

###### 5.1.2.1 Semiconductor photoelectrode

The semiconductor photoelectrode is the important part of the PEC cell. The property of a semiconductor photoelectrode shows the changes in the electrical properties of a cell. The electrons send to the conduction band flow towards the interior, while the holes, the minority carriers, come to the surface of the semiconductor.

1. The maximum region of the solar spectrum should be covered by the band gap ( $E_g$ ) of the photoelectrode materials.

2. It should have high stability in the dark as well as under illumination.
3. It should be of the direct band gap type along with high optical absorption coefficient.
4. There should be high mobility and life time of charge carriers in the material.
5. Thickness should be sufficiently large to absorb all the incident radiation.
6. Cost of manufacturing and efficiency should be agreed.
7. There should be large diffusion length of minority carriers.
8. Shunt resistance  $R_{sh}$  should be large enough and Series resistance  $R_s$  should be as small as possible ideally  $R_s = 0$  and  $R_{sh} = \infty$ .

#### **5.1.2.2 Electrolyte**

Electrolyte is an important parameter in the PEC cell. Electrolytes consist of the oxidized species and the reduced species. Mixtures of totally ionic molten salts and molecular inorganic solvents with supporting electrolytes have been introduced for aqueous electrolytes.

##### **Requirements of electrolytes for the PEC cells:**

1. There should be proper Reduction-oxidation reactions to match with the semiconductor band edges.
2. Charge transfer rates of oxidized and reduced species should be high at both semiconductor and counter electrode.
3. There should be high photo and thermal stability of oxidized, reduced species and solvent components over useful solar spectrum and operating temperature range.
4. Supporting electrolyte concentration and oxidized, reduced species in
5. Solvent should be enough to reach required current densities.

#### **5.1.2.3 The Counter electrode**

For better performance in the PEC cell, the requirements of the counter electrode are:

1. The counter electrode should not react with electrolyte.
2. Fast charge transfer between redox species in electrolyte and counter electrode.
3. To avoid concentration polarization the area should be large.

4. The low reduction potential reaction is desirable for counter electrode.
5. It should have low cost. The most commonly used counter electrodes are platinum and graphite.

### **5.1.3 Survey of Literature**

#### **5.1.3.1 Survey of literature on CdS**

Since last 60 years, metal chalcogenides (sulphides, selenides and tellurides) have been studied for their important applications such as photoconductive cells, photovoltaic cells and other optical devices. CdS thin film is one of the important examples of film SC electrodes. CdS nanocrystalline thin films are used as window material for CdS/CdTe solar cells and it continues as a subject of intense research due to its possible application in solar cells [1-5].

#### **5.1.3.2 Literature survey of chemical bath deposited CdS thin films**

CdS thin films have been prepared by several techniques, such as electrodeposition, chemical bath deposition (CBD), physical vapour deposition and screen printing (SP). Today, there has been an urgent need for efficient, low temperature and low-cost deposition methods for thin films. Chemical bath deposition (CBD) is a soft solution process capable of producing high-quality thin film at relatively low temperature. The CBD growth mechanism consists of different stages like mass transport of reactants, adsorption, surface diffusion, reaction, nucleation and growth. Uniform, adherent and large-area thin films can be produced by simple and low cost CBD method for thin-film electronics applications such as solar cells [6]. The first application of CBD was reported by Reynolds [7] for the fabrication of lead sulfide photoconductive detectors in 1884. Chopra reported the first general review for CBD [8] in 1982. Later on Lokhande [9] published a review on the deposition of metal chalcogenides. Lincot [10] in 1998 reported review along with growth kinetics analysis. Nair [11] and Savadogo [12] reported reviews on solar energy-related issues. The characterization of the post-deposited films and optimization of the deposition processes are equally important together with deposition technique. Many researchers worked on preparation of CdS thin films to obtain smart optoelectronic properties.

Kaur et.al and Pandya et al. reported the CdS as a window layer in CIGS cells [13, 14]. The band gap of the window layer should be high and should possess low thickness to keep low series resistance so that it could be used in hetero-junction solar cells. The high band gap and low thickness of CdS thin film by wet chemical method was tried by number of investigators. Mokrushin et al. and Kitaev et.al studied the potential application of CdS [15, 16]. Moutinho H.R. and co-workers deposited CdS thin film by close-spaced sublimation (CSS) and chemical bath deposition (CBD), to study why CBD CdS is used to obtain the best PV devices. Unlike the CSS CdS, CBD CdS films grew conformal on the underlying SnO<sub>2</sub> film, which was used as a front contact. The conformal growth encourages a film with a more uniform thickness, minimizing shunting paths [17]. Ramanathan et al. reported about 19 % efficiency of CIGS with CdS buffer layer [18].

The quantum size effect is the increase in the band gap of semiconductor due to a decrease in the particle size. Size quantized CdS thin films are applied for the window layer in solar cells. Louis Brus and co-workers reported experimental and theoretical work in the size-dependent development of bulk electronic properties in semiconductor crystallites [19]. The optical effects with small colloidal particles of CdS (<50 Å) observed due to quantization in three dimensions was reported by Nozik and co-workers [20]. Electro chemical atomic layer epitaxy (ECALE) method for size quantized CdS thin film for photoelectrochemical application was reported by Torimoto et al. [21]. Vossmeier et al. [22] reported advanced synthetic routes for the preparation of monodispersed CdS clusters. Synthesis of CdS with different crystalline size by a precipitation technique with CdSO<sub>4</sub>, thiourea and NH<sub>4</sub>OH precursors was reported by K.K. Nanda et al.[23]. They used CdSO<sub>4</sub>, thiourea and NH<sub>4</sub>OH as precursors. By controlling the reaction time period/thickness, temperature and pH of the solution, different crystalline sizes were obtained. Nanocrystalline CdS presenting quantum size effect were prepared at 300 K with solution pH=11.7. They observed blue shift of 0.74 eV due to quantum size effect in CdS nanoparticles.

Yao and co-workers [24] reported preparation and photoelectrochemical characterization of CdS particles in nanospaces of expandable mica. Using XPS

spectra Jinesh and co-workers [25] find out the quantum confinement in chemically deposited CdS. They use XPS spectra for the investigation. They also reported that increased pH of the bath shows CdS clusters of finite size which are embedded in Cd(OH)<sub>2</sub> surroundings making the clusters electrically isolated and thus presenting carrier confinement.

Polymers are commonly used for the synthesis of semiconductor nanoparticles because the polymer matrices offer advantages like solubility, easy processability and control of the growth and morphology of the nanoparticles. Many workers [26-31] prepared CdS nanoparticles embedded in different matrices like polystyrene, polyvinyl alcohol, polyethylene glycol. Z. Qian and co-workers [32] reported CdS-PAMAM composite nanocrystalline thin film useful for photoelectrochemical sensors. Hwang and co-workers [33] reported CdS nanoparticles on the surface of single walled carbon nanotubes (SWNTs).

It is seen that photoelectrochemical performance of CdS thin films can be improved by increasing surface area or by post deposition treatment. Pandey and coworkers and Tiwari [34, 35] reported that polycrystalline CdS thin films show good photoelectrochemical behavior in a polysulphide electrolyte with high conversion efficiency and stability due to surface treatment.

The effect of Cd:S ratio on the photoconducting properties of CdS films have been reported by Jadhav et al. [36]. They chemically deposited CdS films with different Cd:S ratios and studied their electrical and structural properties. The photoconducting studies showed that the photoconductivity has been improved with Cd:S ratio as 1:0.2. Patil and co-workers [37] reported the enhancement in PEC performance due to effect of complexing agents. The air annealed CdS thin film with triethanolamine (TEA) and ammonia as complexing agents shows the better short circuit current. Hillal and co-workers [38] reported that by pre-annealing the electrode at 250°C followed by its slow cooling enhances the PEC performance of CdS thin film prepared by CBD. The electronic quality of chemical bath deposited CdS layers for photovoltaic solar cells was investigated by Chaure and co-workers [39]. The bath composition was 0.02 M CdCl<sub>2</sub>, 0.07 M NH<sub>4</sub>Cl and 0.14 M thiourea. The film thickness was found to be 0.1–0.2 μm after deposition of 15 minutes by maintaining the bath at pH 9.5 and temperature 90°C. Synthesis of flowerlike CdS nanostructured films have

been reported by Dongre and co-workers [40-41]. They studied their application in photoelectrochemical solar cells. A CBD technique has been used to grow CdS films over metal/glass substrates using precursors  $\text{CdSO}_4$ , thiourea and  $\text{NH}_4\text{OH}$ . They observed that the flower like morphology enhances the PEC properties as compare to planer morphology. Dongare et al. also reported nanowires like morphology of CdS thin films but with fewer short circuits current. It explains that, for the applications of solar energy harvesting and conversion, the morphology with complex nanostructures is more interesting.

## **5.2 Synthesis and characterization of Cadmium Sulphide thin films by chemical bath deposition (CBD).**

### **5.2.1 Preparation of CdS thin films by chemical bath deposition:**

All chemical were purchased from s. d. fine-chemicals and used without any further purification. The cadmium sulfate ( $\text{CdSO}_4 \cdot \text{H}_2\text{O}$ ) and thiourea ( $\text{H}_2\text{N} \times \text{CS} \times \text{NH}_2$ ) were used as cadmium (Cd) and sulphur (S) precursors. Ammonia ( $\text{NH}_3$ ) was used as complexing agent for the deposition of nanostructured CdS thin film.

Cadmium sulfide films were prepared from cadmium sulphate and thiourea by CBD in alkaline solution. The typical procedure for the film growth is described as follows. 25%  $\text{NH}_4\text{OH}$  solution was added drop wise into 500 ml beaker containing 150 ml of 1 mM  $\text{CdSO}_4$  solution until the initially formed white precipitate was dissolved completely. The cleaned substrates were mounted vertically in the bath using Teflon holder, such that the substrates were separated by 2 cm distance from each other & the wall of bath. Then 150 ml of 1mM thiourea [ $\text{CS} (\text{NH}_2)_2$ ] was added in the bath solution. The temperature was gradually increased to  $60^\circ\text{C}$  under magnetic stirring for all samples. The films removed from the bath after 20 min. were highly transparent and uniform with well adhesion to the glass substrate and therefore used for further characterization. The deposited CdS films were rinsed with double distilled water and alcohol and allowed to dry at room temperature, in ambient air. Figure 5.2 show the schematic diagram of experimental setup used for chemical bath deposition method for the preparation of Cadmium sulphide thin films.

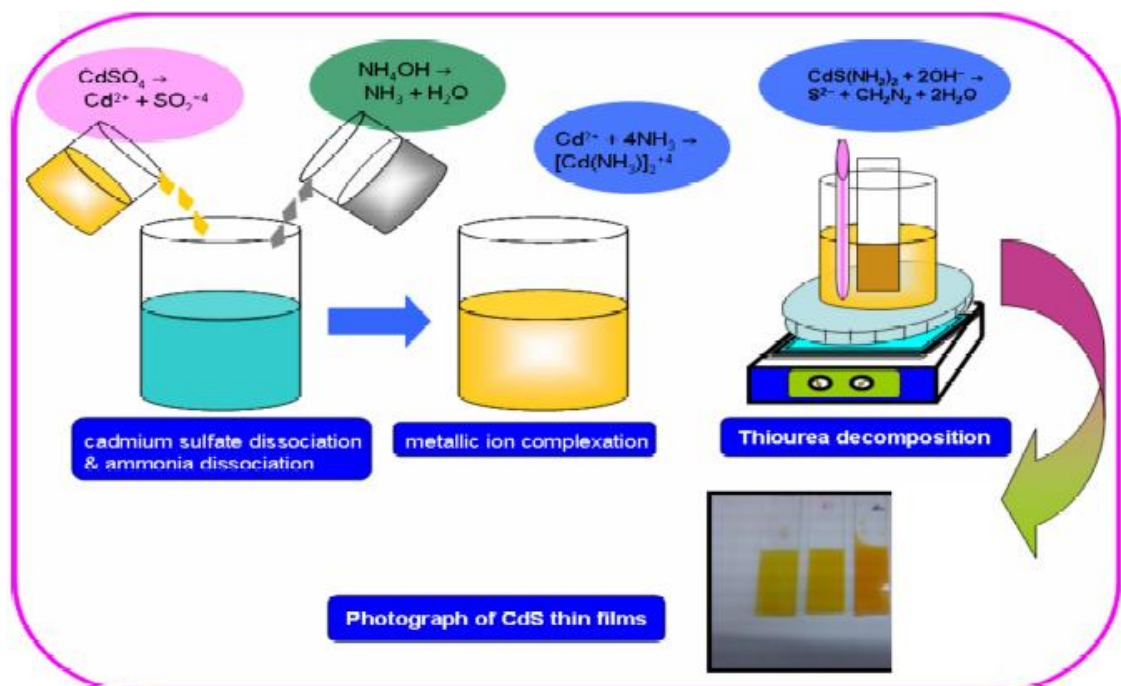
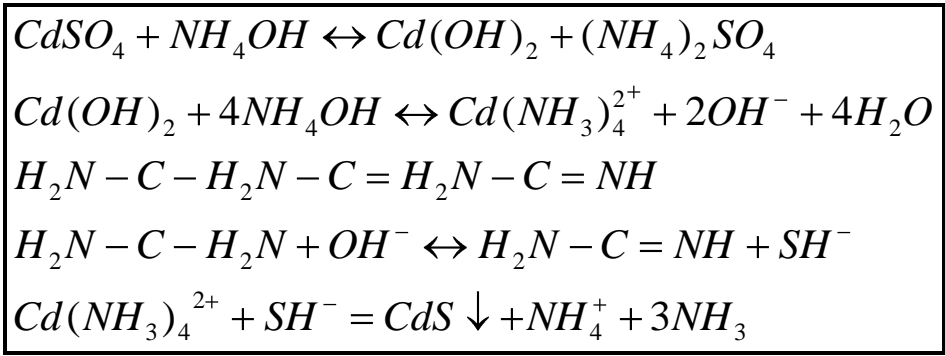
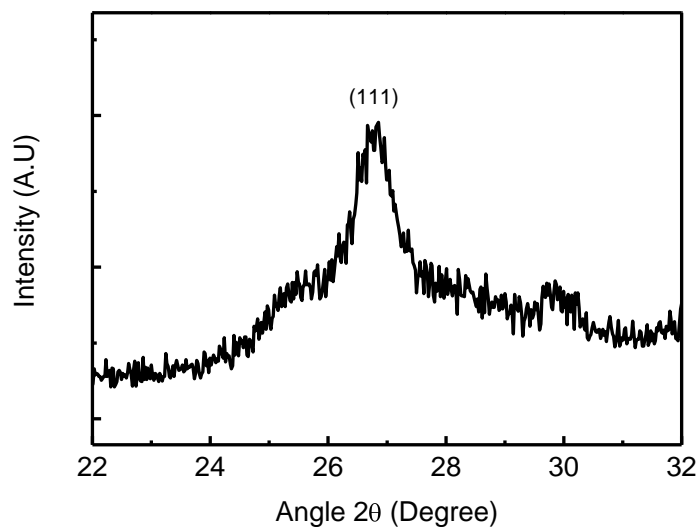
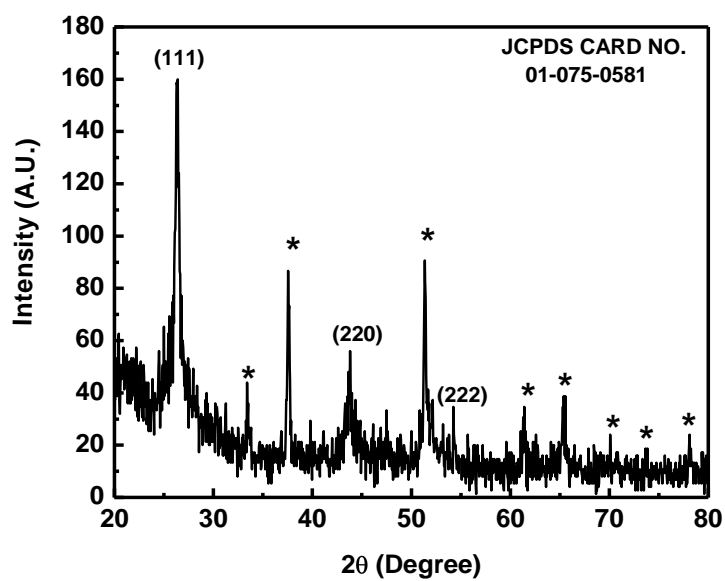


Figure 5.2 Schematic of Chemical Bath Deposition

### 5.2.2 X-ray Diffraction studies of CdS thin films Prepared by chemical bath deposition



**Figure 5.3 Enlarge view of XRD spectra of Cadmium Sulphide (CdS) thin film prepared on glass substrate by CBD method.**



**Figure 5.4 XRD spectra of Cadmium Sulphide (CdS) thin film prepared on FTO substrate by CBD method**

Figure 5.4 shows enlarge view of XRD spectra recorded for cds sample deposited on FTO (conducting Glass). Well defined reflections belonging to cds cubic structure along (111), (220), (311) planes were observed at angles  $26.5^\circ$ ,  $43.9^\circ$ ,  $52.8^\circ$  Figure5.5 shows XRD spectra recorded for CdS sample on glass, it is observed that the glass is having amorphous structure and the CdS (111) peak and glass hump exists at the same  $\theta$  values and therefore the intensity of (111) peak gets reduced.

### 5.2.3 Scanning electron Microscopy (SEM) studies of CdS thin films Prepared by chemical bath deposition

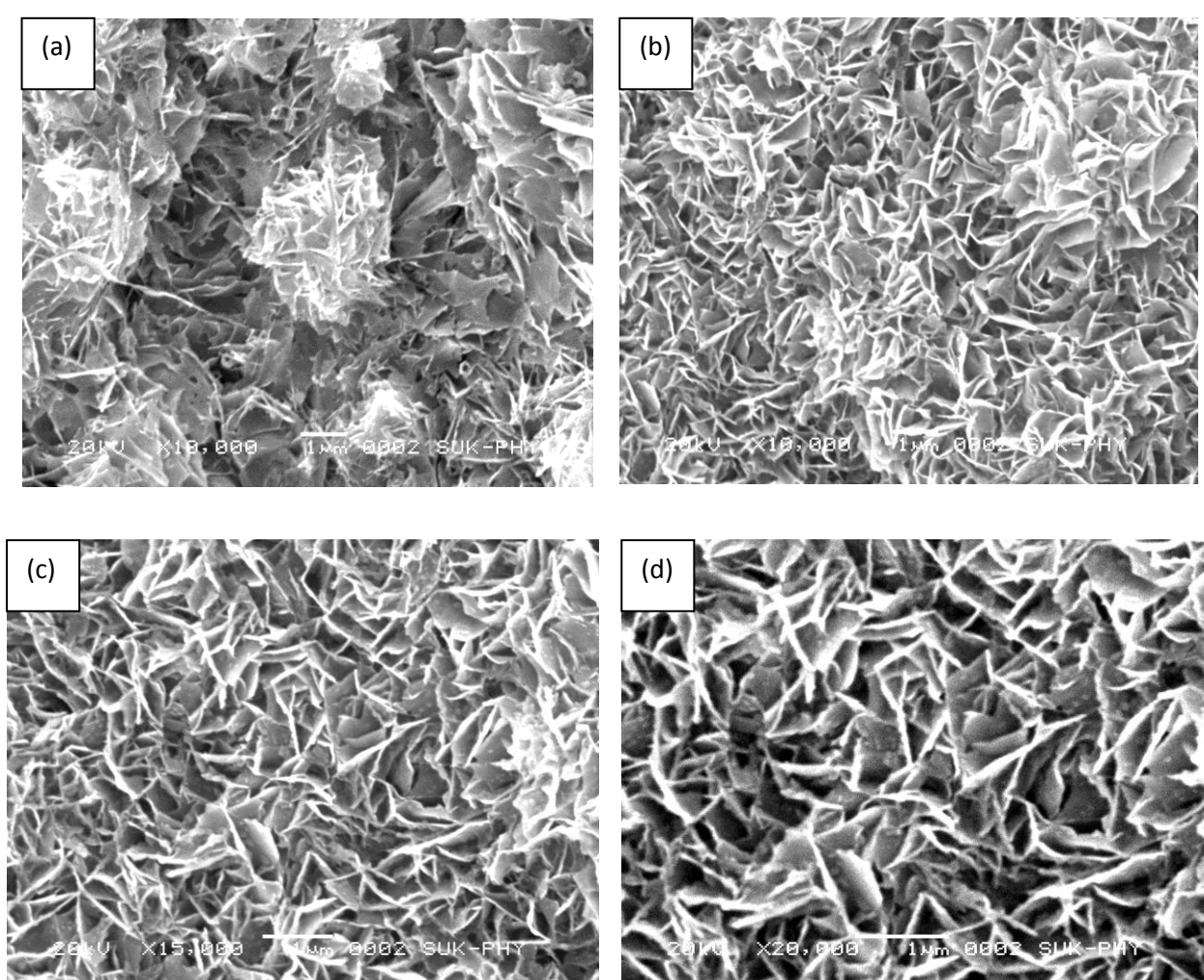


**Figure5.5 (a), (b), (C) and (d) Scanning Electron Microscopy (SEM) micrograph of Cadmium Sulphide (CdS) thin films prepared on glass by CBD method**

Figure 5.5 (a), (b), (C) and (d) shows scanning electron micrographs of CdS thin films prepared by CBD method. From figure it is clearly observed that the sample

exhibits nanocrystalline CdS platelets like morphology. At low magnification structure seems like cabbage. The density of these platelets is uniform throughout the sample. The platelets are having size of  $1\mu\text{m}$  and thickness 10-15 nm. The films are having throughout uniform structure and no cracks are observed in the film.

#### 5.2.4 UV-VIS absorption spectroscopy studies of CdS thin films prepared by chemical bath deposition

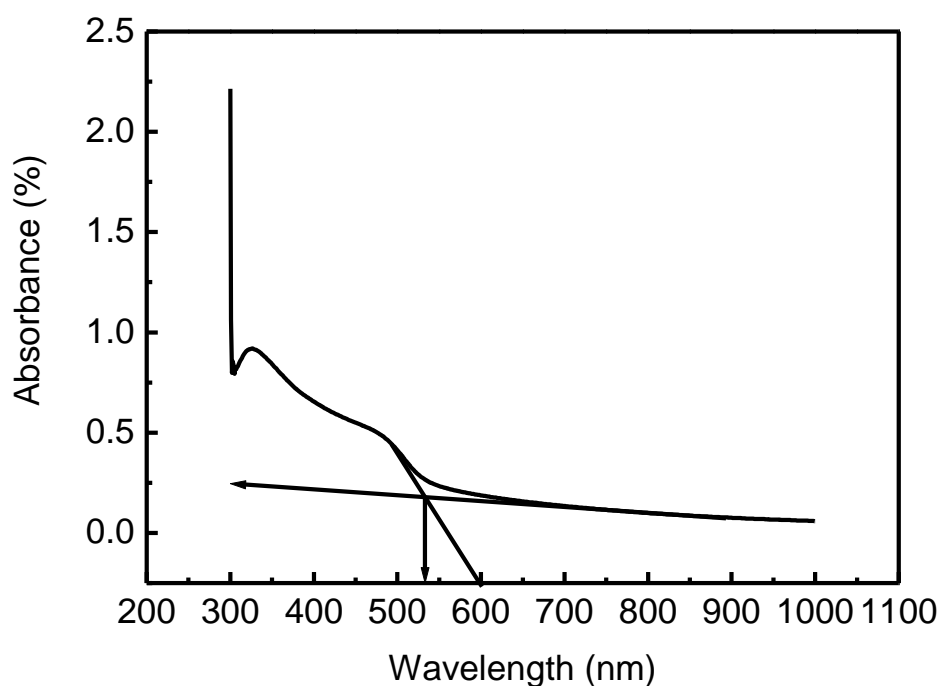


**Figure 5.6 UV-VIS absorption spectra of Cadmium Sulphide (CdS) thin films prepared on glass by CBD method**

Figure 5.6 shows absorption spectra recorded for CdS sample in the wavelength range 300 nm and 1000 nm. Figure clearly shows that the absorption initiates at 524 nm. This gives rise to band gap of  $\sim 2.36$  eV for CdS sample.

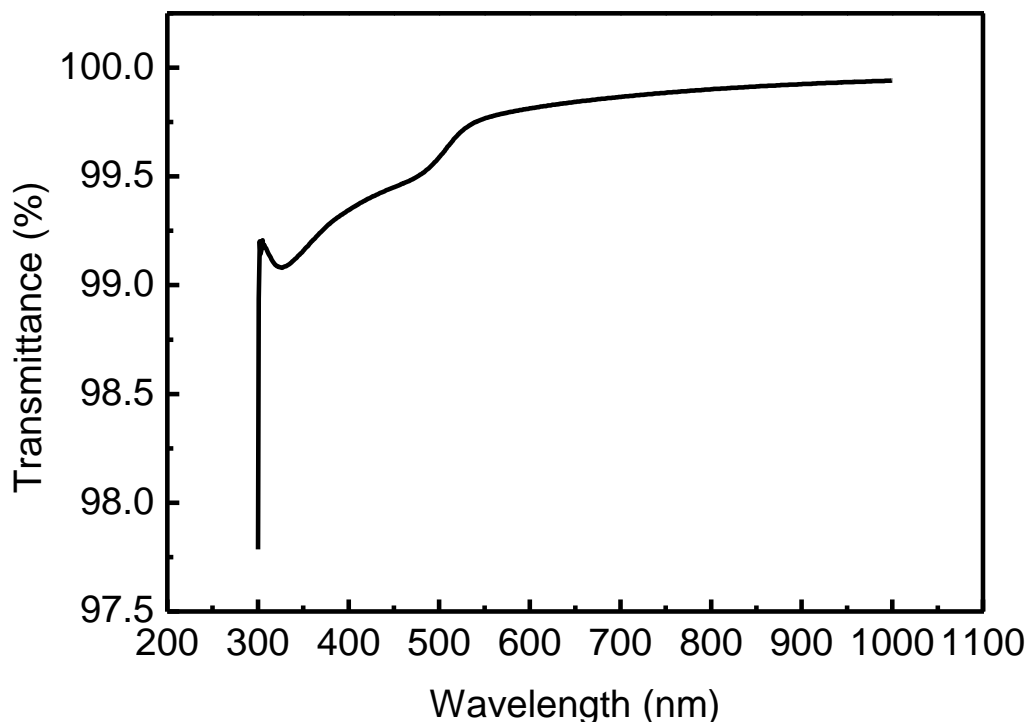


**Figure 5.7 UV-VIS transmission spectra of Cadmium Sulphide (CdS) thin films prepared on glass by CBD method**

Figure 5.7 shows transmission spectra recorded for CdS thin film in the wavelength range 300 nm and 1000 nm. From figure it is clearly observed that the transmittance of CdS film deposited by CBD method is approximately 99% above 400 nm.

### **5.3 Preparation of $Zn_2SnO_4$ /CdS thin films electrodes and their photoelectrochemical solar cell testing**

#### **5.3.1 Introduction**

Within last couple of years wide band gap semiconductors such as  $TiO_2$  and  $ZnO$  have shown remarkable enhancement in their photoelectrochemical (PEC) performance when coupled with low band gap chalcogenides such as CdS, CdTe, CdSe. The improvement in PEC performance is mainly attributed to extended visible light absorption which facilitates electron hole pair generation and charge injection into conduction band of host semiconductor. In the present work we investigate a new interesting system.

Because of wide band gap of 3.2 eV, TiO<sub>2</sub> nanotubes cannot absorb sunlight in the visible region efficiently. A hopeful solution to this difficulty is to use narrow band gap semiconductors along with TiO<sub>2</sub>. A care should be taken that, there should be alignment between energy band levels of TiO<sub>2</sub> with that of semiconductors which facilitates photoinduced electrons transfer to the collector electrode. In order to increase the photoelectric response of TiO<sub>2</sub>, semiconductors such as CdS [81–84], PbS [42, 46], Bi<sub>2</sub>S<sub>3</sub> [42, 47], CdSe [48, 49], CdTe [50, 51] and InP [52] have been extensively used in the visible region. It has been reported that CdS quantum dots(QDs)[44] and CdTe QDs[51] can be implemented into TiO<sub>2</sub> NTs and the performance of the TiO<sub>2</sub> NT array based photoelectrochemical [PEC] solar cell can be improved. Since cadmium chalcogenide semiconducting nanocrystals (CdX; X= S, Se and Te) belonging to II–VI semiconductors have size-tunable optical properties (Peng and Peng [53]; Bilgin *et al* [54]; Robel *et al* [55]), they can be used effectively as sensitizers for TiO<sub>2</sub>.

### **5.3.2 Preparation of Zn<sub>2</sub>SnO<sub>4</sub> thin films by spray pyrolysis technique,**

Cubic phase Zn<sub>2</sub>SnO<sub>4</sub> thin films were prepared by simple and inexpensive spray pyrolysis technique, using Stannic chloride (SnCl<sub>4</sub>.5H<sub>2</sub>O) and zinc Chloride as precursors of Sn and Zn respectively. The solvent used was de-ionized water. With a mole ratio of Zn: Sn as 2:1 the precursor salts were dissolved in DI water and further pneumatically sprayed over FTO coated glass substrates maintained at 400°C.

### 5.3.3 X-ray Diffraction Studies of Zinc Stannate ( $Zn_2SnO_4$ ) thin films

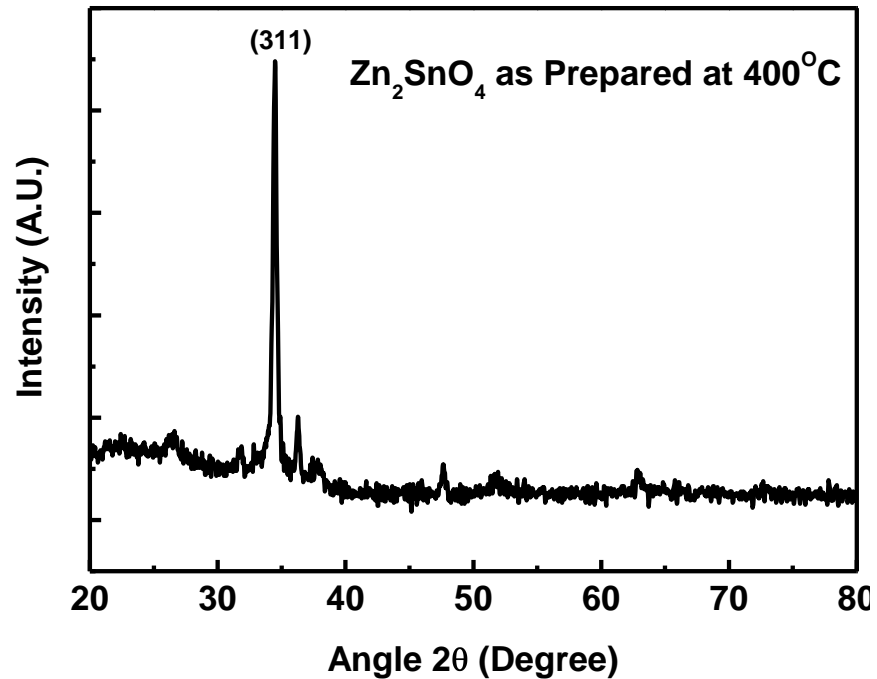


**Figure 5.8 XRD spectra of as prepared  $Zn_2SnO_4$  thin film at 400°C**

Figure 5.8 shows XRD pattern of as  $Zn_2SnO_4$  prepared thin film at 400°C . The existence of well defined reflection along (311) plane at  $2\theta = 34.3^\circ$  and well matching of  $2\theta$  and 'd' values with JCPDS card No. 73-1725 depicts the formation of phase pure  $Zn_2SnO_4$  thin film with cubic face centered crystal structure

### 5.3.4 Scanning electron microscopy (SEM) studies of $Zn_2SnO_4$ thin film electrodes

Figure 5.9 shows the scanning electron micrograph (SEM) of as deposited  $Zn_2SnO_4$  thin film at 400°C (at different magnifications). From the figure it is clear that film surface is smooth crack free and few small crystallites are observed on the surface of film.

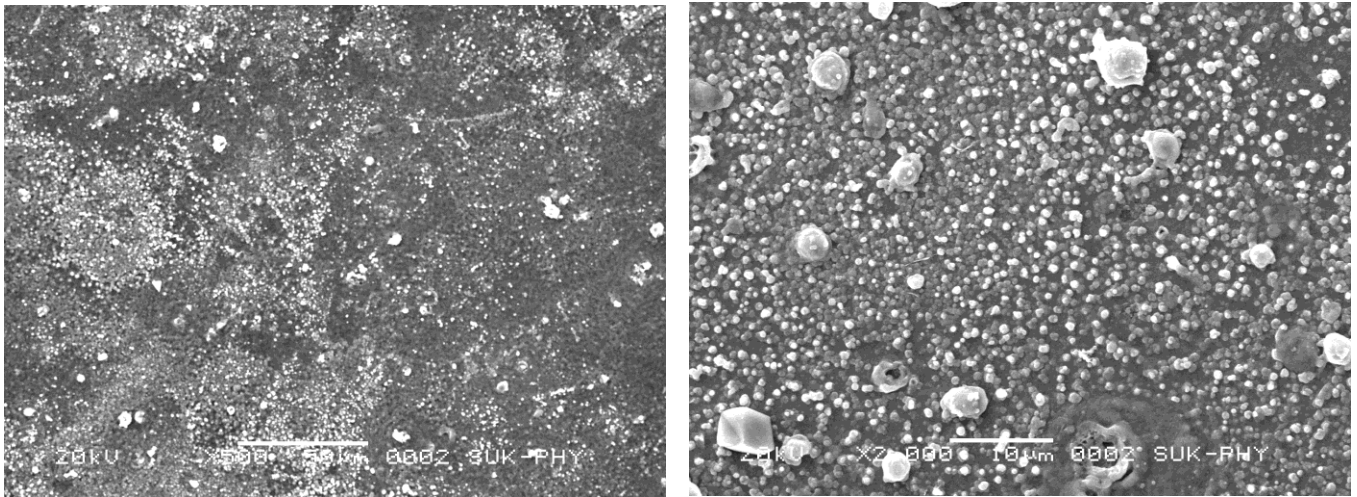


**Figure 5.9 Scanning electron micrograph (SEM) images of as prepared  $Zn_2SnO_4$  thin film at different magnifications.**

### 5.3.5 UV-VIS absorption studies of $Zn_2SnO_4$ thin film electrodes

The band gap energy of  $Zn_2SnO_4$  thin film was calculated from UV-VIS absorption measurement. The estimated value of band gap of  $Zn_2SnO_4$  is 3.8 eV. [From figure 5.10.]

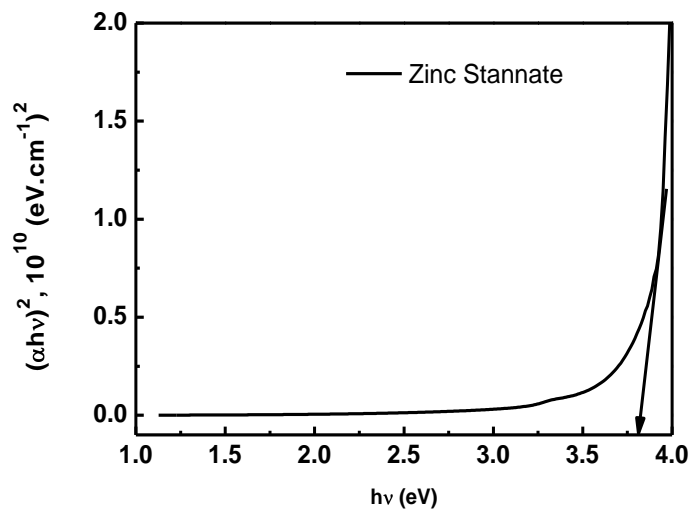


**Figure 5.10 UV-VIS optical absorption spectrum for the  $Zn_2SnO_4$  thin film.**

### 5.3.6 Preparation of $Zn_2SnO_4$ /CdS thin films electrodes

The as prepared (5.3.4)  $Zn_2SnO_4$  electrodes were coated by

nanocrystalline CdS using chemical bath deposition. The thickness of the CdS coating on the glass was varied by removing the samples at the increased interval of 15 min. The photoelectrochemical properties of the samples coated for 15, 30 and 45 min have been studied. Here after the samples are referred as S<sub>1</sub>, S<sub>2</sub> and S<sub>3</sub> respectively.

### 5.3.7 X-ray diffraction studies of Zn<sub>2</sub>SnO<sub>4</sub>/CdS thin films electrodes

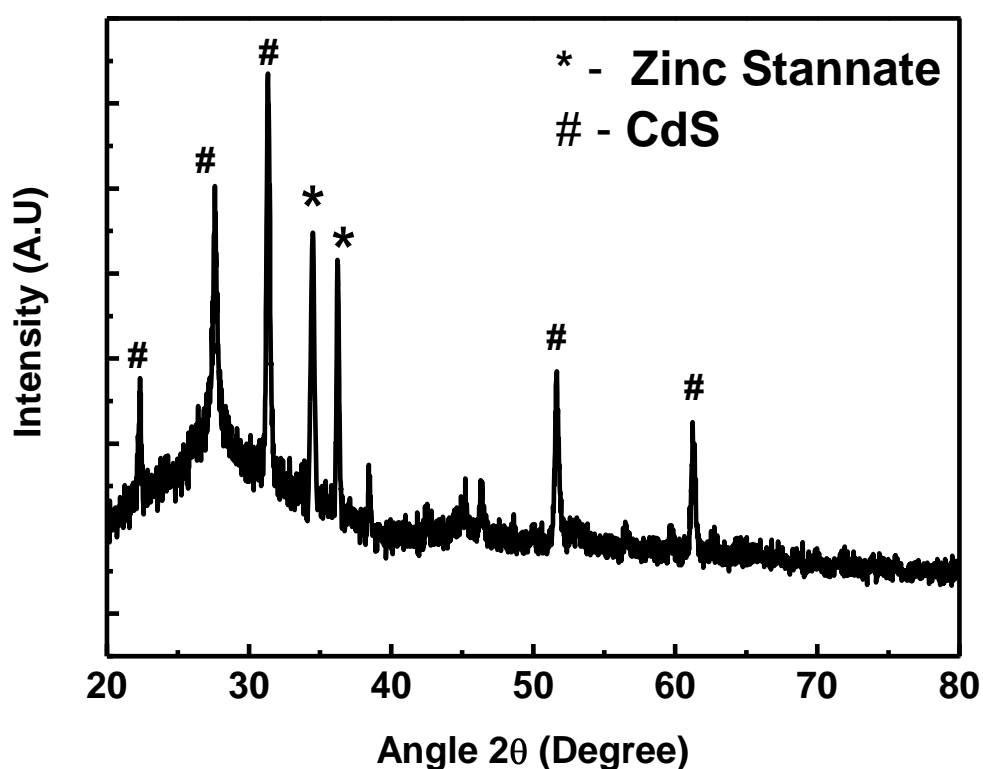


**Figure 5.11 Shows XRD spectra for Zn<sub>2</sub>SnO<sub>4</sub>/CdS thin film**

Figure 5.11 Shows XRD spectra for Zn<sub>2</sub>SnO<sub>4</sub>/CdS thin film. The spectra shows X-ray reflection peaks at angles ( $2\theta$ ), 25.25°, 27.5°, 51.8° and 61.26° with planes(100), (101), (112) and (104). The well matching of observed ' $2\theta$ ' values and typical values from JCPDS file no. 01-080-0006 confirms CdS cubic phase. The existence of well defined reflection along (311) and (222) plane at  $2\theta = 34.3^\circ$  and  $36.1^\circ$  and well matching of  $2\theta$  and 'd' values with JCPDS card No. 73-1725 depicts the formation of phase pure Zn<sub>2</sub>SnO<sub>4</sub> thin film with face centered cubic crystal structure.

### 5.3.8 Scanning electron microscopy (SEM) studies of $Zn_2SnO_4/CdS$ thin film electrodes

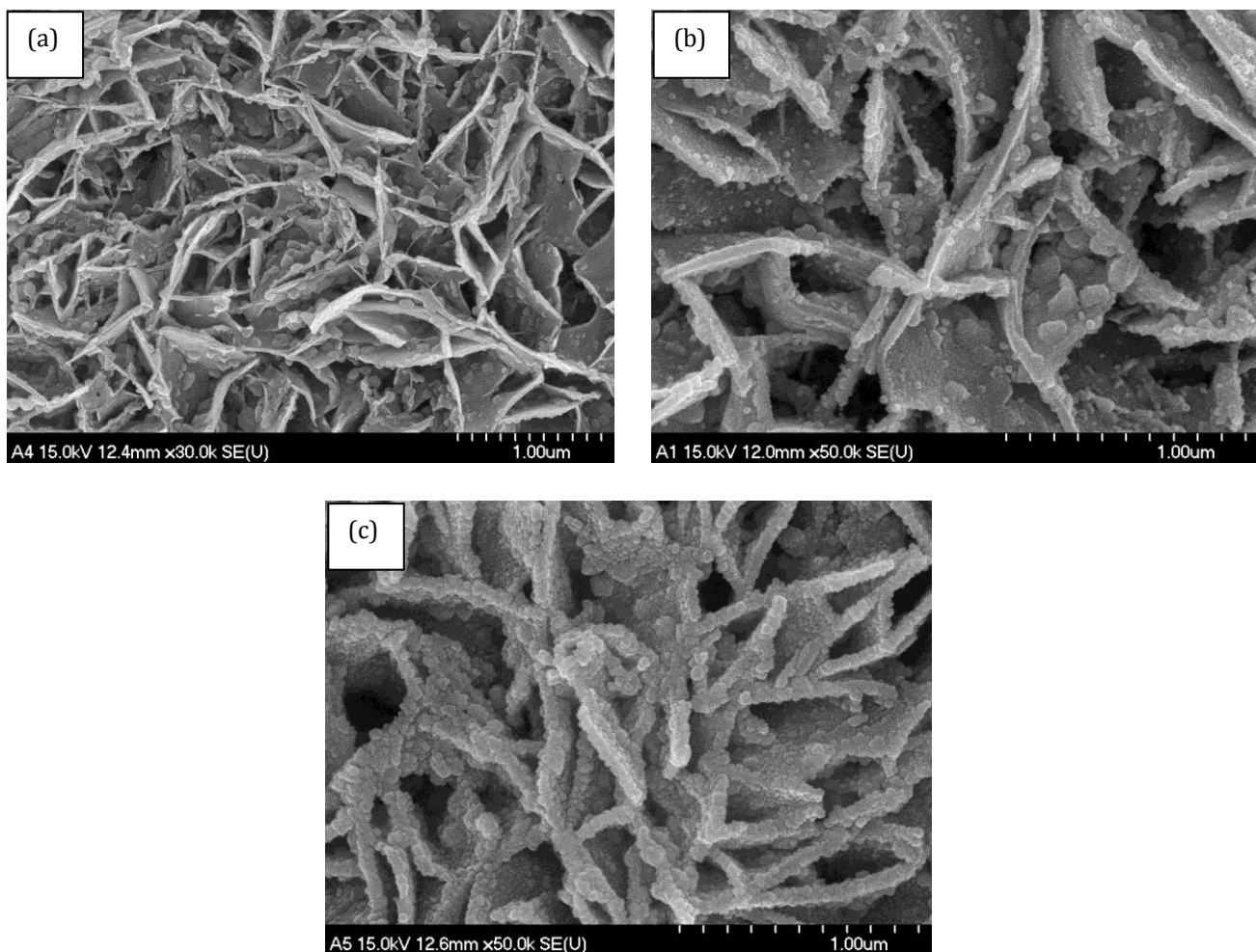


**Figure 5.12 (a), (b) and (c) FESEM micrographs of  $Zn_2SnO_4/CdS$  thin film samples  $S_1$ ,  $S_2$  and  $S_3$  respectively.**

Figure 5.12 represents FESEM micrographs for samples  $S_1$ ,  $S_2$  and  $S_3$  respectively. Figure clearly shows that all the three samples exhibit nanocrystalline structure with platelet like morphology. An approximate platelet thickness of 10-15 nm is observed for Sample  $S_1$  while for Sample  $S_2$ , it is 40-50 nm with some budlike agglomerates initiated over these platelets.

### 5.3.9 UV-VIS absorption studies of $Zn_2SnO_4/CdS$ thin film electrodes

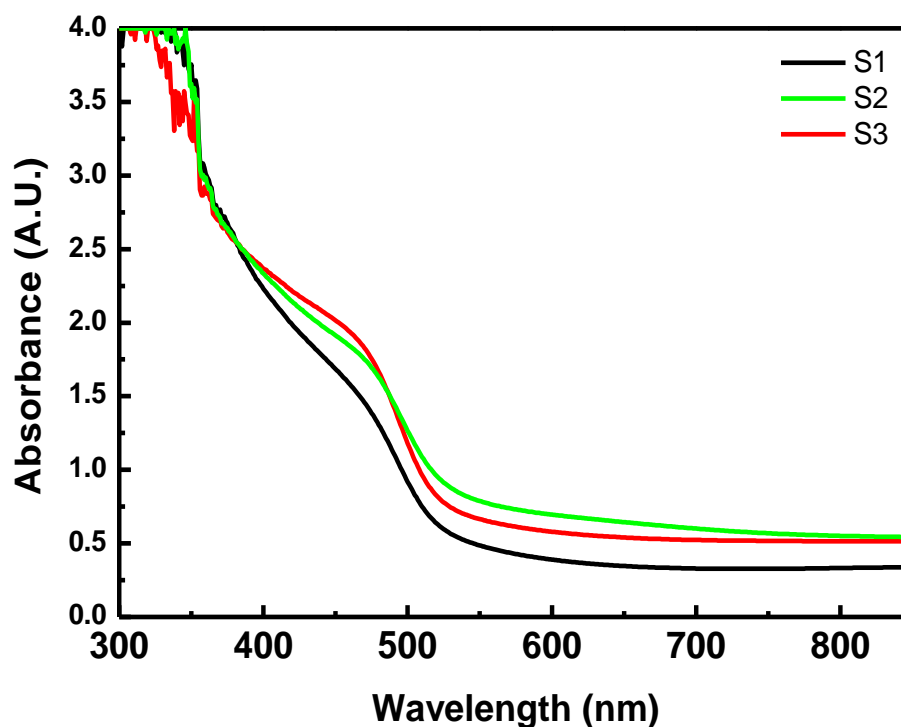


**Figure 5.13 UV-VIS absorption spectra recorded for  $Zn_2SnO_4$ -CdS thin film samples  $S_1$ ,  $S_2$  and  $S_3$ .**

Figure 5.13 shows UV-VIS absorption spectra of  $Zn_2SnO_4$ -CdS sample. From figure it is clearly observed that the absorption edges are seen for all these samples. One of them is at higher wavelength around 500 nm which belongs to absorption due to CdS and the other is at lower wavelength at around 350 nm which belongs to absorption due to bottom  $Zn_2SnO_4$ . With increasing thickness from sample  $S_1$  to  $S_3$ , absorption due to CdS is also increased and it is analogous to observations made by SEM.

#### 5.4 Photoelectrochemical characterization

For the PEC measurement, a three electrode system was used which consists of a working electrode (CdS coated  $Zn_2SnO_4$  film), a counter electrode (platinum foil) and Ag/AgCl as a reference electrode. To sweep the voltage across working and counter electrode, An Autolab PGSTAT 30-ECO-

Chemie instrument was used at scanning rate of 10 mV/S and the current measurement was made in dark and under 1 Sun (AM 1.5 condition using Newport solar simulator) illumination. The electrolyte used was prepared by combination of 0.24 M Na<sub>2</sub>S and 0.35 M Na<sub>2</sub>SO<sub>3</sub>.

#### 5.4.1 Result of photoelectrochemical measurements

Figures 5.14, 5.15(a, b) and 5.16(a, b) represents J-V characteristic for S<sub>1</sub>, S<sub>2</sub> and S<sub>3</sub> samples measured using a standard three electrode system under AM 1.5 xenon arc lamp. Photocurrent densities for all the samples under chopping are also measured S<sub>1</sub>, S<sub>2</sub> and S<sub>3</sub> respectively. The dark current densities values 1.4, 16 and 20 μA/cm<sup>2</sup> were noted for samples S<sub>1</sub>, S<sub>2</sub> and S<sub>3</sub> correspondingly. Sample S<sub>1</sub>, S<sub>2</sub> and S<sub>3</sub> exhibits photocurrent densities 0.782, 1.22 and 1.71 mA/cm<sup>2</sup> respectively at -0.2 V versus Ag/AgCl as a reference electrode. The equation for calculating applied bias photon to current efficiency (ABPE) is

$$ABPE = \left[ \frac{J_{ph} \left[ \frac{mA}{cm^2} \right] \times (1.23 - |V_b|) [V]}{P_{total} \left[ \frac{mW}{cm^2} \right]} \right]$$

where  $J_{ph}$  is the photocurrent density obtained under an applied bias  $V_b$  between the working and counter electrodes and  $P_{total}$  is incident light intensity (100 mW/cm<sup>2</sup>). The sample S<sub>1</sub> shows ABPE value 0.008% whereas it increases upto 0.012 and 0.017% for sample S<sub>2</sub> and S<sub>3</sub>. The observed increase in ABPE values can be attributed to increase in absorber thickness with respect to increase in CdS coating time, which improves number of photo-generated charge carriers.

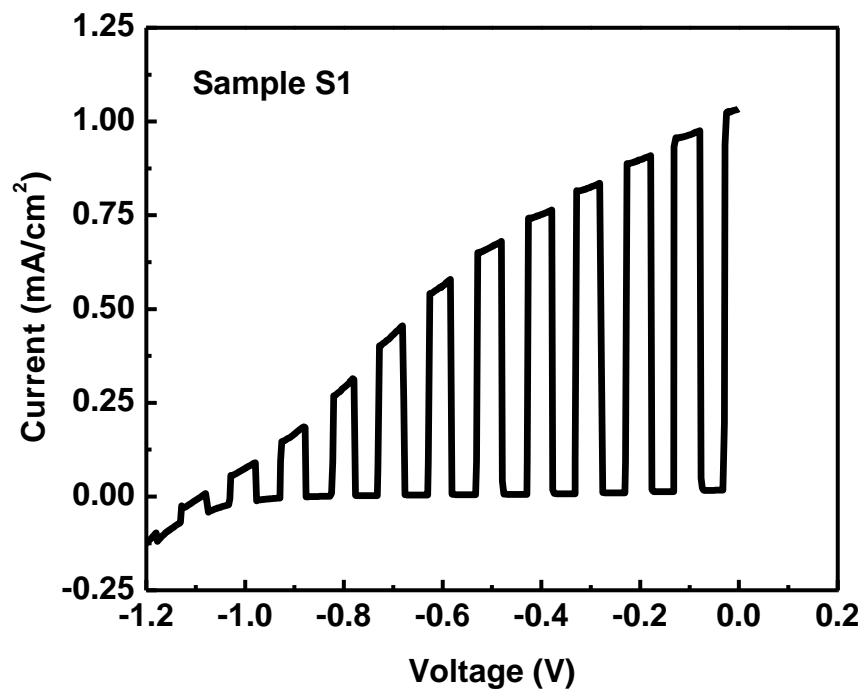
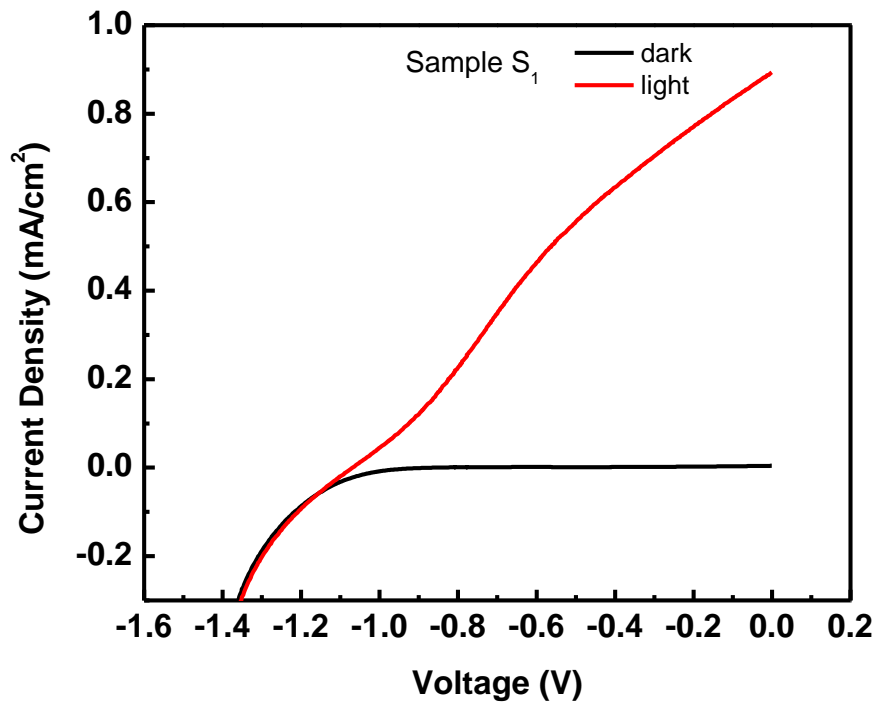


Figure 5.14 (a) J-V characteristic for sample  $S_1$  in dark and under illumination by AM 1.5 xenon arc lamp (b) J-V characteristic with chopping.

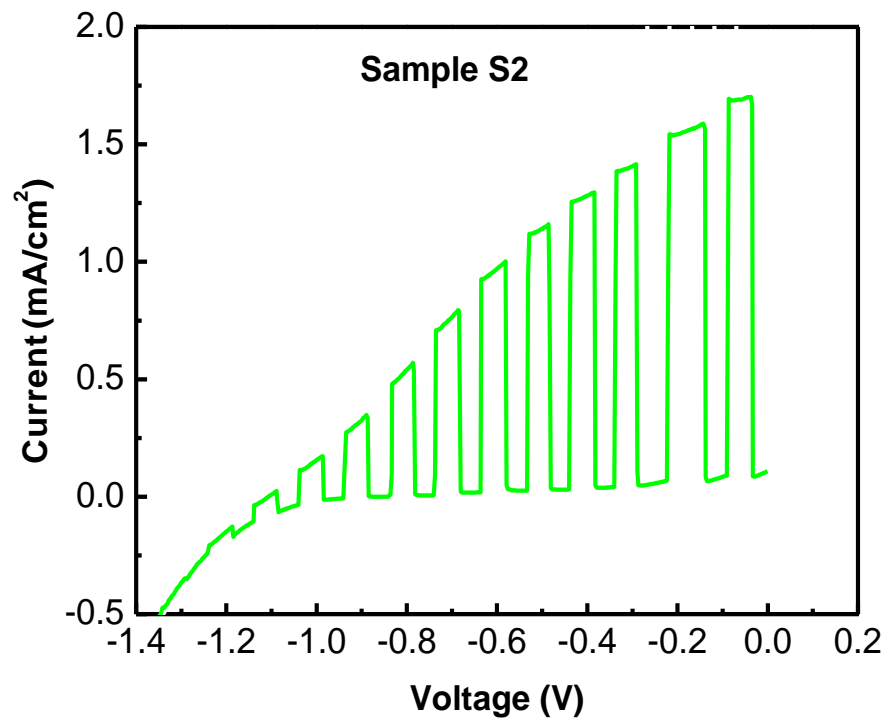
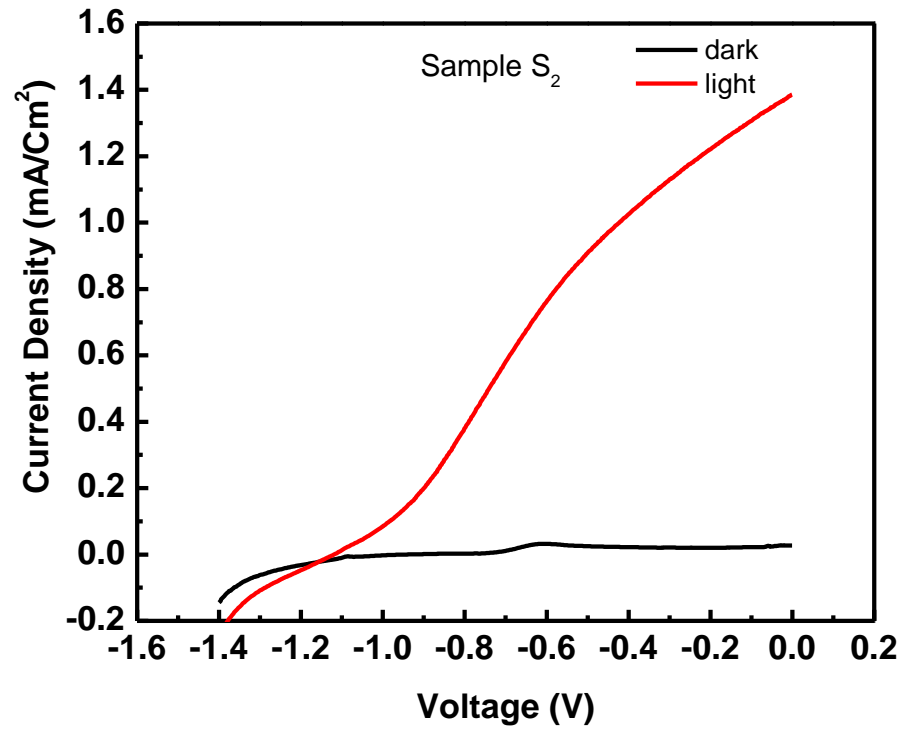
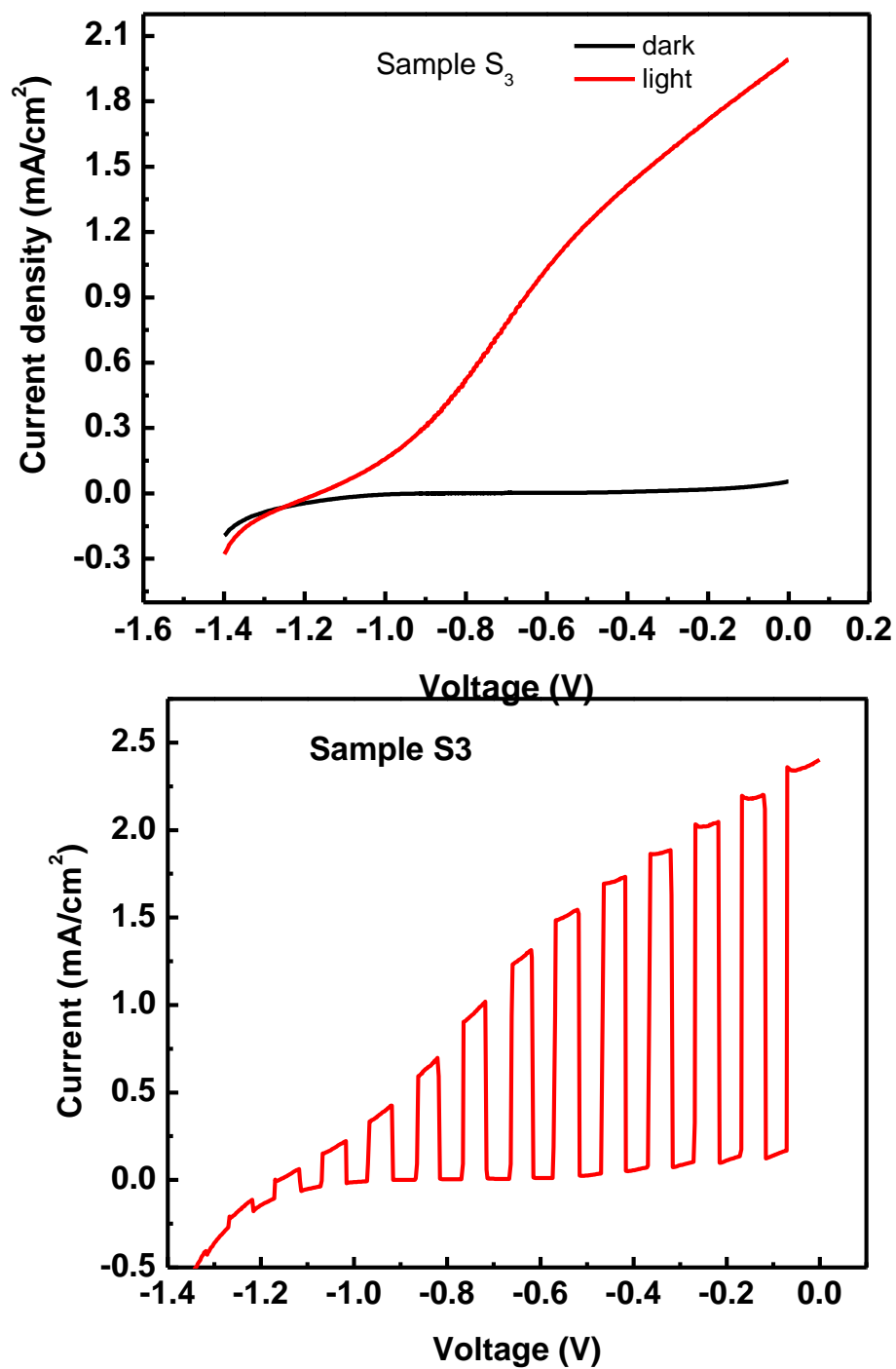


Figure 5.15 (a) J-V characteristic for sample S<sub>2</sub> in dark and under illumination by AM 1.5 xenon arc lamp (b) J-V characteristic with chopping.



**Figure 5.16 (a) J-V characteristic for sample S<sub>3</sub> in dark and under illumination by AM 1.5 xenon arc lamp (b) J-V characteristic with chopping.**

The stability of Zn<sub>2</sub>SnO<sub>4</sub>/CdS photoanodes was studied by potentiostatic [current (I) vs time (t)] measurement by chopping the illuminated light at -0.2 V

Vs Ag/AgCl electrode. Figure shows photoresponse curves of  $Zn_2SnO_4/CdS$  electrodes ( $S_1$ ,  $S_2$  and  $S_3$ ), the photocurrent values increases as soon as the electrode is illuminated and decreases to zero when the illumination is blocked by the shutter. Figure 5.17 shows overlay of J-V characteristics for samples  $S_1$ ,  $S_2$  and  $S_3$ . The prompt switching of current under illumination indicates rapid charge transport in all the three photoelectrodes. The non-decayed photocurrent densities up to 300 sec. illuminations also prove higher stability of all the samples in the electrolyte (figure 5.18)

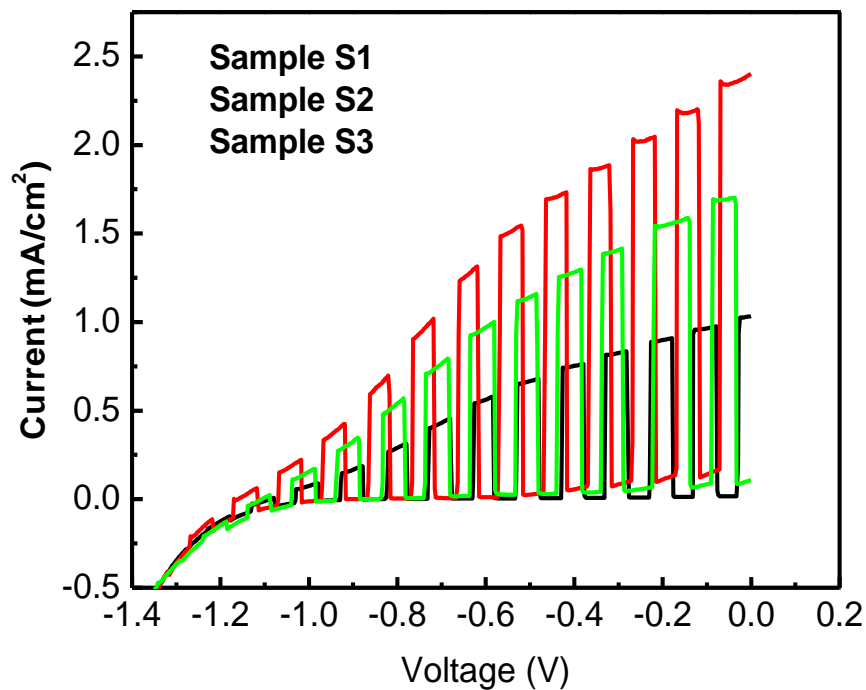


**Figure 5.17 (a) J-V characteristic for sample  $S_1$ ,  $S_2$ ,  $S_3$  in dark and under illumination by AM 1.5 xenon arc lamp (b) J-V characteristic with chopping.**

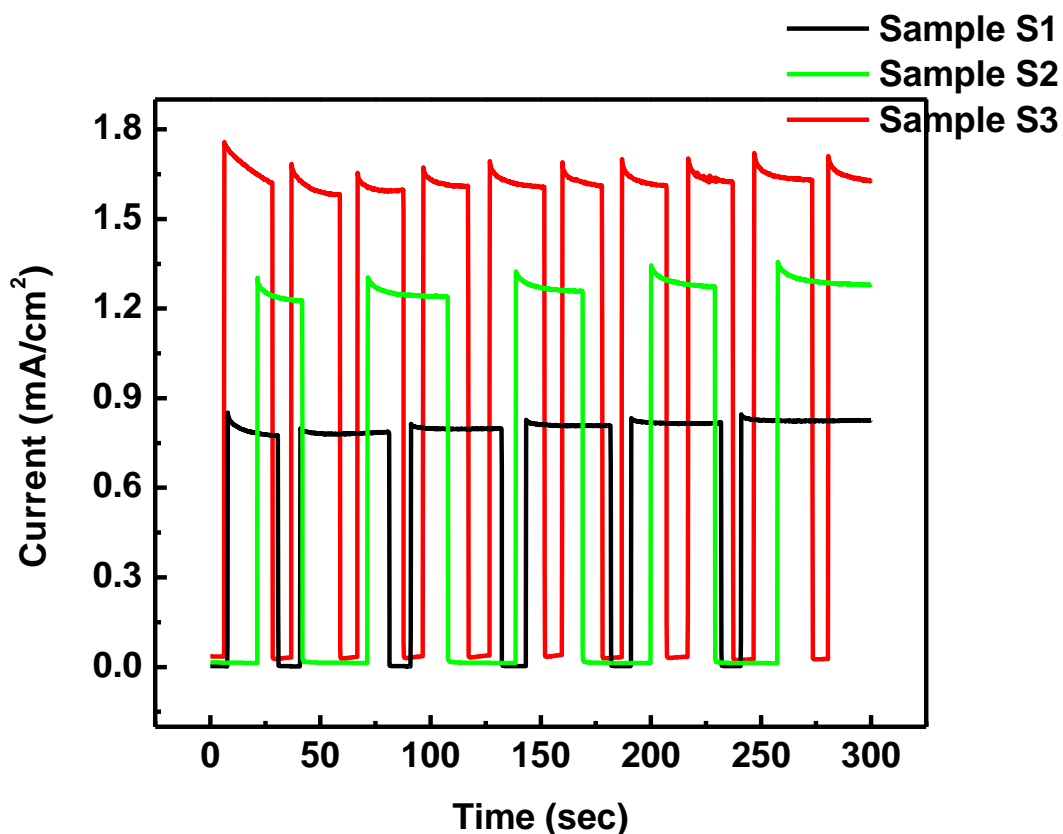


**Figure 5.18 Transient photo-responses of  $Zn_2SnO_4/CdS$  thin films**

### 5.5 conclusions

The zinc stannate thin films were prepared on FTO coated glass substrate using stannic chloride and Zinc chloride with mole ratio of Zn:Sn as 2:1 at 400 °C by spray pyrolysis method. The phase purity of  $Zn_2SnO_4$  thin film was confirmed by XRD pattern. The as prepared  $Zn_2SnO_4$  electrodes were coated with nanocrystalline CdS using chemical bath deposition method. The XRD pattern confirmed formation of CdS/  $Zn_2SnO_4$ . The thickness of the CdS coating was increased by increasing deposition time to study their effect on PEC performance. The PEC performance was studied by using three electrode configurations. The applied bias to photon to current efficiency increases with increase in the thickness of CdS coating, alternately coating time of CdS. The potentiostatic measurements of CdS/  $Zn_2SnO_4$  photoanode confirmed their stability in the electrolyte.

## References

- [1] X. Mathew, G. W. Thompson, V. P. Singh, J. C. McClure, S. Velumani, Mathews, N. R., Sebastian, P. J. *Sol. Energy Mater. Sol. Cells* 76 (2003) 293.
- [2] S. Kutzmutz, G. Lang, K. E. Heusler, *Electrochimica Acta*, 47 (2001) 955.
- [3] C. Shen, X. Zhang, H. Li, *Mater. Sci. Eng. B*, 84 (2001) 265.
- [4] M. Soliman, A. B. Kashyout, M. Shabana, M. Elgamal, *Semi. Renew. Energy*, 23 (2001) 471
- [5] R. K. Sharma, G. Singh, A. C. Rastogi, *Sol. Energy Mater. Sol. Cells*, 82 (2004) 201
- [6] Y. J. Chang, C. L. Munsee, G. S. Herman, J. F. Wager, P. Mugdur, D.-H. Lee and C.-H. Chang, *Surf. Interface Anal*, 37 (2005) 398.
- [7] J. E. Reynolds, *J. Chem. Soc.*, 45 (1984) 162.
- [8] K. L. Chopra, R. C. Kainthla, D. K. Pandya, A. P. Thakoor, In *Physics of Thin Films*, Academic Press: New York, 11 (1982) 167.
- [9] C. D. Lokhande, *Mater. Chem. Phys.*, 28 (1991) 1.
- [10] D. Lincot, M. Froment, H. Cachet, In *Advances in Electrochemical Science Engineering*, Alkire RC, Kolb DM (eds), Wiley-VCH: New York, 6 (1998) 165
- [11] P. K. Nair, MTS Nair, V. M. Garcia, O. L. Arenas, Y. Pena, A. Castillo, I.T. Ayala, O. Gomez-daza, A. Sanchez, J. Campos, H. Hu, R. Suarez, M. E. Rincon, *Sol. Energy Mater. Sol. Cells*, 52 (1998) 313.
- [12] O. Savadogo, *Sol. Energy Mater. Sol. Cells*, 52 (1998) 361.
- [13] J. Kaur, D. K. Pandya, K. L. Chopra, *J. electrochemistry*, 48 (1980) 127.
- [14] D. K. Pandya, K. L. Chopra, *Academic Press: New York*, (1980).
- [15] S. Mokrushin, Y. Tkachev, *Kolloidn Z* 23 (1961) 438
- [16] G. Kitaev, A. Uritskaya, S. Mokrushin, *Russ. J. Phys. Chem.*, 39 (1965)
- [17] H. R. Moutinho, D. Albin, Y. Yan, R. G. Dhere, X. Li, C. Perkins, C. S. Jiang, *Thin Thin Solid Films*, 436 (2003) 175.
- [18] K.L.Chopra, P.D.Paulson, V.Dutta, *Prog. Photovolt. Res. Appl.*, 12 (2004) 69.
- [19] L.Bruss, *J. Phys. Chem.*, 90 (1986) 2560.
- [20] A. J. Nozik, F. Williams, M. T. Nenadovic, T. Rajh, and O. I. MiCiE, *J. Phys. Chem.*, 89 (1985) 397.

- [21] Torimoto, T. Nagakubo, S. Nishizawa, M. Yoneyama, *Langmuir*, 14 (1998) 7077.
- [22] T. Vossmeier, L. Katsikas, M. Gienig, I. G. Popovic, K. Diesner, A. Chemseddine, A. Eychmiiller, and H. Weller, *J. Phys. Chem.*, 98 (1994) 7665.
- [23] K. K. Nanda, S. N. Sarangi and S. N. Sabu, *Nanostr. Mat.*, 10-8 (1988) 1401.
- [24] K. Yao, S. Nishimura, T. Ma, K. Inoue, E. Abe, H. Tateyama, A. Yamagishi, *Eng. Aspects*, 201(2002) 63.
- [25] K. B. Jinesh, K. C. Wilson, S. V. Thampi, C. S. Kartha, K. P. Vijaykumar, T. Abe, Y. Kashiwaba, *Physica A*, 19 (2003) 303.
- [26] K. Senthil, D. Mangalaraj, S. K. Narayandass, *Appl. Surf. Sci.*, 169/170(2001) 476.
- [27] T. Kippeny, L. A. Swafford, S. J. Rosenthal, *J. Chem. Edu.*, 79 (2002) 1094.
- [28] F. Antolini, M. Pentimalli, T. Di Luccio, R. Terzi, M. Schioppa, M. Re L. Mirengi, L. Tapfer, *Mater. Lett.*, 59 (2005) 3181.
- [29] H. Wang, P. Fang, Z. Chen, S. Wang, *Appl. Surf. Sci.*, 253 (2007) 8495.
- [30] J. X. Yao, G. L. Zhao, D. Wang, G. R. Han, *Mater. Lett.*, 59 (2005) 3652.
- [31] D. Wu, X. Ge, Z. Zhang, M. Z. Wang, S. L. Zhang, *Langmuir*, 20 (2004) 5192.
- [32] Z. Qian, H. J. Bai, G. L. Wang, J. J. Xu, H. Y. Chen, *Biosensors and Bioelectronics*, 25 (2010) 2045.
- [33] S. H. Hwang, C. N. Moorefield, P. Wang, K. U. Jeon, S. Z. D. Cheng, K. Kotta, and G. R. Newkome, *J. Am. Chem. Soc.*, 128 (2006) 7505.
- [34] R. K. Pandey, S. Mishra, S. Tiwari, P. Sahu, B. P. Chandra, *Sol. Energy Mater. Sol. Cells*, 60 (2000) 59.
- [35] S. Tiwari, S. Tiwari, *Sol. Energy Mater. Sol. Cells*, 90 (2006) 1621
- [36] U. S. Jadhav, S. Kale, C. D. Lokhande, *Mater. Chem. Phys.*, 69 (2001) 12.
- [37] S. B. Patil, A. K. Singh, *Appl. Surf. Sci.*, 256 (2010) 2884.
- [38] H. S. Hilal, R. M. A. Ismail, A. El-Hamouz, A. Zyouda, I. Saadeddin, *Electrochim. Acta*, 54 (2009) 3433.
- [39] N. B. Chaure, S. Bordas, A. P. Samantilleke, S. N. Chaure, J. Haigh, I. M. Dharmadasa, *Thin Solid Films*, 437 (2003) 10.
- [40] J. K. Dongre, M. Ramrakhiani, *J. Alloy and Comp.*, 487 (2009) 653.
- [41] J. K. Dongre, V. Nogriva, M. Ramrakhiani, *Appl. Surf. Science*, 255 (2009) 6115.

- [42] R. Vogel, P. Hoyer, and H. Weller, *J. Phys. Chem.*, 98(1994) 3183.
- [43] S. C. Lin, Y. L. Lee, C. H. Chang, Y. J. Shen, and Y. M. Yang, *Appl. Phys. Lett.* 90 (2007) 143517.
- [44] W. T. Sun, Y. Yu, H. Y. Pan, X. F. Gao, Q. Chen, and L. M. Peng, *J. Am. Chem. Soc.* 130, 1124 2008.
- [45] S. Banerjee, S. K. Mohapatra, P. P. Das, and M. Misra, *Chem. Mater.* 20(2008) 6784.
- [46] R. Plass, S. Pelet, J. Krueger, and M. Gratzel, *J. Phys. Chem. B* 106(2003) 7578
- [47] L. M. Peter, K. G. U. Wijayantha, D. J. Riley, and J. P. Waggett, *J. Phys. Chem. B* 107(2003) 8378.
- [48] Q. Shen, T. Sato, M. Hashimoto, C. Chen, and T. Toyoda, *Thin Solid Films* 499(2006) 299.
- [49] I. Robel, V. Subramanian, M. Kuno, and P. V. Kamat, *J. Am. Chem. Soc.* 128 (2006) 2385.
- [50] J. A. Seabold, K. Shankar, R. H. T. Wilke, M. Paulose, O. K. Varghese, C. A. Grimes, and K. S. Choi, *Chem. Mater.* 20 (2008) 5266.
- [51] X. F. Gao, H. B. Li, W. T. Sun, Q. Chen, F. Q. Tang, and L. M. Peng, *J. Phys. Chem. C* 113 (2009)7531.
- [52] A. Zaban, O. I. Micic, B. A. Gregg, and A. J. Nozik, *Langmuir* 14 (1998) 3153.
- [53] Z. A. Peng and X. Peng *J. Am. Chem. Soc.* 123(2001). 183
- [54] V. Bilgin, S. Kose, F. Atay and I. Akkyuz *Mater. Chem. Phys.* 94 (2005) 103 .
- [55] I. Robel, M. Kuno , P. V. Kamat *J. Am. Chem. Soc.* 129(2007) 4136.

## Chapter V

### Photoelectrochemical Properties of $Zn_2SnO_4$ /CdS Thin Films

#### 5.1 Introduction.

5.1.1. Construction of PEC solar cell.

5.1.2. Requirements of PEC cells.

5.1.3 Survey of literature on Cadmium sulphide (CdS).

#### 5.2. Synthesis and characterization of Cadmium Sulphide thin films by chemical

##### bath deposition (CBD).

5.2.1. Preparation of CdS thin films by chemical bath deposition.

5.2.2. X-ray Diffraction studies of CdS thin films Prepared by chemical bath deposition.

5.2.3 Scanning electron microscopy (SEM) studies of CdS thin films prepared by chemical bath deposition.

5.2.4. UV-VIS absorption spectroscopy studies of CdS thin films Prepared by chemical bath deposition.

#### 5.3. Preparation of $Zn_2SnO_4$ /CdS thin films electrodes and their photoelectrochemical solar cell testing.

5.3.1. Introduction

5.3.2. Preparation of  $Zn_2SnO_4$  thin films by spray pyrolysis technique.

5.3.3. X-ray Diffraction Studies of Zinc Stannate ( $Zn_2SnO_4$ ) thin films.

5.3.4. Scanning electron microscopy (SEM) studies of  $Zn_2SnO_4$  /CdS thin film electrodes.

5.3.5. UV-VIS absorption studies of  $Zn_2SnO_4$  thin film electrodes.

5.3.6. Preparation of  $Zn_2SnO_4$ /CdS thin films electrodes.

5.3.7. X-ray diffraction studies of  $Zn_2SnO_4$ /CdS thin films electrodes.

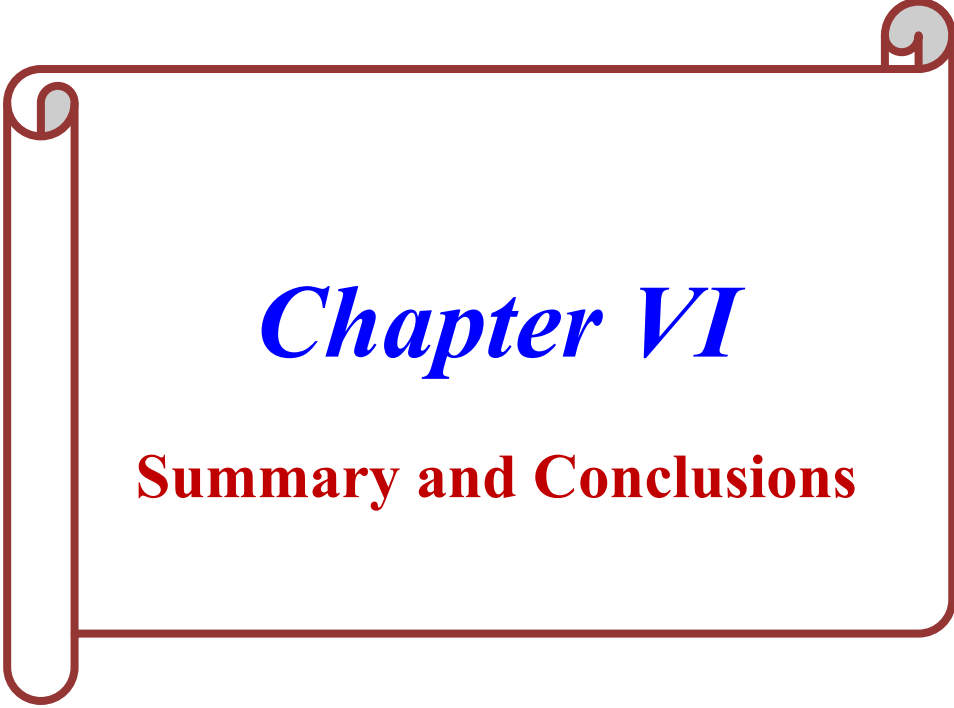
5.3.8. Scanning electron microscopy (SEM) studies of  $Zn_2SnO_4$ /CdS thin film electrodes.

5.3.9. UV-VIS absorption studies of  $Zn_2SnO_4$ /CdS thin film electrodes.

#### 5.4. Photoelectrochemical characterization.

5.4.1. Result of photo-electrochemical measurements.

## **5.5. Conclusion**



# *Chapter VI*

## **Summary and Conclusions**

## CHAPTER VI

### Summary and conclusion

Out of different non-conventional energy sources, thin film solar energy conversion devices are very important and eco-friendly. One of the important alternatives is photovoltaic conversion of solar energy. The use of solar energy as an alternative source mainly depends on providing low cost, large area manufacturing processes. This is achieved by manufacturing solar cells using thin film technology. The photoelectrochemical cell (PEC) based on thin film technology have advantages like low cost, ease of junction formation with electrolyte which provides wide applications.

One of the expanding fields in the physical and chemical sciences is thin film technology. Different branches like material science, nano-science, surface science, applied physics and applied chemistry are related with this technology. Thin film technology is extensively used in thin film electronics. Simple and quick method is favored in the field of materials research to reduce the cost and quick access to the physicochemical properties of the materials.

The synthesis of materials in thin film form is comparatively simple and less expensive than that of growing single crystals. The important techniques for the deposition semiconductors and their alloys may be broadly classified into physical and chemical methods. Among these, spray pyrolysis technique is relatively simple, quick, economic and easy one for thin film deposition over large area. These features are very suitable in applications like gas sensing, dye sensitized solar cell, photoelectrochemical cell (PEC).

In the present work, Zinc Stannate ( $Zn_2SnO_4$ ) thin films have been synthesized on two different substrates which are soda lime glass and FTO coated glass by spray pyrolysis technique. The preparative parameters such as concentration of the precursor solution, substrate temperature, spray solution quantity, substrate to nozzle distance, spray rate have been optimized for the synthesis of ZTO thin films which were phase pure and adherent.

The prepared films were analysed by techniques such as X-ray Diffraction (XRD), Scanning Electron Microscopy (SEM), Atomic Force Microscopy (AFM) and UV-Visible spectroscopy for their detailed study. These films are used to study gas sensing, DSSC and PEC cell performances.

The as-prepared  $\text{Zn}_2\text{SnO}_4$  thin films were used to study gas sensing properties for different gases. Since selectivity of  $\text{Zn}_2\text{SnO}_4$  is more for  $\text{NO}_2$  gas, detailed study of  $\text{NO}_2$  gas sensing is carried out.

The Dye sensitized cells are constructed with proper redox electrolyte and counter electrode. The J-V curves of these cells were used to estimate different performance determining factors like  $J_{sc}$ ,  $V_{oc}$ , FF and PCE. The effect of annealing and CNT doping on DSSC performance of  $\text{Zn}_2\text{SnO}_4$  thin films is also studied.

The CdS layer is coated on spray pyrolytically synthesized thin films of ZTO by CBD method. The photo-electrochemical cell is constructed with proper electrolyte and counter electrode. The current density- voltage (J-V) characteristics of PEC cell are studied to determine the applied bias to photon efficiency (ABPE) with different deposition time of CdS layer over ZTO films.

**Chapter I** deals with brief introduction of study of material i.e.  $\text{Zn}_2\text{SnO}_4$ , gas sensing and solar cells. The applications, classification, characteristics and reaction mechanism of gas sensors are discussed. The importance, generation and applications of solar cells are described in this chapter. The detailed survey of literature on  $\text{Zn}_2\text{SnO}_4$  thin films is described in on the basis of methods of synthesis and applications. In light of work done and the purpose of dissertation is also mentioned at the last.

**Chapter II** deals with the description of the thin film deposition by spray pyrolysis technique. The advantages of the spray pyrolysis technique for thin film deposition over other methods are described in detail. The theoretical background and details of different characterization techniques such as X-ray diffraction (XRD), Scanning Electron Microscopy (SEM), Atomic Force Microscopy (AFM) and UV-Visible spectroscopy are described.

**Chapter III-A** deals with the spray pyrolysis deposition of  $\text{Zn}_2\text{SnO}_4$  thin films and their application for  $\text{NO}_2$  gas sensing. The chapter begins with general introduction of synthesis and applications including gas sensing. In this topic preparation of precursor solution, reaction mechanism for synthesis of  $\text{Zn}_2\text{SnO}_4$  thin films by spray pyrolysis method is explained in detail. 0.1M solutions of  $\text{ZnCl}_2$  and  $\text{SnCl}_2$  were prepared, keeping the Zn/Sn ratio 2:1 by dissolving

required quantity in 50 ml 2-propanol. Table 6.1 represents optimized parameters for synthesis of ZTO thin films.

**Table 6.1 Optimized parameters for spray pyrolytic synthesis of Zn<sub>2</sub>SnO<sub>4</sub> thin films using alcohol solvent**

<b>1</b>	Spray solution concentration	0.1M SnCl <sub>4</sub> .5H <sub>2</sub> O + 0.1 M Zncl <sub>2</sub>
<b>2</b>	Solvent	2-propanol
<b>3</b>	Spray rate	5 ml/min.
<b>4</b>	Spray quantity	50ml
<b>5</b>	Substrate temperature	325 to 400 <sup>0</sup> c
<b>6</b>	Nozzle to substrate distance	28 cm

The as prepared Zn<sub>2</sub>SnO<sub>4</sub> thin films were analyzed by using XRD, SEM, AFM and UV-Visible spectroscopy techniques. The XRD pattern of as-prepared Zn<sub>2</sub>SnO<sub>4</sub> thin films shows nano-crystalline nature evident from broad peaks. The diffraction peaks becomes gradually intense showing improved crystallinity of the material with increasing substrate temperature. The decrease in the film thickness at higher temperature (400°C) may be attributed to the fact that at higher temperature precursor solution decomposes before reaching substrate. With increase in temperature, shift in the position of peak (311) is seen indicating change in the lattice constant and structure becomes perfect cubic. Crystallite sizes calculated by Scherer's formula are listed in table 6.2.

**Table 6.2 Crystallite size and thickness of Zn<sub>2</sub>SnO<sub>4</sub> thin films deposited at various substrate temperatures.**

<b>Substrate</b>	<b>Crystallite</b>	<b>Thickness</b>
------------------	--------------------	------------------

temperature (°c)	size (nm)	(nm)
325	10.3	375
350	12.5	315
375	14.4	267
400	16.7	148

SEM images of Zn<sub>2</sub>SnO<sub>4</sub> thin films were uniform having moderately packed grains with different grain size. No considerable change in the surface structure was seen at increased temperature but particle size increased, small spherical grains are transformed into irregular cuboids. This change in grain shape from spherical to cubic is important to increase gas response. At higher temperature, (> 400°C) films becomes non- uniform. The AFM images of Zn<sub>2</sub>SnO<sub>4</sub> thin showed that morphology of the sample becomes rougher at higher substrate temperature. The RMS (root mean square) surface roughness and actual surface area of the films are listed in table 6.3.

**Table 6.3 RMS roughnesses and actual surface area of projected 9 μm<sup>2</sup> image area of Zn<sub>2</sub>SnO<sub>4</sub> thin films deposited at various substrate temperatures.**

Substrate temperature (°c)	RMS Roughness (nm)	Actual surface area of 3× 3 μm <sup>2</sup>
325	9.5	9.34
350	18.2	9.49
375	24.4	9.68
400	12.4	9.39

It is observed that highest roughness and hence surface area supports for increase in the gas response.

A UV-Visible spectrum of  $Zn_2SnO_4$  thin films shows that, they are extremely transparent in the visible region and the average transmission in the visible region varies from 70% to 90%. 90% transmittance at 850 nm wavelength is observed for the film deposited at 375 °c has been observed. This higher transparency is due to better crystallinity and homogeneity, may show better gas response. From the Tauc plot it is observed that band gap of  $Zn_2SnO_4$  varies from 3.71 eV. to 3.45 eV.

The details of the gas sensing properties of  $Zn_2SnO_4$  thin films are described in this chapter.

The selectivity of the  $Zn_2SnO_4$  thin films was tested using different analyte gases viz.  $NH_3$ , CO, LPG,  $SO_2$ ,  $H_2S$ , and  $NO_2$ . The films deposited at 375 °c were exposed to 200 ppm concentration of above listed gases at 200 °c operating temperature. The maximum response about 25 times the response of other gases was noticed for  $NO_2$  gas. The selectivity of  $Zn_2SnO_4$  thin films towards the gases varied as  $NH_3 < CO < LPG < SO_2 < H_2S < NO_2$ . The sensor based on  $Zn_2SnO_4$  thin films can be used for the selective detection of  $NO_2$  in presence of other gases.

The effect of operating temperature and gas concentration on gas sensing performance of the  $Zn_2SnO_4$  thin films towards  $NO_2$  gas is studied. The operating temperature was optimized by studying gas response for  $Zn_2SnO_4$  thin films (deposited at various substrate temperatures) at different operating temperatures for 200 ppm  $NO_2$ . The maximum sensitivity has been observed at 200 °c operating temperature for the film deposited at 375 °c.

The variations of the gas response for different  $NO_2$  concentrations (50-200 ppm) at 200 °c operating temperature of the  $Zn_2SnO_4$  thin films (deposited at different temperatures) have been studied. The gas response increased noticeably with increase in gas concentration and saturated at 200 ppm. The highest response was noted for the film deposited at 375 °c for all the three concentrations.

The transient response of  $Zn_2SnO_4$  thin films deposited at various temperatures (325- 400 °c) for 50- 200 ppm  $NO_2$  gas concentration at 200 °c operating temperature was also studied. It showed that gas response increases

with NO<sub>2</sub> concentration and also response and recovery time simultaneously. From the film deposited at 375 °c the gas response changes 20 times in 25 sec and recovers in 282 sec. for NO<sub>2</sub> gas. To test durability and ruggedness of the sensor, NO<sub>2</sub> response of the film deposited at 375°C was tested after every month. It was observed that gas response decreases fast initially and remains nearly constant after 240 days After annealing the film gas response was increased and the value was restored.

To improve the response and recovery time, the films were sensitized with palladium (Pd) keeping all the sensing parameters constant. Pd sensitization of ZTO thin films improved all the performance parameters of the gas sensor. The comparison of Zn<sub>2</sub>SnO<sub>4</sub> thin films deposited at 375°C and Pd sensitized Zn<sub>2</sub>SnO<sub>4</sub> films towards NO<sub>2</sub> gas sensing is shown in table 6.4 .

**Table 6.4 Comparison of Pd sensitized and Zn<sub>2</sub>SnO<sub>4</sub> thin film deposited at 375°C for 200 ppm gas concentration at 200° C operating temperature.**

Gas concentration (ppm)	Zn <sub>2</sub> SnO <sub>4</sub>			Pd sensitized Zn <sub>2</sub> SnO <sub>4</sub>		
	Response time (s)	Recovery time (s)	Gas response	Response time (s)	Recovery time (s)	Gas response
50	17	290	2.31	5	179	2.78
100	20	325	2.44	5	201	3.01
200	25	282	2.66	6	221	3.31

**Chapter III-B** deals with the spray pyrolysis deposition of Zn<sub>2</sub>SnO<sub>4</sub> thin films and their application for NO<sub>2</sub> gas sensing

The preparation of precursor solution is explained in detail. The precursor solutions were prepared using water as solvent. The structural characterization was carried out using usual techniques. From the XRD pattern phase pure synthesis of Zn<sub>2</sub>SnO<sub>4</sub> thin films occurs at 400 °c was verified. The SEM micrographs showed cubical flakelike geometry for the Zn<sub>2</sub>SnO<sub>4</sub> thin films

(400 °c substrate temperature). The AFM images showed that, the maximum roughness appears for the film deposited at 400 °c. The band gap of Zn<sub>2</sub>SnO<sub>4</sub> was about 4.9 eV.

The gas (NO<sub>2</sub>) sensing properties of Zn<sub>2</sub>SnO<sub>4</sub> thin films at various substrate temperatures have been studied. The Zn<sub>2</sub>SnO<sub>4</sub> thin films deposited at 400 °c showed higher selectivity and sensitivity towards NO<sub>2</sub> gas. Gas response was found to vary from 1.32 to 29.27 for NO<sub>2</sub> concentration increasing from 8 to 80 ppm. Table 6.5 shows Selectivity coefficient of Zn<sub>2</sub>SnO<sub>4</sub> thin films towards various gases.

**Table 6.5 Selectivity coefficient of Zn<sub>2</sub>SnO<sub>4</sub> thin films deposited at 400 °C towards various gases.**

Gas	Selectivity Coefficient
H <sub>2</sub> S	24.2
NH <sub>3</sub>	19.3
CO	18.1
CO <sub>2</sub>	22.3
SO <sub>2</sub>	20.7
NO <sub>2</sub>	1.00
LPG	24.2

Gas response was found vary from 1.32 to 29.27 for 8 to 80 ppm NO<sub>2</sub> concentration.

The response time for the Zn<sub>2</sub>SnO<sub>4</sub> thin films varies from 3 to 8 s while recovery time is relatively higher than the response time. Response and recovery times of Zn<sub>2</sub>SnO<sub>4</sub> thin films towards NO<sub>2</sub> gas sensing are represented in table 6.6

**Table 6.6 Response and recovery times of Zn<sub>2</sub>SnO<sub>4</sub> films deposited at different substrate temperatures.**

Gas concentrati on (ppm)	300 °C		350 °C		400 °C	
	Respons e time	Recover y time	Respons e time	Recover y time	Respons e time	Recover y time

<b>8</b>	4	35	1	23	8	35
<b>16</b>	5	35	3	27	8	40
<b>24</b>	6	45	4	34	9	45
<b>32</b>	6	50	4	34	9	55
<b>40</b>	8	55	5	36	8	58
<b>60</b>	8	71	8	42	9	61
<b>80</b>	8	34	8	46	7	55

**Chapter IV** deals with Spray Deposited  $Zn_2SnO_4$  thin films and their Dye Sensitized Solar Cell properties.. This chapter begins with history of Dye-Sensitized Solar Cells. The components, basic operating principle and cell performance with time scale of DSSC is described in detail. The survey of literature on zinc stannate as a working electrode for DSSC is described.

Thermo-gravimetric analysis of stannic chloride powder showed thermal decomposition in three steps. The weight loss of 30% is observed in the temperature range  $40^\circ$  to  $80^\circ C$  due to loss of water content in the sample. Further weight loss of 15% is noted in the temperature range  $80^\circ$  to  $275^\circ C$  due to removal of chlorine from  $SnCl_4$  powder. In the third step, 50% weight loss is noted in the temperature range  $275^\circ$  to  $700^\circ C$  which suggests decomposition and crystallization of  $SnO_2$ . The substrate cleaning, preparation of precursor solutions and spray pyrolytic synthesis of tin oxide ( $SnO_2$ ) have been described.

The preparation of precursor solution and spray pyrolytic synthesis of Zinc stannate ( $Zn_2SnO_4$ ) thin film is described. The parameters for deposition of  $Zn_2SnO_4$  thin films by spray pyrolysis method are listed in table 6.7.

**Table 6.7 parameters for spray pyrolytic synthesis of  $Zn_2SnO_4$  thin films**

<b>1</b>	Spray solution composition	0.1M $SnCl_4 \cdot 5H_2O$ + 0.1M $ZnCl_2$
----------	----------------------------	---

2	solvent	De-ionized (DI) water
3	Spray rate	9-10 ml/min.
4	Spray quantity	100ml
5	Substrate temperature	300, 350 and 400 <sup>o</sup> c
6	Nozzle to substrate distance	28 cm

The XRD pattern for thin film prepared by using Zn:Sn ratio other than 2:1 shows mix phases. For the further optimization Zn:Sn ratio is kept constant as 2:1. The XRD pattern of as prepared ZTO thin films at 300, 350 and 400<sup>o</sup>c are studied. The film prepared at 300<sup>o</sup>c shows mixed phases of SnO<sub>2</sub>, ZnO and Zn<sub>2</sub>SnO<sub>4</sub> with major contribution of Zn<sub>2</sub>SnO<sub>4</sub>. The sample prepared at 350<sup>o</sup>c shows less contribution of SnO<sub>2</sub> and ZnO disappeared with major contribution of Zn<sub>2</sub>SnO<sub>4</sub>. XRD pattern of thin film sample prepared at 400<sup>o</sup>c confirms phase pure Zn<sub>2</sub>SnO<sub>4</sub> with cubic phase centered structure.

Comparing XRD patterns of as prepared and annealed Zn<sub>2</sub>SnO<sub>4</sub> samples, it is concluded that there is shift in (311) peak towards higher 2θ upon annealing. The marginal enhancement in the peak intensity after annealing suggests improvement in the crystallinity of Zn<sub>2</sub>SnO<sub>4</sub> thin films. The lattice parameter calculated is 8.6098 Å. From the slow scan XRD pattern between 34<sup>o</sup> to 37<sup>o</sup> of both as prepared and annealed sample, the crystalline size was determined using Scherer's formula. The values were 13 nm and 41 nm respectively. The existence of single peak in the XRD pattern reveals preferential growth of nano-crystallites along (311) plane. The preferential orientation minimizes the surface energy due to which heterogeneous nucleation readily happens at the interface of thin film and substrate.

The comparative XRD spectra for hydrothermally synthesized Zn<sub>2</sub>SnO<sub>4</sub> nanoparticles and spray pyrolytically deposited thin films show that, there exists single peak for spray pyrolytically synthesized thin film. The hydrothermal synthesis of Zn<sub>2</sub>SnO<sub>4</sub> nanoparticles is also described in detail.

SEM images of as deposited Zn<sub>2</sub>SnO<sub>4</sub> thin films showed that no well defined grains have been observed where as annealed sample showed

crystallites of an average diameter of 700 nm developed in the film. Tauc plot of  $Zn_2SnO_4$  thin films before and after annealing showed that the optical band gap decreased from 3.9 to 3.7 eV after annealing. The increase in the band gap of ZTO nanocrystals was observed in comparison with bulk ZTO (3.6 eV). The Tauc plot for the sample prepared with Zn:Sn ratio other than 2:1 showed two absorption edges. The morphology of ZTO thin films was also studied by AFM technique. The surface roughness of as prepared film was 166 nm and for annealed film 71 nm. This decrease in surface roughness is due to increased crystallinity of  $Zn_2SnO_4$  thin films after annealing (51.8 nm to 278 nm) shown in table 6.8.

**Table 6.8 Roughness and particle size measurement of as deposited and annealed  $Zn_2SnO_4$  thin films.**

Sample ID	Roughness (nm)	Particle size (nm)
As prepared	166	51.8
Annealed	71	278

The cyclic voltametric studies of  $SnO_2$ , ZnO and  $Zn_2SnO_4$  thin films prepared by SPT showed that the redox curves of all the three samples have different areas.  $Zn_2SnO_4$  films have maximum area showing maximum conductivity and charge storage capacity as compared to  $SnO_2$  and ZnO thin films. The observed different oxidation peak potential and charge storage capacity proves that the samples are of different chemical composition.

The solar cells were fabricated using a dye-sensitized photoanode. A sputtered Pt electrode and a redox ( $I^-/I_3^-$ ) electrolyte solution. For the photovoltaic measurements of DSCs, the current density-voltage (J-V) curves are studied. From J-V characteristics plots of as prepared, annealed and CNT doped ZTO based solar cells, the photoelectrochemical parameters such as short circuit current density ( $J_{sc}$ ), Open circuit voltage ( $V_{oc}$ ), Fill factor (FF) and power conversion efficiency (PCE) are summarized in table 6.9.

**Table 6.9 Photo-electrochemical parameters of DSSCs of as deposited, annealed and CNT doped Zn<sub>2</sub>SnO<sub>4</sub> thin films.**

Sample ID	J <sub>sc</sub> (mA/cm <sup>2</sup> )	V <sub>oc</sub> (V)	Fill Factor	Efficiency (%)
<b>As-prepared</b>	6.4	0.73	57.72	2.7
<b>Annealed</b>	8.4	0.68	48.86	2.85
<b>CNT doped</b>	7.5	0.75	57.3	3.1

The improvement in the J<sub>sc</sub> for post annealed ZTO device may be due to the improved crystallinity of the sample which can promote easy charge transport within the film due to less grain boundary scattering. The shrinkage in the band gap causing the lowering of conduction band is observed in annealed sample. The observed increase in the photo-conversion efficiency of CNT- doped sample may be the collective effect of provision of conducive channels by CNTs for transport of photo-generated electrons and decreased reflectance of CNT doped ZTO films trapping more photons and enhancing photo-generated charge carriers.

**Chapter V** deals with the photo electrochemical properties of Zn<sub>2</sub>SnO<sub>4</sub>/cds thin films. Chapter begins with general introduction of PEC solar cell including construction and requirements of PEC cells. A detailed survey of literature on preparation of CdS thin films by CBD technique has been described. The preparation of solution and experimental setup of CBD for CdS is described in this chapter. The 1mM concentration solution of CdSO<sub>4</sub> and thiourea [CS(NH<sub>2</sub>)<sub>2</sub>] were used as precursors for thin film deposition on soda line glass and FTO coated glass. The as prepared CdS films were examined by different characterization techniques.

The XRD pattern of deposited CdS films shows nano crystalline nature having cubic structure. From scanning electron micrographs of CdS thin films, it is observed that the sample exhibits nanocrystalline platelets like morphology. Cabbage like structure is seen at low magnification. The platelets are having size of 1 μm and thickness 10-15nm. The films were uniform in structural without

cracks. The UV visible absorption spectra of CdS thin film showed that the absorption starts at 524 nm suggesting band gap of CdS 2.36 eV. The UV-visible transmission spectra of CdS thin films showed 99% transmittance above 400 nm.

The  $Zn_2SnO_4$  thin films were prepared by spray pyrolysis method. The precursors stannic chloride and Zinc chloride with a mole ratio of Zn:Sn as 2:1 were dissolved in DI water and sprayed over FTO coated glass substrates maintained at 400°C. The XRD pattern of as prepared  $Zn_2SnO_4$  thin film by spray pyrolysis shows the formation of phase pure  $Zn_2SnO_4$  thin film with face centered crystal structure. The scanning electron micrograph of as deposited  $Zn_2SnO_4$  thin film clearly showed that the film surface is smooth and crack free and small crystallites are observed on the surface of the film. From UV-visible absorption studies of  $Zn_2SnO_4$  thin film, the band gap of  $Zn_2SnO_4$  was found to be 3.8 eV.

The as prepared  $Zn_2SnO_4$  electrodes were coated by nanocrystalline CdS using chemical bath deposition. The thickness of CdS coating was varied by removing the samples from the bath at the interval of 15 min. The samples were prepared by varying CdS layer thickness (on  $Zn_2SnO_4$  thin films) by changing deposition time for 15, 30 and 45 mins.

The XRD pattern of  $Zn_2SnO_4$ /CdS thin film confirms that it possess both phases i.e. phases of CdS (cubic structure) and  $Zn_2SnO_4$  (face centered cubic crystal structure). The FESEM micrographs of all three samples showed nanocrystalline structure with platelet like morphology. Sample  $S_1$  showed platelets of thickness about 10-15nm, samples  $S_2$  40-50nm thickness with some bud like agglomerates and sample  $S_3$  platelets of thickness 50nm fully covered by CdS particulate.

UV-VIS absorption spectra for  $Zn_2SnO_4$ /CdS thin films showed two absorption edges. One at higher wavelength around 500 nm corresponding to absorption due to CdS and the other at the lower wavelength at around 350 nm which belongs to absorption due to  $Zn_2SnO_4$ . It is noted that with increasing thickness from sample  $S_1$  to  $S_3$ , absorption due to CdS was also increases.

The current density-voltage (J-V) characteristics of PEC are studied under dark and illuminated conditions using three electrode configurations. From the observed value of dark densities and photocurrent densities, the applied bias

photon to current efficiency (ABPE) is calculated. The obtained values are listed in Table 6.10.

**Table 6.10 Dark current densities, photocurrent densities and the applied bias photon to current efficiencies due to variation in deposition time of CdS layer over ZTO thin films.**

<b>Sample ID</b>	<b>Deposition time (min)</b>	<b>Dark current densities (<math>\mu\text{A}/\text{cm}^2</math>)</b>	<b>Photocurrent densities (<math>\text{mA}/\text{cm}^2</math>)</b>	<b>ABPE %</b>
<b>S<sub>1</sub></b>	15	1.4	0.782	0.008
<b>S<sub>2</sub></b>	30	16	1.22	0.012
<b>S<sub>3</sub></b>	45	20	1.71	0.017

The increase in ABPE values may be due to increase in absorber thickness with respect to increase in CdS coating time, which improves number of photo-generated charge carriers.

The stability of  $\text{Zn}_2\text{SnO}_4/\text{CdS}$  photoanodes was studied by potentiostatic measurement [current (I) Vs time(t)] by chopping the light. The photo-response curves of  $\text{CdS}/\text{Zn}_2\text{SnO}_4$  electrodes showed that, the photocurrent value increases as soon as the electrode is illuminated and decreases to zero when the illumination is blocked by the shutter. The prompt switching of current under illumination indicates rapid charge transport in all the three photo-anodes. The non-decayed photocurrent density over 300 sec illuminations proves higher stability of all the samples in the electrolyte.

The stability of  $\text{Zn}_2\text{SnO}_4/\text{CdS}$  photoanodes was studied by potentiostatic measurement [current (I) Vs time (t)] by chopping the light. The photo-response

curves of CdS/Zn<sub>2</sub>SnO<sub>4</sub> electrodes showed that, the photocurrent value increases as soon as the electrode is illuminated and decreases to zero when the illumination is blocked by the shutter. The prompt switching of current under illumination indicates rapid charge transport in all the three photo-anodes. The non-decayed photocurrent density over 300 sec illuminations proves higher stability of all the samples in the electrolyte.

### **Future Scope**

In the present work authors have synthesized Zinc Stannate thin films by simple and inexpensive spray pyrolysis technique. The plausible applications of these films were investigated for gas sensing, DSSC, PEC Solar cell etc.

The authors would like to investigate these films in pristine and doped form for

1. Photocatalytic degradation of organic dyes.
2. Li-Ion rechargeable batteries.
3. Electrochemical supercapacitor etc.

### **List of publication in refereed journals**

1) Development of Zn<sub>2</sub>SnO<sub>4</sub> thin films deposited by spray pyrolysis method and their utility for NO<sub>2</sub> gas sensors at moderate operating temperature, *Journal of Analytical and Applied Pyrolysis*, 107 (2014) 233-241.

2) Synthesis and Characterization of Zinc Stannate Thin films Prepared by Spray Pyrolysis Technique. (*submitted: Journal of Materials Engineering and Performance*).

3) Effect of substrate temperature on gas (NO<sub>2</sub>) sensing properties of Zn<sub>2</sub>SnO<sub>4</sub> thin films. (*submitted: Current Applied Physics*).

4) Photoelectrochemical properties of Zn<sub>2</sub>SnO<sub>4</sub>/CdS thin films. (*Under Preparation*)

### **Paper presented in International and National level conferences.**

1. International Conference on Nanomaterials and Applications, Dept. of physics Shivaji University, Kolhapur during 9-11<sup>th</sup> December, 2008.

2. National conference on Application of Nanomaterials In Synthesis S.M.Joshi College, Hadapsar, pune 28. 13-15<sup>th</sup> feb.2012.

3. International Conference on Environment and Humanity, Eco-Revolution 2012, Colombo, Shrilanka, during 18-20<sup>th</sup> August 2012.

4. International workshop on Nanotechnology and Advanced Functional Materials (NTAFM-2013) at National Chemical Laboratory, Pune, during 24-25<sup>th</sup> July, 2013.

5. International Conference on Physics of Materials and Materials Based Device Fabrication, (ICPM-MDF-2014) Dept. of Physics, Shivaji University, Kolhapur Jan.13-14, 2014.

**Conference / Seminar / Meeting / Workshop / School / Training in International and National levels.**

1. International Conference on: Nanotechnology Materials and Composites for Frontier Applications at Bharati Vidyapeeth Deemed University, Pune during 14<sup>th</sup>-15<sup>th</sup> Oct, 2010.
2. National Conference on Functional Nanomaterials: Synthesis, Characterization and Applications, Department of Physics, University of Pune during 31<sup>st</sup> Jan – 2<sup>nd</sup> Feb, 2013.
3. UGC Sponsored National Seminar on “Developments in Thin Film Processing & Characterization Technology” at BVDU, Yashwantrao Mohite College, Pune during 8<sup>th</sup> – 9<sup>th</sup> Oct, 2012.
4. National conference on Evolving of Scientific terminology in Environmental Science in Regional (Marathi) Language. Sponsored by Govt.of India, Commission for scientific and technical Terminolgy, B. N. Bandodkar College of Science, Thane, 2-3<sup>rd</sup> July 2011.